

# Skoltech

Skolkovo Institute of Science and Technology

Skolkovo Institute of Science and Technology

NASICON-TYPE  
 $\text{Na}_{3+x}\text{Mn}_x\text{V}_{2-x}(\text{PO}_4)_3$   
CATHODE MATERIALS  
FOR SODIUM-ION BATTERIES

*Doctoral Thesis*

by

MAKSIM ZAKHARKIN

DOCTORAL PROGRAM IN MATERIALS SCIENCE AND ENGINEERING

Supervisor  
Professor Keith Stevenson

Moscow – 2020

© Maksim Zakharkin 2020

I hereby declare that the work presented in this thesis was carried out by myself at Skolkovo Institute of Science and Technology, Moscow, except where due acknowledgement is made, and has not been submitted for any other degree.

Candidate (Maksim Zakharkin)

Supervisor (Prof. Keith Stevenson)

## Abstract

The prospects of developing cheaper energy storage technologies along with the applicability of knowledge gained from designing lithium insertion electrodes motivate studies of Na-ion batteries. NASICON-type  $\text{Na}_3\text{V}_2(\text{PO}_4)_3$  cathode materials are considered as promising candidates for high-performance Na-ion batteries due to extremely long cyclic stability and an outstanding ability to operate at high (dis)charge rates. However, its cost-effectiveness can still be improved using transition metals cheaper than vanadium. The replacement of V with Mn in  $\text{Na}_3\text{V}_2(\text{PO}_4)_3$  lowers the cost of the material and enhances the operation voltage compared to that in  $\text{Na}_3\text{V}_2(\text{PO}_4)_3$ .

The  $\text{Na}_{3+x}\text{Mn}_x\text{V}_{2-x}(\text{PO}_4)_3$  ( $0 \leq x \leq 1$ ) materials were obtained by evaporation of a solution followed by thermal annealing. The as-prepared materials were thoroughly analyzed using X-ray diffraction, electron microscopy, atomic emission spectrometry, infrared spectroscopy, thermogravimetry to confirm their composition, morphology and crystal structure.

Electrochemical properties of the  $\text{Na}_{3+x}\text{Mn}_x\text{V}_{2-x}(\text{PO}_4)_3$  ( $0 \leq x \leq 1$ ) materials were studied within two voltage windows: 2.5-3.8 V and 2.5-4.1 V vs.  $\text{Na}/\text{Na}^+$ . Increase in the average charge/discharge voltage is the main visible result of the Mn substitution for the cycling between 2.5 V and 3.8 V. All Mn-substituted samples are characterized by additional high-voltage plateau ( $\sim 3.9$  V) at charge-discharge curves.  $\text{Na}_{3+x}\text{Mn}_x\text{V}_{2-x}(\text{PO}_4)_3$  ( $x \geq 0.4$ ) compositions exhibit 8-10% energy density gain in comparison to  $\text{Na}_3\text{V}_2(\text{PO}_4)_3$  material, and  $\text{Na}_{3.2}\text{Mn}_{0.2}\text{V}_{1.8}(\text{PO}_4)_3$  and  $\text{Na}_{3.4}\text{Mn}_{0.4}\text{V}_{1.6}(\text{PO}_4)_3$  are most preferable in terms of cycling stability.

In order to link electrochemical features with the phase transformations in  $\text{Na}_{3+x}\text{Mn}_x\text{V}_{2-x}(\text{PO}_4)_3$  ( $0 \leq x \leq 1$ ) samples *operando* X-ray powder diffraction was carried out for two charge-discharge cycles in different voltage windows. An intermediate “ $\text{Na}_2\text{M}_2(\text{PO}_4)_3$ ” phase was found for all compounds. When Mn content is low ( $x \sim 0-0.4$ ), it coexists with  $\text{Na}_{3+x}\text{Mn}_x\text{V}_{2-x}(\text{PO}_4)_3$  or  $\text{Na}_{1+x}\text{Mn}_x\text{V}_{2-x}(\text{PO}_4)_3$ . Increase in Mn content extends the length of the solid solution region corresponding to sodiated, intermediate and desodiated phases. The evolution of the Mn and V oxidation states during charge and discharge of  $\text{Na}_4\text{MnV}(\text{PO}_4)_3$  was studied by *operando* X-ray absorption spectroscopy. It was shown that at  $\sim 3.4$  V the redox transition  $\text{V}^{3+}/\text{V}^{4+}$  occurs, and at  $\sim 3.65$  V – the transition  $\text{Mn}^{2+}/\text{Mn}^{3+}$ . An additional voltage plateau at  $\sim 3.9$  V in the  $\text{Na}_4\text{MnV}(\text{PO}_4)_3$  was associated with “unlocking” of the Na1 site in the rhombohedral phase. Reverse insertion of  $\text{Na}^+$  cations proceeds via the entire solid solution region. The experimentally observed discharge capacity increases by  $\approx 14\%$  after raising cut-off voltage. The Mn-rich materials, which demonstrate wider single-phase regions, are shown to outperform the unsubstituted materials in terms of rate-capability and should be preferred for high-power applications.

## Publications

1. Zakharkin, M. V.; Drozhzhin, O. A.; Tereshchenko, I. V.; Chernyshov, D.; Abakumov, A. M.; Antipov, E. V.; Stevenson, K. J. Enhancing Na<sup>+</sup> Extraction Limit through High Voltage Activation of the NASICON-Type Na<sub>4</sub>MnV(PO<sub>4</sub>)<sub>3</sub> Cathode. *ACS Appl. Energy Mater.* **2018**, 1 (11), 5842–5846.
2. Zakharkin M.V., Drozhzhin O.A., Ryazantsev S., Chernyshov D., Kirsanova M.A., Mikheev I. V., Pazhetnov E.M., Antipov E.V., Stevenson K.J. Electrochemical Properties and Evolution of the Phase Transformation Behavior in the NASICON-type Na<sub>3+x</sub>Mn<sub>x</sub>V<sub>2-x</sub>(PO<sub>4</sub>)<sub>3</sub> (0≤x≤1) Cathodes for Na-ion batteries. *J. Power Sources* **2020**, 470, 1–8
3. Anishchenko, D. V.; Zakharkin, M. V.; Nikitina, V. A.; Stevenson, K. J.; Antipov, E. V. Phase Boundary Propagation Kinetics Predominately Limit the Rate Capability of NASICON-Type Na<sub>3+x</sub>Mn<sub>x</sub>V<sub>2-x</sub>(PO<sub>4</sub>)<sub>3</sub> (0≤x≤1) Materials. *Electrochim. Acta* **2020**, 354, 136761.

## Author's Contribution

1. The author is mainly responsible for this work. The author performed the synthesis of the materials, their structural, morphological and electrochemical characterization, analyzed and visualized the data, wrote the original draft and submitted the manuscript.

The co-authors performed the TG analysis, the *operando* X-ray diffraction experiment at the ESRF, performed the sequential Rietveld refinement and the Rietveld refinement of selected patterns, as well as supervised the work.

2. The author is mainly responsible for this work. The author performed the synthesis of the materials, their structural, morphological and electrochemical characterization, the laboratory *operando* X-ray diffraction experiments, performed the sequential Rietveld refinement and the Rietveld refinement of selected patterns, analyzed and visualized the data, wrote the original draft and submitted the manuscript.

The co-authors performed the ATR-FTIR, ICP, EDX, XPS experiments, the *operando* X-ray diffraction experiment at the ESRF, as well as supervised the work.

3. The author performed the synthesis of the materials, their structural and morphological characterization, analyzed and visualized the data, contributed to the manuscript preparation.

The co-authors performed the electrochemical measurements and analyzed its results, wrote the original draft as well as supervised the work.

- The author participated in preparation of the XAS experiments; the co-authors performed the experiments, analyzed and visualized the data.

## Novelty

1. NASICON-type  $\text{Na}_{3+x}\text{Mn}_x\text{V}_{2-x}(\text{PO}_4)_3$  ( $x = 0.1, 0.2, 0.4, 0.6, 0.8$ ) materials are obtained for the first time and their main structural and morphological properties are determined

2. The relationship between their chemical composition and electrochemical properties is found. The compositions with the highest energy density ( $x=0.8$ ) and the compositions with the highest cyclic stability ( $x=0.2, x=0.4$ ) are identified.

3. The kinetic properties of the  $\text{Na}_{3+x}\text{Mn}_x\text{V}_{2-x}(\text{PO}_4)_3$  electrodes are studied. It is found that introduction of Mn adds to NASICON's tolerance of high current rate loads.

4. The (de)intercalation mechanisms of Na in  $\text{Na}_{3+x}\text{Mn}_x\text{V}_{2-x}(\text{PO}_4)_3$  ( $x = 0.2, 0.4, 0.6, 0.8$ ) are revealed for the first time. The phase diagram V-Mn-Na is constructed, and the range of existence of solid solutions  $\text{Na}_{3+x}\text{Mn}_x\text{V}_{2-x}(\text{PO}_4)_3$  is demonstrated.

5. The evolution of the Mn and V oxidation states during charge and discharge of  $\text{Na}_4\text{MnV}(\text{PO}_4)_3$  is shown for the first time in *operando* mode.

## Acknowledgements

I would like to thank my advisor Professor Keith Stevenson who encouraged me with research projects at the time when even the lab has not existed. It has shaped all the following work with its challenging spirit. I would also like to thank Professor Evgeny Antipov for his support of my beginnings and I owe my gratitude to Dr. Oleg Drozhzhin for being always willing to comprehensively respond to my questions.

I am grateful to my colleagues at the Skoltech Center for Energy Sciences and Technologies A. Abakumov, S. Ryazantsev, V. Nikitina, M. Kirsanova, S. Fedotov, D. Aksenov, D. Rupasov, E. Pazhetnov, A. Buchachenko, N. Katorova and A. Zaikin for their significant contributions to research and fruitful discussion of the results as well as to my colleagues at the Chemistry Department of Lomonosov Moscow State University Yu. Velikodniy, S. Istomin, T. Shatalova, N. Khasanova, A. Alekseeva, D. Itkis, D. Anischenko, I. Mikheev, Z. Bobyleva, T. Perfilieva, D. Bonar, I. Tereshchenko, V. Sumanov, A. Shevtsov, V. Shevchenko, N. Luchinin, N. Buryak. I also thank our collaborators V. Shapovalov and A. Guda from the Southern Federal University, as well as D. Chernyshov from the European Center for Synchrotron Radiation. I would also like to express my gratitude to all my labmates for their invaluable contribution to weekdays and weekends.

I finally extend my gratitude to Skolkovo Institute of Science and Technology for the grand opportunity to learn from all these splendid people as well as to Moscow State University, Haldor Topsøe A/S, LG Chem, International Centre for Diffraction Data and Russian Science Foundation for the support of this work.

I would only add my greatest appreciation of the love, support and patience of my friends and family. It would not have been possible without you.

## Table of Contents

Abstract.....	3
Publications.....	5
Author’s Contribution.....	6
Novelty.....	7
Acknowledgements.....	8
Table of Contents.....	9
List of Symbols, Abbreviations.....	12
List of Figures.....	14
List of Tables.....	25
Chapter 1. Introduction.....	26
Chapter 2. Review of the Literature.....	28
2.1 Layered oxides.....	30
2.2 Prussian Blue Analogs.....	33
2.3 Polyanionic compounds.....	35
2.3.1 Sodium transition metal phosphates $\text{NaMPO}_4$ .....	35
2.3.2 Sodium transition metal phosphates $\text{Na}_y\text{M}_2(\text{PO}_4)_3$ .....	40
2.3.3 Structure of $\text{Na}_3\text{V}_2(\text{PO}_4)_3$ .....	43
2.3.4 Synthesis of $\text{Na}_3\text{V}_2(\text{PO}_4)_3$ .....	45
2.3.5 Electrochemical properties of $\text{Na}_3\text{V}_2(\text{PO}_4)_3$ .....	47
2.3.6 Phase transformations during charge and discharge of $\text{Na}_3\text{V}_2(\text{PO}_4)_3$	49
2.3.7 Properties of single and binary transition metal NASICON-type cathodes	52

2.4	Motivation and Objective.....	56
Chapter 3.	Methodology and techniques .....	58
3.1	Synthesis methods .....	58
3.2	Characterization methods .....	59
Chapter 4.	Composition, structure and morphology of the $\text{Na}_{3+x}\text{Mn}_x\text{V}_{2-x}(\text{PO}_4)_3$ .....	65
Chapter 5.	Electrochemical properties of $\text{Na}_{3+x}\text{Mn}_x\text{V}_{2-x}(\text{PO}_4)_3$ .....	74
Chapter 6.	Phase transformation behavior during charge and discharge of $\text{Na}_{3+x}\text{Mn}_x\text{V}_{2-x}(\text{PO}_4)_3$ ( $0 \leq x \leq 1$ ).....	81
6.1	Phase transformations in the 2.5-3.8 V voltage window.....	81
6.1.1	$\text{Na}_3\text{V}_2(\text{PO}_4)_3$ .....	83
6.1.2	$\text{Na}_{3.2}\text{Mn}_{0.2}\text{V}_{1.8}(\text{PO}_4)_3$ and $\text{Na}_{3.4}\text{Mn}_{0.4}\text{V}_{1.6}(\text{PO}_4)_3$ .....	84
6.1.3	$\text{Na}_{3.6}\text{Mn}_{0.6}\text{V}_{1.4}(\text{PO}_4)_3$ .....	85
6.1.4	$\text{Na}_{3.8}\text{Mn}_{0.8}\text{V}_{1.2}(\text{PO}_4)_3$ and $\text{Na}_4\text{MnV}(\text{PO}_4)_3$ .....	86
6.2	Phase transformations in 2.5-4.1 V voltage window. ....	93
Chapter 7.	Kinetic properties of the $\text{Na}_{3+x}\text{Mn}_x\text{V}_{2-x}(\text{PO}_4)_3$ .....	102
7.1	The shape of cyclic voltammograms.....	102
7.2	High-rate performance of the $\text{Na}_{3+x}\text{Mn}_x\text{V}_{2-x}(\text{PO}_4)_3$ .....	106
7.3	Quantitative estimates of kinetic parameters .....	109
7.3.1	Diffusional limitations.....	109
7.3.2	Charge transfer limitations .....	112
7.3.3	Nucleation-induced limitations .....	115
7.3.4	Practical manifestations of the measured rate-limitations.....	117
Chapter 8.	Summary and Outlook .....	119
	Bibliography .....	122

Appendices A.....149

## List of Symbols, Abbreviations

LIB – lithium-ion batteries

UPS – uninterruptible power supplies

SIB – sodium-ion batteries

PVdF – polyvinylidene fluoride

PBA – Prussian blue analogs

DFT – density function theory

GITT – galvanostatic intermittent titration test

NASICON – NA SuperIonic CONductors

NVP –  $\text{Na}_3\text{V}_2(\text{PO}_4)_3$

PEG – polyethylene glycol

TEG – tetraethylene glycol

PAN – polyacrylonitrile ( $\text{C}_3\text{H}_3\text{N}$ )<sub>n</sub>

DMFA – dimethylformamide

BVS – bond valence sum analysis

EPR – electron paramagnetic resonance experiments

ICP-AES – inductively coupled plasma atomic emission spectrometry

EDX – energy dispersive X-ray analysis

SEM – Scanning Electron Microscopy

ATR-FTIR – Attenuated total reflectance Fourier transform infrared  
spectroscopy

MCT – Mercury-Cadmium-Telluride detector

XRPD – X-ray powder diffraction

PITT – Potentiostatic intermittent titration tests

CV – Cyclic voltammetry

EIS – electrochemical impedance spectra

SXRPD – high-resolution synchrotron X-ray powder diffraction

ESRF – European Synchrotron Radiation Facilities

SNBL – Swiss-Norwegian beamline

XANES – X-ray absorption near edge structure

XAS – X-ray absorption spectroscopy

$\theta$  – State of discharge

$\text{Mn}_0\text{V}_2 - \text{Na}_3\text{V}_2(\text{PO}_4)_3$

$\text{Mn}_{0.1}\text{V}_{1.9} - \text{Na}_{3.1}\text{Mn}_{0.1}\text{V}_{1.9}(\text{PO}_4)_3$

$\text{Mn}_{0.5}\text{V}_{1.5} - \text{Na}_{3.5}\text{Mn}_{0.5}\text{V}_{1.5}(\text{PO}_4)_3$

$\text{Mn}_1\text{V}_1 - \text{Na}_4\text{MnV}(\text{PO}_4)_3$

$\Delta E$  – Hysteresis

CEI – cathode/electrolyte interface

$R_{\text{CEI}}$  – resistance of surface layers

$C_{\text{CEI}}$  – capacitance of surface layers

$R_{\text{ct}}$  – charge transfer resistance

$\Omega$  – Ohm

$C_{\text{dl}}$  – double layer capacitance

$\eta$  – overvoltage

## List of Figures

Fig. 2. 1 Construction of a lithium-ion battery comprised of a graphitic anode on copper current collector and a layered oxide cathode on an aluminum current collector [1].....	28
Fig. 2. 2 Cathode materials used in Sodium-ion-based commercialization activities and their locations. The map was created with mapchart.net / CC BY.....	30
Fig. 2. 3 Classification of A-Me-O layered materials [8] .....	31
Fig. 2. 4 Comparison of reversible capacity in charge-discharge cycles of O3-NaFeO <sub>2</sub> cell terminated at different voltages [4] .....	32
Fig. 2. 5 Comparison of operating voltage and reversible capacity of the layered sodium insertion materials [12].....	33
Fig. 2. 6 The schematic diagram of the original Prussian Blue Fe <sub>4</sub> [Fe(CN) <sub>6</sub> ] <sub>3</sub> ·nH <sub>2</sub> O and of the typical Prussian Blue Analogue Na <sub>x</sub> MnFe(CN) <sub>6</sub> [15] .....	34
Fig. 2. 7 Galvanostatic charge-discharge curves at different current densities of Na <sub>x</sub> MnFe(CN) <sub>6</sub> compounds and cyclic stability of half-cells based on Na <sub>x</sub> MnFe(CN) <sub>6</sub> [30].....	35
Fig. 2. 8 Structure of LiFePO <sub>4</sub> [40] and its discharge/charge curve [31] .....	36
Fig. 2. 9 Structures of NaFePO <sub>4</sub> in triphylite (left) and maricite (right) framework (a and b). (c) Coordinations of neighboring FeO <sub>6</sub> octahedra [41].....	37
Fig. 2. 10 Electrochemical profile of NaFePO <sub>4</sub> [43] and discharge curves for NaFe <sub>0.5</sub> Mn <sub>0.5</sub> PO <sub>4</sub> [50].....	39
Fig. 2. 11 NASICON ( <i>e.g.</i> rhombohedral Na <sub>3</sub> V <sub>2</sub> (PO <sub>4</sub> ) <sub>3</sub> ) and anti-NASICON ( <i>e.g.</i> monoclinic Li <sub>3</sub> V <sub>2</sub> (PO <sub>4</sub> ) <sub>3</sub> ) frameworks of general formula A <sub>y</sub> M <sub>2</sub> (XO <sub>4</sub> ) <sub>3</sub> [66].....	41

Fig. 2. 12 The NASICON framework of the $\text{Na}_3\text{V}_2(\text{PO}_4)_3$ described as array of parallel columns linked by $\text{PO}_4$ tetrahedra [69] (left), Electrostatic interactions within a column of the NASICON-type $\text{Na}_3\text{L}_2(\text{PO}_4)_3$ [68] (right) .....	43
Fig. 2. 13 Crystal structure of $\text{Na}_3\text{V}_2(\text{PO}_4)_3$ and the basic repeating lantern unit $\text{V}_2(\text{PO}_4)_3$ , V-O and P-O bond lengths are indicated in Å [72].....	44
Fig. 2. 14 Na-O polyhedra structures of (a) Na1 site (CN=6, octahedral) and (b) Na2 site (CN = 8, four faces are quadrangles, three faces are triangles) in the structure of the $\text{Na}_3\text{V}_2(\text{PO}_4)_3$ [73] .....	44
Fig. 2. 15 Schematic representation of the phase transformations in $\text{Na}_3\text{V}_2(\text{PO}_4)_3$ upon heating [74] .....	45
Fig. 2. 16 Schematic representation of the steps for the $\text{Na}_3\text{V}_2(\text{PO}_4)_3$ synthesis [77].....	46
Fig. 2. 17 Electrochemical properties of $\text{Na}_3\text{V}_2(\text{PO}_4)_3$ , material loading $\sim 3 \text{ mg/cm}^2$ [85] .....	48
Fig. 2. 18 The relative amount of $\text{V}^{4+}$ component, V K-edge XANES spectra and selected Fourier transform spectra of $k^3$ -weighted V EXAFS spectra during first cycle as determined from <i>in situ</i> V XAS experiment in NVP sample [86] .....	48
Fig. 2. 19 Electrochemical voltage-composition curve for $\text{Na}_x\text{V}_2(\text{PO}_4)_3$ [88] and crystal structures of $\text{Na}_4\text{V}_2(\text{PO}_4)_3$ and $\text{Na}_5\text{V}_2(\text{PO}_4)_3$ [87] .....	49
Fig. 2. 20 <i>Operando</i> XRD patterns of electrochemical cell $\text{Na}_3\text{V}_2(\text{PO}_4)_3/\text{Na}$ on charge and discharge at current rate C/10, $\blacklozenge$ - $\text{Na}_3\text{V}_2(\text{PO}_4)_3$ , $\clubsuit$ - $\text{NaV}_2(\text{PO}_4)_3$ [83] .....	51
Fig. 2. 21 (top) Two-dimentional <i>operando</i> XRD pattern of $\text{Na}_3\text{V}_2(\text{PO}_4)_3$ on charge and discharge and (bottom) phase diagram corresponding to two current rates,	

which indicates an increased domain of the solid solution mechanism of Na<sup>+</sup> (de)intercalation in Na<sub>3</sub>V<sub>2</sub>(PO<sub>4</sub>)<sub>3</sub> at lower temperature [91].....51

Fig. 2. 22 Galvanostatic cycling of Na<sub>3</sub>Fe<sub>2</sub>(PO<sub>4</sub>)<sub>3</sub> vs Na in 1.5-3.5 V [96], Na<sub>3</sub>Cr<sub>2</sub>(PO<sub>4</sub>)<sub>3</sub> vs Na in 2.5-4,7 V [97], Na<sub>3</sub>Ti<sub>2</sub>(PO<sub>4</sub>)<sub>3</sub> vs Na between 2.5 and 0 V for the first charge/discharge and subsequent charge/discharge[94].....53

Fig. 2. 23 Galvanostatic cycling of Na<sub>2</sub>TiV(PO<sub>4</sub>)<sub>3</sub>, Na<sub>3</sub>FeV(PO<sub>4</sub>)<sub>3</sub>, Na<sub>4</sub>NiV(PO<sub>4</sub>)<sub>3</sub>, Na<sub>3</sub>CrV(PO<sub>4</sub>)<sub>3</sub>, Na<sub>3</sub>Al<sub>0.5</sub>V<sub>1.5</sub>(PO<sub>4</sub>)<sub>3</sub> [98,100,101,106].....55

Fig. 2. 24 Galvanostatic cycling of Na<sub>3</sub>MnTi(PO<sub>4</sub>)<sub>3</sub> [109], Na<sub>3</sub>MnZr(PO<sub>4</sub>)<sub>3</sub> [110], Na<sub>4</sub>MnCr(PO<sub>4</sub>)<sub>3</sub> [111].....56

Fig. 3. 1 Exterior and design of the electrochemical cell for *operando* X-ray measurements on a Bruker diffractometer [120–122] 63

Fig. 3. 2 Exterior and design of the electrochemical cell for *operando* X-ray measurements at the European Synchrotron [123] 63

Fig. 3. 3 Exterior and design of the electrochemical cell for *operando* X-ray measurements at the Rigaku spectrometer [126] 64

Fig. 4. 1 X-ray powder diffraction data of Na<sub>3+x</sub>Mn<sub>x</sub>V<sub>2-x</sub>(PO<sub>4</sub>)<sub>3</sub> (0≤x≤1). (a) XRPD patterns of Na<sub>3+x</sub>Mn<sub>x</sub>V<sub>2-x</sub>(PO<sub>4</sub>)<sub>3</sub> (0≤x≤1) (21-43°, Co<sub>Kα1</sub>), (b) Unit cell volume and parameters of Na<sub>3+x</sub>Mn<sub>x</sub>V<sub>2-x</sub>(PO<sub>4</sub>)<sub>3</sub> (0≤x≤1). 66

Fig. 4. 2 SEM images of the as-synthesized (a) Na<sub>3</sub>V<sub>2</sub>(PO<sub>4</sub>)<sub>3</sub>, (b) Na<sub>3.2</sub>Mn<sub>0.2</sub>V<sub>1.8</sub>(PO<sub>4</sub>)<sub>3</sub>, (c) Na<sub>3.4</sub>Mn<sub>0.4</sub>V<sub>1.6</sub>(PO<sub>4</sub>)<sub>3</sub>, (d) Na<sub>3.6</sub>Mn<sub>0.6</sub>V<sub>1.4</sub>(PO<sub>4</sub>)<sub>3</sub>, (e) Na<sub>3.8</sub>Mn<sub>0.8</sub>V<sub>1.2</sub>(PO<sub>4</sub>)<sub>3</sub>, (f) Na<sub>4</sub>MnV(PO<sub>4</sub>)<sub>3</sub> 67

Fig. 4. 3 Elemental composition of the as-synthesized  $\text{Na}_{3+x}\text{Mn}_x\text{V}_{2-x}(\text{PO}_4)_3$  ( $x=0, 0.5, 1$ ) according to the results of the ICP-AES and EDX measurements. Na content can be underestimated by EDX due to partial absorption of Na X-rays by the sample. 68

Fig. 4. 4 Thermogravimetric curves of the as-synthesized  $\text{Na}_{3+x}\text{Mn}_x\text{V}_{2-x}(\text{PO}_4)_3$  powders in air. 68

Fig. 4. 5 Infrared spectroscopy data of  $\text{Na}_{3+x}\text{Mn}_x\text{V}_{2-x}(\text{PO}_4)_3$  ( $0 \leq x \leq 1$ ). (a) ATR FTIR spectra of pristine  $\text{Na}_{3+x}\text{Mn}_x\text{V}_{2-x}(\text{PO}_4)_3$  materials revealing the characteristic absorptions bands due to internal vibrations in the phosphate group, (b) The  $\nu_3(\text{PO}_4)$  band position as a function of elemental composition. 70

Fig. 4. 6 (a) XRPD patterns of  $\text{Na}_{3+x}\text{Mn}_x\text{V}_{2-x}(\text{PO}_4)_3$  ( $x = 0, 0.1, 0.5, 1$ ) ( $21-43^\circ$ ,  $\text{CoK}\alpha_1$ ), (b) Unit cell volume and parameters of  $\text{Na}_{3+x}\text{Mn}_x\text{V}_{2-x}(\text{PO}_4)_3$  ( $x = 0, 0.1, 0.5, 1$ ). 71

Fig. 4. 7 SEM images of the  $\text{Na}_{3+x}\text{Mn}_x\text{V}_{2-x}(\text{PO}_4)_3$  ( $x=0, 0.1, 0.5, 1$ ) 72

Fig. 4. 8 CVs of  $\text{Na}_3\text{V}_2(\text{PO}_4)_3$  electrodes: (left) oxalic-based samples without carbon coating (10% Super P carbon in the composite electrode), with glucose-derived coating and with PAN-derived coating. (right) oxalic-based samples with glucose-derived coating and citric-based samples without additional carbon coating. Scan rate is  $0.2 \text{ mV s}^{-1}$ . 73

Fig. 5. 1 Charge/discharge curves for  $\text{Na}_{3+x}\text{Mn}_x\text{V}_{2-x}(\text{PO}_4)_3$  ( $0 \leq x \leq 1$ ) cycled in the 2.5-3.8 V and 2.5-4.1 V voltage windows at C/10 current rate (1<sup>st</sup>, 3<sup>rd</sup> and 4<sup>th</sup> cycles are shown). A voltage step on discharge of  $\text{Na}_{3.4}\text{Mn}_{0.4}\text{V}_{1.6}(\text{PO}_4)_3$  is most probably due to the side reaction with metallic Na electrode [133,134]. 75

Fig. 5. 2 Selected regions of the dQ/dE patterns of  $\text{Na}_{3+x}\text{Mn}_x\text{V}_{2-x}(\text{PO}_4)_3$  ( $0 \leq x \leq 1$ ) cycled in (a) 2.5-3.8V and (b) 2.5-4.1V voltage windows. 76

Fig. 5. 3 PITT measurements upon two successive cycles in the 2.5-3.8V (left) and 2.5-4.1V (right) voltage windows for  $\text{Na}_3\text{V}_2(\text{PO}_4)_3$ ,  $\text{Na}_{3.5}\text{Mn}_{0.5}\text{V}_{1.5}(\text{PO}_4)_3$ , and  $\text{Na}_4\text{MnV}(\text{PO}_4)_3$ . A biphasic “ $\text{Na}_3\text{Mn}_x\text{V}_{2-x}(\text{PO}_4)_3$ ” – “ $\text{Na}_2\text{Mn}_x\text{V}_{2-x}(\text{PO}_4)_3$ ” transition is highlighted for clarity of presentation. A voltage step on discharge of  $\text{Na}_3\text{V}_2(\text{PO}_4)_3$  is most probably due to the side reaction with metallic Na electrode [133,134]. 77

Fig. 5. 4 (a) Discharge capacity for  $\text{Na}_{3+x}\text{Mn}_x\text{V}_{2-x}(\text{PO}_4)_3$  compounds ( $x = 0, 0.2, 0.4, 0.5, 0.6, 0.8, 1$ ) charged to 3.8 V (blue line) and to 4.1 V (red line). (b) Capacity retention for  $\text{Na}_{3+x}\text{Mn}_x\text{V}_{2-x}(\text{PO}_4)_3$  compounds, cycled two times in 2.5-3.8 V voltage window and then in 2.5-4.1 V voltage window at C/10 current rate. (c) Energy density for  $\text{Na}_{3+x}\text{Mn}_x\text{V}_{2-x}(\text{PO}_4)_3$  samples ( $x = 0, 0.2, 0.4, 0.6, 0.8, 1$ ) charged to 3.8 V (blue line) and to 4.1 V (red and green lines) 78

Fig. 5. 5 (a) Discharge capacity retention and coulombic efficiency for  $\text{Na}_4\text{MnV}(\text{PO}_4)_3$  electrodes cycled at C/5 current rate within different potential intervals. At first cycle potential limit was set as 3.8V for all cells. (b) Charge-discharge curves corresponding to the 2<sup>nd</sup> cycle. 79

Fig. 6. 1 (top image) Transformations of the selected region (024 reflection,  $28.5\text{-}30.0^\circ$ ,  $\text{Cu}_{K\alpha 1/K\alpha 2}$ ) of XRPD patterns during *operando* charge-discharge in the 2.5-3.8 V (bottom) and 2.5-4.1 V (top) voltage windows for (a)  $\text{Na}_3\text{V}_2(\text{PO}_4)_3$ , (b)  $\text{Na}_{3.2}\text{Mn}_{0.2}\text{V}_{1.8}(\text{PO}_4)_3$ , (c)  $\text{Na}_{3.4}\text{Mn}_{0.4}\text{V}_{1.6}(\text{PO}_4)_3$ , (d)  $\text{Na}_{3.6}\text{Mn}_{0.6}\text{V}_{1.4}(\text{PO}_4)_3$ , (e)  $\text{Na}_{3.8}\text{Mn}_{0.8}\text{V}_{1.2}(\text{PO}_4)_3$ , (f)  $\text{Na}_4\text{MnV}(\text{PO}_4)_3$ . Transformations of other reflections are

presented on Fig. A 6. Voltage steps on discharge are most probably due to side reactions with metallic Na electrode [133,134]. 82

Fig. 6. 2 (central image) Schematic illustration of the Na<sup>+</sup> deintercalation regimes from Na<sub>3+x</sub>Mn<sub>x</sub>V<sub>2-x</sub>(PO<sub>4</sub>)<sub>3</sub> (0 ≤ x ≤ 1) during Na<sup>+</sup> extraction. The scheme is based on the unit cell volume variation obtained from *operando* XRPD patterns (Table A 1) and electrochemical data. Upper dashed line corresponds to the 4.1 V voltage cut-off. 82

Fig. 6. 3 Transformations of the selected regions (20.0-21.5°, 23.5-25.0°, 28.5-30.0°, 31.5-33.5°, 34.5-37.5°, Cu<sub>Kα1/Kα2</sub>) of XRPD patterns during *operando* charge-discharge in the 2.5-3.8V and 2.5-4.1V voltage windows for Na<sub>3</sub>V<sub>2</sub>(PO<sub>4</sub>)<sub>3</sub>, synthesized by the same procedure, but using different precursors, which are specified on the top graphs. 84

Fig. 6. 4 Appearance of monoclinic 110 reflection at 5.5 degrees during Na<sup>+</sup> (de)intercalation from Na<sub>3.8</sub>Mn<sub>0.8</sub>V<sub>1.2</sub>(PO<sub>4</sub>)<sub>3</sub> 87

Fig. 6. 5 (a) Transformations of the selected region of SXRPD patterns during *operando* charge, (b) unit cell volume of 1 monoclinic and 1 rhombohedral Na<sub>3.8-x</sub>Mn<sub>0.8</sub>V<sub>1.2</sub>(PO<sub>4</sub>)<sub>3</sub> phases, (c) corresponding Le Bail fit for a selected SXRPD pattern (#34) 88

Fig. 6. 6 Similar structural transitions may result in different electrochemical signatures. (a) Electrochemical charge curves, (b) transformations of the selected region of SXRPD patterns and (c) unit cell parameters of Na<sub>3.8-x</sub>Mn<sub>0.8</sub>V<sub>1.2</sub>(PO<sub>4</sub>)<sub>3</sub> (left) and Na<sub>4-x</sub>MnV(PO<sub>4</sub>)<sub>3</sub> (right) within 2.5–3.8 V voltage ranges. 89

Fig. 6. 7 X-ray absorption spectra of Na<sub>4-x</sub>MnV(PO<sub>4</sub>)<sub>3</sub> at the K-edge of Mn during one *operando* charge-discharge cycle 90

Fig. 6. 8 Selected X-ray absorption spectra of  $\text{Na}_{4-x}\text{MnV}(\text{PO}_4)_3$  at the K-edge of Mn during one *operando* charge-discharge cycle 91

Fig. 6. 9 Change in the position of the K-edge of Mn (blue, first cycle) and V (red, cycles 2-4) in  $\text{Na}_4\text{MnV}(\text{PO}_4)_3$  during *operando* charge and discharge in a potential window of 2.5-3.8 V 92

Fig. 6. 10 Transformations of the selected of XRPD patterns during *operando* charge-discharge in the 2.5-3.8V, 2.5-4.1V and 2.5-3.8V voltage windows for  $\text{Na}_{3.4}\text{Mn}_{0.4}\text{V}_{1.6}(\text{PO}_4)_3$  94

Fig. 6. 11 Charge-discharge curves and transformations of the selected regions of SXPD patterns and unit cell parameters of  $\text{Na}_{4-x}\text{MnV}(\text{PO}_4)_3$  cathode material within 2.5 – 3.8 V (a, b, c, d) and 2.5 – 4.0 V (e, f, g, h) voltage range. 95

Fig. 6. 12 Theoretical patterns for  $\text{Na}_{2.96}\text{MnV}(\text{PO}_4)_3$  (electrode charged to 3.5 V) in monoclinic (a) and rhombohedral (b) settings 96

Fig. 6. 13 Theoretical patterns for  $\text{Na}_x\text{MnV}(\text{PO}_4)_3$  in monoclinic setting. a) occupancy of Na sites corresponds to experimentally observed for  $\text{Na}_{2.96}\text{MnV}(\text{PO}_4)_3$  (electrode charged to 3.5 V); b) occupancy of Na1 = 0, c) occupancy of Na2 = 0, d) occupancy of Na3 = 0. 97

Fig. 6. 14 Crystal structure of the (a) initial ( $\text{Na}_{3.66}\text{MnV}(\text{PO}_4)_3$ , rhombohedral structure) and (b) charged to 3.5 V ( $\text{Na}_{2.96}\text{MnV}(\text{PO}_4)_3$ , monoclinic structure) phases [148]. Details of the refinement are given in supplementary materials (Table A 4-Table A 8, Fig. A 8-Fig. A 12). 98

Fig. 7. 1 CVs of  $\text{Na}_{3+x}\text{Mn}_x\text{V}_{2-x}(\text{PO}_4)_3$  ( $x=0, 0.1, 0.5, 1$ ) electrodes at  $50 \mu\text{V}\cdot\text{s}^{-1}$  scan rate in 1 M  $\text{NaPF}_6$  EC/PC (5% FEC) electrolyte. The blue dots and arrows show the direction of the potential steps in chronoamperometric measurements. 103

Fig. 7. 2 Intercalation isotherms for  $\text{Mn}_0\text{V}_2$ ,  $\text{Mn}_{0.1}\text{V}_{1.9}$ ,  $\text{Mn}_{0.5}\text{V}_{1.5}$ ,  $\text{Mn}_1\text{V}_1$  materials constructed from PITT data. Sharp rises in  $\theta$  correspond to biphasic regions. 104

Fig. 7. 3 CVs of  $\text{Mn}_0\text{V}_2$ ,  $\text{Mn}_{0.1}\text{V}_{1.9}$ ,  $\text{Mn}_{0.5}\text{V}_{1.5}$ ,  $\text{Mn}_1\text{V}_1$  electrodes at 0.05, 0.1, 0.15, 0.2 and 0.3 mV/s. 105

Fig. 7. 4 Charge/discharge profiles for  $\text{Mn}_0\text{V}_2$ ,  $\text{Mn}_{0.5}\text{V}_{1.5}$  and  $\text{Mn}_1\text{V}_1$  materials at C/10, C/5, C/2, 1C, 2C and 5C rates. Dashed line shows the state-of-charge where the  $\Delta E$  values were estimated. 107

Fig. 7. 5 Hysteresis ( $\Delta E$ ) between charging curve at C/10 and discharge curves at C/10, C/5, C/2, 1C, 2C and 5C rates. 109

Fig. 7. 6 Apparent diffusion coefficients for  $\text{Mn}_0\text{V}_2$ ,  $\text{Mn}_{0.1}\text{V}_{1.9}$ ,  $\text{Mn}_{0.5}\text{V}_{1.5}$  and  $\text{Mn}_1\text{V}_1$  materials as determined from PITT data in the single-phase regions as a function of formal potential (left) and of Na content (right). Dashed line indicates the phase transformation potential. 111

Fig. 7. 7 EIS spectra (symbols) of  $\text{Mn}_0\text{V}_2$ ,  $\text{Mn}_{0.1}\text{V}_{1.9}$ ,  $\text{Mn}_{0.5}\text{V}_{1.5}$ ,  $\text{Mn}_1\text{V}_1$  electrodes and the fits to the equivalent circuit. Potential values are indicated in the plots. 113

Fig. 7. 8 Equivalent circuit used to fit the experimental impedance spectra.  $R_{\text{sol}}$  – solution resistance;  $R_{\text{CEI}}$  – resistance of surface layers;  $C_{\text{CEI}}$  – capacitance of surface layers;  $R_{\text{ct}}$  – charge transfer resistance, W – finite Warburg element for the case of 3D diffusion ( $R_{\text{d}}$ ,  $C_{\text{d}}$  – resistance and capacitance of diffusion);  $C_{\text{dl}}$  – double layer

capacitance. In the fitting procedure CPE elements were used instead of pure capacities. 113

Fig. 7. 9 Impedance spectra of  $\text{Na}_{3+x}\text{Mn}_x\text{V}_{2-x}(\text{PO}_4)_3$  ( $x=0, 0.1, 0.5, 1$ ) electrodes at  $E = 3.360$  V ( $\text{Mn}_0\text{V}_2$ ),  $E = 3.360$  V ( $\text{Mn}_{0.1}\text{V}_{1.9}$ ),  $E = 3.400$  V ( $\text{Mn}_{0.5}\text{V}_{1.5}$ ),  $E = 3.445$  V ( $\text{Mn}_1\text{V}_1$ ). 115

Fig. 7. 10 Current transients for the  $\text{Mn}_0\text{V}_2$ ,  $\text{Mn}_{0.1}\text{V}_{1.9}$ ,  $\text{Mn}_{0.5}\text{V}_{1.5}$  and  $\text{Mn}_1\text{V}_1$  electrodes registered after potential steps corresponding to  $\eta \sim 25$  mV in linear (a) and semilogarithmic (b) coordinates. Potential dependence of the nucleation rate constants,  $k_{\text{nucl}}$  (c). 117

Fig. 7. 11 C-rate dependence of the reduction in the specific energy (%). 118

Fig. A 1 Schematic representation of the “lantern” units  $\text{Mn}_x\text{V}_{2-x}(\text{PO}_4)_3$  in the as-synthesized  $\text{Na}_{3+x}\text{Mn}_x\text{V}_{2-x}(\text{PO}_4)_3$  ( $x=0, 0.5, 1$ ), with Na ions located in the interstitial positions [148]. 149

Fig. A 2 Na1 and Na2 polyhedra structures in the as-synthesized  $\text{Na}_{3+x}\text{Mn}_x\text{V}_{2-x}(\text{PO}_4)_3$  ( $x=0$  and  $1$ ) [148] 149

Fig. A 3 (left) X-ray absorption spectra of the  $\text{Na}_4\text{MnV}(\text{PO}_4)_3$  powder at the K-edge of Mn (left) and  $\text{Mn}2p_{3/2}$  X-ray photoelectron spectra of the  $\text{Na}_{3.5}\text{Mn}_{0.5}\text{V}_{1.5}(\text{PO}_4)_3$  and  $\text{Na}_4\text{MnV}(\text{PO}_4)_3$  powders with the  $\text{Mn}^{2+}$  and  $\text{Mn}^{3+}$  standards. 150

Fig. A 4 SEM images and the histograms of the  $\text{Na}_{3+x}\text{Mn}_x\text{V}_{2-x}(\text{PO}_4)_3$  particle size distributions derived with the ImageJ software [184] (a)  $x=0$ , synthesized with oxalic acid, (b)  $x=1$ , synthesized with oxalic acid, (c)  $x=1$ , synthesized with citric acid. 150

Fig. A 5 Le Bail fit of XRPD data of the as-synthesized  $\text{Na}_{3+x}\text{Mn}_x\text{V}_{2-x}(\text{PO}_4)_3$  ( $0 \leq x \leq 1$ ) in the  $R3c$  space group. The peculiarities in the small angle area below 10 degrees are related to the features of the particular Image Plate detector. Measured with a Huber G670 Guiner Camera (Co  $K\alpha_1$  radiation). 151

Fig. A 6 Transformations of the selected regions (20.0-21.5°, 23.5-25.0°, 28.5-30.0°, 31.5-33.5°, 34.5-37.5°,  $\text{Cu}_{K\alpha 1/K\alpha 2}$ ) of XRPD patterns during *operando* charge-discharge in the 2.5-3.8V and 2.5-4.1V voltage windows for  $\text{Na}_3\text{V}_2(\text{PO}_4)_3$ ,  $\text{Na}_{3.2}\text{Mn}_{0.2}\text{V}_{1.8}(\text{PO}_4)_3$ ,  $\text{Na}_{3.4}\text{Mn}_{0.4}\text{V}_{1.6}(\text{PO}_4)_3$ ,  $\text{Na}_{3.5}\text{Mn}_{0.5}\text{V}_{1.5}(\text{PO}_4)_3$ ,  $\text{Na}_{3.6}\text{Mn}_{0.6}\text{V}_{1.4}(\text{PO}_4)_3$ ,  $\text{Na}_{3.8}\text{Mn}_{0.8}\text{V}_{1.2}(\text{PO}_4)_3$ ,  $\text{Na}_4\text{MnV}(\text{PO}_4)_3$ . 152

Fig. A 7 Schematic illustration of the  $\text{Na}^+$  deintercalation regimes from  $\text{Na}_{3+x}\text{Mn}_x\text{V}_{2-x}(\text{PO}_4)_3$  ( $0 \leq x \leq 1$ ) during  $\text{Na}^+$  extraction 153

Fig. A 8 Experimental, calculated and difference synchrotron X-ray diffraction patterns of pristine  $\text{Na}_{4-x}\text{MnV}(\text{PO}_4)_3$  after the Rietveld refinement. The contributions from the cell, anode and current collectors are omitted. Top row of bars indicate the reflections of the  $\text{NaMnPO}_4$  admixture (2.7 wt.%). 159

Fig. A 9 Experimental, calculated and difference synchrotron X-ray diffraction patterns of  $\text{Na}_{4-x}\text{MnV}(\text{PO}_4)_3$  charged to 3.5V after the Rietveld refinement. The contributions from the cell, anode and current collectors are omitted. Top row of bars indicate the reflections of the  $\text{NaMnPO}_4$  admixture. 160

Fig. A 10 Experimental, calculated and difference synchrotron X-ray diffraction patterns of  $\text{Na}_{4-x}\text{MnV}(\text{PO}_4)_3$  charged to 3.8V after the Rietveld refinement. The contributions from the cell, anode and current collectors are omitted. Top row of bars indicate the reflections of the  $\text{NaMnPO}_4$  admixture. 161

Fig. A 11 Experimental, calculated and difference synchrotron X-ray diffraction patterns of  $\text{Na}_{4-x}\text{MnV}(\text{PO}_4)_3$  charged to 4.0V after the Rietveld refinement. The contributions from the cell, anode and current collectors are omitted. Top row of bars indicate the reflections of the  $\text{NaMnPO}_4$  admixture. 162

Fig. A 12 Experimental, calculated and difference synchrotron X-ray diffraction patterns of  $\text{Na}_{4-x}\text{MnV}(\text{PO}_4)_3$  discharged to 2.5V after the Rietveld refinement. The contributions from the cell, anode and current collectors are omitted. Top row of bars indicate the reflections of the  $\text{NaMnPO}_4$  admixture. 163

## List of Tables

Table 4. 1 Unit cell parameters for the as-synthesized $\text{Na}_{3+x}\text{Mn}_x\text{V}_{2-x}(\text{PO}_4)_3$ ( $0 \leq x \leq 1$ ) in the s.g. <i>R3c</i> . .....	65
Table 4. 2 Unit cell parameters for the as-synthesized $\text{Na}_{3+x}\text{Mn}_x\text{V}_{2-x}(\text{PO}_4)_3$ ( $0 \leq x \leq 1$ ) in the s.g. <i>R3c</i> . .....	70
Table A 1 Unit Cell Volume ( $\text{Å}^3$ ) of $\text{Na}_{3+x}\text{Mn}_x\text{V}_{2-x}(\text{PO}_4)_3$ ( $0 \leq x \leq 1$ ) at different states of charge .....	153
Table A 2 Crystallographic data for $\text{Na}_{4-x}\text{MnV}(\text{PO}_4)_3$ at different state of charge. ....	154
Table A 3 Selected interatomic distances ( $\text{Å}$ ) for $\text{Na}_{4-x}\text{MnV}(\text{PO}_4)_3$ at different states of charge .....	155
Table A 4 Fractional atomic coordinates, occupancy factors and atomic displacement parameters for pristine $\text{Na}_{4-x}\text{MnV}(\text{PO}_4)_3$ . ....	157
Table A 5 Fractional atomic coordinates, occupancy factors and atomic displacement parameters for $\text{Na}_{4-x}\text{MnV}(\text{PO}_4)_3$ charged to 3.5V. ....	157
Table A 6 Fractional atomic coordinates, occupancy factors and atomic displacement parameters for $\text{Na}_{4-x}\text{MnV}(\text{PO}_4)_3$ charged to 3.8V. ....	157
Table A 7 Fractional atomic coordinates, occupancy factors and atomic displacement parameters for $\text{Na}_{4-x}\text{MnV}(\text{PO}_4)_3$ charged to 4.0V. ....	158
Table A 8 Fractional atomic coordinates, occupancy factors and atomic displacement parameters for $\text{Na}_{4-x}\text{MnV}(\text{PO}_4)_3$ discharged to 2.5V. ....	158

## Chapter 1. Introduction

The development of lithium-ion batteries (LIB) is one of the most significant achievements of the XX century. High specific energy of ~250 Wh/kg and stability over 1000 cycles allowed using LIBs in portable phones and laptops providing people with an opportunity to stay in touch almost everywhere and work far from the office. Despite the fact that various types of batteries find many new applications today in various industries, LIBs are not the optimal solution for all of them. For instance, the progress of IT industry is impossible without continuous storage of large amounts of data in data-centers, therefore uninterruptible power supplies (UPS) are needed for them. For these purposes LIBs are too expensive today, and heavy lead-acid batteries are generally used, which are housed over large areas adhering to a number of strict safety measures and should be replaced every few years due to their short service life. Different battery specifications are necessary for peak shifting in electricity grids, load leveling on electric car charging stations, powering of warehouse loaders or in many other niche application. Active materials used in sodium-ion batteries (SIB) vary from LIB materials in capacity, power and cost. At the same time LIB manufacturing facilities vastly built in recent years are suitable for production of SIBs. Thus SIBs can be an appropriate alternative for energy storage technologies used today in various industries as well as can open new niche applications for energy storage.

One of the most prospective cathode materials for high power SIBs are polyanionic compounds with the NASICON structure. In order to effectively employ their superionic properties it is necessary to increase the energy density of materials based on this structural type. This work is devoted to the study of effect of vanadium

substitution by manganese in  $\text{Na}_3\text{V}_2(\text{PO}_4)_3$  compounds. In addition to increasing the operating potential of the materials, this substitution made it possible to increase the reversibly extractable amount of sodium cations, as well as to reduce the relative capacity losses at increased current rates.

## Chapter 2. Review of the Literature

A typical metal-ion battery consists of an anode, a cathode and a porous separator soaked in electrolyte (Fig. 2. 1). The difference in electrode's electrochemical potentials is the driving force for an atom to oxidize, leave an electrode structure in the ionic form and be carried by electrolyte to the opposite electrode. Correspondingly, electron released from the oxidation reaction feeds the load while flowing through the external circuit on discharge and is accepted on the opposite electrode by reduction reaction.

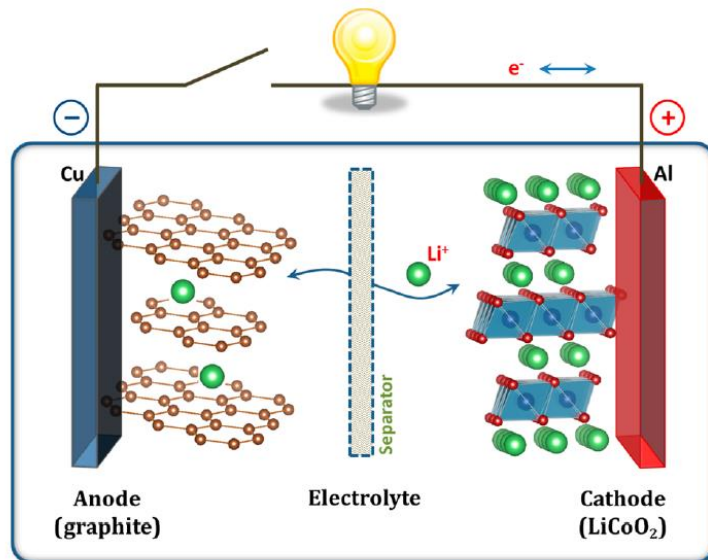


**Fig. 2. 1 Construction of a lithium-ion battery comprised of a graphitic anode on copper current collector and a layered oxide cathode on an aluminum current collector [1]**

The prospects of developing cheaper energy storage technologies along with the applicability of knowledge gained from designing lithium insertion electrodes motivate investigation of SIB. Sodium is an abundant metal, its concentration in Earth's crust is ca. 23000 ppm compared to 20 ppm for lithium [1,2]. The price of sodium-containing precursors for Na-ion cathode materials is about \$150/ton, which is much lower than ca. \$5000/ton of lithium carbonate [3]. Sodium has a suitable

redox potential of  $\text{Na}^+/\text{Na}$  only 0.3 V less electropositive than lithium, so the voltage of Na-ion cells remains high enough in comparison with other types of batteries with the advantage of utilizing electrolytes with lower decomposition potential. Atomic weight of sodium is 3.33 times heavier than that of lithium, so lower gravimetric capacities are expected for Na-ion batteries, however, molecular weights of e.g.  $\text{A}_3\text{V}_2(\text{PO}_4)_3$  for  $\text{A}=\text{Na}$  (465 g/mol) is only 10% heavier than for  $\text{A}=\text{Li}$  (408 g/mol). Also sodium does not form alloys with aluminum, therefore Al foil can replace expensive Cu negative current collector.

Historically, sodium-ion batteries were on development track together with lithium-ion batteries, however, due to better performance exhibited by LIBs and, which is of no small importance, due to insufficient research conditions to handle sodium metal, SIBs did not attract enough attention in the XX century [4]. Nowadays, SIBs experience a rebirth in scientific community and provide the promise for implementation of Na-ion batteries in large scale energy applications. As next steps, recent developments in Na-ion field will be reviewed and assessed [5,6].

In the last 10 years more than 10 companies proposed solutions based on Na-ion technologies. Majority of them use hard carbon as an anode active material and one of the three types of cathode materials: layered oxides, Prussian blue analogs or polyanionic materials (Fig. 2. 2). The advantages and drawbacks of these types of materials are discussed in details in the next sections.

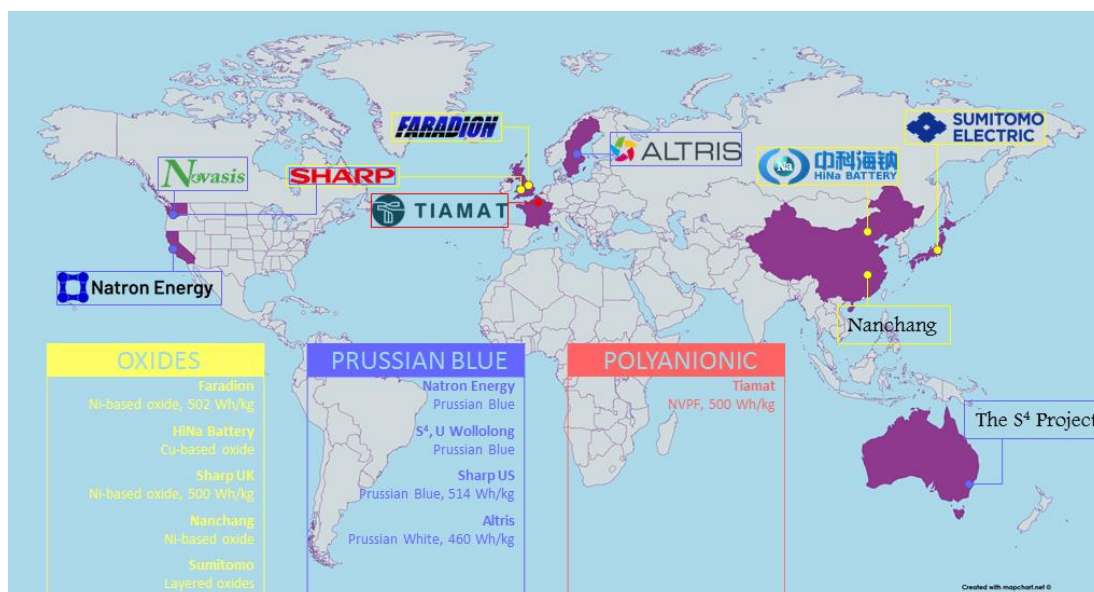


**Fig. 2. 2 Cathode materials used in Sodium-ion-based commercialization activities and their locations. The map was created with [mapchart.net](http://mapchart.net) / [CC BY](https://creativecommons.org/licenses/by/4.0/).**

## 2.1 Layered oxides

In the 1970s, the structures of dichalcogenides and layered oxides were extensively studied, and a classification based on the accommodation of alkali-ions at different environment was proposed by Delmas *et al.* [7], which is illustrated in Fig. 2. 3.

O3-type layered structure comprises ABCABC oxygen layers stacking, where A, B and C correspond to one of three possible ways of oxygen atoms arrangement relative to other hexagonal layers  $(MO_2)_n$ . Alkali ions occupy octahedral (O) sites between three (3) possible layers (AB, CA, BC).  $LiMO_2$  materials form O3 type structure for  $M = Ni, Co$  and mixtures with Mn, however Ti, Fe and Mn do not form O3- $LiMO_2$  in this type as single metal compositions. Among  $NaMO_2$  materials a well-known  $\alpha$ - $NaFeO_2$  forms in the O3-type layered structure.

P2-type phases comprise prismatic (P) sites for alkali ions between two (2) possible layers (AA and BB). Li-containing compounds do not form such phases as small lithium ions cannot stabilize the P2 structure.

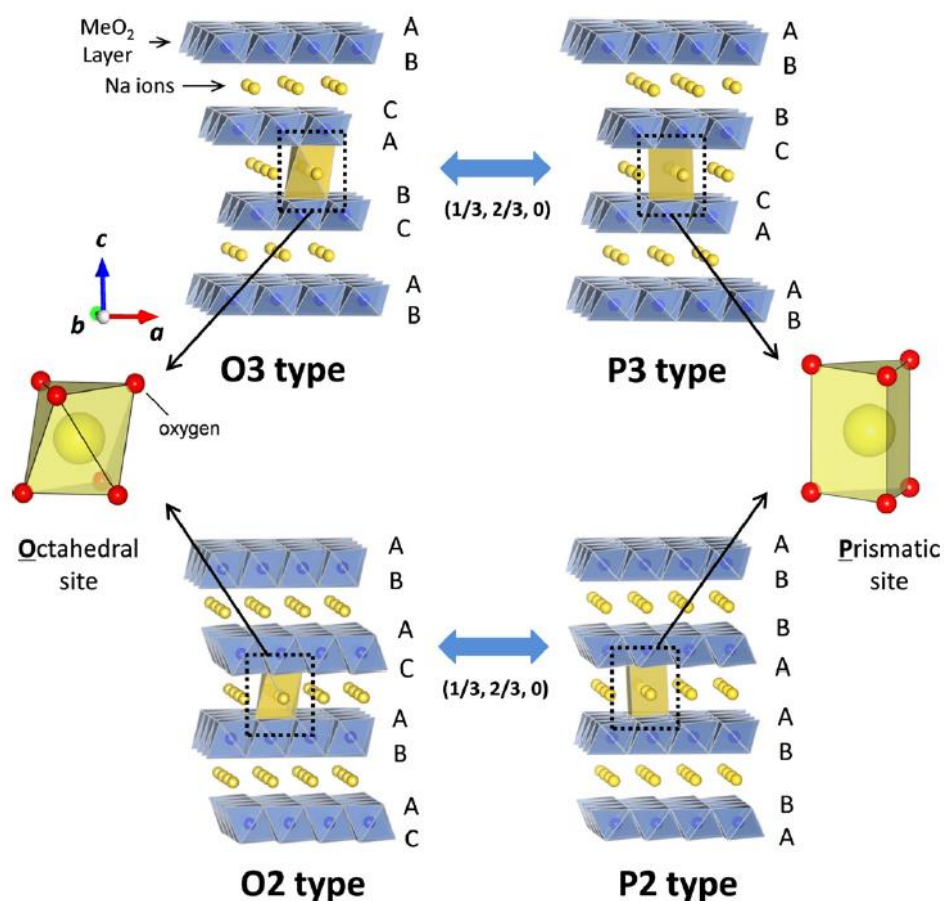
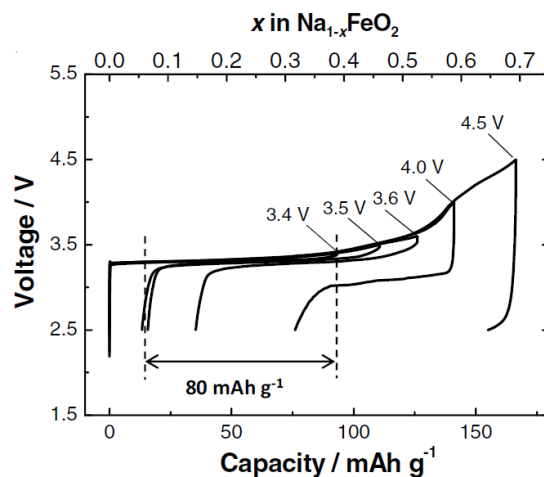


Fig. 2. 3 Classification of A-Me-O layered materials [8]

A vast range of electrochemically active sodium layered compounds has been studied as possible cathode materials for Na-ion batteries. Generally, they can be categorized as O3- and P2-type layered materials.

O3-type materials experience the same capacity limitation ( $<120-140$  mAh/g) corresponding to irreversible structural changes with extracting of more than 0.5 Na as their lithium counterparts as shown in Fig. 2. 4. This is due to migration of

transition metal from their site in the slab  $(\text{MO}_2)_n$  to the interslab space [4], which can be suppressed by selection of an adequate combination of d-metals.



**Fig. 2. 4 Comparison of reversible capacity in charge-discharge cycles of O3-NaFeO<sub>2</sub> cell terminated at different voltages [4]**

Due to differences in the structure P2-type layered oxides do not suffer from this problem, so they utilize Na-poor region in  $\text{Na}_x\text{MO}_2$  for  $x < 2/3$ , which leads to higher energy densities generally provided by P2-type layered oxides. However, large volume changes accompany Na extraction and lead to isolation of the active material from conductive coating and current collector, which was shown for P2-type structure material [9]. Another issue for layered oxides is that many of them were found to be hygroscopic [10], which can complicate the production process. The particles absorb atmospheric water, which increases interslab distance and induces phase-change [11] or leads to NaOH formation, following by defluorination of PVdF binder and agglomeration of particles, which hampers uniform pasting of slurry on current collector [4].

Some of the remarkable layered cathodes include  $\text{Na}_x[\text{Fe}_{0.5}\text{Mn}_{0.5}]\text{O}_2$ , which was shown to deliver 190 mAh/g [12],  $\text{NaNi}_{1/3}\text{Fe}_{1/3}\text{Mn}_{1/3}\text{O}_2$  was able to maintain at

100 mAh/g for 150 cycles at C/2 rate [13] or lithium-substituted layered oxide  $\text{Na}_{0.85}\text{Li}_{0.17}\text{Ni}_{0.21}\text{Mn}_{0.64}\text{O}_2$  to exhibit 65 mAh/g of discharge capacity at high rate of 25C [14] (Fig. 2. 5).

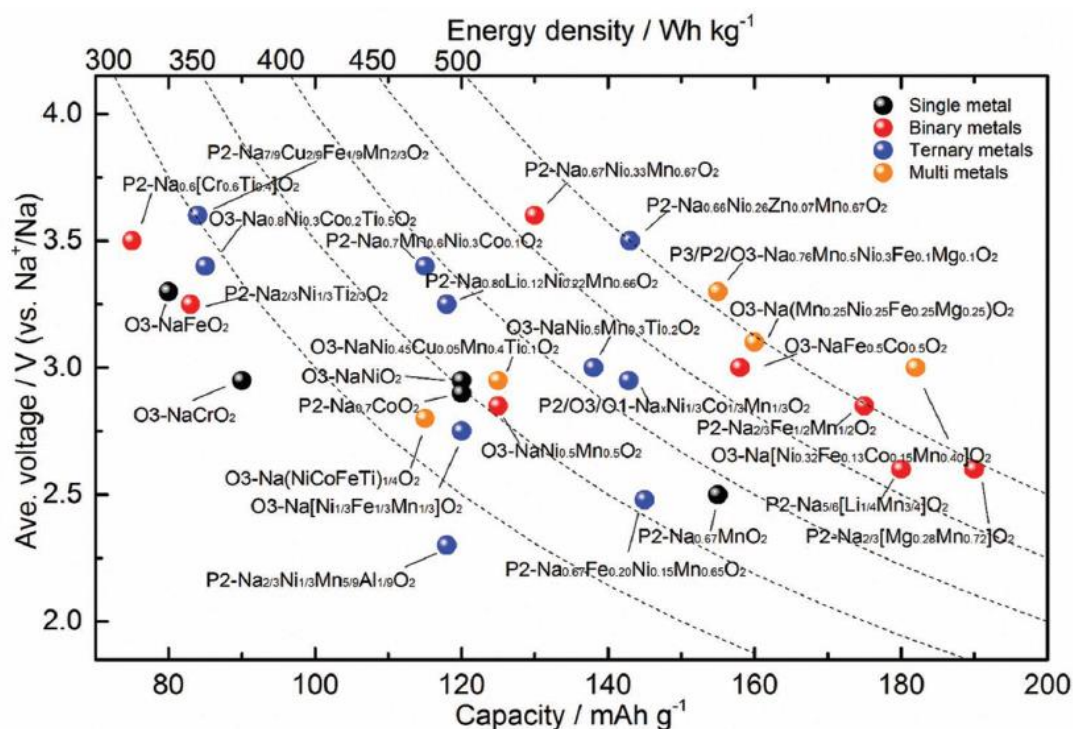


Fig. 2. 5 Comparison of operating voltage and reversible capacity of the layered sodium insertion materials [12]

## 2.2 Prussian Blue Analogs

Prussian blue ( $\text{Fe}[\text{Fe}(\text{CN})_6] \cdot n\text{H}_2\text{O}$ ) and its analogs ( $\text{A}_x\text{M}[\text{M}'(\text{CN})_6]_{(1-y)} \cdot \square_y \cdot n\text{H}_2\text{O}$ ; A: alkali metal, M: transition metal ion coordinated to the nitrogen atom, M': transition metal ion coordinated to the carbon atom and  $\square$ :  $[\text{M}'(\text{CN})_6]$  vacancy;  $0 \leq x \leq 2$ ,  $0 \leq y < 1$ ) are a large family of transition-metal hexacyanometallates, which are prospective electrode materials for sodium- and potassium-ion batteries (Fig. 2. 6).

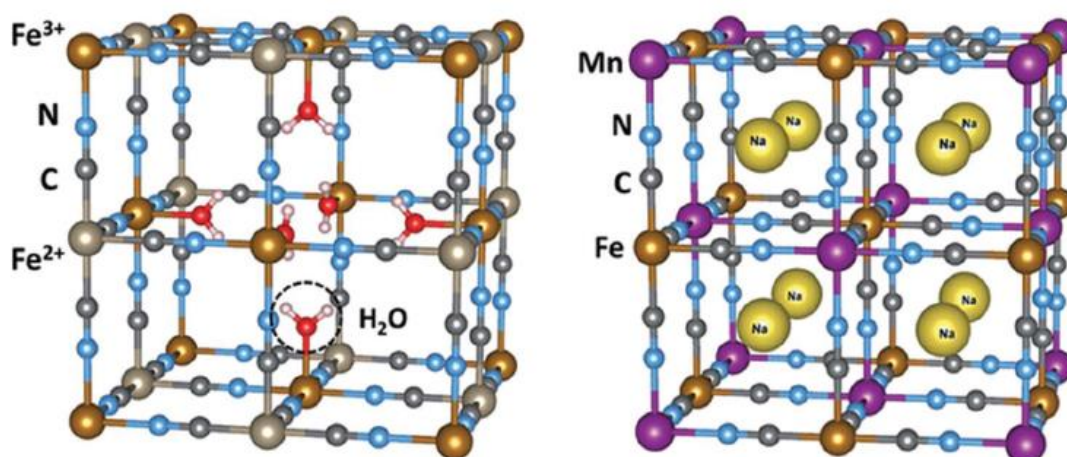
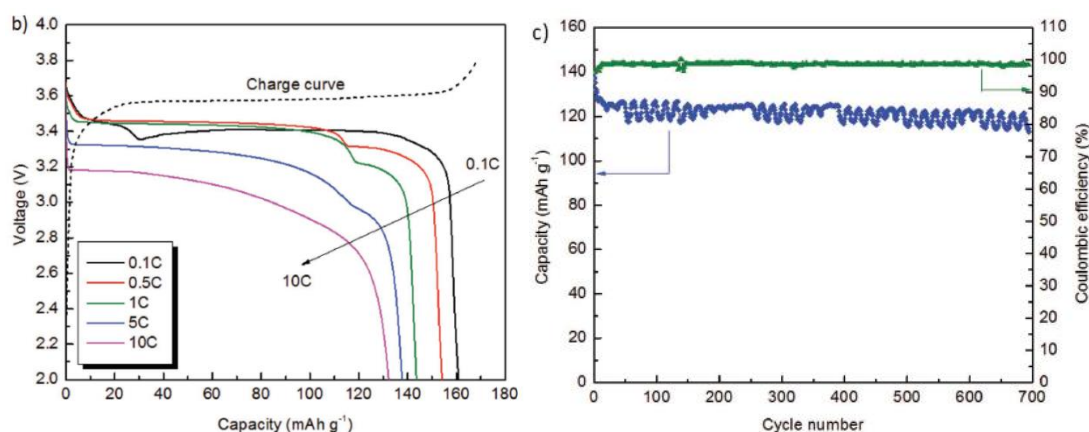


Fig. 2. 6 The schematic diagram of the original Prussian Blue  $\text{Fe}_4[\text{Fe}(\text{CN})_6]_3 \cdot n\text{H}_2\text{O}$  and of the typical Prussian Blue Analogue  $\text{Na}_x\text{MnFe}(\text{CN})_6$  [15]

Since the Prussian Blue analogs (PBA) are commonly prepared by chemical precipitation synthesis methods, their crystal structure often contains vacancies and coordinated water, which leads to weakened M-CN-M' framework resulting in structure distortions [16]. This can cause low values of electrochemical capacity and coulombic efficiency, as well as losses at high current rates [17]. In order to obtain water free Prussian Blue Analogs, several approaches are used such as developing macro-sized mesoporous material particles [18], various methods of samples dehydration [19,20], introducing of higher Na amount into octahedral centers of the subunits [21,22]. Synthesis by hydrothermal methods or implementation of slow chemical precipitation techniques may also result in high-quality Prussian Blue Analogs. Nevertheless, above 15% of coordinated, interstitial and adsorbed water is still present in their lattices [18]. Some of the best-performing Prussian Blue Analogs are submicro-sized cubes, mesoporous particles are developed to improve the rate capability by means of shorter  $\text{Na}^+$  diffusion path [23–26]. In order to increase the operating potential of Prussian Blue Analogs different transition metals are employed

at M and M' sites [27]. Among various Prussian Blue Analogues several examples should be noted, such as  $\text{Na}_{0.61}\text{Fe}[\text{Fe}(\text{CN})_6]_{0.94} \cdot 0.06 \cdot 2.6 \text{H}_2\text{O}$  with low defect concentration exhibiting high capacity of 170 mAh/g without evident capacity loss for 150 cycles [28].  $\text{Ni}_{0.3}\text{Co}_{0.7}[\text{Fe}(\text{CN})_6]$  shows specific capacity of 140 mAh/g and 83% capacity retention at 5C rate over 600 cycles [29]. In sodium-ion batteries of Novasis and Sharp Labs of America  $\text{Na}_x\text{MnFe}(\text{CN})_6 \cdot y\text{H}_2\text{O}$  are used, which deliver 160 mAh/g at C/10 rate and display reversible capacity of 120 mAh/g after 700 cycles (Fig. 2. 7) [30]



**Fig. 2. 7 Galvanostatic charge-discharge curves at different current densities of  $\text{Na}_x\text{MnFe}(\text{CN})_6$  compounds and cyclic stability of half-cells based on  $\text{Na}_x\text{MnFe}(\text{CN})_6$  [30]**

## 2.3 Polyanionic compounds

### 2.3.1 Sodium transition metal phosphates $\text{NaMPO}_4$

The polyanionic compounds based on  $\text{LiMPO}_4$  ( $\text{M} = \text{Fe}, \text{Mn}, \text{Ni}, \text{Co}$ ) are widely studied as materials for electrodes since the discovery of the electrochemical performance of  $\text{LiFePO}_4$  [31]. The use of polyanions such as  $(\text{SO}_4)^{2-}$ ,  $(\text{PO}_4)^{3-}$ ,  $(\text{AsO}_4)^{3-}$  etc. is motivated by the inductive effect of  $(\text{XO}_n)^{m-}$ , which allows tuning the potential of the of the  $\text{M}^{n+}/\text{M}^{(n+1)+}$  redox couple.

Crystal structure of  $\text{LiFePO}_4$  is classified as triphylite-type (derived from the natural mineral olivine  $(\text{Mg, Fe})_2\text{SiO}_4$  structure type) structure with distorted hexagonal close-packed oxygen lattice. Li and Fe are located in two distinct octahedral sites in the framework structure of  $\text{PO}_4$  tetrahedra (Fig. 2. 8). The unit-cell adopts an orthorhombic symmetry described in the  $Pnma$  space group. Lithium diffusion is one-dimensional and proceeds along  $[010]$  [32]. Its capacity almost reaches theoretical values of 170 mAh/g, which is highly reversible (more than 1000 cycles [33]).  $\text{LiFePO}_4$  exhibits a two-phase behavior, has a small (6.9%) unit cell volume change between  $\text{LiFePO}_4$  and  $\text{FePO}_4$  end members. The ability to work at enhanced temperatures [34] and high rates [35], its low cost and environmental friendliness are also important advantages. Low volumetric density, low electronic conductivity  $\sim 10^{-9}$  S/cm [36] and low lithium diffusion coefficients of  $\sim 10^{-13}$ - $10^{-16}$   $\text{cm}^2/\text{s}$  are the major drawbacks of  $\text{LiFePO}_4$ . To improve these properties the following techniques are used: particle size reduction [37], carbon coating [36,38], doping [36,39], etc.

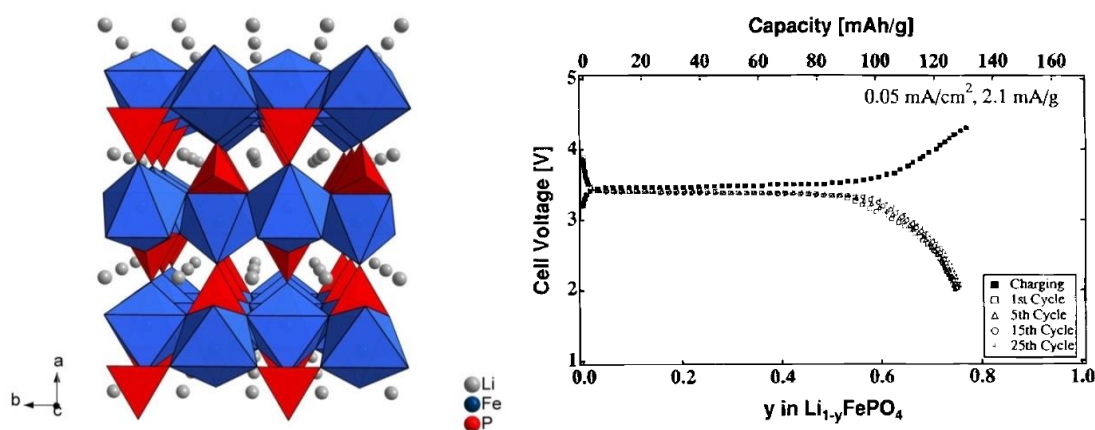
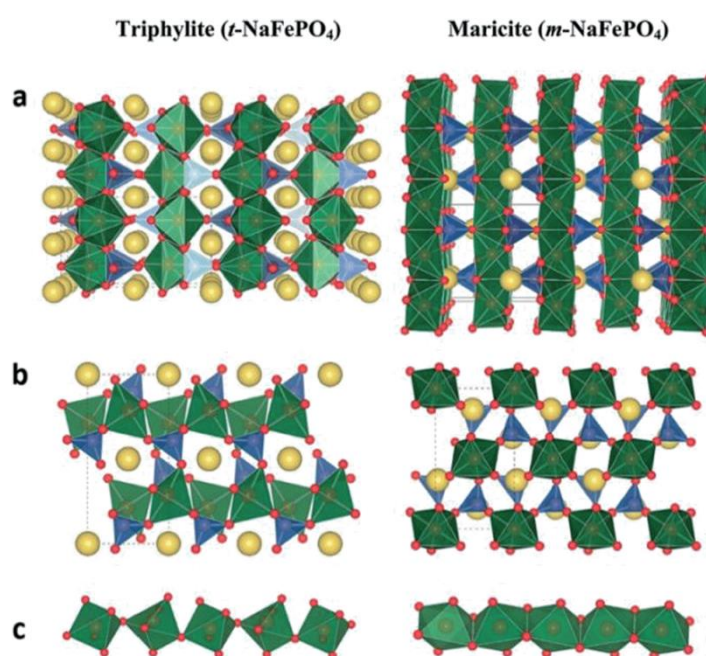


Fig. 2. 8 Structure of  $\text{LiFePO}_4$  [40] and its discharge/charge curve [31]

Due to the impressive performance of  $\text{LiFePO}_4$  for practical applications, the electrochemical and structural study of triphylite  $\text{NaFePO}_4$  has attracted much

interest. Moreover,  $\text{NaFePO}_4$  has the highest theoretical specific capacity 154 mAh/g among phosphate polyanionic cathode materials for sodium-ion batteries. The thermodynamically stable form of  $\text{NaFePO}_4$  is maricite, which is structurally similar to  $\text{LiFePO}_4$ , but presents some important differences. In the maricite framework,  $\text{Fe}^{2+}$  and  $\text{Na}^+$  occupy M1 and M2 sites, respectively, which is the opposite in the triphylite  $\text{LiFePO}_4$ . In the maricite framework  $\text{Na}^+$  is trapped in the cavities, which are not connected by appropriate pathways resulting in high barriers for  $\text{Na}^+$  diffusion in the maricite structure.



**Fig. 2. 9 Structures of  $\text{NaFePO}_4$  in triphylite (left) and maricite (right) framework (a and b). (c) Coordinations of neighboring  $\text{FeO}_6$  octahedra [41]**

Conventional synthetic routes of  $\text{NaFePO}_4$  such as solid-state method [42] produce an electrochemically inactive maricite phase. Currently, the electrochemically active  $\text{NaFePO}_4$  is mainly obtained by electrochemical sodiation of heterosite  $\text{FePO}_4$ , which was shown by Moreau *et al.* [43]. They employed chemical oxidation in acetonitrile using  $\text{NO}_2\text{BF}_4$  [44] to delithiate  $\text{LiFePO}_4$  and then discharged

a Na cell with the obtained heterosite  $\text{FePO}_4$  as a positive electrode. Some researchers [41,45] on the second step employed chemical reduction in acetonitrile using NaI to sodiate  $\text{FePO}_4$ . These methods are cumbersome; however, they enable to study various properties of triphylite-type  $\text{NaFePO}_4$ .

Charge/discharge curve is presented in Fig. 2. 10. Two voltage plateaus are observed on charge with a voltage discontinuity occurred at  $\text{Na}_{0.7}\text{FePO}_4$  on the potential-composition curve and are reversibly reproduced in the charge-discharge cycles [46]. Appearance of several plateaus on charge is associated with a formation of an intermediate phase during the transition between  $\text{NaFePO}_4$  and  $\text{FePO}_4$ . It was explained [32] by the need of a buffer between both end members, which reduces the internal stresses due to the large ( $\sim 17.58\%$ ) volumetric change during  $\text{Na}^+$  insertion. The solid-solution mechanism of sodium extraction in  $\text{Na}_x\text{FePO}_4$  when  $1 < x < 0.7$  was revealed [47] by *in-situ* X-ray Diffraction. Compared to lithium diffusion in  $\text{LiFePO}_4$ , triphylite-type  $\text{NaFePO}_4$  has 1-2 orders of magnitude lower sodium diffusion coefficients ( $\sim 10^{-17} \text{ cm}^2/\text{s}$ ), which was measured by galvanostatic intermittent titration test (GITT) and electrochemical impedance spectroscopy (EIS) by Zhu *et al.* [48]. It is consistent with findings of density function theory (DFT) calculation of diffusion barriers, which are higher for sodium in  $\text{NaFePO}_4$  (270 meV) rather than for lithium in  $\text{LiFePO}_4$  (150 meV) [49].

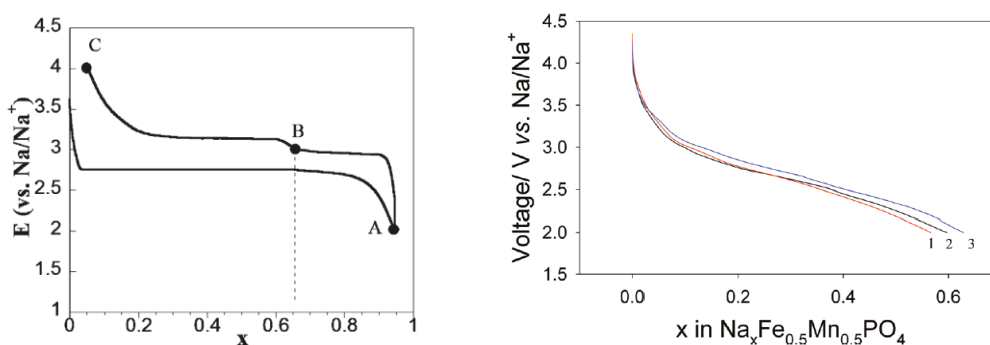


**Fig. 2.10** Electrochemical profile of  $\text{NaFePO}_4$  [43] and discharge curves for  $\text{NaFe}_{0.5}\text{Mn}_{0.5}\text{PO}_4$  [50]

Among other sodium metal phosphates  $\text{NaMnPO}_4$  is of interest; however its thermodynamically stable form is also maricite [49,51,52]. A polymorph of  $\text{NaMnPO}_4$ , which is isostructural to triphylite, was studied by Byström [53]. He calculated the trial structure factor for disordered and ordered octahedral cations (Na and Mn) and concluded that the structure involves disordered ( $\text{Na}_{0.5}\text{Mn}_{0.5}$ ) populations over the M1 and M2 sites of the triphylite structure type. Moore [54] argued that based on simple electrostatic arguments involving cation-cation repulsion natrophilite has to have ordered cations. However, the crystallographic database ICSD possesses the  $\text{NaMnPO}_4$  structure from [51] with disordered population.

On the basis of the improved electrochemical properties of  $\text{LiFe}_x\text{Mn}_{1-x}\text{PO}_4$  in comparison with  $\text{LiFePO}_4$ , mixed compounds of  $\text{NaFe}_x\text{Mn}_{1-x}\text{PO}_4$  with triphylite-type structure were found to be promising. The difference in the unit cell volume between  $\text{NaFePO}_4$  and  $\text{NaMnPO}_4$  is approximately 5%. The only known direct synthesis method of  $\text{NaMPO}_4$  compounds with triphylite-like structure was introduced by Nazar's group [50]. It employed a low-temperature topotactic molten-salt reaction that converts  $\text{NH}_4\text{Mn}_{0.5}\text{Fe}_{0.5}\text{PO}_4 \cdot \text{H}_2\text{O}$  to  $\text{NaMn}_{0.5}\text{Fe}_{0.5}\text{PO}_4$ . On the basis of identity between the iron and phosphate polyhedra in the (101) plane of  $\text{NH}_4\text{Mn}_{0.5}\text{Fe}_{0.5}\text{PO}_4 \cdot \text{H}_2\text{O}$  ( $Pmn2_1$  space group) and (100) plane of  $\text{NaMn}_{0.5}\text{Fe}_{0.5}\text{PO}_4$

(*Pnma* space group) ion exchange of  $\text{NH}_4^+$  bulky ion for  $\text{Na}^+$  is possible. Corresponding large lattice mismatch between  $d_{010}(\text{NH}_4\text{Mn}_{0.5}\text{Fe}_{0.5}\text{PO}_4 \cdot \text{H}_2\text{O})$  and  $d_{100}(\text{NaMn}_{0.5}\text{Fe}_{0.5}\text{PO}_4)$  induces cleavage during ion exchange, which leads to the  $\text{NaMn}_{0.5}\text{Fe}_{0.5}\text{PO}_4$  nanorods formation. The obtained material exhibits a single-phase behavior on desodiation and is capable to reversibly intercalate 60% of sodium (Fig. 2. 10 right).

Besides the great hopes placed in the  $\text{NaMPO}_4$  to stand as a material of choice for the next generation polyanionic cathode materials for sodium-ion batteries, alternative compositions were also investigated in search for higher performing electrodes.

### 2.3.2 Sodium transition metal phosphates $\text{Na}_y\text{M}_2(\text{PO}_4)_3$

$\text{A}_y\text{M}_2(\text{XO}_4)_3$  (A: generally an alkali metal, but also Mg, Zn, etc. and their combinations are known; M: either a single or a combination of transition metals or elements like Sn, Ge, Sc, Mg, etc.; X: mainly P, Si as well as W, Mo, S, As, etc.;  $0 \leq y \leq 5$ ) compounds are studied as prospective superionic conductors and electrode materials in metal-ion batteries. Compounds  $\text{Na}_y\text{M}_2(\text{PO}_4)_3$  were first reported in the 1880s [55], then again in the 1960s [56,57] and a mineralogical example kosnarite was described in 1993 [58]. In 1976 Goodenough and Hong [59] showed fast ionic conduction of  $\text{Na}^+$  cations in the  $\text{Na}_{1+x}\text{Zr}_2\text{P}_{3-x}\text{Si}_x\text{O}_{12}$  system comparable with the best ceramics of  $\beta$ -alumina ( $\text{NaAl}_{11}\text{O}_{17}$ ). As a result these compounds were called NASuperIonic CONductors or NASICONs. In the next two decades a large attention was focused on structural features which could increase ionic conductivity [60–64]. As intercalation electrodes NASICON-type compounds are examined since 1980s [65].

The 3D framework based on the NASICON structure consists of  $M_2(XO_4)_3$  repeating units, commonly called “lantern” (Fig. 2. 13). It is built on three  $XO_4$  tetrahedra connected via corners to two  $MO_6$  octahedra. Each lantern is surrounded by six other lanterns, which can be stacked parallel to the  $[001]$  direction of the hexagonal unit cell forming typical NASICON structure commonly described with rhombohedral space group. As an example from metal-ion battery materials, the high-temperature  $\gamma$ - $Na_3V_2(PO_4)_3$  adopts this crystal structure (Fig. 2. 11). Besides, lantern units can be stacked alternately along the directions  $\sim(2b\pm c)$  of the monoclinic unit cell forming anti-NASICON structure, which is adopted by the  $Li_3V_2(PO_4)_3$ .

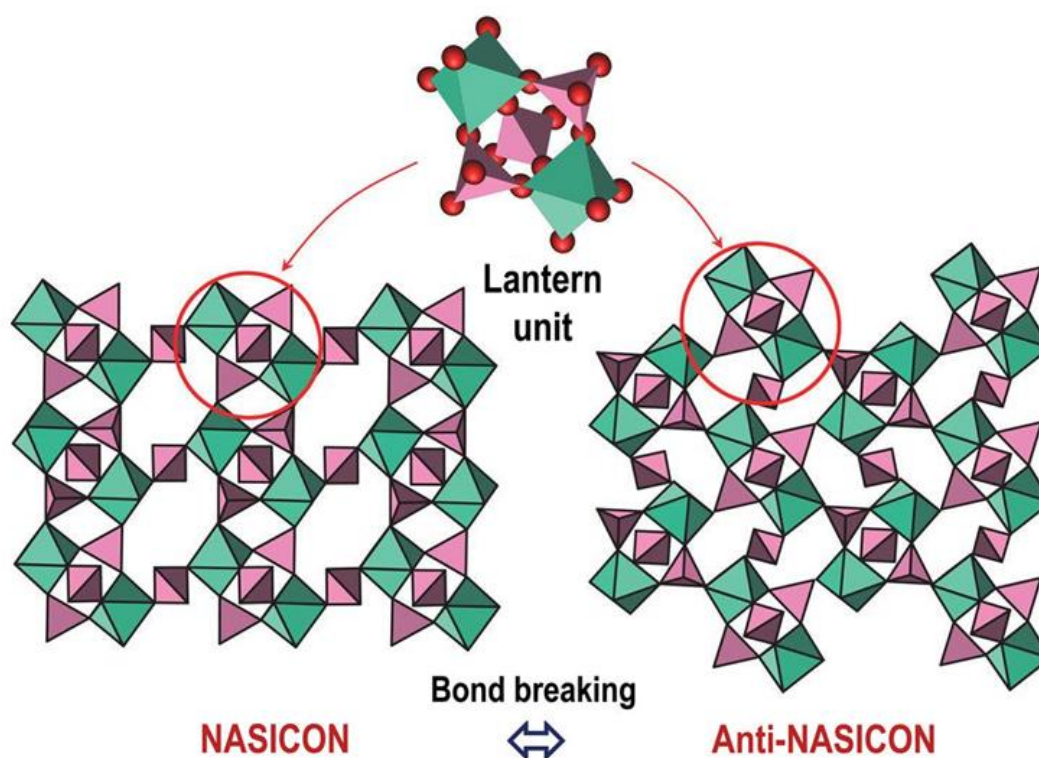


Fig. 2. 11 NASICON (*e.g.* rhombohedral  $Na_3V_2(PO_4)_3$ ) and anti-NASICON (*e.g.* monoclinic  $Li_3V_2(PO_4)_3$ ) frameworks of general formula  $A_yM_2(XO_4)_3$  [66]

In the NASICON framework three independent sites can be occupied by alkali ions. The first one is an octahedral A1 position located between the lower and upper

MO<sub>6</sub> octahedra of neighboring “lantern” units, which form infinite columns of [O<sub>3</sub>A1O<sub>3</sub>MO<sub>3</sub>A1O<sub>3</sub>] along *c*-axis. These columns are connected by three XO<sub>4</sub> tetrahedra in such a way that empty trigonal prisms are created in the center of the M<sub>2</sub>(XO<sub>4</sub>)<sub>3</sub> “lantern” units. The second site is located in an eight-fold A2 position between these infinite columns. Together they form the 3D framework, which leads to the crystallographic formula (A1)(A2)<sub>3</sub>M<sub>2</sub>(XO<sub>4</sub>)<sub>3</sub> (Fig. 2. 12 left). The third site is an octahedral A3 position located between MO<sub>6</sub> octahedra inside the M<sub>2</sub>(XO<sub>4</sub>)<sub>3</sub> “lantern” unit resulting in (A1)(A2)<sub>3</sub>(A3)M<sub>2</sub>(XO<sub>4</sub>)<sub>3</sub> or A<sub>5</sub>M<sub>2</sub>(XO<sub>4</sub>)<sub>3</sub>. Its filling is energetically unfavorable due to the great Coulombic repulsion.

Therefore, the lattice may be described as composed of infinite [O<sub>3</sub>A1O<sub>3</sub>MO<sub>3</sub>A1O<sub>3</sub>] columns parallel to the *c*-axis linked by PO<sub>4</sub> tetrahedra placed perpendicularly to the *c*-direction [67,68]. The A1 position is located within the columns. The A2 position is situated between the columns above the PO<sub>4</sub> tetrahedra. Then, the *a*-parameter is directly related to the column diameter (*i.e.* a function of the M<sup>n+</sup> radius) as well as to the inter-column distance (*i.e.* a function of the occupancy of the A2 positions). The *c*-parameter is influenced by the competition between several interactions summarized in Fig. 2. 12 right:

- the M<sup>n+</sup> radius
- the M<sup>n+</sup>-M<sup>n+</sup> electrostatic repulsions
- the O<sup>2-</sup>-O<sup>2-</sup> repulsions occurring when the A1 position is empty
- the A<sup>+</sup>(A1)-O<sup>2-</sup> attractions
- the A<sup>+</sup>(A1)-M<sup>n+</sup> repulsions through the shared faces

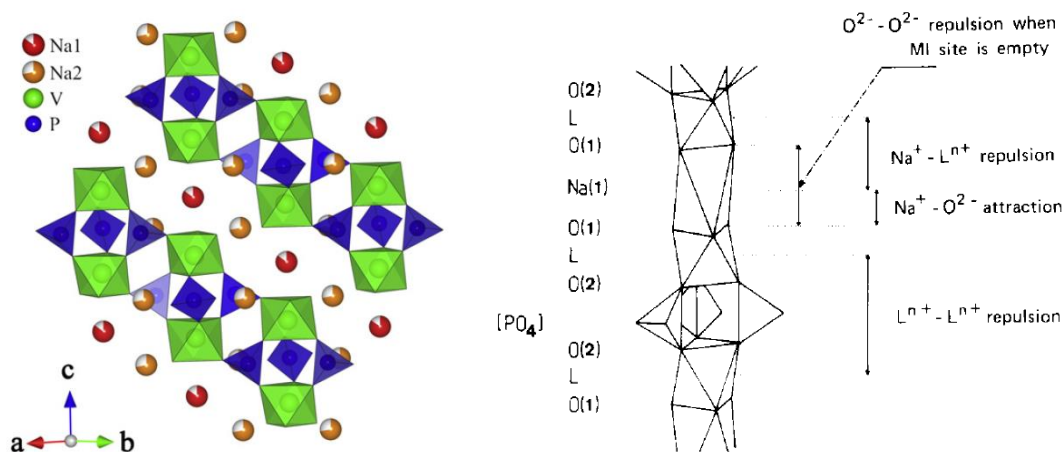


**Fig. 2. 12** The NASICON framework of the  $\text{Na}_3\text{V}_2(\text{PO}_4)_3$  described as array of parallel columns linked by  $\text{PO}_4$  tetrahedra [69] (left), Electrostatic interactions within a column of the NASICON-type  $\text{Na}_3\text{L}_2(\text{PO}_4)_3$  [68] (right)

It should be noted that in the case of  $\text{M}^{3+}$  the obtained  $\text{Na}_y\text{M}_2(\text{PO}_4)_3$  compounds would have  $\text{Na}_3\text{M}_2(\text{PO}_4)_3$  composition. Partial substitution of  $\text{M}^{3+}$  by  $x$  moles of  $\text{M}'^{2+}$  would require filling of the A sites with sodium ions, therefore compositions of  $\text{Na}_{3+x}\text{M}'_x\text{M}_{2-x}(\text{PO}_4)_3$  will be reached. Similarly, deintercalation of  $x$  moles of sodium from  $\text{Na}_3\text{M}_2(\text{PO}_4)_3$  would induce  $\text{M}^{3+}$  to  $\text{M}^{4+}$  redox transition and  $\text{Na}_{3-x}\text{M}_2(\text{PO}_4)_3$  will be obtained.

### 2.3.3 Structure of $\text{Na}_3\text{V}_2(\text{PO}_4)_3$

One of the first and most extensively studied NASICON-type cathode materials for batteries was  $\text{Na}_3\text{V}_2(\text{PO}_4)_3$ . It was mentioned for the first time in 1978 by Delmas [70].  $\text{Na}_3\text{V}_2(\text{PO}_4)_3$  (NVP) crystallizes in trigonal system, s.g.  $R\bar{3}c$  [71]. Its NASICON structure consists of corner-sharing  $\text{PO}_4$  tetrahedra and  $\text{VO}_6$  octahedra with sodium cations in interstitial positions (Fig. 2. 13).

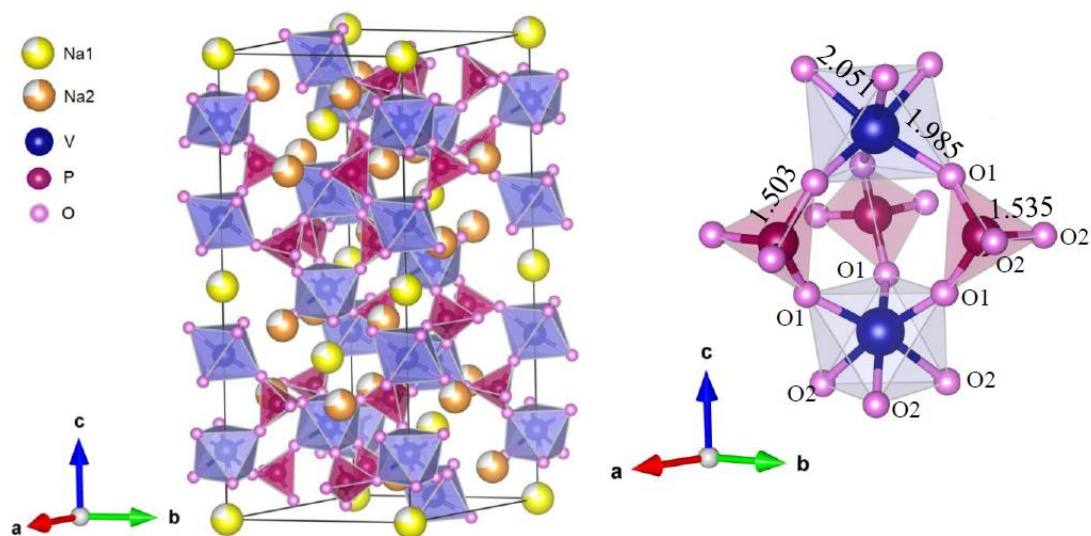


**Fig. 2. 13** Crystal structure of  $\text{Na}_3\text{V}_2(\text{PO}_4)_3$  and the basic repeating lantern unit  $\text{V}_2(\text{PO}_4)_3$ , V-O and P-O bond lengths are indicated in Å [72]

Three  $\text{Na}^+$  cations are located in two crystallographic sites: 1 cation in 6b site (Na1, six-fold coordination) and 2 cations in 18e site (Na2, eight-fold coordination) (Fig. 2. 14) [71]. The 6a site (Na3) is empty in NVP.

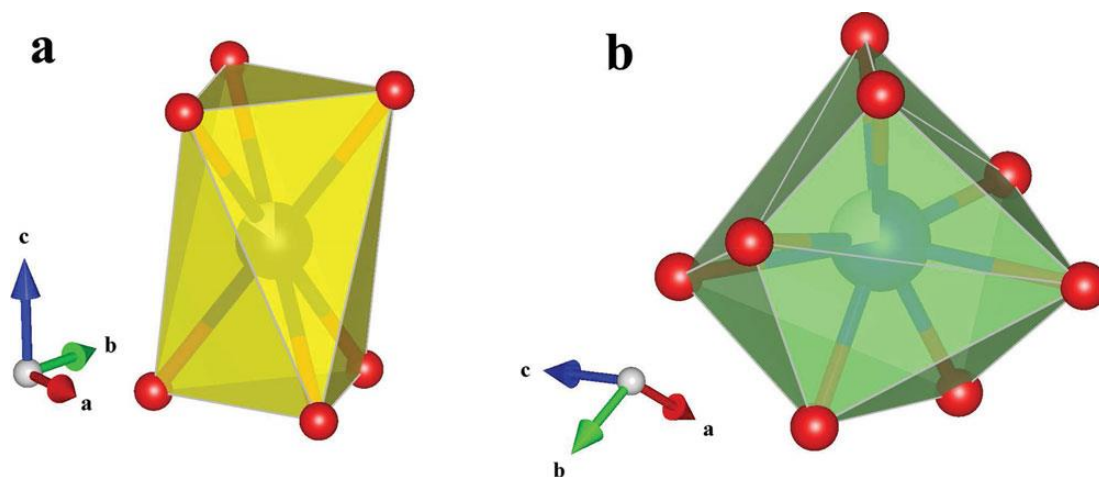


**Fig. 2. 14** Na-O polyhedra structures of (a) Na1 site (CN=6, octahedral) and (b) Na2 site (CN= 8, four faces are quadrangles, three faces are triangles) in the structure of the  $\text{Na}_3\text{V}_2(\text{PO}_4)_3$  [73]

Four polymorphs of NVP exist between  $-30^\circ\text{C}$  and  $225^\circ\text{C}$  (Fig. 2. 15) [74]. The high-temperature ( $>200^\circ\text{C}$ )  $\gamma\text{-Na}_3\text{V}_2(\text{PO}_4)_3$  crystallizes in the rhombohedral cell (s.g.  $R\bar{3}c$ ), the low-temperature ( $<10^\circ\text{C}$ )  $\alpha\text{-Na}_3\text{V}_2(\text{PO}_4)_3$  undergoes monoclinic

distortion (s.g.  $C2/c$ ) together with the ordering of  $\text{Na}^+$  cations and vacancies. In the intermediate temperature range two incommensurate modulated structures  $\beta'$ - and  $\beta''$ - $\text{Na}_3\text{V}_2(\text{PO}_4)_3$  may be adopted by the NVP crystal.

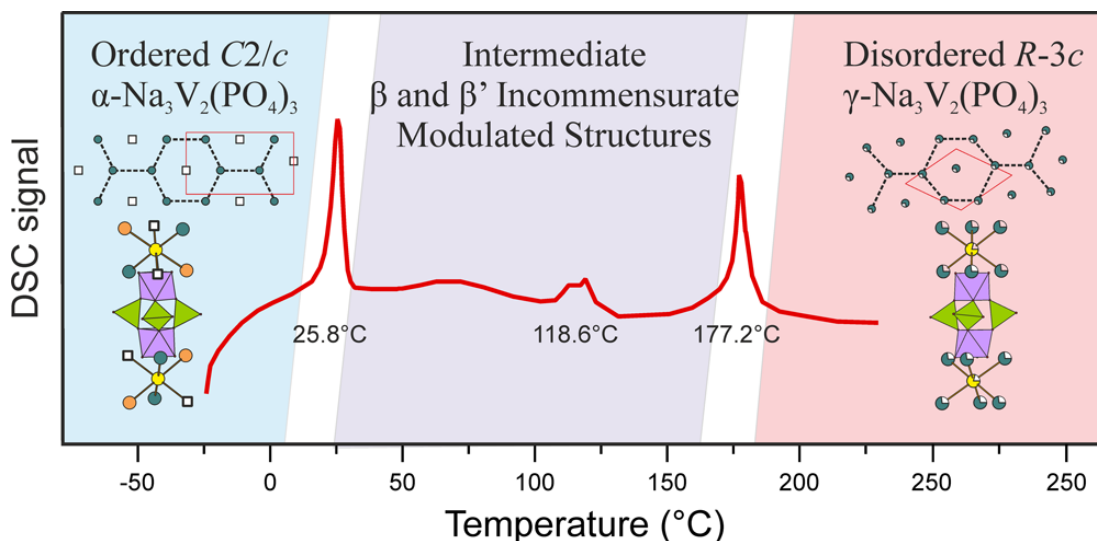


**Fig. 2. 15 Schematic representation of the phase transformations in  $\text{Na}_3\text{V}_2(\text{PO}_4)_3$  upon heating** [74]

### 2.3.4 Synthesis of $\text{Na}_3\text{V}_2(\text{PO}_4)_3$

There are three common routes for the synthesis of  $\text{Na}_3\text{V}_2(\text{PO}_4)_3$ : sol-gel, hydrothermal and solid-state methods. As a phosphate source  $\text{H}_3\text{PO}_4$  [75],  $\text{NH}_4\text{H}_2\text{PO}_4$  [76–81],  $\text{NaH}_2\text{PO}_4$  [69,82,83] are usually used. As a vanadium source  $\text{V}_2\text{O}_5$  [77,79,81],  $\text{NH}_4\text{VO}_3$  [75,78,82,84], vanadium acetylacetonate  $\text{VO}(\text{C}_5\text{H}_7\text{O}_2)_2$  [76,80,84] are most often involved. Various organic components such as oxalic [79], ascorbic [79] or citric acids [75,78,82], polyvinylpyrrolidone [77], glucose [81], sugar [69,83], sodium acetate [76,77,84] are added in order to decrease oxidation state of vanadium, to use as a complexing agent and often as a carbon source.  $\text{NH}_4\text{OH}$  is added to increase the pH to the values at which metal ions can be successfully chelated [75]. Besides mentioned sodium sources  $\text{NaOH}$  [75,78] and  $\text{Na}_2\text{CO}_3$  [79–81]

are employed as well. The synthesis is carried out in water [75,77,78,80], alcohol [76], polyethylene glycol (PEG) [79], tetraethylene glycol (TEG) [84], in some cases with the addition of hydrogen peroxide [77]. The high temperature annealing media is usually argon [76,79,81,83,84], argon/hydrogen [76,77,80,84] and nitrogen [75,78,82] gases.

The sol-gel route consists of dissolving the reactants in aqueous media and further evaporation at temperatures from 50°C to 120°C or under vacuum. In the case of cryochemical approach the solution is frozen under liquid nitrogen and subsequently dried under vacuum (Fig. 2. 16) [77,78]. Next, the product is mortared and in most cases in order to remove the residues CO<sub>2</sub>, H<sub>2</sub>O, NH<sub>3</sub> is heat-treated for less than 6 hours at 320°C [84], 350°C [75,79] in inert atmosphere, at 350°C in air [78] or in vacuum [77]. The dried powder is additionally grounded and annealed for longer than 6 hours in inert atmosphere at 650°C [76,84], 700°C [75,82], 750°C [77,79], 800°C [78,84]. In some cases several high-temperature treatments in different atmospheres are used [76,84].

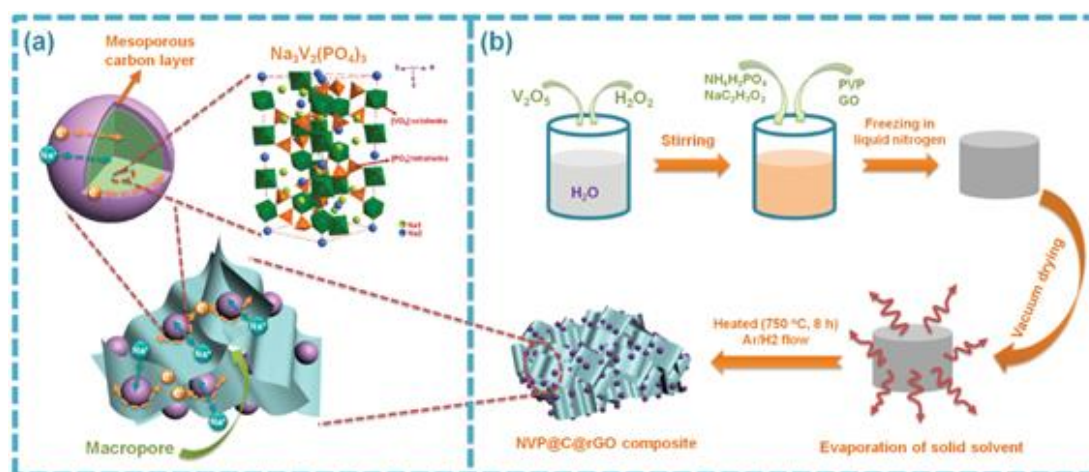


Fig. 2. 16 Schematic representation of the steps for the Na<sub>3</sub>V<sub>2</sub>(PO<sub>4</sub>)<sub>3</sub> synthesis [77]

In the case of hydrothermal synthesis of  $\text{Na}_3\text{V}_2(\text{PO}_4)_3$  high-temperature annealing is still necessary to obtain a crystalline product. Here, the reactants are also dissolved in aqueous media with continuous stirring including using ultrasonication. The obtained solution is kept in autoclave at  $100^\circ\text{C}$  [82],  $180^\circ\text{C}$  [79,80] from several hours [80] to several days [79]. Next, the solution is dried to form a gel at temperatures from  $80^\circ\text{C}$  [82] to  $120^\circ\text{C}$  [79] or heat-treated at  $350^\circ\text{C}$  [79], dried under vacuum [82], or freeze-dried [80], followed by mortaring. The final stage is high-temperature annealing analogous to the sol-gel route.

In the case of solid state synthesis dry powders of reactants are mixed in stoichiometric ratio in a ball-mill and annealed. In most cases  $\text{V}_2\text{O}_3$  is used as a vanadium source [69,83,84]. In some cases pre-treatment at  $400^\circ\text{C}$  is used [81], which is followed by more than 10 h of annealing in inert atmosphere at  $800^\circ\text{C}$  [81,83] or  $900^\circ\text{C}$  [69].

### 2.3.5 *Electrochemical properties of $\text{Na}_3\text{V}_2(\text{PO}_4)_3$*

The cathode material  $\text{Na}_3\text{V}_2(\text{PO}_4)_3$  is of particular interest due to its ability to sustain high current rates during long-term cycling. The use of various conductive coating and morphology control allows to sustain 90% of initial capacity at the 5000<sup>th</sup> cycle (20C rate, 2.4-3.8V), 80% of initial capacity at current rates of 100C (the current rate corresponding to (dis)charge in 36 s), specific energy of 200 Wh/kg at 300C rate (Fig. 2. 17) [85]. Theoretical specific capacity of the  $\text{Na}_3\text{V}_2(\text{PO}_4)_3$  is 117.55 mAh/g corresponds to extraction of 2 sodium ions from Na2 sites via the  $\text{V}^{3+}/\text{V}^{4+}$  redox couple. Electrochemical extraction via the  $\text{V}^{4+}/\text{V}^{5+}$  redox couple of 1 remaining sodium ion in Na1 site from  $\text{NaV}_2(\text{PO}_4)_3$  has not been realized.

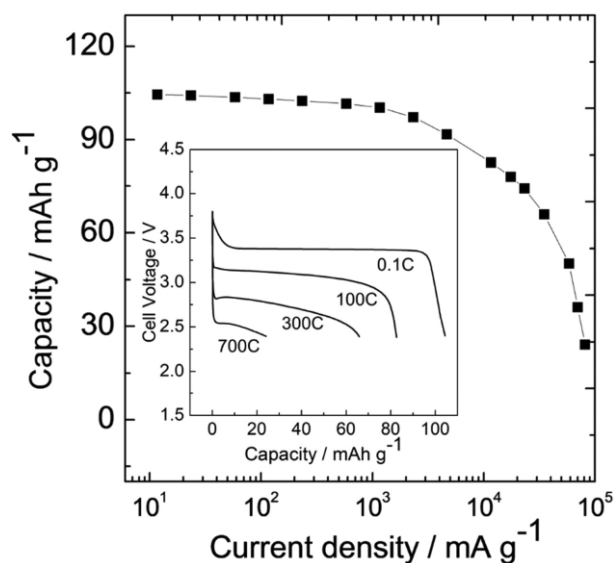


Fig. 2. 17 Electrochemical properties of  $\text{Na}_3\text{V}_2(\text{PO}_4)_3$ , material loading  $\sim 3 \text{ mg/cm}^2$  [85]

Pivko et al. probed the local environment of vanadium oxidation state in NVP by *in-situ* X-ray absorption spectroscopy (Fig. 2. 18) [86]. The operating potential 3.4 V was determined to correspond to the  $\text{V}^{3+}/\text{V}^{4+}$  redox transition by V K-edge XANES. Vanadium-oxygen interatomic distances in the first coordination sphere were probed by V K-edge EXAFS during cycling. In NVP three oxygen atoms are at 1.95 Å and three at 2.07 Å. After charging three oxygen atoms were found at 1.86 Å and three oxygen atoms at 1.97 Å. During battery discharging both V-O distances are gradually increased and reach the same values as in the as prepared sample.

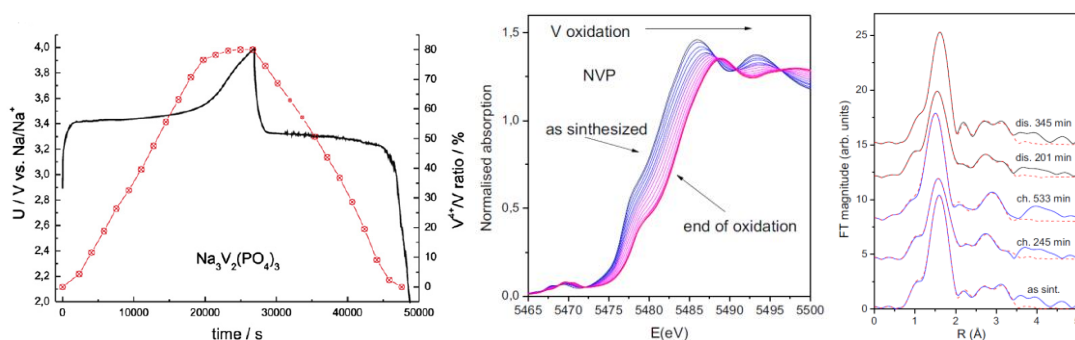
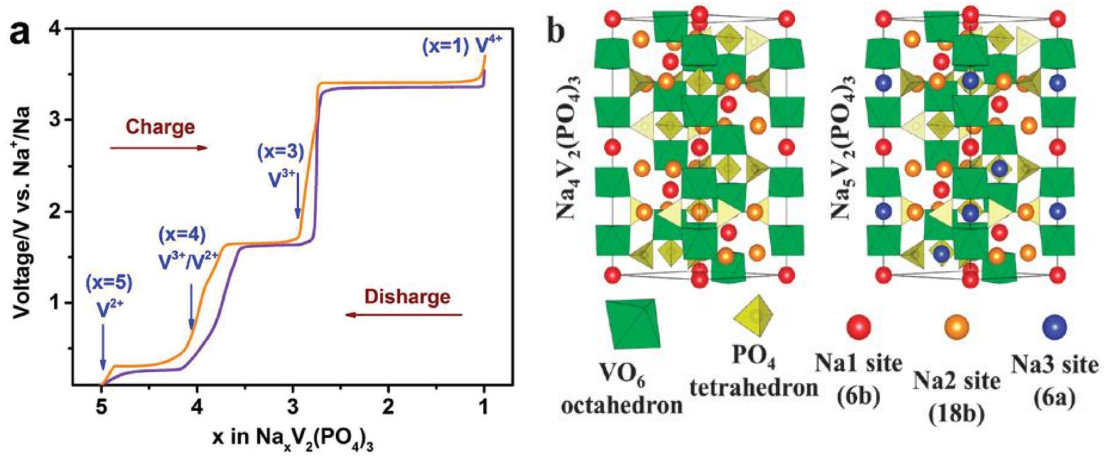


Fig. 2. 18 The relative amount of  $\text{V}^{4+}$  component, V K-edge XANES spectra and selected Fourier transform spectra of  $k^3$ -weighted V EXAFS spectra during first cycle as determined from *in situ* V XAS experiment in NVP sample [86]

In addition to opportunity to extract sodium ions from  $\text{Na}_3\text{V}_2(\text{PO}_4)_3$ , it is possible to insert sodium since Na1, Na2 and Na3 sites are not completely filled. When 1 sodium ion is inserted to  $\text{Na}_3\text{V}_2(\text{PO}_4)_3$ ,  $\text{Na}_4\text{V}_2(\text{PO}_4)_3$  is formed, the plateau at 1.6 V corresponds to this process at galvanostatic curve [69]. To that point occupancies of Na2 and Na1 sites is equivalent to 1. Na3 site is filled at 0.3 V (Fig. 2. 19) [87]. Such low voltage is related to strong coulombic repulsion in  $\text{Na}_5\text{V}_2(\text{PO}_4)_3$ , which is energetically disadvantageous. The steps at 1.6 V and 0.3 V correspond to the  $\text{V}^{2+}/\text{V}^{3+}$  redox process.



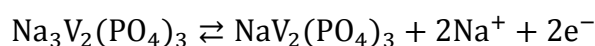
**Fig. 2. 19** Electrochemical voltage-composition curve for  $\text{Na}_x\text{V}_2(\text{PO}_4)_3$  [88] and crystal structures of  $\text{Na}_4\text{V}_2(\text{PO}_4)_3$  and  $\text{Na}_5\text{V}_2(\text{PO}_4)_3$  [87]

### 2.3.6 Phase transformations during charge and discharge of $\text{Na}_3\text{V}_2(\text{PO}_4)_3$

According to Gibbs' phase rule, there can be zero degrees of freedom in the intensive variables in the two-phase regime of a two-component system (given constant temperature and pressure), which leads to the characteristic flat galvanostatic curve of phase-separating electrode materials such as  $\text{LiFePO}_4$  or  $\text{Na}_3\text{V}_2(\text{PO}_4)_3$  during alkali ion (de)intercalation. Materials, forming single-phase solid-solutions over wide alkali ion concentration range, are characterized by sloping potential-composition curves. However, a sloping voltage curve may also originate from a wide size

distribution of materials' particles each undergoing a phase transition [89], which adds to the non-triviality of such systems' thermodynamics. The first-order phase transitions may arise from various reasons such as charge ordering, particularities of electronic structure, possible charge disproportionation or interfacial effects [90]. Understanding the mechanism of (de)intercalation is highly relevant to the thermodynamics and kinetics of battery materials and is important for the improvement of their properties like specific energy and power density. While a great number of research is published on the Li insertion mechanism in LiFePO<sub>4</sub>, not that much of studies are devoted to the Na insertion mechanisms in NASICON-type electrode materials.

In the NASICON-type NVP a reversible reaction takes place during (de)intercalation of sodium:



Lim et al [75] using *ex situ* X-Ray diffraction showed that the reaction on charge and discharge of Na<sub>3</sub>V<sub>2</sub>(PO<sub>4</sub>)<sub>3</sub> is biphasic. Upon sodium deintercalation the intensity of Na<sub>3</sub>V<sub>2</sub>(PO<sub>4</sub>)<sub>3</sub> reflections decreases and the intensity of NaV<sub>2</sub>(PO<sub>4</sub>)<sub>3</sub> increases. The authors confirmed the preference of the two-phase reaction by DFT calculations.

Subsequent studies of phase transformation behavior of Na<sub>3</sub>V<sub>2</sub>(PO<sub>4</sub>)<sub>3</sub> during charge and discharge confirmed these conclusions (Fig. 2. 20) [83,85].

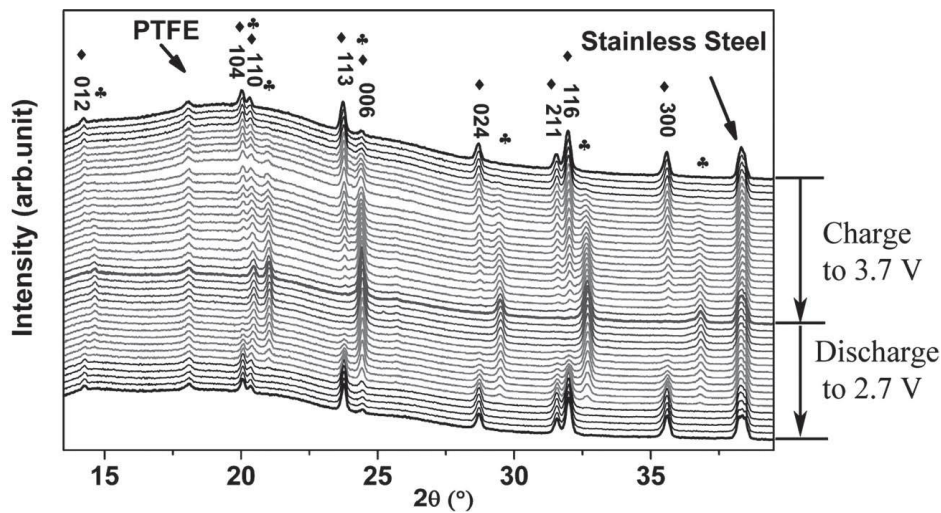


Fig. 2. 20 *Operando* XRD patterns of electrochemical cell  $\text{Na}_3\text{V}_2(\text{PO}_4)_3/\text{Na}$  on charge and discharge at current rate  $C/10$ ,  $\blacklozenge$  -  $\text{Na}_3\text{V}_2(\text{PO}_4)_3$ ,  $\blackspade$  -  $\text{NaV}_2(\text{PO}_4)_3$  [83]

Zhang et al [91] studied phase transformations in  $\text{Na}_3\text{V}_2(\text{PO}_4)_3$  using cyclic voltammetry at three different scan rates (0.5, 2 and 5 mV/s), galvanostatic charge-discharge (3C and 5C) at three different temperatures (273, 293 and 313 K) (Fig. 2. 21).

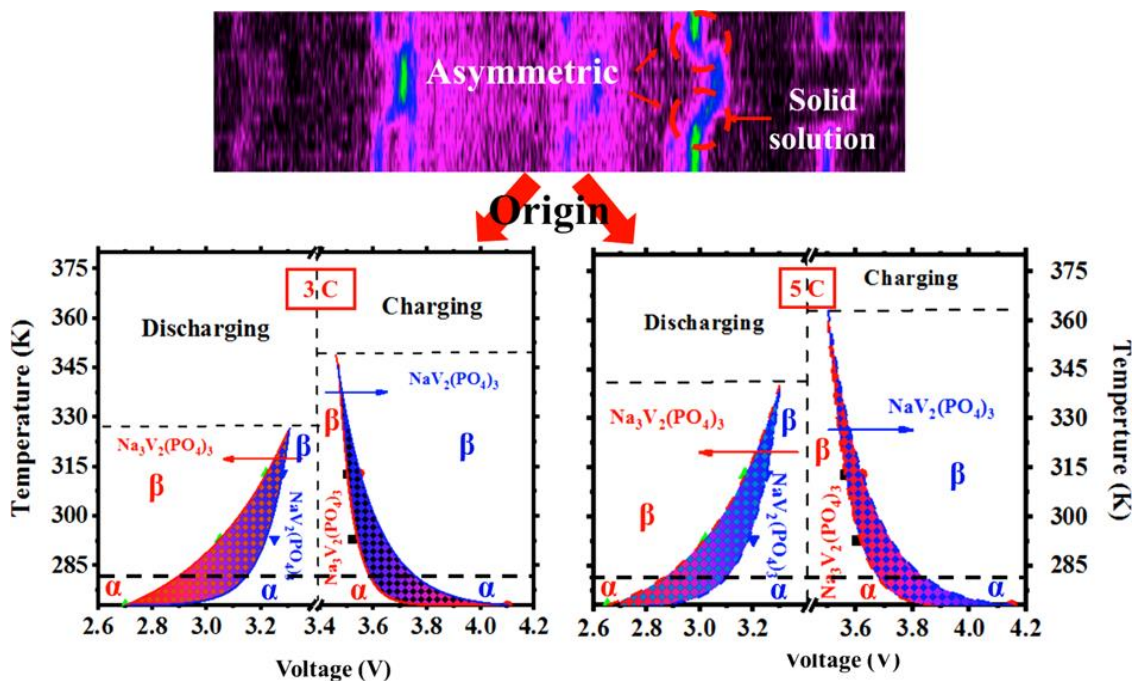


Fig. 2. 21 (top) Two-dimensional *operando* XRD pattern of  $\text{Na}_3\text{V}_2(\text{PO}_4)_3$  on charge and discharge and (bottom) phase diagram corresponding to two current rates, which indicates an increased

**domain of the solid solution mechanism of Na<sup>+</sup> (de)intercalation in Na<sub>3</sub>V<sub>2</sub>(PO<sub>4</sub>)<sub>3</sub> at lower temperature [91]**

The authors note that on charge a continuous shift of reflections is observed towards Na-deficient NaV<sub>2</sub>(PO<sub>4</sub>)<sub>3</sub> phase, which corresponds to solid-solution deintercalation mechanism. On discharge the reflections shift towards Na-rich Na<sub>3</sub>V<sub>2</sub>(PO<sub>4</sub>)<sub>3</sub> phase is also observed, but appears with breaks, corresponding to biphasic transition. The lower is the temperature and higher the current rate, the more obvious is the occurrence of solid-solution mechanism of sodium (de)intercalation. At higher temperature and slow scan rate authors obtained the result that is consistent with the generally accepted conception of the biphasic mechanism of (de)intercalation in Na<sub>3</sub>V<sub>2</sub>(PO<sub>4</sub>)<sub>3</sub>. Ren et al [92] also studied phase transformations in Na<sub>3</sub>V<sub>2</sub>(PO<sub>4</sub>)<sub>3</sub> at high rates of 1C and showed the data consistent with the conclusions of Zhang et al regarding the presence of the solid-solution (de)intercalation domain.

### 2.3.7 *Properties of single and binary transition metal NASICON-type cathodes*

Apart from Na<sub>3</sub>V<sub>2</sub>(PO<sub>4</sub>)<sub>3</sub> d'Yvoire and Delmas studied Na<sub>3</sub>Ti<sub>2</sub>(PO<sub>4</sub>)<sub>3</sub>, Na<sub>3</sub>Cr<sub>2</sub>(PO<sub>4</sub>)<sub>3</sub> and Na<sub>3</sub>Fe<sub>2</sub>(PO<sub>4</sub>)<sub>3</sub> compounds in 1980s [63,65]. Na<sub>3</sub>Ti<sub>2</sub>(PO<sub>4</sub>)<sub>3</sub> was initially reported as rhombohedral, s.g.  $R\bar{3}c$ , which was then revisited using single-crystal XRD [93] and confirmed via synchrotron XRD [94] that the real symmetry is triclinic, s.g.  $P\bar{1}$ , with an ordering of Na ions and vacancies within the Na<sub>2</sub> site. Two Na cations can be deintercalated from Na<sub>3</sub>Ti<sub>2</sub>(PO<sub>4</sub>)<sub>3</sub> at ~2.1 V via Ti<sup>3+</sup>/Ti<sup>4+</sup> redox process and since Na<sup>+</sup> is removed from Na<sub>2</sub> sites, the Na/vacancy ordering is destroyed and rhombohedral NaTi<sub>2</sub>(PO<sub>4</sub>)<sub>3</sub> is obtained. On sodium insertion to Na<sub>3</sub>Ti<sub>2</sub>(PO<sub>4</sub>)<sub>3</sub> down to 0 V vs. Na/Na<sup>+</sup> ~50% of Ti<sup>3+</sup> is converted to Ti<sup>2+</sup> resulting in

additional plateau on galvanostatic curve at 0.4 V, as was confirmed by BVS and EPR results [94].

$\text{Na}_3\text{Fe}_2(\text{PO}_4)_3$  crystallizes into a monoclinic structure, s.g. C2/c [63,95]. It can be reversibly cycled via biphasic (de)intercalation mechanism at 2.5 V during 500 cycles delivering  $\sim 60$  mAh/g [96].

Electrochemical tests revealed an extremely high reversible activity at 4.5 V for  $\text{Na}_3\text{Cr}_2(\text{PO}_4)_3$  [97]. 68% of theoretical discharge capacity ( $\sim 80$  mAh/g) corresponding to the extraction of 2 Na per formula unit was attained. *Ex situ* Cr K-edge XANES experiments confirmed the  $\text{Cr}^{3+}/\text{Cr}^{4+}$  redox reaction.

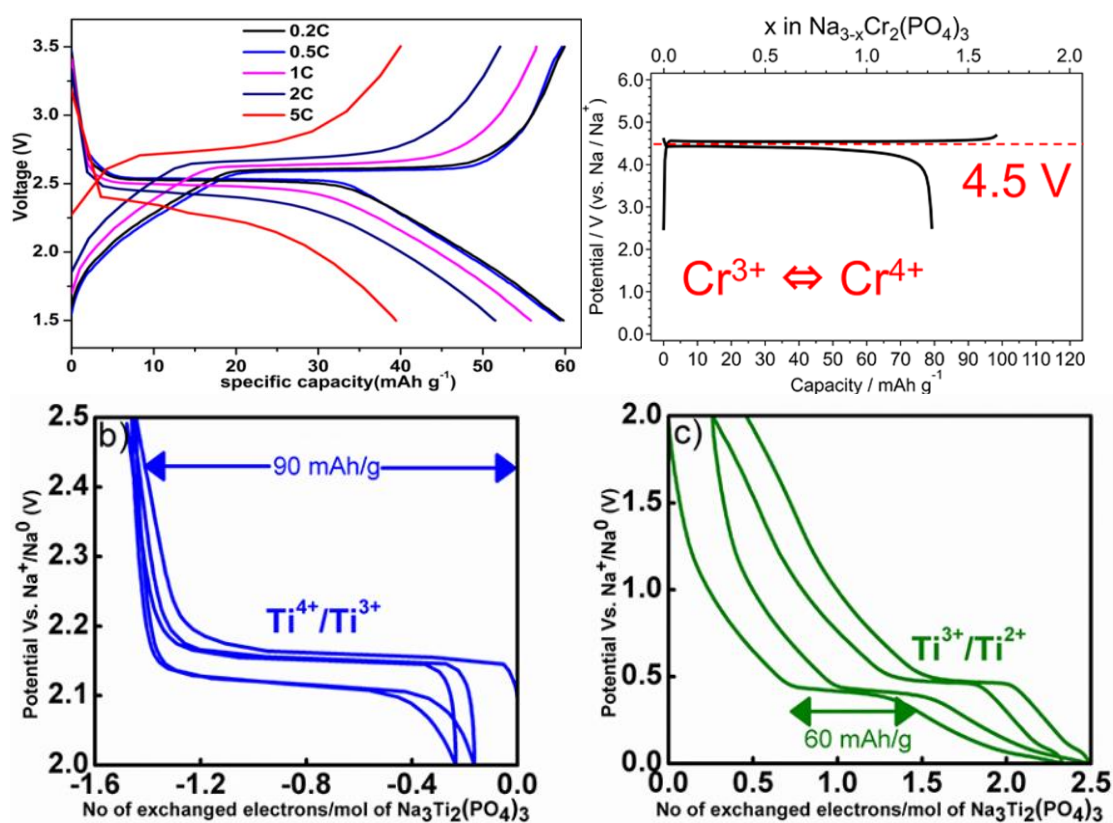


Fig. 2. 22 Galvanostatic cycling of  $\text{Na}_3\text{Fe}_2(\text{PO}_4)_3$  vs Na in 1.5-3.5 V [96],  $\text{Na}_3\text{Cr}_2(\text{PO}_4)_3$  vs Na in 2.5-4.7 V [97],  $\text{Na}_3\text{Ti}_2(\text{PO}_4)_3$  vs Na between 2.5 and 0 V for the first charge/discharge and subsequent charge/discharge[94]

Several binary NASICON-type  $\text{Na}_x(\text{V},\text{M})_2(\text{PO}_4)_3$  compounds were also synthesized.  $\text{Na}_2\text{TiV}(\text{PO}_4)_3$  was investigated as anode and cathode. Three distinctive redox activities were found in the voltage window 1.5-4.5 V [98]. The 3.4 V plateau corresponds to a biphasic reaction between  $\text{Na}_2\text{TiV}(\text{PO}_4)_3$  and  $\text{NaTiV}(\text{PO}_4)_3$  through  $\text{V}^{3+}/\text{V}^{4+}$  transition [99]. The reduction from  $\text{Na}_2\text{TiV}(\text{PO}_4)_3$  to  $\text{Na}_4\text{TiV}(\text{PO}_4)_3$  is more complex and includes several successive two-phase and single-phase steps at 2.1 V and 1.6 V corresponding to the redox of  $\text{Ti}^{3+}/\text{Ti}^{4+}$  and  $\text{V}^{2+}/\text{V}^{3+}$ , respectively. Besides, an intermediate composition  $\text{Na}_3\text{TiV}(\text{PO}_4)_3$  was formed during the reaction (Fig. 2. 23).

The  $\text{Na}_3\text{FeV}(\text{PO}_4)_3$  shows two plateaus centered at 3.3 V and 2.5 V, which were attributed to the redox of  $\text{V}^{3+}/\text{V}^{4+}$  and  $\text{Fe}^{2+}/\text{Fe}^{3+}$  couples, respectively [100].

The  $\text{Na}_4\text{NiV}(\text{PO}_4)_3$  shows a sloped plateau from 3.3 to 3.9 V with capacities near 80 mAh/g at 1C, indicating that more than 1 sodium ion can be reversibly extracted. When charged to 3.5 V exclusively, oxidation  $\text{V}^{3+}/\text{V}^{4+}$  took place. Since less than two sodium ions were extracted from  $\text{Na}_4\text{NiV}(\text{PO}_4)_3$ , both  $\text{Ni}^{2+}/\text{Ni}^{3+}$  and  $\text{V}^{4+}/\text{V}^{5+}$  were partially oxidized on the charge from 3.5 to 4.0 V, as shown by *ex situ* XPS experiments [100].

The  $\text{Na}_3\text{CrV}(\text{PO}_4)_3$  shows a 1.5 electron reaction corresponding solely to  $\text{V}^{3+}/\text{V}^{4+}/\text{V}^{5+}$  oxidation on charge to 4.3 V as confirmed by *ex situ* XANES at the K-edge of V and Cr [101]. Interestingly, capacity fade observed on cycling at room temperature was suppressed at low temperature  $-15^\circ\text{C}$  possibly because of kinetic reasons of this fade.

In the  $\text{Na}_3\text{Al}_{0.5}\text{V}_{1.5}(\text{PO}_4)_3$  as well as in the other cases of partial vanadium substitution with trivalent metal cations, which are not electrochemically active (*e.g.*

$\text{Al}^{3+}$ ) or not active at the typical working potential range ( $\text{Cr}^{3+}$  etc.),  $\text{V}^{4+}/\text{V}^{5+}$  redox couple is activated at  $\sim 3.9\text{--}4.1$  V, which increases average operating voltage [101–106].

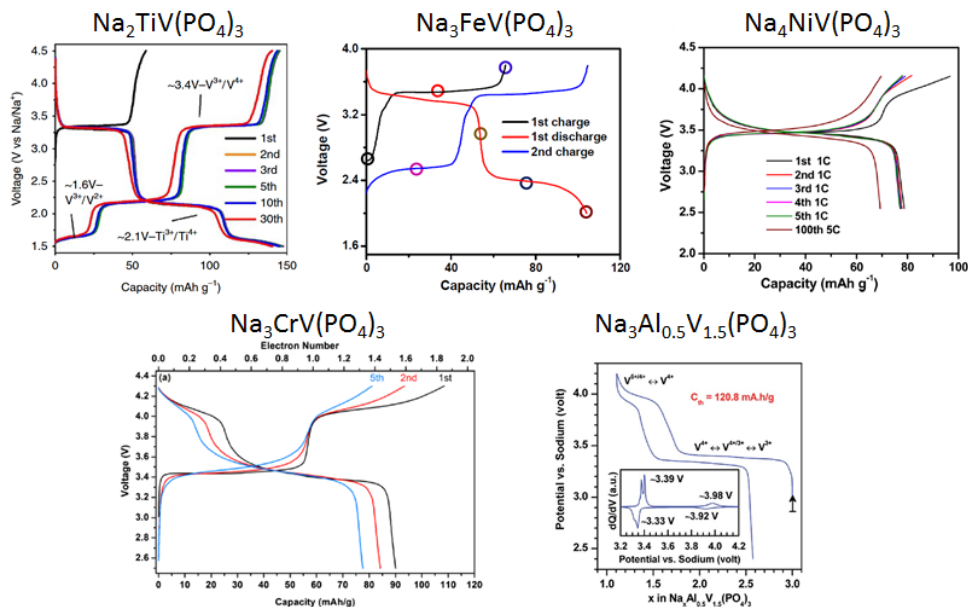


**Fig. 2. 23** Galvanostatic cycling of  $\text{Na}_2\text{TiV}(\text{PO}_4)_3$ ,  $\text{Na}_3\text{FeV}(\text{PO}_4)_3$ ,  $\text{Na}_4\text{NiV}(\text{PO}_4)_3$ ,  $\text{Na}_3\text{CrV}(\text{PO}_4)_3$ ,  $\text{Na}_3\text{Al}_{0.5}\text{V}_{1.5}(\text{PO}_4)_3$  [98,100,101,106]

Another group of binary NASICON compounds is represented by  $\text{Na}_x(\text{Mn},\text{M})_2(\text{PO}_4)_3$ .  $\text{Na}_3\text{MnTi}(\text{PO}_4)_3$  was investigated as anode and cathode. Three distinctive redox activities were found in the voltage window 1.5–4.2 V [107]. The 3.6 V plateau corresponds to a biphasic reaction between  $\text{Na}_3\text{MnTi}(\text{PO}_4)_3$  and  $\text{Na}_2\text{MnTi}(\text{PO}_4)_3$  through  $\text{Mn}^{2+}/\text{Mn}^{3+}$  transition, the 4.0 V plateau corresponds to further sodium extraction from  $\text{Na}_2\text{MnTi}(\text{PO}_4)_3$  to  $\text{NaMnTi}(\text{PO}_4)_3$  via another two-phase reaction through the utilization of the  $\text{Mn}^{3+}/\text{Mn}^{4+}$  redox couple [108,109]. The reduction from  $\text{Na}_3\text{MnTi}(\text{PO}_4)_3$  to  $\text{Na}_4\text{MnTi}(\text{PO}_4)_3$  includes a single-phase reaction at 2.1 V corresponding to the redox of  $\text{Ti}^{3+}/\text{Ti}^{4+}$ . (Fig. 2. 23).

A two-phase transformation from  $\text{Na}_3\text{MnZr}(\text{PO}_4)_3$  to  $\text{Na}_2\text{MnZr}(\text{PO}_4)_3$  was observed on sodium extraction at 3.6 V through  $\text{Mn}^{2+}/\text{Mn}^{3+}$  transition, followed by another two-phase transformation process at 4.0 V from  $\text{Na}_2\text{MnZr}(\text{PO}_4)_3$  to  $\text{NaMnZr}(\text{PO}_4)_3$  on sodium extraction through utilization of the  $\text{Mn}^{3+}/\text{Mn}^{4+}$  redox couple [110].

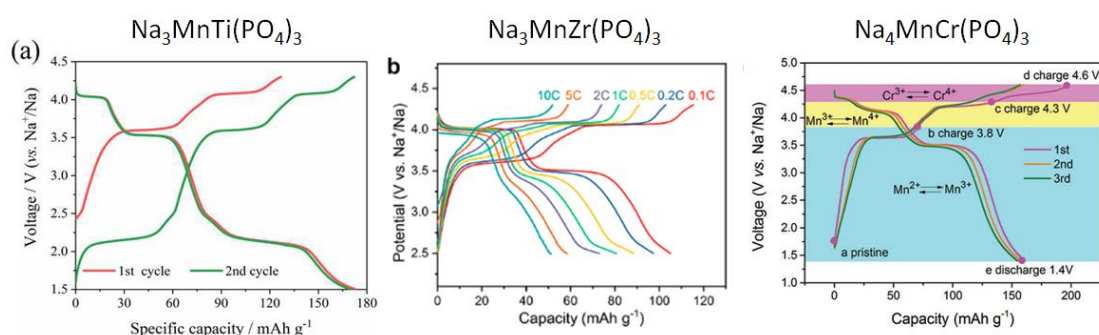


**Fig. 2. 24 Galvanostatic cycling of  $\text{Na}_3\text{MnTi}(\text{PO}_4)_3$  [109],  $\text{Na}_3\text{MnZr}(\text{PO}_4)_3$  [110],  $\text{Na}_4\text{MnCr}(\text{PO}_4)_3$  [111]**

Cycling  $\text{Na}_4\text{MnCr}(\text{PO}_4)_3$  in the voltage window 1.5-4.5 V utilizes high-voltage  $\text{Mn}^{2+/3+}$  (3.5 V),  $\text{Mn}^{3+/4+}$  (4.1 V), and  $\text{Cr}^{3+/4+}$  (4.35 V) transition metal redox undergoing several successive two-phase and single-phase steps [111–113].

## 2.4 Motivation and Objective

The Na-ion batteries concept is re-emerging today and the first solutions based on this technology appear on the market. However, to fit this technology for a wide range of applications, better electrode materials are required. Layered oxides are a low-cost high-energy solution, which still needs improvements in high-rate and long-life performance. Prussian Blue Analogs achieve attractive rate capability, but they have lower volumetric energy density due to low tap density. Polyanionic materials are one more promising class of cathodes due to their structural, thermal and moisture stability. Among them, NASICON-type cathode materials are considered prospective

candidates for high-performance Na-ion batteries due to extremely long cyclic stability and an outstanding ability to operate at high (dis)charge rates. However, its cost-effectiveness can still be improved using transition metals cheaper than vanadium, which at the same time show higher operating voltage and lead to larger gravimetric capacity resulting in higher energy density and lower \$/kWh. Therefore an opportunity to reversibly cycle more than 2 sodium ions in NASICON-type materials in a cathode-related voltage window ( $>2.5$  V vs. Na/Na<sup>+</sup>) is highly desirable. One of the ways to achieve this is to find an appropriate combination of transition metals, which would allow extracting either all 3 sodium ions per formula unit from Na2 sites and/or additionally utilize sodium ions residing in Na1 site (in terms of rhombohedral setting). A remarkable diversity of redox couples attained by vanadium (V<sup>3+</sup>/V<sup>4+</sup>, V<sup>4+</sup>/V<sup>5+</sup>) and manganese (Mn<sup>2+</sup>/Mn<sup>3+</sup>, Mn<sup>3+</sup>/Mn<sup>4+</sup>) at high operating potentials in NASICON-type compounds allows expecting to utilize both transition metals in one material to extract more than 2 sodium ions per formula unit. Thus, the present work aims to explore such compounds as potential cathode materials for sodium-ion batteries.

## Chapter 3. Methodology and techniques

The  $\text{Na}_{3+x}\text{Mn}_x\text{V}_{2-x}(\text{PO}_4)_3$  ( $0 \leq x \leq 1$ ) samples were prepared by mixing reactants in deionized water followed by evaporation of the solution and subsequent annealing in inert atmosphere. There were two major synthesis routes: using oxalic or citric acid as a reducing agent. Different reducing agents provide two types of morphologies, each having its particular advantages to obtain specific information on sample's properties. Kinetic parameters registered using electrochemical methods were obtained from samples made with oxalic acid. Structural and transition metal valence state data were obtained from samples made with citric acid as a reducing agent.

### 3.1 Synthesis methods

The synthesis of  $\text{Na}_{3+x}\text{Mn}_x\text{V}_{2-x}(\text{PO}_4)_3$  ( $0 \leq x \leq 1$ ,  $\Delta x = 0.2$ ) samples consisted of two stages. At the first stage manganese(II) acetylacetonate, ammonium metavanadate and citric or oxalic acid were dissolved in deionized water in the molar ratio  $x:(2-x):3$  and stirred for 40 min at  $70^\circ\text{C}$ . Then sodium carbonate and ammonium dihydrophosphate solution in deionized water in the molar ratio  $(3+x):3$  was drop-wise added and stirred for 40 min followed by evaporation at  $95^\circ\text{C}$  overnight. Vanadium oxide and sodium dihydrophosphate were also used to obtain  $\text{Na}_3\text{V}_2(\text{PO}_4)_3$ . After that the solid residue was mortared and pre-heated at  $350^\circ\text{C}$  for 3 hours under argon atmosphere following by grinding in a high-energy SPEX-8000M ball-mill for 5 min and subsequent annealing at  $750^\circ\text{C}$  for 8 h in Ar atmosphere. In case of citric acid, the annealed samples already have enough amount of carbon coating. In order to improve the conductive carbon coating of the oxalic acid based samples, they were carbon-coated using a solution of polyacrylonitrile (PAN,  $(\text{C}_3\text{H}_3\text{N})_n$ ) in dimethylformamide (DMFA, Sigma-Aldrich, extra-pure) casted on the initial powder

and then annealed at 600°C for 2 h (3 K min<sup>-1</sup> heating rate) under Ar to yield the Na<sub>3+x</sub>Mn<sub>x</sub>V<sub>2-x</sub>(PO<sub>4</sub>)<sub>3</sub>/C composite [114].

### 3.2 Characterization methods

The chemical composition of the obtained samples was measured with an inductively coupled plasma atomic emission spectrometer (ICP-AES) Agilent 720 (Australia). The weighted sample (*ca.* 70-100 mg) of material was placed in a glass triangle beaker (Erlenmeyer flask) of 100 ml, 45 ml of aqua regia (conc. nitric (HNO<sub>3</sub>) and conc. hydrochloric acid (HCl, Panreac, Spain, (1:3) by volume) was added and heated at a temperature of 110°C for 1.5 hours. Then 15 ml of conc. sulfuric H<sub>2</sub>SO<sub>4</sub> was added and heated at 80°C for 2.0 hours to the gaining (i) yellowish-blue clear solution in case of oxalic acid synthesis of materials and (ii) slightly dark due to undissolved amorphous carbon in case of citric acid synthesis of materials. Solution transferred to a volumetric flask (100.0 ml) and deionized water added to the mark. A standards reference solution of Na, Mn, V, and P (Merck, Germany) was used. Stock solution 100 ppm was prepared, and stabilized by 5 mass.% HNO<sub>3</sub>. The reference solutions with concentrations 0.1, 0.5, 1, 5, 10, 25, 50, 75, and 100 ppm were prepared. 10 ppm Sc solution was used as internal standard to improve reproducibility of the results.

The chemical composition of the synthesized samples was also measured using energy dispersive X-ray analysis (EDX, FEI Titan Themis Z operated at 200 kV). The samples were prepared in air by crushing the crystals in a mortar in acetone and depositing drops of suspension onto Cu-supported holey carbon grids.

Scanning Electron Microscopy (SEM) images were obtained with a JEOL JSM-6490LV electron microscope (tungsten hairpin electron gun, 30 kV) equipped with an Everhart-Thornley detector.

The carbon content in the resultant products was measured by thermogravimetric analyzer Netzsch STA 449 F3 Jupiter under Ar:O<sub>2</sub> (80:20) flow at 10 K min<sup>-1</sup> heating rate in corundum crucible with lids. Empty crucible was used as a reference sample.

Attenuated total reflectance Fourier transform infrared (ATR-FTIR) spectra of the Na<sub>3+x</sub>Mn<sub>x</sub>V<sub>2-x</sub>(PO<sub>4</sub>)<sub>3</sub> samples were collected with a stand-alone FTIR microscope LUMOS (Bruker) equipped with Ge ATR crystal and liquid N<sub>2</sub> cooled Mercury-Cadmium-Telluride (MCT) detector. Spectra were recorded in the 1800-600 cm<sup>-1</sup> range with 2 cm<sup>-1</sup> resolution and averaging of 64 scans. The reproducibility was checked by probing different spots of the same powder sample.

X-ray powder diffraction (XRPD) patterns were recorded with a Huber G670 Guiner Camera (Co K $\alpha$ <sub>1</sub> radiation, Ge(111) monochromator, 10-100°, 40 kV / 30 mA, transmission mode) equipped with an image plate detector.

Electrochemical measurements of the citric acid-based samples were carried out in two-electrode cells. The working electrodes were composed of active material, carbon black (*Timcal Super P*) and polyvinylidene fluoride in 6:1:1 ratio, respectively. The dry mixture was blended with N-methyl-2-pyrrolidone, spread on aluminum foil and vacuum dried at 110°C for at least 1 h. Metallic sodium was used as a negative electrode. During assembling of the electrochemical cells in a glovebox metallic sodium was additionally cleaned by slicing off the unreacted shiny part of a sodium piece followed by its rolling and further polishing immediately before clamping the

electrochemical cell. The negative electrode was separated from the positive electrode by a sheet of borosilicate glass fiber soaked in 0.5M NaPF<sub>6</sub> solution of propylene carbonate and fluorinated ethylene carbonate in 95:5 volume ratio.

Galvanostatic tests of the citric acid-based samples were performed with *Elins* P20x8 potentiostat-galvanostat (*ES8* software) between 2.5 and 4.1 V vs. Na/Na<sup>+</sup> at C/10 current rate (long-term cycling), with *Biologic* SP-150 potentiostat-galvanostat (*EC-Lab* software) between 2.5 and 4.1 V at ~C/8 current rate (laboratory *operando* experiments) and with *Neware* battery cycler (*BTSCient* software) between 2.5 and 3.8 V at ~C/5 current rate (synchrotron *operando* experiments). Potentiostatic intermittent titration tests (PITT) were performed with *Biologic* VMP3 potentiostat-galvanostat (*EC-Lab* software) using potential steps of 10 mV between 3.0 and 4.1 V terminated at C/50 current cut-off.

Cyclic voltammetry, chronoamperometry and electrochemical impedance spectroscopy measurements were performed in three-electrode cells. The cells were assembled in an Ar-filled glove box. Glass microfiber filters were used as separators. The cathode material slurries were prepared by mixing active material, carbon black (*Timcal* Super P) and polyvinylidene fluoride in the weight ratio 77:13:10 with N-methyl-2-pyrrolidone. Working electrodes were fabricated by casting the slurries on aluminum foil (Doctor Blade). The electrodes were dried at 110°C under dynamic vacuum for at least 2 hours. The mass loading of cathode materials was 0.8–1.0 mg cm<sup>-2</sup>. Metallic sodium was used as a counter electrode. For the three-electrode measurements, reference electrodes were fabricated by charging the Na<sub>3</sub>V<sub>2</sub>(PO<sub>4</sub>)<sub>3</sub> electrodes to reach the state-of-charge of 0.5 [115]. The potential of the reference

electrodes was 3.370 V vs.  $\text{Na}^+/\text{Na}$  and was found to be stable during continuous measurements. The electrolyte was 1.0 M  $\text{NaPF}_6$  solution in propylene carbonate/ethylene carbonate (PC/EC 1:1) with the addition of 5% (by volume) of fluoroethylene carbonate (FEC).

Galvanostatic curves, cyclic voltammograms (CV), electrochemical impedance spectra (EIS) and chronoamperometric responses were registered using Biologic potentiostat/galvanostat and EC-lab software. Potentiostatic intermittent titration (PITT) was performed in 10 mV steps in the single-phase regions of the intercalation isotherms of  $\text{Na}_{3+x}\text{Mn}_x\text{V}_{2-x}(\text{PO}_4)_3$  ( $0 \leq x \leq 1$ ) materials. Diffusion coefficients were calculated from PITT data following the approaches described in refs [116,117]. Impedance spectra were registered in the frequency range 100 kHz – 10 mHz with a 4 mV alternating current amplitude. The analysis of the nucleation kinetics based on large-amplitude chronoamperometry was performed as described in refs [118,119].

*Operando* X-ray powder diffraction patterns were recorded with a Bruker D8 ADVANCE diffractometer (Cu  $\text{K}\alpha_{1,2}$  radiation, 19-38°, 40 kV / 40 mA) equipped with the energy-dispersive LYNXEYE XE position-sensitive detector using an electrochemical cell with Be windows supplied with the diffractometer (Fig. 3. 1) [120].

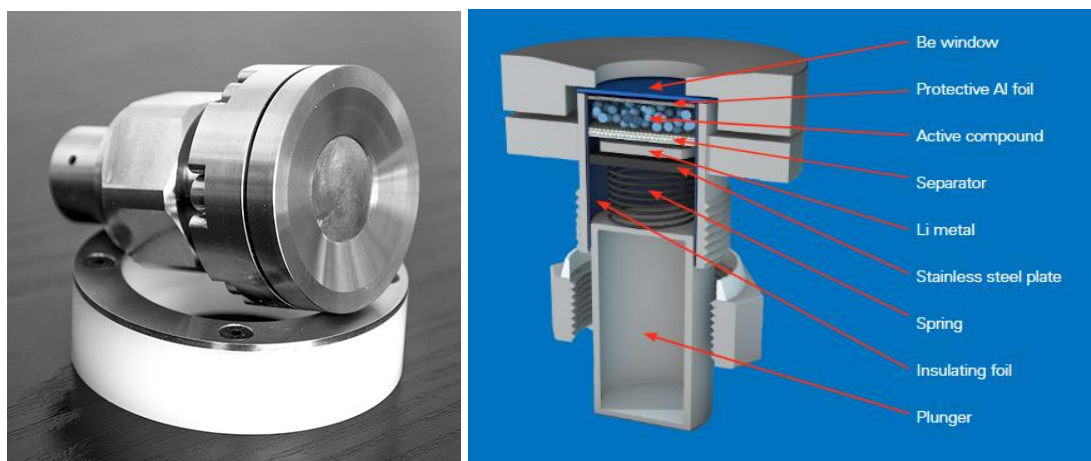


**Fig. 3. 1** Exterior and design of the electrochemical cell for *operando* X-ray measurements on a Bruker diffractometer [120–122]

*Operando* high-resolution synchrotron X-ray powder diffraction (SXRPD) patterns were recorded at the Swiss-Norwegian beamline (SNBL) BM01 at the European Synchrotron Radiation Facility ( $\lambda=0.68987$  Å, 2D Detector Pilatus 2M, transmission mode) using an electrochemical cell with sapphire windows (Fig. 3. 2) [123].

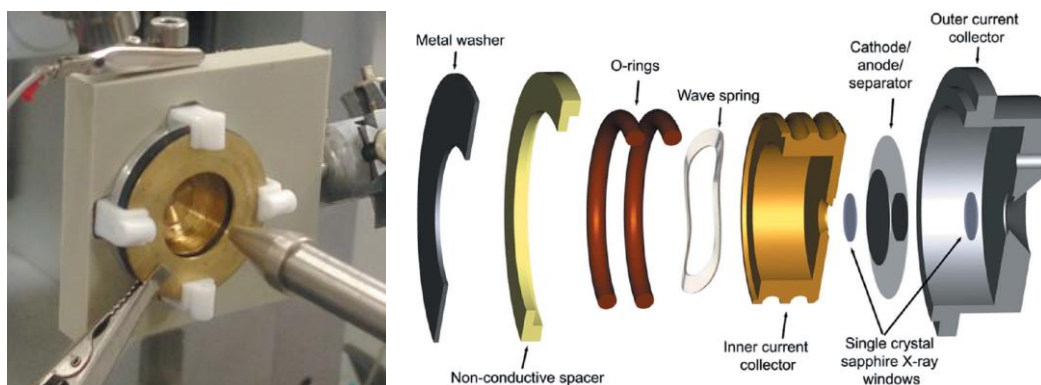


**Fig. 3. 2** Exterior and design of the electrochemical cell for *operando* X-ray measurements at the European Synchrotron [123]

Sequential LeBail fitting was performed using *Jana2006* software [124]. Selected patterns were refined using *Fullprof* software [125]. For precise refinement

the background was adjusted as interpolation between 150-200 points selected manually (see examples in Fig. A 8-Fig. A 12).

V and Mn K-edge X-ray absorption near edge structure (XANES) spectra were collected in series in transmission mode with a Rigaku R-XAS Looper spectrometer equipped with 3 kW X-ray tube and Ge(311) monochromator, resolution  $\Delta E=1.4$  eV.  $I_0$  and  $I_1$  were measured using an Ar-filled ionization chamber (300 mbar) and a scintillation detector, respectively. Slits were used to size the X-ray beam on the sample position by  $3 \times 10$  mm. *Operando* X-ray absorption spectroscopy (XAS) experiments were carried out using in-house electrochemical cell equipped with the X-ray transparent  $300 \mu\text{m}$  thick glassy carbon windows (Fig. 3. 3) [126]. The collection time for a single XAS spectrum was approximately 20 minutes; for each charge-discharge curve, at least 60 *operando* spectra were obtained. This amount allows to adequately analyze changes in the charge states of transition metal cations in a material.

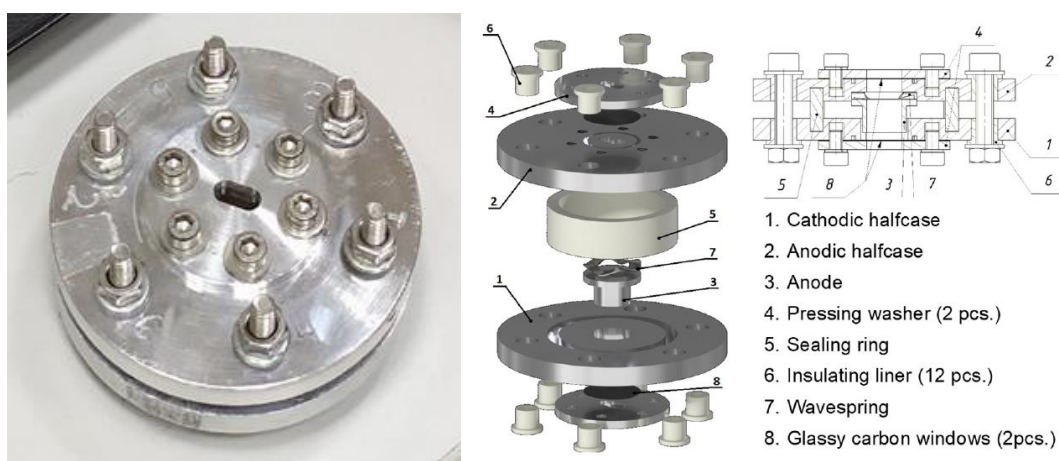


**Fig. 3. 3 Exterior and design of the electrochemical cell for *operando* X-ray measurements at the Rigaku spectrometer [126]**

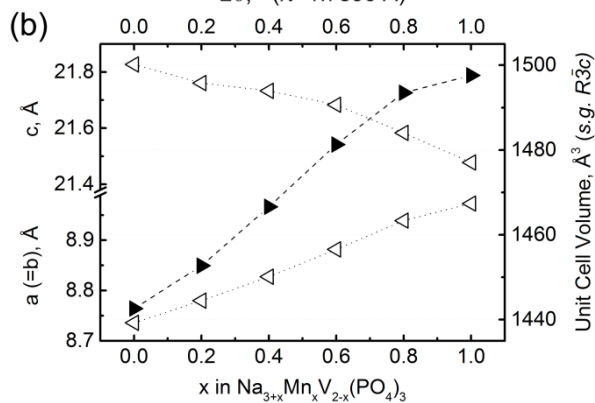
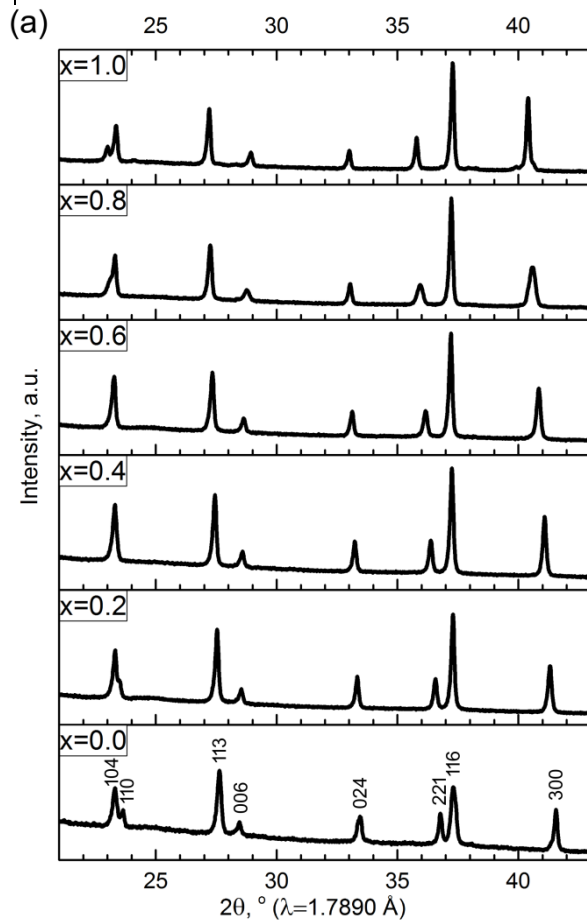
## Chapter 4.      Composition, structure and morphology of the $\text{Na}_{3+x}\text{Mn}_x\text{V}_{2-x}(\text{PO}_4)_3$

Fig. 4. 1a shows selected region of the XRPD patterns of the as-prepared  $\text{Na}_{3+x}\text{Mn}_x\text{V}_{2-x}(\text{PO}_4)_3$  ( $0 \leq x \leq 1$ ) samples made with citric acid. The XRPD patterns of the whole series can be indexed in the well-known NASICON unit cell with  $R\bar{3}c$  space group [71]. Rising the  $\text{Mn}^{2+}$  content leads to the  $a$  parameter increase,  $c$  parameter decrease and an overall growth of the unit cell volume (Fig. 4. 1b, Table 4. 1). The increase of the  $a$  parameter is due to the replacement of smaller  $\text{V}^{3+}$  cations with larger  $\text{Mn}^{2+}$  (ionic radii are 0.64 Å and 0.83 Å, respectively) [127], which increases the  $[\text{O}_3\text{NaO}_3(\text{V/Mn})\text{O}_3\text{NaO}_3]$  column diameter, in addition to incorporation of neutralizing excess of  $\text{Na}^+$  cations into Na2 sites, which increase the intercolumn distance (Chapter 2.3.2, Fig. 2. 12). The decrease of the  $c$  parameter could be related to the weakening of the  $\text{TM}^{n+}\text{-TM}^{n+}$  and  $\text{Na}^+\text{-TM}^{n+}$  electrostatic repulsions [68]. Due to a steep rise of the parameter  $a$  (and a slight fall of the parameter  $c$ ) the 110 and 104 reflections positions show an evident interchange as  $\text{Mn}^{2+}$  content increases. The changes in the NASICON framework caused by  $\text{Mn}^{2+}$  substitution are presented in Fig. A 1 and Fig. A 2. The XAS and XPS spectra confirming that Mn is divalent in the as-prepared samples are shown in Fig. A 3.

**Table 4. 1** Unit cell parameters for the as-synthesized  $\text{Na}_{3+x}\text{Mn}_x\text{V}_{2-x}(\text{PO}_4)_3$  ( $0 \leq x \leq 1$ ) in the s.g.  $R\bar{3}c$ .

Substitution level $x$	Volume, Å <sup>3</sup>	$a$ , Å	$c$ , Å	$c/a$
0	1442.6	8.7358(1)	21.8271(4)	2.4985
0.2	1452.7	8.7798(1)	21.7606(3)	2.4784
0.4	1466.6	8.8274(1)	21.7329(3)	2.4619
0.5	1468.5	8.8366(1)	21.7279(5)	2.4588

0.6	1481.3	8.8817(1)	21.6831(4)	2.4413
0.8	1493.5	8.9390(2)	21.5830(5)	2.4144
1	1497.6	8.9731(1)	21.4775(3)	2.3935



**Fig. 4. 1 X-ray powder diffraction data of  $\text{Na}_{3+x}\text{Mn}_x\text{V}_{2-x}(\text{PO}_4)_3$  ( $0 \leq x \leq 1$ ). (a) XRPD patterns of  $\text{Na}_{3+x}\text{Mn}_x\text{V}_{2-x}(\text{PO}_4)_3$  ( $0 \leq x \leq 1$ ) ( $21\text{-}43^\circ$ ,  $\text{Co}_{K\alpha 1}$ ), (b) Unit cell volume and parameters of  $\text{Na}_{3+x}\text{Mn}_x\text{V}_{2-x}(\text{PO}_4)_3$  ( $0 \leq x \leq 1$ ).**

The samples consist of irregularly shaped agglomerated platelets with the size of 0.1–1.5  $\mu\text{m}$  (Fig. 4. 2, Fig. A 4). The actual stoichiometry of the  $\text{Na}_{3+x}\text{Mn}_x\text{V}_{2-x}(\text{PO}_4)_3$  ( $0 \leq x \leq 1$ ) samples is confirmed by the ICP-AES and EDX measurements (Fig. 4. 3). The carbon content in the resultant samples was about 10% as measured by thermogravimetric analysis (Fig. 4. 4).

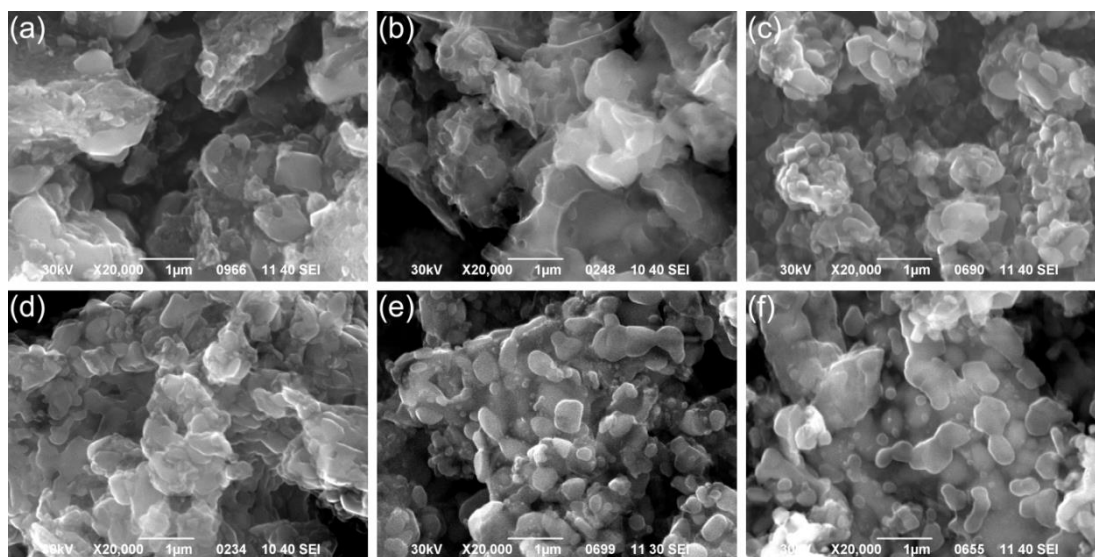


**Fig. 4. 2** SEM images of the as-synthesized (a)  $\text{Na}_3\text{V}_2(\text{PO}_4)_3$ , (b)  $\text{Na}_{3.2}\text{Mn}_{0.2}\text{V}_{1.8}(\text{PO}_4)_3$ , (c)  $\text{Na}_{3.4}\text{Mn}_{0.4}\text{V}_{1.6}(\text{PO}_4)_3$ , (d)  $\text{Na}_{3.6}\text{Mn}_{0.6}\text{V}_{1.4}(\text{PO}_4)_3$ , (e)  $\text{Na}_{3.8}\text{Mn}_{0.8}\text{V}_{1.2}(\text{PO}_4)_3$ , (f)  $\text{Na}_4\text{MnV}(\text{PO}_4)_3$

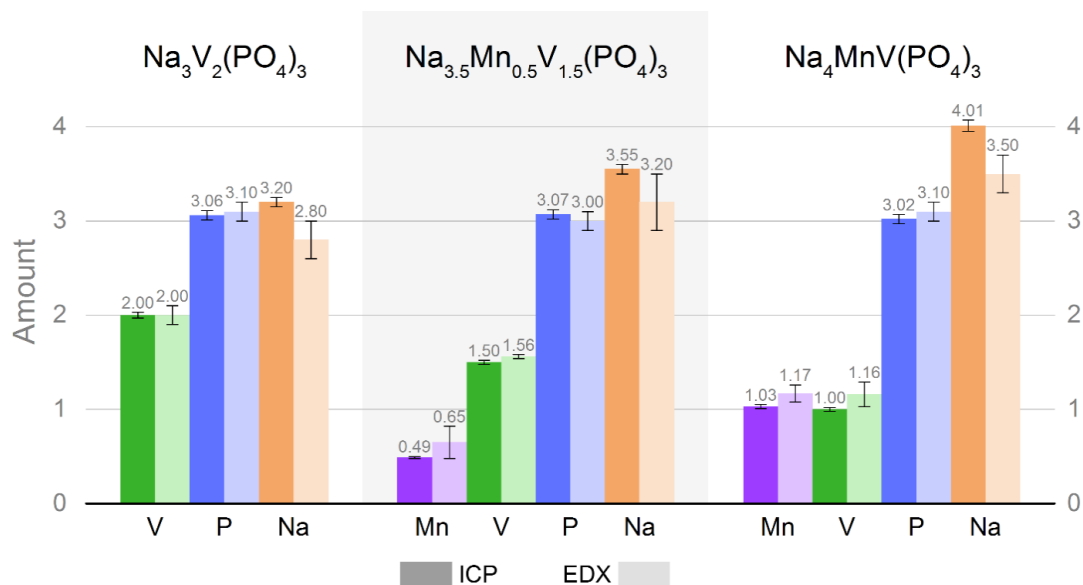


**Fig. 4. 3** Elemental composition of the as-synthesized  $\text{Na}_{3+x}\text{Mn}_x\text{V}_{2-x}(\text{PO}_4)_3$  ( $x=0, 0.5, 1$ ) according to the results of the ICP-AES and EDX measurements. Na content can be underestimated by EDX due to partial absorption of Na X-rays by the sample.

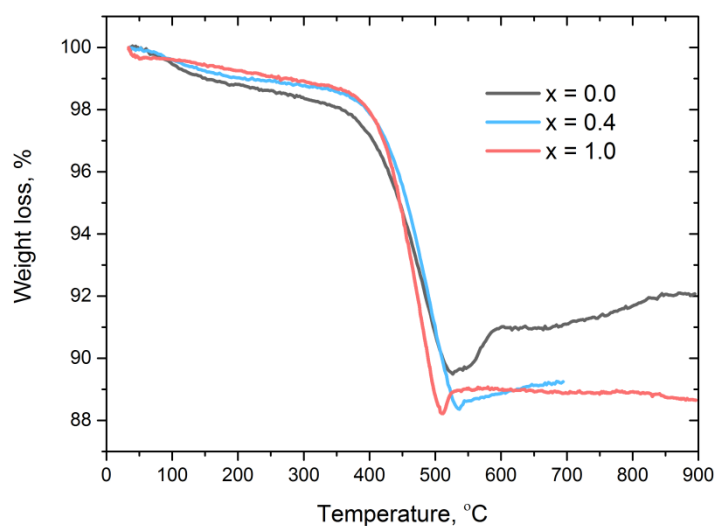


**Fig. 4. 4** Thermogravimetric curves of the as-synthesized  $\text{Na}_{3+x}\text{Mn}_x\text{V}_{2-x}(\text{PO}_4)_3$  powders in air.

Infrared spectra of  $\text{Na}_{3+x}\text{Mn}_x\text{V}_{2-x}(\text{PO}_4)_3$  materials presented in Fig. 4. 5a are dominated by absorption bands due to internal vibrational modes of the  $\text{PO}_4^{3-}$  anion.

These spectral features are typical for various NASICON-type compounds [128–132]. The band near  $620\text{ cm}^{-1}$  is assigned with antisymmetric bending vibrational mode of the O–P–O unit ( $\nu_4$ ). The broad structured absorption in the  $900\text{--}1100\text{ cm}^{-1}$  range includes bands due to both the symmetric ( $\nu_1$ ) and the antisymmetric ( $\nu_3$ ) stretching vibrations in  $\text{PO}_4^{3-}$  tetrahedra. The  $\nu_3$  vibrational mode is also featured by the higher-frequency band near  $1160\text{ cm}^{-1}$ . It is known that  $\nu_3$  mode is sensitive to phosphate-group distortion caused by the polarizing effect of the neighboring metal ions in the crystal structure [128]. The more polarizing the ion (smaller size, larger charge), the more localized are the electrons on the P–O (M) bond, which results in higher force constants and hence the higher vibrational frequencies [132]. Such effect has been previously reported for  $\text{NaM}_2(\text{PO}_4)_3$  ( $\text{M} = \text{Ti}^{4+}, \text{Zr}^{4+}$ ) [128] and  $\text{AgSbM}(\text{PO}_4)_3$  ( $\text{M} = \text{Al}^{3+}, \text{Ga}^{3+}, \text{Cr}^{3+}, \text{Fe}^{3+}$ ) [130] NASICON-type materials. We observed that in a series of the  $\text{Na}_{3+x}\text{Mn}_x\text{V}_{2-x}(\text{PO}_4)_3$  materials, the partial substitution of the  $\text{V}^{3+}$  ions with less polarizing  $\text{Mn}^{2+}$  ions leads to the evident lower-frequency shift of the  $\nu_3(\text{PO}_4)$  band position: from  $1182\text{ cm}^{-1}$  for  $\text{Na}_3\text{V}_2(\text{PO}_4)_3$  to  $1147\text{ cm}^{-1}$  for  $\text{Na}_4\text{MnV}(\text{PO}_4)_3$ . In fact, the absorption maxima of the  $\nu_3(\text{PO}_4)$  band in FTIR spectra shows virtually linear dependence on the  $\text{Mn}^{2+}$ -substitution degree  $x$  in  $\text{Na}_{3+x}\text{Mn}_x\text{V}_{2-x}(\text{PO}_4)_3$ , as shown in Fig. 4. 5b. This observation is an additional experimental evidence for monotonous chemical composition changes in a series of synthesized  $\text{Na}_{3+x}\text{Mn}_x\text{V}_{2-x}(\text{PO}_4)_3$  materials.

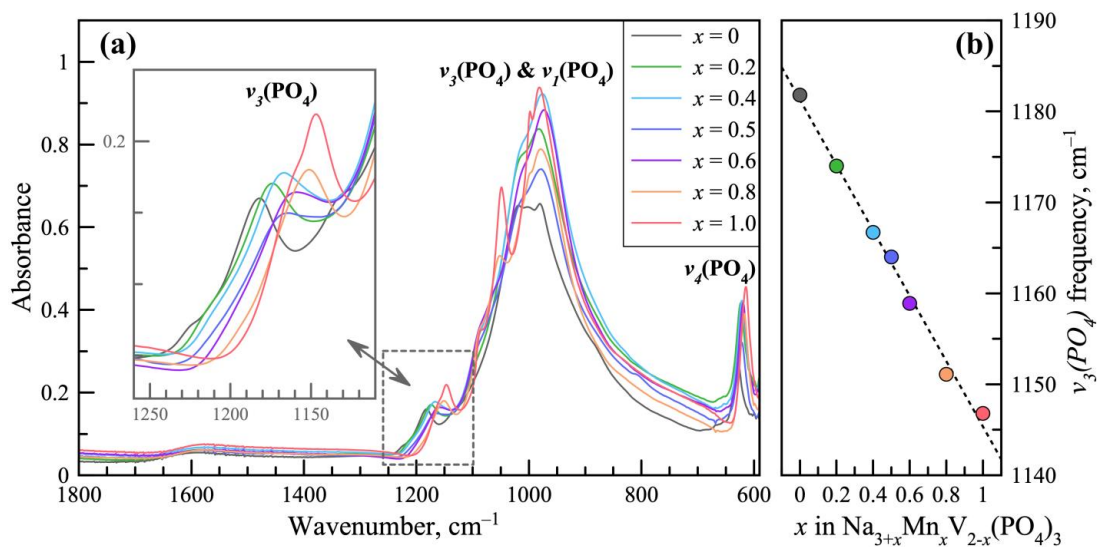


**Fig. 4. 5** Infrared spectroscopy data of  $\text{Na}_{3+x}\text{Mn}_x\text{V}_{2-x}(\text{PO}_4)_3$  ( $0 \leq x \leq 1$ ). (a) ATR FTIR spectra of pristine  $\text{Na}_{3+x}\text{Mn}_x\text{V}_{2-x}(\text{PO}_4)_3$  materials revealing the characteristic absorptions bands due to internal vibrations in the phosphate group, (b) The  $\nu_3(\text{PO}_4)$  band position as a function of elemental composition.

To study the effect of Mn substitution on the kinetic properties of  $\text{Na}_{3+x}\text{Mn}_x\text{V}_{2-x}(\text{PO}_4)_3$ , materials with  $x = 0, 0.1, 0.5$  and  $1$  were synthesized with the use of oxalic acid as the reducing agent. Fig. 4. 6 shows the XRD patterns of the as-synthesized materials can be indexed in the well-known NASICON unit cell with  $R\bar{3}c$  space group [71]. The unit cell parameters are similar to those, obtained for the citric-based samples (Fig. 4. 6b, Table 4. 2).

**Table 4. 2** Unit cell parameters for the as-synthesized  $\text{Na}_{3+x}\text{Mn}_x\text{V}_{2-x}(\text{PO}_4)_3$  ( $0 \leq x \leq 1$ ) in the s.g.  $R\bar{3}c$ .

Substitution level $x$	Volume, $\text{\AA}^3$	$a$ , $\text{\AA}$	$c$ , $\text{\AA}$	$c/a$
0	1444.5(6)	8.7404(2)	21.8337(6)	2.4980
0.1	1448.4(3)	8.7569(1)	21.8096(4)	2.4905
0.5	1475.7(2)	8.8556(1)	21.7295(2)	2.4537
1	1499.4(5)	8.9737(1)	21.5002(5)	2.3959

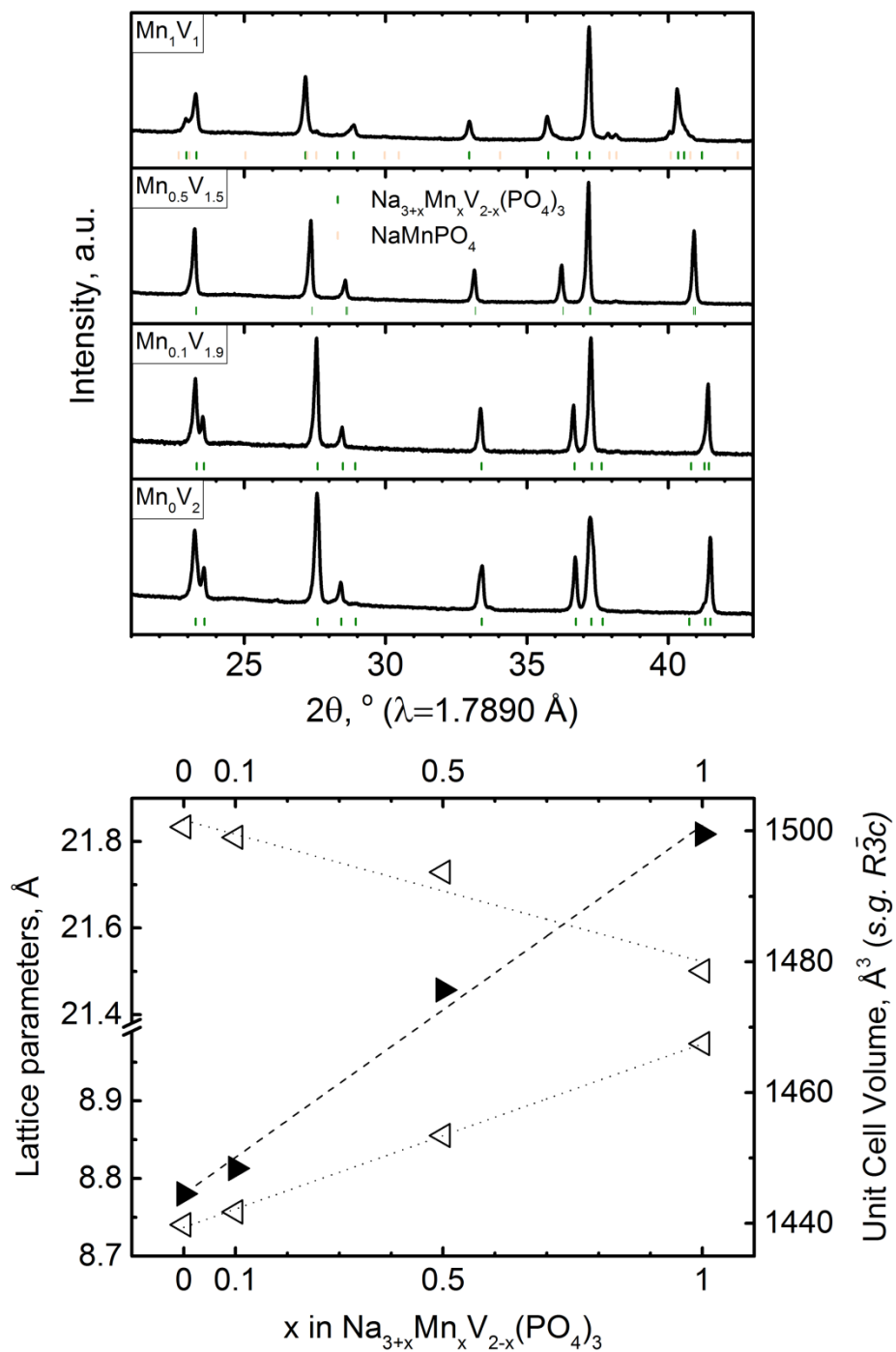


**Fig. 4. 6 (a)** XRPD patterns of  $\text{Na}_{3+x}\text{Mn}_x\text{V}_{2-x}(\text{PO}_4)_3$  ( $x = 0, 0.1, 0.5, 1$ ) ( $21\text{-}43^\circ$ ,  $\text{Co}_{\text{Ka}1}$ ), **(b)** Unit cell volume and parameters of  $\text{Na}_{3+x}\text{Mn}_x\text{V}_{2-x}(\text{PO}_4)_3$  ( $x = 0, 0.1, 0.5, 1$ ).

Electrochemical studies impose specific requirements on the morphology of the electrode material samples. In order to extract kinetic data, the polydispersity of

cathode materials should be minimized [119], while for a comparative study of four Mn-substituted materials the morphology of the samples should be very similar to focus on the effects of structural and compositional differences, and not on the effects of different particle sizes. The samples made with citric acid as a reducing agent show higher amount of large particles (Fig. A 4 b and c), which may be associated with a shoulder on the cathodic peak (Fig. 4. 8 right). The adopted synthetic route based on the use of oxalic acid allowed us to obtain  $\text{Na}_{3+x}\text{Mn}_x\text{V}_{2-x}(\text{PO}_4)_3$  ( $x=0, 0.1, 0.5, 1$ ) samples with similar morphologies. The samples consist of agglomerated platelets with the size of 0.1–1  $\mu\text{m}$  (Fig. 4. 7, Fig. A 4). Despite the observed complex morphology, the individual particles in the agglomerates do not demonstrate high polydispersity, while the porous morphology of the agglomerates allows for the involvement of the individual particles into the de/intercalation processes. The  $\text{Na}_4\text{MnV}(\text{PO}_4)_3$  sample shows a higher tendency for the agglomeration of primary particles and considerably wider particle size distribution, which might result in less accurate estimates of kinetic parameters.

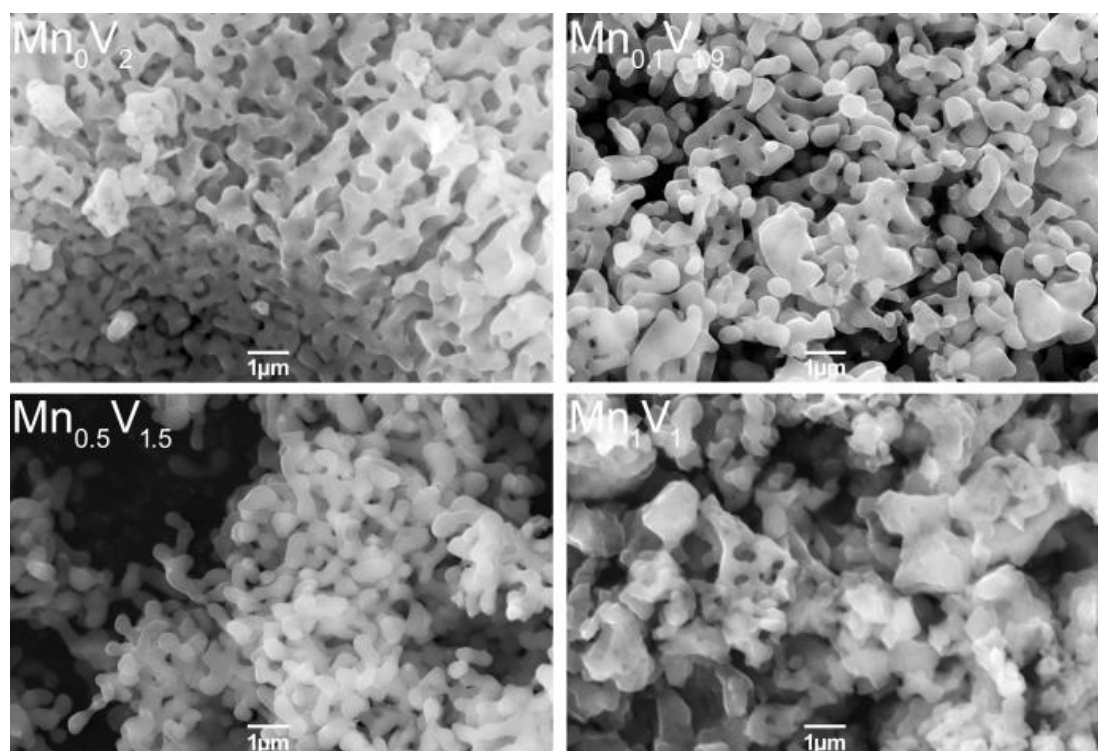


**Fig. 4. 7 SEM images of the  $\text{Na}_{3+x}\text{Mn}_x\text{V}_{2-x}(\text{PO}_4)_3$  ( $x=0, 0.1, 0.5, 1$ )**

Another important issue concerns the differences in the electronic conductivity of the  $\text{Na}_{3+x}\text{Mn}_x\text{V}_{2-x}(\text{PO}_4)_3$  materials. Since ohmic effects in porous electrodes

complicate the data analysis significantly [119] special care was taken to maximize the electronic conductivity of the composite electrodes. Among various conductive additives polyacrylonitrile (PAN)-derived carbon coating provided the minimal ohmic distortions of the CVs of  $\text{Na}_3\text{V}_2(\text{PO}_4)_3$  materials (Fig. 4. 8) and the respective carbon-coating procedure was applied to all the studied cathode material samples [114].

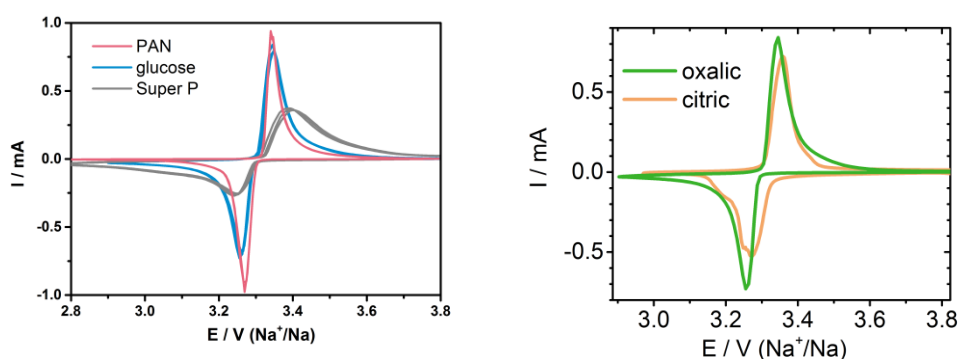


**Fig. 4. 8 CVs of  $\text{Na}_3\text{V}_2(\text{PO}_4)_3$  electrodes: (left) oxalic-based samples without carbon coating (10% Super P carbon in the composite electrode), with glucose-derived coating and with PAN-derived coating. (right) oxalic-based samples with glucose-derived coating and citric-based samples without additional carbon coating. Scan rate is  $0.2 \text{ mV s}^{-1}$ .**

To sum up, the as-prepared materials were thoroughly analyzed using X-ray diffraction, electron microscopy, atomic emission spectrometry, infrared spectroscopy to confirm their composition, morphology and crystal structure.

## Chapter 5. Electrochemical properties of $\text{Na}_{3+x}\text{Mn}_x\text{V}_{2-x}(\text{PO}_4)_3$

With the increase of the substitution level  $x$  electrochemical properties of  $\text{Na}_{3+x}\text{Mn}_x\text{V}_{2-x}(\text{PO}_4)_3$  also change. We investigated them within two voltage windows: 2.5-3.8 V and 2.5-4.1 V vs.  $\text{Na}/\text{Na}^+$  (Fig. 5. 1).

Several points can be highlighted for the cycling between 2.5 V and 3.8 V. For the ( $0.2 \leq x \leq 0.8$ ) samples electrochemical responses of vanadium and manganese cations are very close (details are shown in differential capacity plots presented in Fig. 5. 2a). Rise of the average charge/discharge voltage is the main visible result of the Mn substitution. However, further increase of the Mn content above  $x=0.8$  transforms the shape of the charge/discharge curve. The voltage plateau at  $\sim 3.4$  V ceases to be flat, and the slope splits for two steps, the lower step remains to be inclined, the upper becomes flat again. Zhou *et al.* proposed that for  $\text{Na}_4\text{MnV}(\text{PO}_4)_3$  lower plateau corresponds to  $\text{V}^{3+}/\text{V}^{4+}$  and the upper one – to  $\text{Mn}^{2+}/\text{Mn}^{3+}$  redox transition [100].

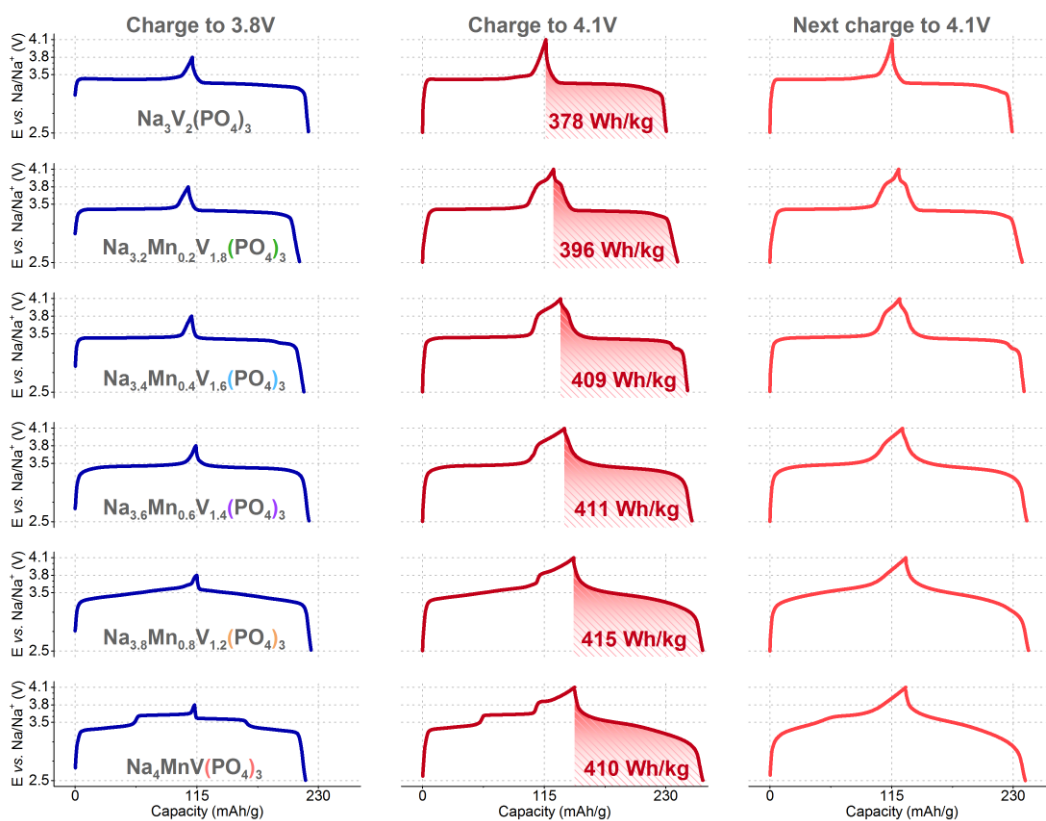


**Fig. 5. 1** Charge/discharge curves for  $\text{Na}_{3+x}\text{Mn}_x\text{V}_{2-x}(\text{PO}_4)_3$  ( $0 \leq x \leq 1$ ) cycled in the 2.5-3.8 V and 2.5-4.1 V voltage windows at C/10 current rate (1<sup>st</sup>, 3<sup>rd</sup> and 4<sup>th</sup> cycles are shown). A voltage step on discharge of  $\text{Na}_{3.4}\text{Mn}_{0.4}\text{V}_{1.6}(\text{PO}_4)_3$  is most probably due to the side reaction with metallic Na electrode [133,134].

When the voltage rises above 3.8 V, an additional voltage plateau appears on charge at ~3.9 V for all Mn-substituted compounds. For different compositions this feature has a slightly different shape and position (Fig. 5. 2b). For the low Mn contents ( $x=0.2, 0.4$ ) the 3.9 V plateau is reversible on discharge, however for  $x \geq 0.6$  the 3.9 V step vanishes on the first discharge and then does not reappear on either charge or discharge in case of lower cut-off voltage of 2.5 V. Further discussion of the irreversibility can be found in the subsection 6.2.

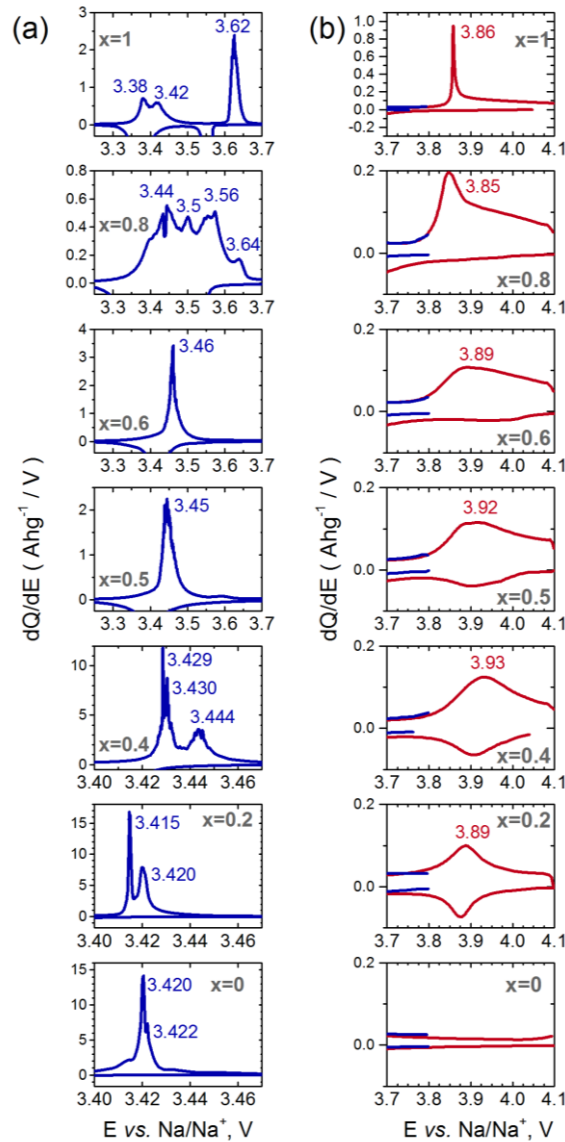


**Fig. 5. 2** Selected regions of the  $dQ/dE$  patterns of  $\text{Na}_{3+x}\text{Mn}_x\text{V}_{2-x}(\text{PO}_4)_3$  ( $0 \leq x \leq 1$ ) cycled in (a) 2.5-3.8V and (b) 2.5-4.1V voltage windows.

Fig. 5. 3 shows the results of experiments on potentiostatic intermittent titration (PITT). By the shape of the current transients, it is possible to determine the regions of the single-phase and two-phase mechanism of sodium ions (de)intercalation. For samples with Mn content  $x = 0, 0.5, 1$  the presence of a two-phase transition between the phases of the supposed composition “ $\text{Na}_3\text{Mn}_x\text{V}_{2-x}(\text{PO}_4)_3$ ” and “ $\text{Na}_2\text{Mn}_x\text{V}_{2-x}(\text{PO}_4)_3$ ” is shown. When charged up to 4.1 V, the current transients

on discharge of  $\text{Na}_{3+x}\text{Mn}_x\text{V}_{2-x}(\text{PO}_4)_3$  ( $x = 0.5, 1$ ) samples indicate the intercalation reaction proceeding only by the solid-solution mechanism.

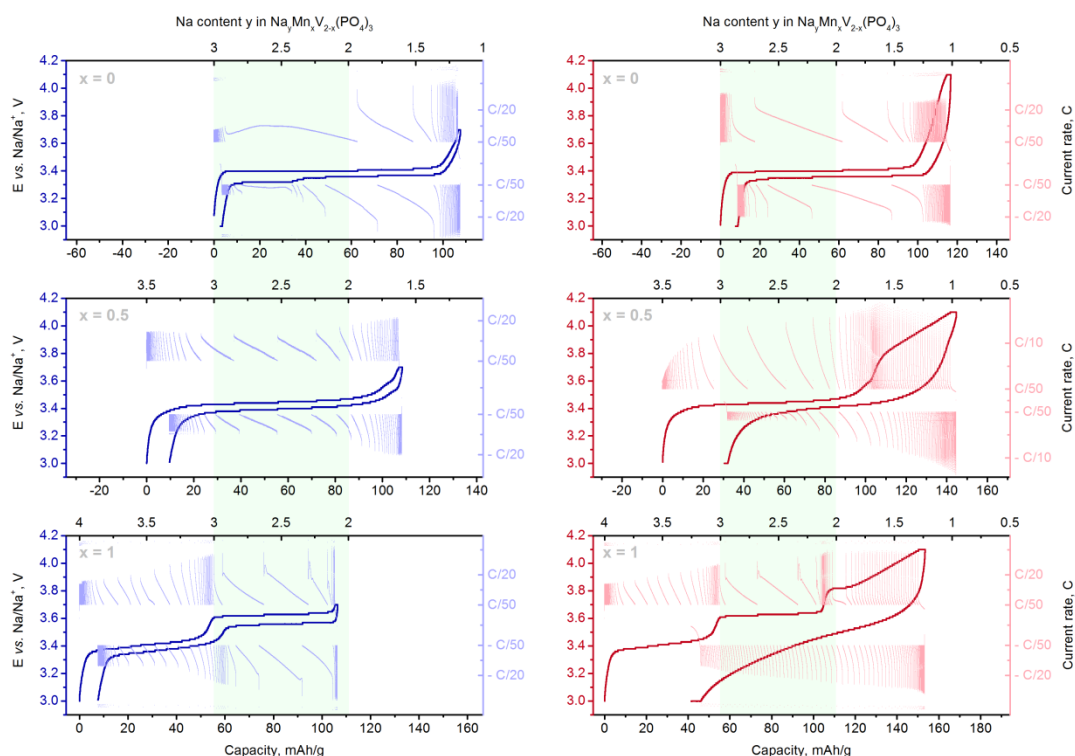


**Fig. 5.** 3 PITT measurements upon two successive cycles in the 2.5-3.8V (left) and 2.5-4.1V (right) voltage windows for  $\text{Na}_3\text{V}_2(\text{PO}_4)_3$ ,  $\text{Na}_{3.5}\text{Mn}_{0.5}\text{V}_{1.5}(\text{PO}_4)_3$ , and  $\text{Na}_4\text{MnV}(\text{PO}_4)_3$ . A biphasic “ $\text{Na}_3\text{Mn}_x\text{V}_{2-x}(\text{PO}_4)_3$ ” – “ $\text{Na}_2\text{Mn}_x\text{V}_{2-x}(\text{PO}_4)_3$ ” transition is highlighted for clarity of presentation. A voltage step on discharge of  $\text{Na}_3\text{V}_2(\text{PO}_4)_3$  is most probably due to the side reaction with metallic Na electrode [133,134].

In addition, the compositions with  $x \geq 0.6$  have low capacity retention, and the fade is the stronger the higher the Mn content is (Fig. 5. 1, Fig. 5. 4b). It is essential that the expansion of the voltage window beyond 3.8 V leads to a capacity increase above the theoretical values for (de)intercalation of 2 Na ions (Fig. 5. 4a). Energy density improvement for all  $\text{Na}_{3+x}\text{Mn}_x\text{V}_{2-x}(\text{PO}_4)_3$  ( $x \geq 0.4$ ) exceeds 8%. As it is shown in the following chapter, deintercalation of extra  $\text{Na}^+$  ions in  $\text{Na}_4\text{MnV}(\text{PO}_4)_3$  proceeds

through depletion of Na1 position [135,136], which possibly also takes place in  $\text{Na}_{3+x}\text{Mn}_x\text{V}_{2-x}(\text{PO}_4)_3$  compounds with lower Mn content.

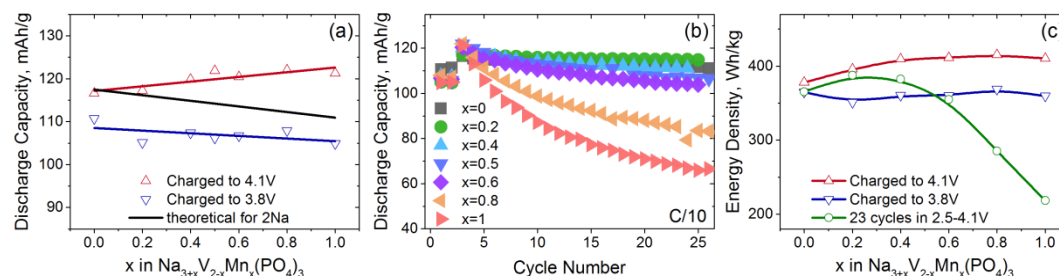


**Fig. 5. 4 (a) Discharge capacity for  $\text{Na}_{3+x}\text{Mn}_x\text{V}_{2-x}(\text{PO}_4)_3$  compounds ( $x = 0, 0.2, 0.4, 0.5, 0.6, 0.8, 1$ ) charged to 3.8 V (blue line) and to 4.1 V (red line). (b) Capacity retention for  $\text{Na}_{3+x}\text{Mn}_x\text{V}_{2-x}(\text{PO}_4)_3$  compounds, cycled two times in 2.5-3.8 V voltage window and then in 2.5-4.1 V voltage window at C/10 current rate. (c) Energy density for  $\text{Na}_{3+x}\text{Mn}_x\text{V}_{2-x}(\text{PO}_4)_3$  samples ( $x = 0, 0.2, 0.4, 0.6, 0.8, 1$ ) charged to 3.8 V (blue line) and to 4.1 V (red and green lines)**

Cycling stability is another important factor determining the level of attractiveness of electrode materials. As it was reported for  $\text{Na}_4\text{MnV}(\text{PO}_4)_3$  [135,136], rising the cut-off voltage above 3.8 V leads to fast capacity fade during cycling. We studied cycling stability of the  $\text{Na}_{3+x}\text{V}_{2-x}\text{Mn}_x(\text{PO}_4)_3$  samples ( $0 \leq x \leq 1$ ) and found a straightforward dependence between substitution degree  $x$  and the rate of capacity fading (Fig. 5. 4b and Fig. 5. 4c). The cases of  $x=0.2$  and  $x=0.4$  compositions still demonstrate ~5% energy density gain towards  $\text{Na}_3\text{V}_2(\text{PO}_4)_3$  after 23 charge-discharge cycles within 2.5-4.1 V potential window. Yet stabilization of the practical energy density above  $410 \text{ Wh kg}^{-1}$  observed for  $x>0.4$  samples (Fig. 5. 1, Fig. 5. 4c) is still an important challenge.

Short-range cycling of the electrodes within different voltage thresholds (with upper potential varying from 3.8 to 4.4 V, Fig. 5. 5) revealed 2.5 – 4.0 V interval as

the most promising for practical application because of combining sufficient discharge capacity and cycling stability.

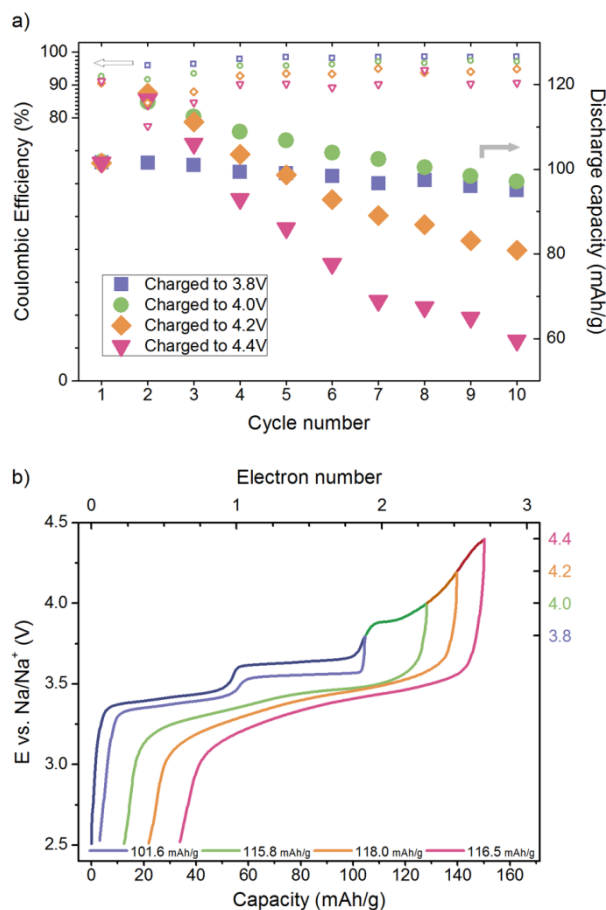


**Fig. 5. 5 (a) Discharge capacity retention and coulombic efficiency for  $\text{Na}_4\text{MnV}(\text{PO}_4)_3$  electrodes cycled at  $C/5$  current rate within different potential intervals. At first cycle potential limit was set as 3.8V for all cells. (b) Charge-discharge curves corresponding to the 2<sup>nd</sup> cycle.**

To sum up, electrochemical properties of the  $\text{Na}_{3+x}\text{Mn}_x\text{V}_{2-x}(\text{PO}_4)_3$  ( $0 \leq x \leq 1$ ) materials were studied within two voltage windows: 2.5-3.8 V and 2.5-4.1 V vs.  $\text{Na}/\text{Na}^+$ . Increase in the average charge/discharge voltage is the main visible result of the Mn substitution for the cycling between 2.5 V and 3.8 V. All Mn-substituted samples are characterized by additional high-voltage plateau ( $\sim 3.9$  V) at charge-

discharge curves. Utilization of this high-voltage step at 3.9 V results in attaining discharge capacities, which correspond to reversible extraction of more than 2 sodium ions from Mn-substituted materials. The following chapter investigates the processes occurring in the crystal structure of  $\text{Na}_{3+x}\text{Mn}_x\text{V}_{2-x}(\text{PO}_4)_3$  materials during charge and discharge.

## Chapter 6. Phase transformation behavior during charge and discharge of $\text{Na}_{3+x}\text{Mn}_x\text{V}_{2-x}(\text{PO}_4)_3$ ( $0 \leq x \leq 1$ )

In order to link electrochemical features with the phase transformations in  $\text{Na}_{3+x}\text{Mn}_x\text{V}_{2-x}(\text{PO}_4)_3$  ( $0 \leq x \leq 1$ ) samples *operando* XRPD was carried out for two charge-discharge cycles in different voltage windows using an electrochemical cell supplied with the Bruker D8 diffractometer [120]. Fig. 6. 1 shows a 2D profile of the 024 reflection evolution for the cases of cut-off voltage at 3.8 V on the bottom plots and at 4.1 V on the top plots overlaid with the corresponding galvanostatic curves.

### 6.1 Phase transformations in the 2.5-3.8 V voltage window

General overview of the *operando* patterns in 2.5-3.8 V window suggests that several single and two-phase domains exist during  $\text{Na}^+$  (de)intercalation from  $\text{Na}_{3+x}\text{Mn}_x\text{V}_{2-x}(\text{PO}_4)_3$  compounds. To systemize the phase transformation behavior over  $\text{Na}_{3+x}\text{Mn}_x\text{V}_{2-x}(\text{PO}_4)_3$  ( $0 \leq x \leq 1$ ) family a schematic diagram was constructed (Fig. 6. 2). It illustrates how the composition of the present phases change, and what the deintercalation mechanism is at different states of charge. According to the scheme, at the beginning extraction of  $\text{Na}^+$  from the initial  $\text{Na}_{3+x}\text{Mn}_x\text{V}_{2-x}(\text{PO}_4)_3$  leads to a “ $\text{Na}_3\text{Mn}_x\text{V}_{2-x}(\text{PO}_4)_3$ ” through a solid solution mechanism. Then  $\text{Na}^+$  extraction proceeds by a biphasic “ $\text{Na}_3\text{Mn}_x\text{V}_{2-x}(\text{PO}_4)_3$ ”–“ $\text{Na}_2\text{Mn}_x\text{V}_{2-x}(\text{PO}_4)_3$ ” transition. Importantly, we note that around “ $\text{Na}_2\text{Mn}_x\text{V}_{2-x}(\text{PO}_4)_3$ ” composition a narrow solid-solution domain is observed. Further  $\text{Na}^+$  extraction occurs *via* a biphasic reaction until the “ $\text{Na}_{1+x}\text{Mn}_x\text{V}_{2-x}(\text{PO}_4)_3$ ” composition is reached around 3.8 V. Towards this

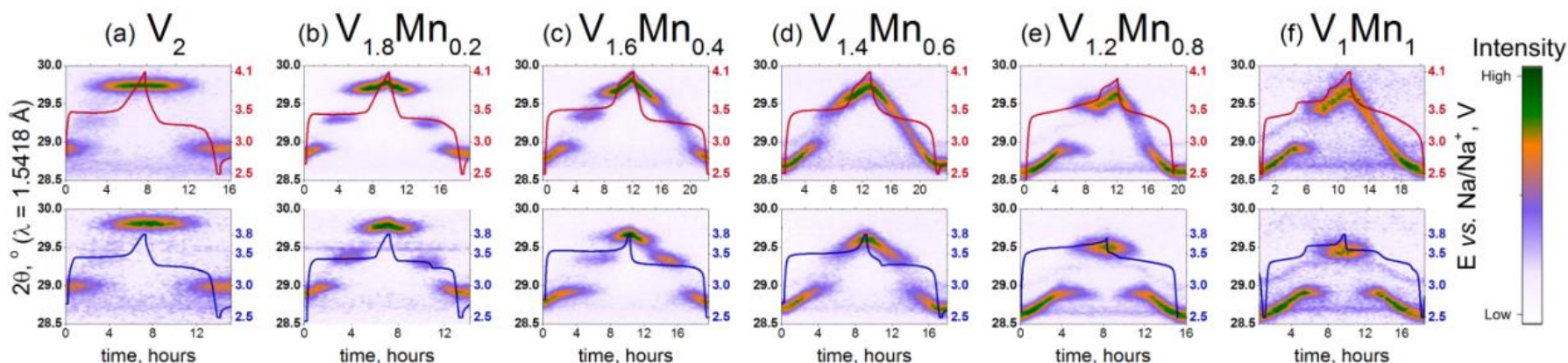


Fig. 6. 1 (top image) Transformations of the selected region (024 reflection, 28.5-30.0°,  $\text{Cu}_{\text{K}\alpha 1/\text{K}\alpha 2}$ ) of XRPD patterns during *operando* charge-discharge in the 2.5-3.8 V (bottom) and 2.5-4.1 V (top) voltage windows for (a)  $\text{Na}_3\text{V}_2(\text{PO}_4)_3$ , (b)  $\text{Na}_{3.2}\text{Mn}_{0.2}\text{V}_{1.8}(\text{PO}_4)_3$ , (c)  $\text{Na}_{3.4}\text{Mn}_{0.4}\text{V}_{1.6}(\text{PO}_4)_3$ , (d)  $\text{Na}_{3.6}\text{Mn}_{0.6}\text{V}_{1.4}(\text{PO}_4)_3$ , (e)  $\text{Na}_{3.8}\text{Mn}_{0.8}\text{V}_{1.2}(\text{PO}_4)_3$ , (f)  $\text{Na}_4\text{MnV}(\text{PO}_4)_3$ . Transformations of other reflections are presented on Fig. A 6. Voltage steps on discharge are most probably due to side reactions with metallic Na electrode [133,134].

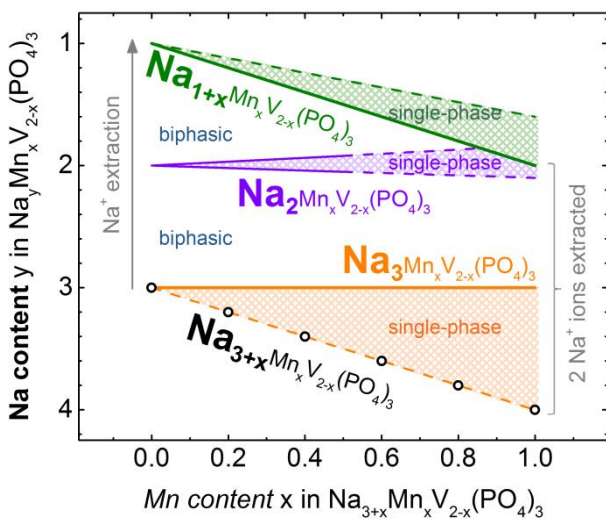
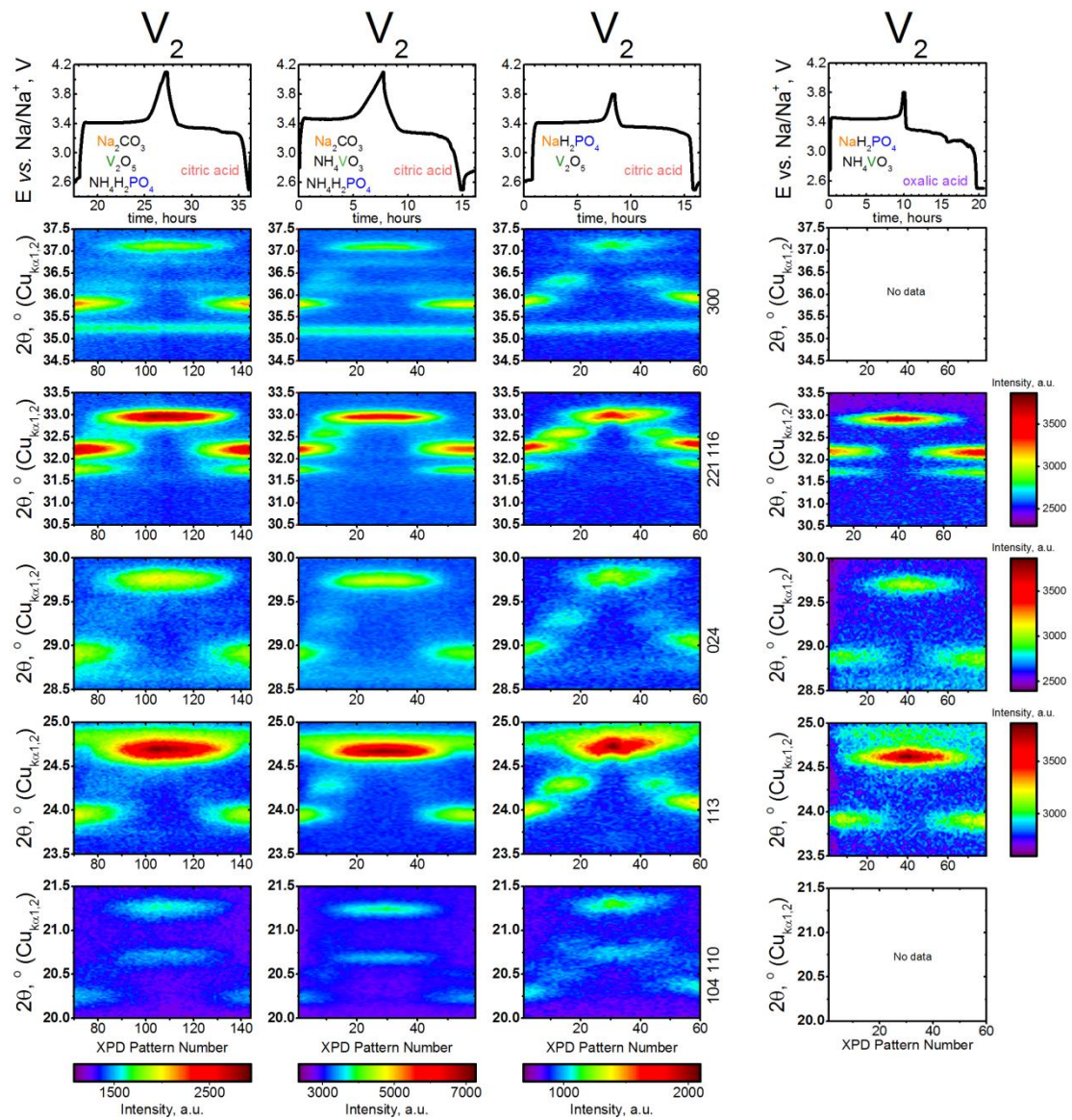


Fig. 6. 2 (central image) Schematic illustration of the  $\text{Na}^+$  deintercalation regimes from  $\text{Na}_{3+x}\text{Mn}_x\text{V}_{2-x}(\text{PO}_4)_3$  ( $0 \leq x \leq 1$ ) during  $\text{Na}^+$  extraction. The scheme is based on the unit cell volume variation obtained from *operando* XRPD patterns (Table A 1) and electrochemical data. Upper dashed line corresponds to the 4.1 V voltage cut-off.

point,  $\text{Na}^+$  reinsertion on discharge would be reversible passing through the same (de)intercalation domains. In addition, this accords with the PITT data, which clearly represent the diffusion- and the phase-transition-limited processes by the shape of the current transients (Fig. 5. 3). Apparently, the end-members ( $x=0$  and  $x=1$ ) demonstrate the least diverse phase transformation processes composed of only two distinguishable domains. As discussed below we provide greater detail of the phase transformations in the 2.5-3.8 V voltage window for the studied compositions.

#### 6.1.1 $\text{Na}_3\text{V}_2(\text{PO}_4)_3$ .

The *operando* pattern for  $\text{Na}_3\text{V}_2(\text{PO}_4)_3$  shows an entirely biphasic mechanism:  $\text{Na}_3\text{V}_2(\text{PO}_4)_3$  phase reflections disappear during  $\text{Na}^+$  deintercalation followed by the  $\text{NaV}_2(\text{PO}_4)_3$  reflections intensity enhancement on charge (Fig. 6. 1). These data are consistent with the previous findings [83]. Interestingly, on charge deintercalation proceeds through an intermediate phase, possibly  $\text{Na}_2\text{V}_2(\text{PO}_4)_3$ , manifesting itself in appearance of well-discernible reflections at 20.5, 24.3, 29.3, 32.6 and 36.4° (Fig. 6. 3). Careful examination of the  $\text{Na}_3\text{V}_2(\text{PO}_4)_3$  *operando* patterns in the former works confirms the presence of this intermediate phase on charge [83,91]. Moreover, electrochemical curves and XRPD patterns of  $\text{Na}_3\text{V}_2(\text{PO}_4)_3$  synthesized by different routes have respectively slightly different shape and distinct reflection intensities of the intermediate phase both on charge and discharge (Fig. 6. 3), which is probably related to the different size of the coherently scattering regions of the “ $\text{Na}_2\text{V}_2(\text{PO}_4)_3$ ” nuclei. Hence, on charge  $\text{Na}_3\text{V}_2(\text{PO}_4)_3$  demonstrates two biphasic phase transitions ( Fig. 6. 2).



**Fig. 6.** 3 Transformations of the selected regions ( $20.0-21.5^\circ$ ,  $23.5-25.0^\circ$ ,  $28.5-30.0^\circ$ ,  $31.5-33.5^\circ$ ,  $34.5-37.5^\circ$ ,  $\text{Cu}_{\text{Ka}1/\text{Ka}2}$ ) of XRPD patterns during *operando* charge-discharge in the 2.5-3.8V and 2.5-4.1V voltage windows for  $\text{Na}_3\text{V}_2(\text{PO}_4)_3$ , synthesized by the same procedure, but using different precursors, which are specified on the top graphs.

### 6.1.2 $\text{Na}_{3.2}\text{Mn}_{0.2}\text{V}_{1.8}(\text{PO}_4)_3$ and $\text{Na}_{3.4}\text{Mn}_{0.4}\text{V}_{1.6}(\text{PO}_4)_3$ .

Heterovalent substitution of  $\text{V}^{3+}$  to  $\text{Mn}^{2+}$  in  $\text{Na}_3\text{V}_2(\text{PO}_4)_3$  requires an excess of  $\text{Na}^+$  cations for charge compensation. Extraction of this excess  $\text{Na}^+$  ions from the

initial  $\text{Na}_{3+x}\text{Mn}_x\text{V}_{2-x}(\text{PO}_4)_3$  leads to a “ $\text{Na}_3\text{Mn}_x\text{V}_{2-x}(\text{PO}_4)_3$ ” through a solid solution mechanism, the unit cell volume change  $\Delta V$  varying almost concomitantly as Na-excess  $x$  (Table A 1, Fig. A 7). Further charge to 3.8 V leads to a composition “ $\text{Na}_{1+x}\text{Mn}_x\text{V}_{2-x}(\text{PO}_4)_3$ ” by extracting  $(2-x)$   $\text{Na}^+$  ions as can be deduced from the electrochemical measurements (Fig. 5. 1). For  $x=0.2$  and  $x=0.4$  the “ $\text{Na}_3\text{Mn}_x\text{V}_{2-x}(\text{PO}_4)_3$ ”–“ $\text{Na}_{1+x}\text{Mn}_x\text{V}_{2-x}(\text{PO}_4)_3$ ” process exhibits two first-order phase transitions, which reversibly proceeds through an intermediate “ $\text{Na}_2\text{Mn}_x\text{V}_{2-x}(\text{PO}_4)_3$ ” composition. The  $2\theta$  position of the clearly visible reflections of the “ $\text{Na}_2\text{Mn}_x\text{V}_{2-x}(\text{PO}_4)_3$ ” slightly shifts during the charge and discharge processes indicating the presence of a narrow solid-solution domain (Fig. 6. 1). Such an intermediate was also present in Al- and Ti-substituted  $\text{Na}_3\text{V}_2(\text{PO}_4)_3$  [106,137]. Examples from Li-ion systems are also well-known, *e.g.* intermediate Li-deficient phase in Mn-substituted  $\text{LiFePO}_4$  [138,139]. Its appearance in olivine-type cathode materials was associated with dilution of phase-separating interactions between alkali cations and transition metal cations, which transformed the first-order transition into a second-order forming a metastable solid solution [140,141]. While it is hardly discernable on the galvanostatic curves, the signatures of two biphasic transitions are clearly shown by differential capacity plots on Fig. 5. 2a, the derivative reflections show separation increasing from 0.002 V for  $\text{Na}_3\text{V}_2(\text{PO}_4)_3$  to 0.15 V for  $\text{Na}_{3.4}\text{Mn}_{0.4}\text{V}_{1.6}(\text{PO}_4)_3$  on charge.

### 6.1.3 $\text{Na}_{3.6}\text{Mn}_{0.6}\text{V}_{1.4}(\text{PO}_4)_3$ .

The case of  $x=0.6$  has several unique features for the  $\text{Na}_{3+x}\text{Mn}_x\text{V}_{2-x}(\text{PO}_4)_3$  family. Firstly,  $\text{Na}_{3.6}\text{Mn}_{0.6}\text{V}_{1.4}(\text{PO}_4)_3$  does not display definite borders of the biphasic “ $\text{Na}_3\text{Mn}_{0.6}\text{V}_{1.4}(\text{PO}_4)_3$ ”–“ $\text{Na}_2\text{Mn}_{0.6}\text{V}_{1.4}(\text{PO}_4)_3$ ” transition, well-marked for other compositions by essentially unchanged  $2\theta$  positions of each phase’s reflections.

Secondly, since the unit cell volume of the intermediate phase “ $\text{Na}_2\text{Mn}_x\text{V}_{2-x}(\text{PO}_4)_3$ ” becomes closer to the volume of “ $\text{Na}_{1+x}\text{Mn}_x\text{V}_{2-x}(\text{PO}_4)_3$ ” with increasing the Mn-content  $x$ , the “ $\text{Na}_2\text{Mn}_{0.6}\text{V}_{1.4}(\text{PO}_4)_3$ ”–“ $\text{Na}_{1.6}\text{Mn}_{0.6}\text{V}_{1.4}(\text{PO}_4)_3$ ” transition seems to occur through a solid solution reaction (Fig. 6. 1). However, even in a case of actual presence of a biphasic domain, the  $2\theta$  positions of their reflections are too close to each other, so that they can hardly be resolved by standard laboratory X-ray diffraction methods. As a result, these two expanded single-phase transitions with a short biphasic domain are characterized by a sharp differential capacity peak with wide shoulders (Fig. 5. 2a). This phase transformation behavior is believed to be effective for reducing the volume strain and was also shown to occur at non-equilibrium conditions in several other compounds such as  $\text{LiMn}_{0.4}\text{Fe}_{0.6}\text{PO}_4$  [139],  $\text{NaFePO}_4$  [47,142] and  $\text{Li}_2\text{VPO}_4\text{O}$  [143].

#### 6.1.4 $\text{Na}_{3.8}\text{Mn}_{0.8}\text{V}_{1.2}(\text{PO}_4)_3$ and $\text{Na}_4\text{MnV}(\text{PO}_4)_3$ .

The *operando* XRPD pattern for the  $\text{Na}_4\text{MnV}(\text{PO}_4)_3$  is already known [135,136]. It adopts two phase transitions: a single-phase  $\text{Na}_4\text{MnV}(\text{PO}_4)_3$ – $\text{Na}_3\text{MnV}(\text{PO}_4)_3$  and a biphasic  $\text{Na}_3\text{MnV}(\text{PO}_4)_3$ – $\text{Na}_2\text{MnV}(\text{PO}_4)_3$  transitions. Closer inspection of the  $dQ/dE$  and PITT data (Fig. 5. 2 and Fig. 5. 3) for the  $\text{Na}_4\text{MnV}(\text{PO}_4)_3$ – $\text{Na}_3\text{MnV}(\text{PO}_4)_3$  transition suggests a presence of 2 separate processes, which are hardly visible on the X-ray diffraction data at the applied current rates.

Similarly to  $\text{Na}_4\text{MnV}(\text{PO}_4)_3$ , in the case of  $x=0.8$  deintercalation of 0.8 Na ions from  $\text{Na}_{3.8}\text{Mn}_{0.8}\text{V}_{1.2}(\text{PO}_4)_3$  occurs *via* a solid-solution regime followed by a biphasic reaction until the “ $\text{Na}_{1.8}\text{Mn}_{0.8}\text{V}_{1.2}(\text{PO}_4)_3$ ” composition is reached (Fig. 6. 1).

Utilization of a higher resolving synchrotron radiation (Fig. 6. 6) allows to clearly observe that at approximately 50% state of charge the “ $\text{Na}_3\text{Mn}_{0.8}\text{V}_{1.2}(\text{PO}_4)_3$ ” reflection broadens, and concurrently reflection of a new “ $\text{Na}_2\text{Mn}_{0.8}\text{V}_{1.2}(\text{PO}_4)_3$ ” phase appears and shifts to higher  $2\theta$  angles until the “ $\text{Na}_{1.8}\text{Mn}_{0.8}\text{V}_{1.2}(\text{PO}_4)_3$ ” composition is reached. On the one hand, this *operando* SXRPD pattern is very similar to the case of  $x=1.0$ . It has a broad domain of concurrent co-existence of two phases (“ $\text{Na}_3\text{Mn}_{0.8}\text{V}_{1.2}(\text{PO}_4)_3$ ” and “ $\text{Na}_{1.8}\text{Mn}_{0.8}\text{V}_{1.2}(\text{PO}_4)_3$ ”), but on the other hand the mentioned broadening and reflection shifting resembles the case of  $x=0.6$  in that two single-phase domains exist between “ $\text{Na}_3\text{Mn}_x\text{V}_{2-x}(\text{PO}_4)_3$ ” and “ $\text{Na}_{1+x}\text{Mn}_x\text{V}_{2-x}(\text{PO}_4)_3$ ”. Since the synchrotron *operando* SXRPD pattern reveals symmetry reduction from rhombohedral to monoclinic due to the appearance of additional reflections (Fig. 6. 4) exactly as for the  $\text{Na}_4\text{MnV}(\text{PO}_4)_3$  [135], we used a well-known monoclinic modification of the NASICON structure with  $C2/c$  symmetry for the sequential Le Bail fitting of the  $\text{Na}_{3.8}\text{Mn}_{0.8}\text{V}_{1.2}(\text{PO}_4)_3$  *operando* SXRPD pattern [144].

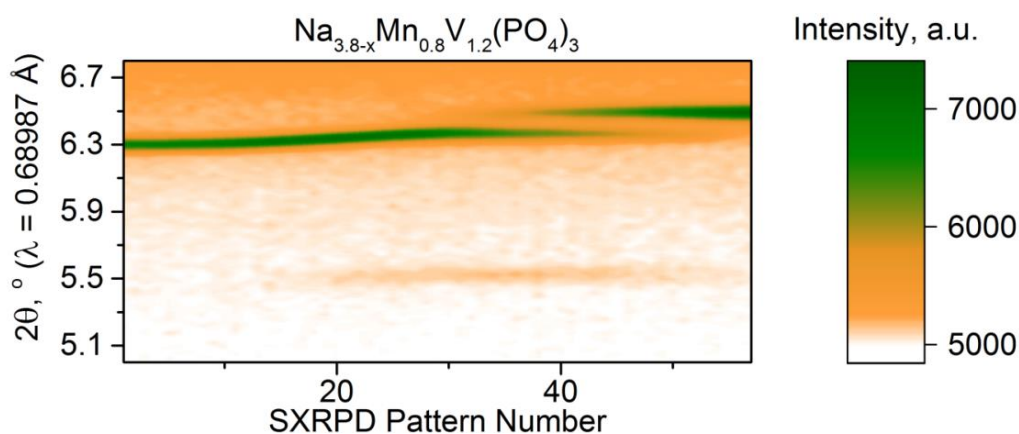


**Fig. 6. 4** Appearance of monoclinic 110 reflection at 5.5 degrees during  $\text{Na}^+$  (de)intercalation from  $\text{Na}_{3.8}\text{Mn}_{0.8}\text{V}_{1.2}(\text{PO}_4)_3$

Using the monoclinic symmetry enable indexing the additional reflections and fit the aforementioned broadening (Fig. 6. 5, Fig. 6. 6c).

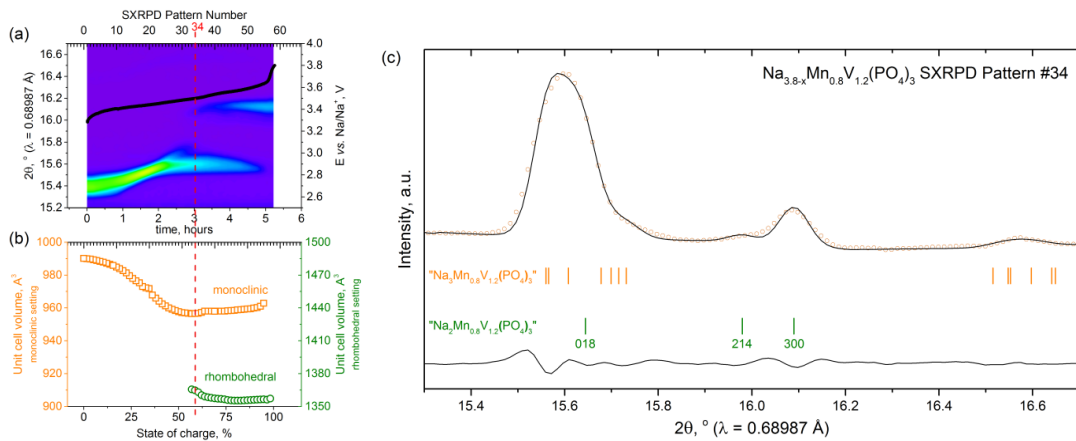


**Fig. 6. 5 (a) Transformations of the selected region of SXRPD patterns during *operando* charge, (b) unit cell volume of 1 monoclinic and 1 rhombohedral  $\text{Na}_{3.8-x}\text{Mn}_{0.8}\text{V}_{1.2}(\text{PO}_4)_3$  phases, (c) corresponding Le Bail fit for a selected SXRPD pattern (#34)**

Le Bail fitting indicates an ongoing alteration of the unit cell parameters of both phases present during the biphasic domain on charge to 3.8 V, which explains the sloped shape of the E-x curve, unlike  $\text{Na}_4\text{MnV}(\text{PO}_4)_3$ , which has a plateau at the same two-phase domain (Fig. 6. 6b, Fig. 6. 6c).

To determine the redox reactions occurring during charge and discharge of  $\text{Na}_4\text{MnV}(\text{PO}_4)_3$ , *operando* X-ray absorption spectroscopy (XAS) experiments were carried out at energies corresponding to absorption by manganese and vanadium. After alignment and normalization of the spectra sets, the position of the absorption edge was automatically extracted for each spectrum. A monotonous change in the position of the absorption edge on charge or discharge is the evidence of a change in the oxidation state of the corresponding transition metal ion. Thus, information on redox transitions can be extracted from the analysis of changes in the position of the absorption edge.

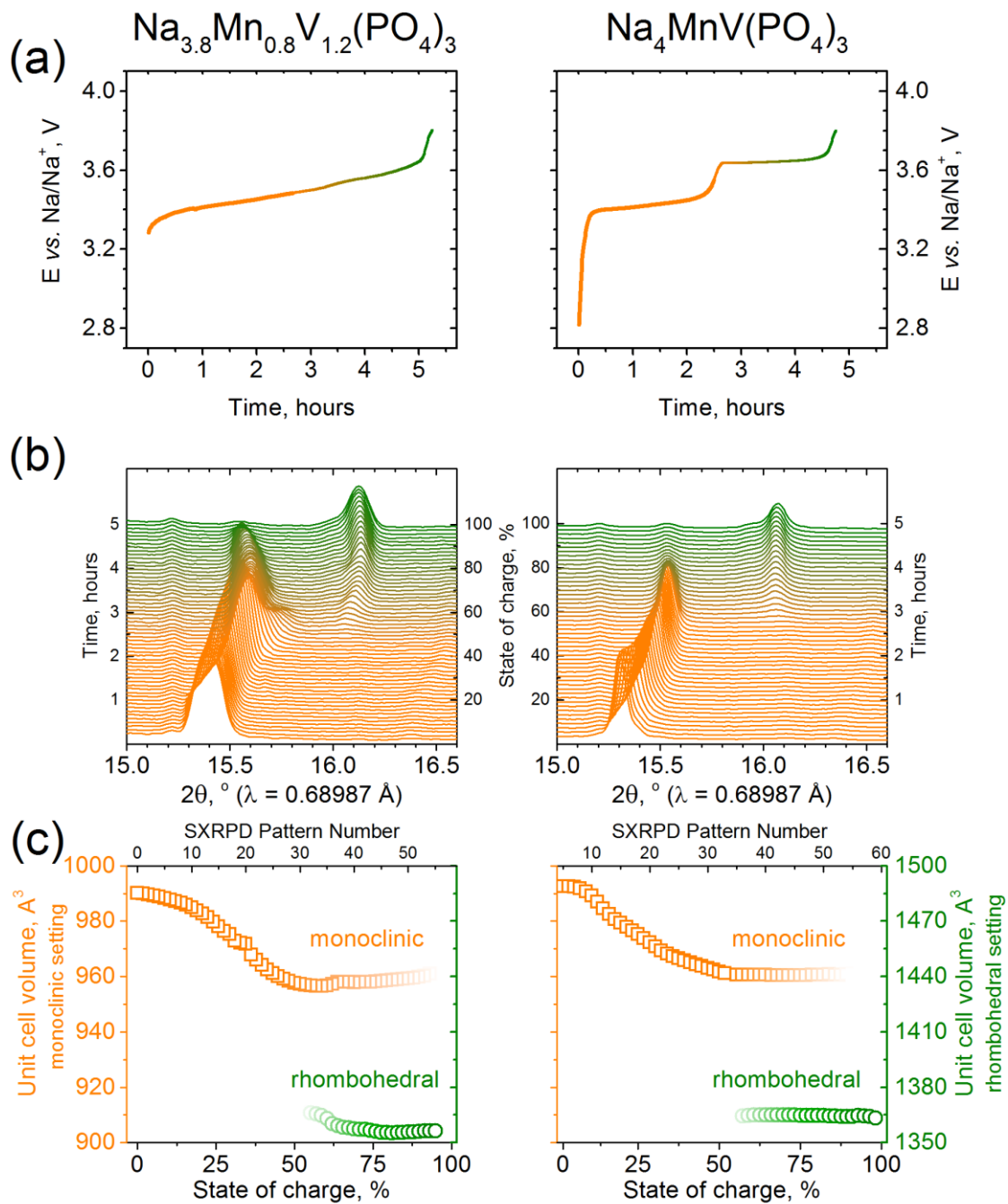


**Fig. 6. 6** Similar structural transitions may result in different electrochemical signatures. (a) Electrochemical charge curves, (b) transformations of the selected region of SXRPD patterns and (c) unit cell parameters of  $\text{Na}_{3.8-x}\text{Mn}_{0.8}\text{V}_{1.2}(\text{PO}_4)_3$  (left) and  $\text{Na}_{4-x}\text{MnV}(\text{PO}_4)_3$  (right) within 2.5–3.8 V voltage ranges.

As noted above, the galvanostatic curve of the  $\text{Na}_4\text{MnV}(\text{PO}_4)_3$  below 3.8 V consists of two steps: at ~3.4 V and ~3.6 V. Fig. 6. 7 illustrates the changes in the

position of Mn K-edge in the  $\text{Na}_4\text{MnV}(\text{PO}_4)_3$  and corresponding galvanostatic curve during cycling in the potential window of 2.5-3.8 V.

It is clearly seen that at the lower steps of the charge and discharge curves, the position of the K-edge of manganese remains at  $\sim 6537$  eV, that is, the oxidation state of Mn does not change. On the upper plateau, there is an obvious shift of the absorption edge (oxidation  $\text{Mn}^{2+} \rightarrow \text{Mn}^{3+}$ , as shown below). On discharge the reverse motion of the Mn K-edge occurs on the upper plateau, which corresponds to the reduction of  $\text{Mn}^{3+} \rightarrow \text{Mn}^{2+}$ , and at the lower step, the position of the Mn edge remains unchanged. It is clearly seen that the transformation at Mn K-edge occurs reversibly on the 3.6 V step.

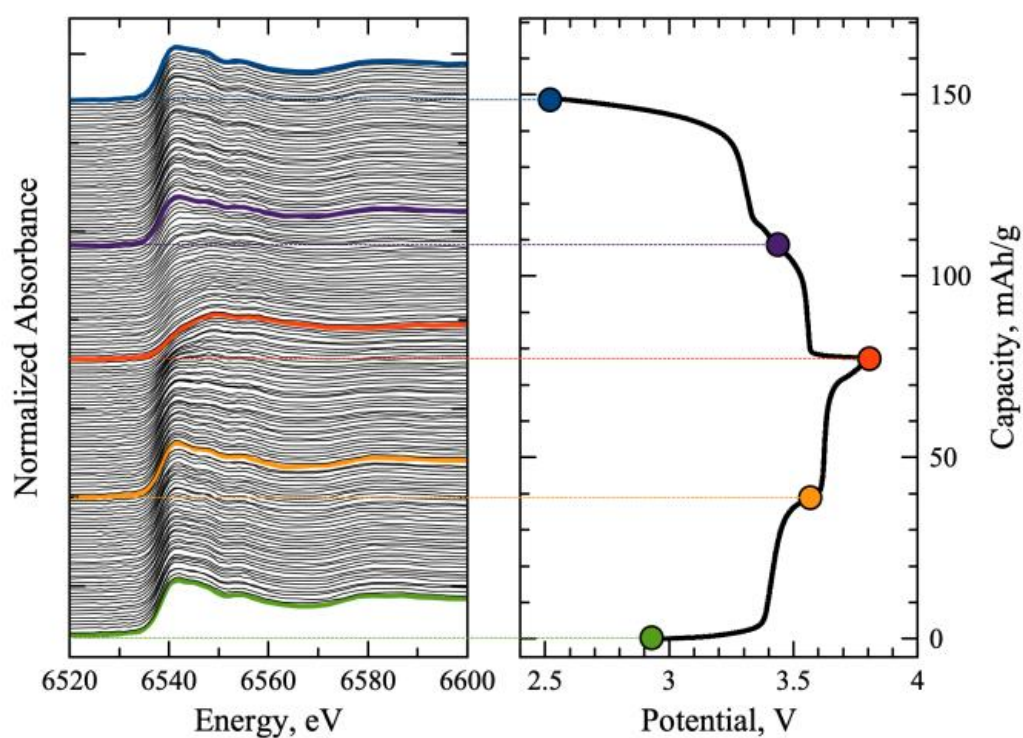
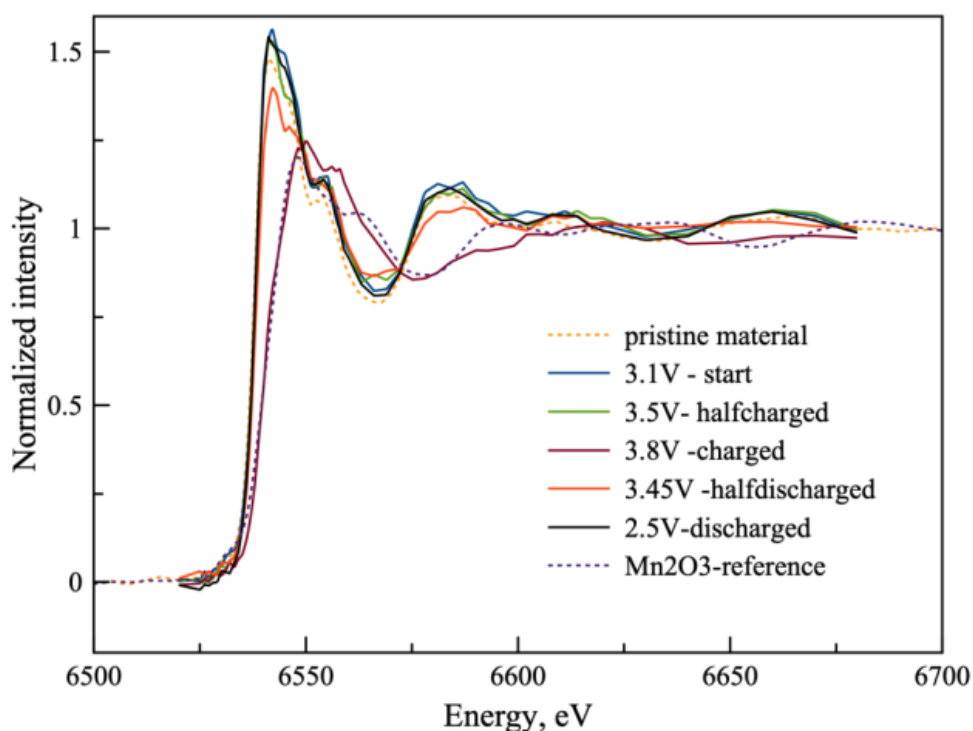


Fig. 6. 7 X-ray absorption spectra of  $\text{Na}_{4-x}\text{MnV}(\text{PO}_4)_3$  at the K-edge of Mn during one *operando* charge-discharge cycle

The Fig. 6. 8 compares the Mn spectra at different states of charge of  $\text{Na}_4\text{MnV}(\text{PO}_4)_3$  with the spectra of the pristine material as well as with the standard  $\text{Mn}_2\text{O}_3$ .

Upon charge to 3.5 V, though the position of the Mn edge does not change, the shape of the spectrum is somewhat different. The position of the Mn edge of the material charged to 3.8 V corresponds to  $\text{Mn}^{3+}$  fairly well. Upon discharge, the spectrum returns to its original state. The spectrum of the pristine material is close to the spectrum of the discharged electrode in the *operando* cell.



**Fig. 6. 8** Selected X-ray absorption spectra of  $\text{Na}_{4-x}\text{MnV}(\text{PO}_4)_3$  at the K-edge of Mn during one *operando* charge-discharge cycle

For technical reasons the spectra at the K-edge of vanadium are noisier than those at the K-edge of manganese; therefore, measurements for vanadium were carried out over several cycles to collect enough signals (Fig. 6. 9). The result indicate

an evident change in the position of the V edge at the ~3.4 V step, which corresponds to the  $V^{3+}/V^{4+}$  transition. However, the data on the position of the K-edge of vanadium on the 3.6 V plateau is obviously too scattered to be sure that there are no changes in this region.

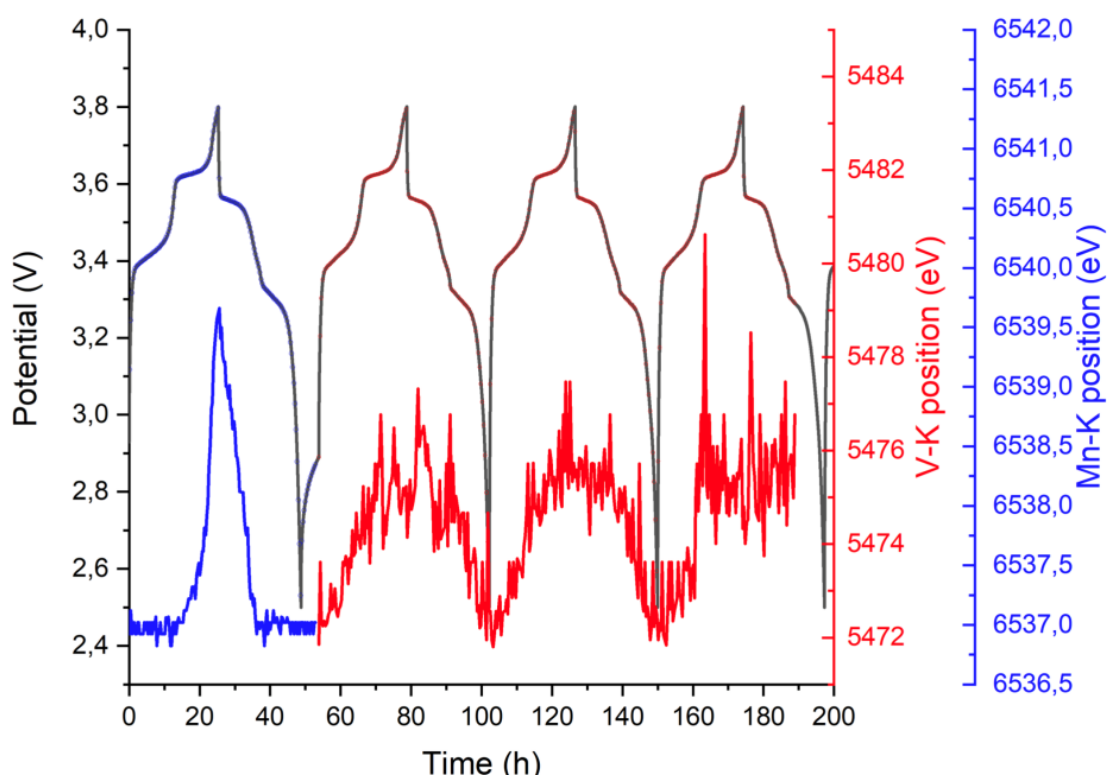


**Fig. 6. 9** Change in the position of the K-edge of Mn (blue, first cycle) and V (red, cycles 2-4) in  $Na_4MnV(PO_4)_3$  during *operando* charge and discharge in a potential window of 2.5-3.8 V

These results give a general idea of redox transitions: the  $V^{3+}/V^{4+}$  pair operates at the lower step of ~3.4 V of the charge-discharge galvanostatic curve, and  $Mn^{2+}/Mn^{3+}$  pair – at the upper plateau of ~3.65 V. Additional subtle effects, *e.g.* minor variations in the shape of the spectra at the K-edge of manganese on the ~3.4 V step, could be associated with small changes in the local structure caused by the oxidation of vanadium ions and deintercalation of sodium ions.

## 6.2 Phase transformations in 2.5-4.1 V voltage window.

According to galvanostatic curves and *operando* XRPD patterns, cycling  $\text{Na}_{3+x}\text{Mn}_x\text{V}_{2-x}(\text{PO}_4)_3$  ( $0 \leq x \leq 1$ ) samples below 3.8 V demonstrates that deintercalation process is reversible on discharge.

Charging  $\text{Na}_3\text{V}_2(\text{PO}_4)_3$  from 3.8 V to 4.1 V does not change positions of  $\text{NaV}_2(\text{PO}_4)_3$  reflections. Charging  $\text{Na}_{3+x}\text{Mn}_x\text{V}_{2-x}(\text{PO}_4)_3$  ( $0.2 \leq x \leq 1$ ) compounds above 3.8 V gradually shifts the reflections towards higher  $2\theta$  angles due to further  $\text{Na}^+$  extraction via a single-phase mechanism. This shift and the corresponding unit cell volume change become greater as Mn-content increases and are associated with a voltage step at  $\sim 3.9$  V. In the case of  $x=0$  this step was also found on charge. It was induced by superstoichiometry in the  $\text{Na}_{3-3\delta}\text{V}_{2+\delta}(\text{PO}_4)_3$  phases [145].

It is important to note that extraction of Na above the  $\text{Na}_{1+x}\text{Mn}_x\text{V}_{2-x}(\text{PO}_4)_3$  ( $x \geq 0.4$ ) limit smooths features of biphasic reactions on subsequent cycling (Fig. 6. 10).

The higher cut-off voltage upon charge and the higher the Mn-content is, the stronger the disappearance of this transition. Careful analysis of the differential capacity plots (Fig. 5. 2b) and the *operando* pattern of the  $\text{Na}_{3.4}\text{Mn}_{0.4}\text{V}_{1.6}(\text{PO}_4)_3$  on discharge after charge to 3.8 V (Fig. 6. 1c) indicate that for some compounds this threshold occurs between 3.7 and 3.8 V.

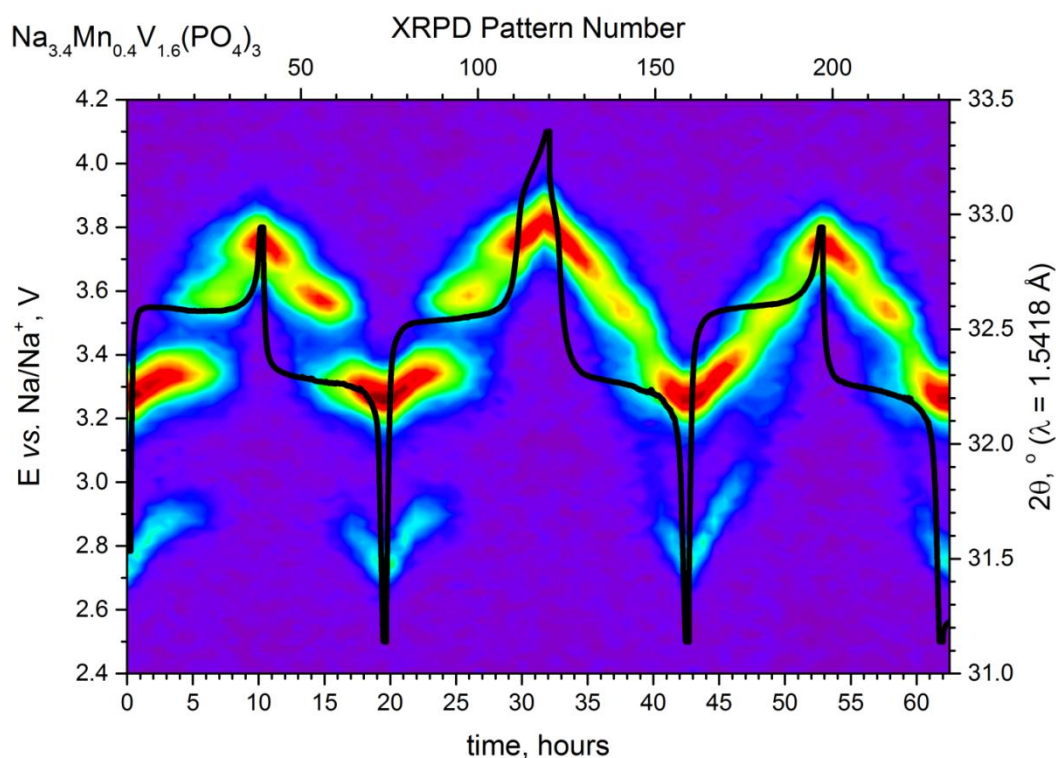


**Fig. 6. 10** Transformations of the selected of XRPD patterns during *operando* charge-discharge in the 2.5-3.8V, 2.5-4.1V and 2.5-3.8V voltage windows for  $\text{Na}_{3.4}\text{Mn}_{0.4}\text{V}_{1.6}(\text{PO}_4)_3$

In order to reveal the (de)intercalation mechanism, *operando* synchrotron X-ray powder diffraction (SXPD) experiments have been performed at the ESRF using an electrochemical cell with sapphire windows [123,146]. As it has already been reported [100], sodium extraction and insertion in  $\text{Na}_4\text{MnV}(\text{PO}_4)_3$  proceeds via two steps in the 2.5-3.8 voltage window, with one sloping and one flat plateau at appr. 3.4 and 3.6 V (Fig. 6. 11a). After the very beginning of the  $\text{Na}^+$  deintercalation, SXPD patterns reflect a symmetry reduction from rhombohedral to monoclinic, which is evident from appearance of additional reflections (Fig. 6. 11d). Therefore for the structure refinements we used both rhombohedral and a well-known monoclinic modification of the NASICON structure with  $C2/c$  symmetry (Figure 2).[144]

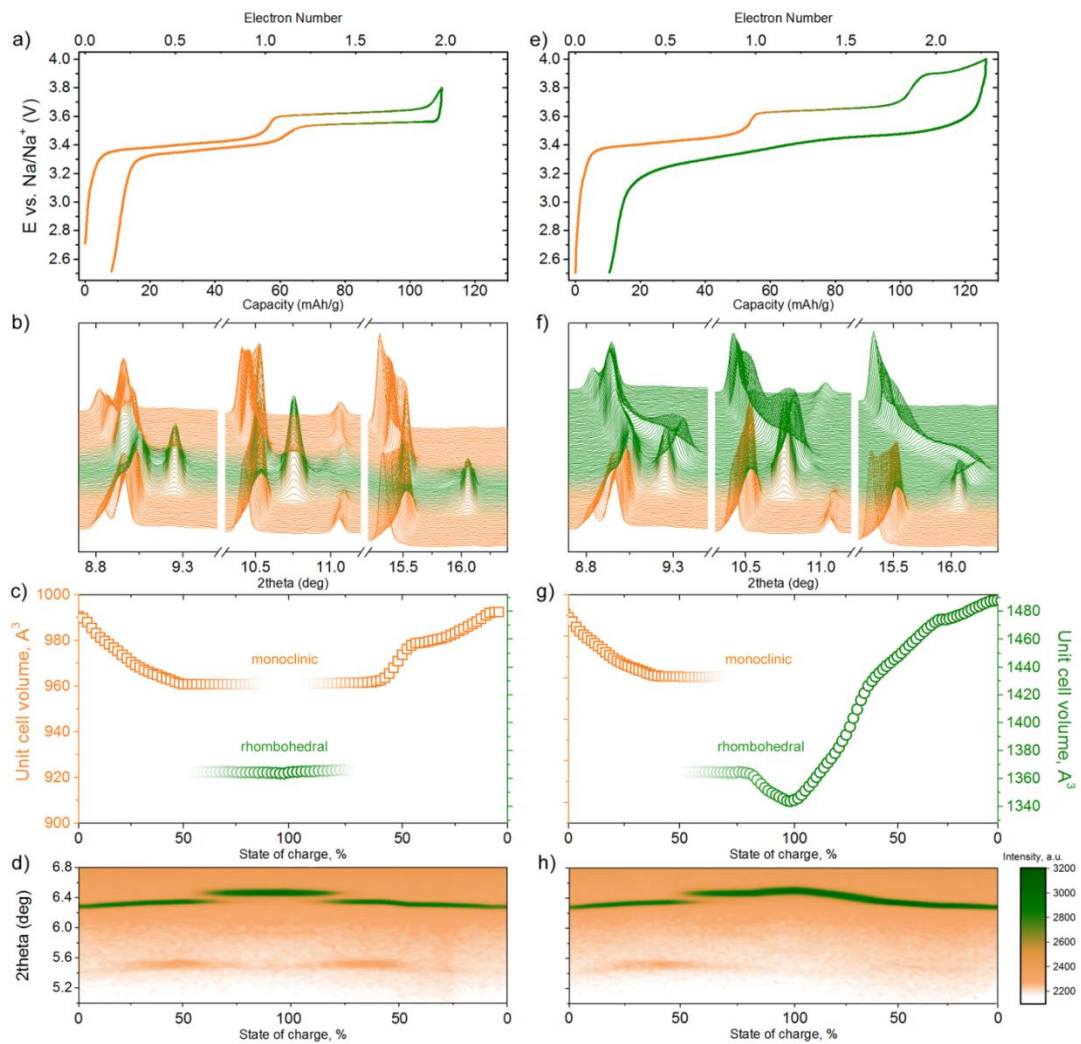


**Fig. 6. 11** Charge-discharge curves and transformations of the selected regions of SXPD patterns and unit cell parameters of  $\text{Na}_{4-x}\text{MnV}(\text{PO}_4)_3$  cathode material within 2.5 – 3.8 V (a, b, c, d) and 2.5 – 4.0 V (e, f, g, h) voltage range.

It must be pointed out that X-ray powder diffraction patterns of rhombohedral and monoclinic  $\text{Na}_{4-x}\text{MnV}(\text{PO}_4)_3$  are very similar (Fig. 6. 12). The monoclinic phase manifests itself in the 110, -423 and 040 reflections (at  $\approx 5.5^\circ$ ,  $16.5^\circ$  and  $18.0^\circ$   $2\theta$  for  $\lambda = 0.68987 \text{ \AA}$ ) which are absent in the rhombohedral pattern. Their intensity is very sensitive to the Na distribution between available crystallographic positions (see examples in Fig. 6. 13). Evolution of the intensity of 110 monoclinic reflection during cycling is shown in Fig. 6. 11d.

Unit cell parameters of the initial electrode in the monoclinic setting are  $a = 15.4679(7) \text{ \AA}$ ,  $b = 8.9438(4) \text{ \AA}$ ,  $c = 8.8048(3) \text{ \AA}$ ,  $\beta = 125.756(3)^\circ$ . The first step of the charge process up to 3.5 V is a solid solution reaction, which is illustrated by a continuous shift of the reflection positions (Fig. 6. 11b) and variation of the unit cell parameters (Fig. 6. 11c, Table A 2) associated with extraction of  $\text{Na}^+$  until the “ $\text{Na}_3\text{MnV}(\text{PO}_4)_3$ ” composition is reached. Such behavior is quite atypical for the NASICON-based cathode materials, where the initial extraction of Na or Li usually proceeds via a two-phase reaction [83,147] because of cation-vacancy ordering.

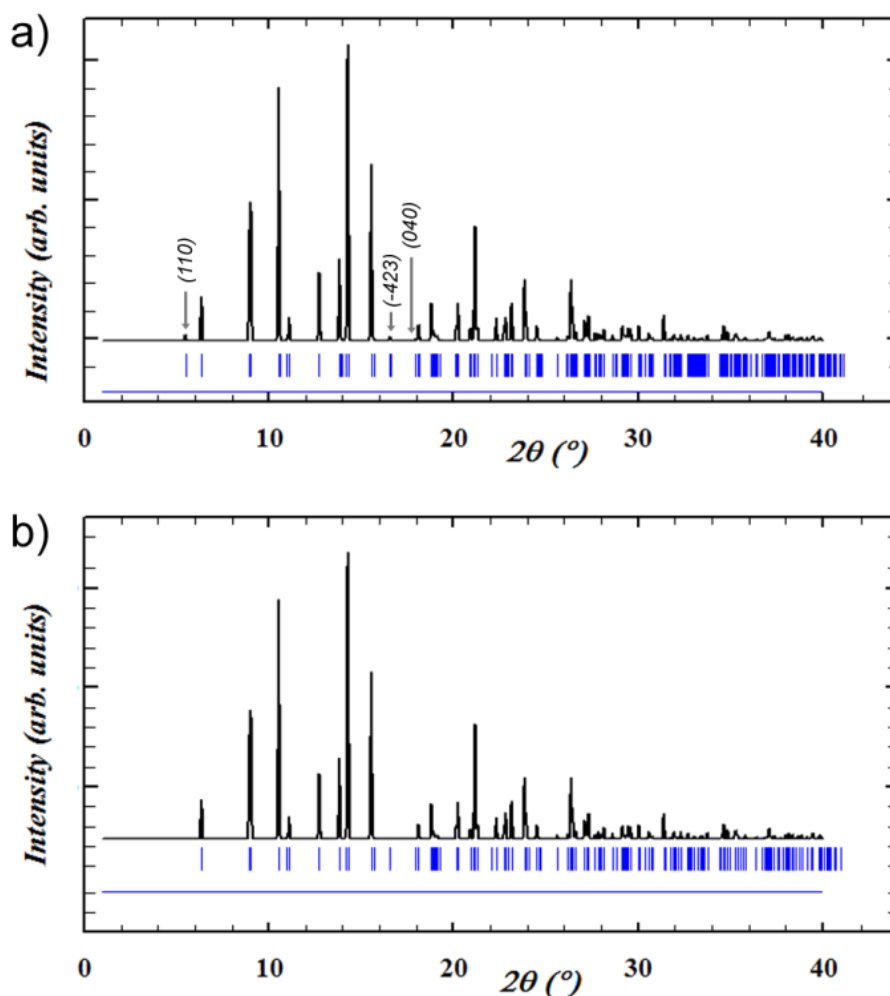


**Fig. 6. 12** Theoretical patterns for  $\text{Na}_{2.96}\text{MnV}(\text{PO}_4)_3$  (electrode charged to 3.5 V) in monoclinic (a) and rhombohedral (b) settings

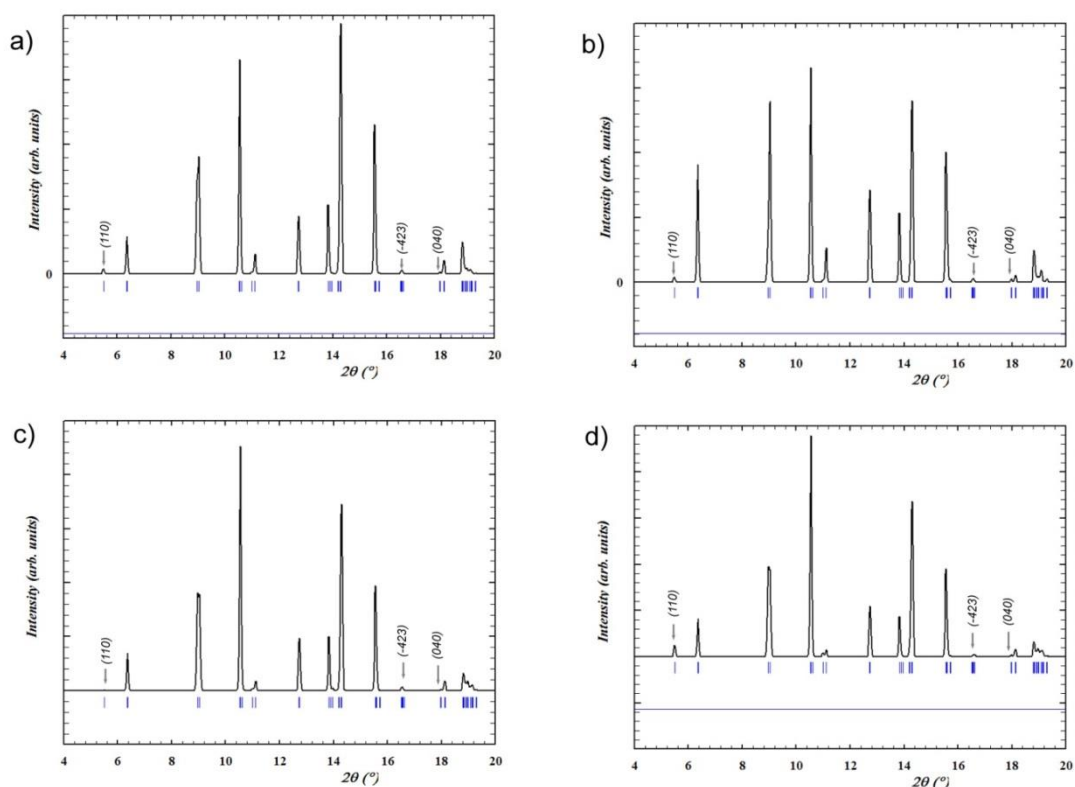


**Fig. 6. 13 Theoretical patterns for  $\text{Na}_x\text{MnV}(\text{PO}_4)_3$  in monoclinic setting. a) occupancy of Na sites corresponds to experimentally observed for  $\text{Na}_{2.96}\text{MnV}(\text{PO}_4)_3$  (electrode charged to 3.5 V); b) occupancy of Na1 = 0, c) occupancy of Na2 = 0, d) occupancy of Na3 = 0.**

The maximum of the intensity of additional monoclinic reflections corresponds to the end of the solid solution region (Fig. 6. 11d) concurrent with strong distortions of the transition metal octahedra  $\text{MO}_6$  (compare the octahedral distortion parameter  $\Delta d$  at different state of charge in Table A 3). Further charge follows a two-phase reaction at 3.65 V plateau, resulting in a formation of sodium-poor “ $\text{Na}_2\text{MnV}(\text{PO}_4)_3$ ” at 3.8 V. Since the typical monoclinic reflections are absent in the SXPD pattern of the charged electrode, we designated “ $\text{Na}_2\text{MnV}(\text{PO}_4)_3$ ” phase as rhombohedral. Transition metal octahedral distortions at this point are minimal. Dependence of the unit cell volumes of the monoclinic and rhombohedral phases on the state of charge is shown in Fig. 6. 11c and Fig. 6. 11g.

In case of the 4.0 V cut-off, a new voltage step is observed on charge at 3.9 V (Fig. 6. 11e). This step is associated with a solid-solution-type reaction illustrated by a smooth shift of reflections towards higher  $2\theta$  angles (Fig. 6. 11f). Extraction of  $\text{Na}^+$  up to the  $\text{Na}_{1.77}\text{MnV}(\text{PO}_4)_3$  composition is accompanied by 1.6% volume contraction. Experimental reversible capacity is above the theoretical value of 111 mAh/g for 2  $\text{Na}^+$  ions extraction, in contrast with  $\approx 100$  mAh/g obtained after charge to 3.8 V.

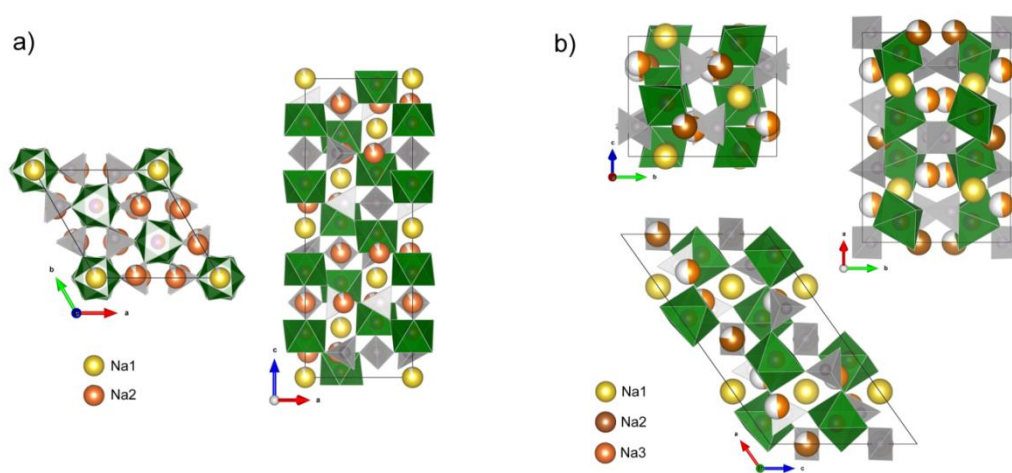


**Fig. 6. 14** Crystal structure of the (a) initial ( $\text{Na}_{3.66}\text{MnV}(\text{PO}_4)_3$ , rhombohedral structure) and (b) charged to 3.5 V ( $\text{Na}_{2.96}\text{MnV}(\text{PO}_4)_3$ , monoclinic structure) phases [148]. Details of the refinement are given in supplementary materials (Table A 4-Table A 8, Fig. A 8-Fig. A 12).

Three Na positions exist in the monoclinic structure:  $4d$  (Na1),  $4e$  (Na2) and  $8f$  (Na3), and only two -  $6b$  (Na1) and  $18e$  (Na2) – in the rhombohedral structure (Figure 2). Rhombohedral Na2 (contains 3 Na atoms per f.u.) site splits into Na2 (1 Na per f.u.) and Na3 (2 Na per f.u.) in the monoclinic cell. During desodiation  $\text{Na}^+$  cations are extracted mainly from the Na2 and Na3 positions while occupancy of Na1 remains almost steady. Inequality of Na2 and Na3 sites and their uneven occupation may result from distortions of transition metal octahedra with one short M-O distance of  $1.82(3)$  Å (Table A 3) possibly due to formation of a vanadyl bond. During the 3.4 V

voltage step transition metal octahedral deformations increase by an order of magnitude from  $\Delta d(\text{pristine}) = 0.398 \cdot 10^{-3}$  to  $\Delta d(3.5\text{V}) = 3.85 \cdot 10^{-3}$ . Nevertheless, at the beginning of the two-phase process occupation of the Na2 and Na3 positions becomes almost equal. This is followed by consolidation of the Na2 and Na3 sites back into the single Na2 position of the rhombohedral cell. Overall Na content in the rhombohedral phase at 3.8 V was refined to 1.9, with the Na1 and Na2 occupancy factors of 1 and 0.300(5), respectively. Transition metal octahedra at this point are almost regular with the distortion value of  $\Delta d = 3 \cdot 10^{-6}$ , which is atypical for Jahn-Teller active  $\text{Mn}^{3+}$  octahedra, shown to be present in “ $\text{Na}_2\text{MnV}(\text{PO}_4)_3$ ” upon charge to 3.8 V [100]. Such low distortions may indicate either suppression of cooperative Jahn-Teller distortion because of the  $\text{Mn}^{3+}/\text{V}^{4+}$  mixing or concurrent existence of both  $\text{Mn}^{3+}$  octahedra with long Mn-O bonds [149] and  $\text{V}^{4+}$  octahedra with short V-O bonds [150] at the local level. These effects cannot be resolved by X-ray powder diffraction.

Further charge from 3.8 to 4.0 V is accompanied by extraction of  $\text{Na}^+$  mainly from the Na1 position; its occupancy decreases to 0.87(1). In contrast to  $\text{Na}_3\text{V}_2(\text{PO}_4)_3$  [71,73],  $\text{Na}_4\text{MnV}(\text{PO}_4)_3$  and desodiated  $\text{NaV}_2(\text{PO}_4)_3$  [151], at this state of charge the average Na1-O distance is longer than the average Na2-O distance (Table A 3), which can be related to the “unlocking” of the Na1 site. Total Na content in the electrode charged to 4.0 V, as determined from Rietveld refinement, is 1.77, which is in a good agreement with the electrochemical data.

Thus, we conclude that raising the voltage above 3.8 V enhances the limit of  $\text{Na}^+$  extraction above 2 sodium atoms per formula unit through depletion of the Na1 position, which was not shown to take part in desodiation of the  $\text{Na}_3\text{V}_2(\text{PO}_4)_3$  [73]. This activation drastically affects the nature of the reverse charge process. A sloping

discharge curve was observed (Fig. 6. 11e), corresponding to continuous shift of the SXPD reflections and unit cell parameters without any signature of the first order phase transition. Reinsertion of  $\text{Na}^+$  into  $\text{Na}_{1.77}\text{MnV}(\text{PO}_4)_3$  on discharge down to 2.5 V proceeds via continuous solid solution in contrast with biphasic  $\text{Na}^+$  reinsertion into  $\text{Na}_{1.9}\text{MnV}(\text{PO}_4)_3$ . The observed relation between  $\text{Na}^+$  extraction level and the (de)intercalation mechanism in  $\text{Na}_{4-x}\text{MnV}(\text{PO}_4)_3$  is in part consistent with the results of Chen *et al.* [136] Moreover, such asymmetry was previously observed for the  $\text{Li}^+$  extraction from monoclinic  $\text{LiV}_2(\text{PO}_4)_3$  causing oxidation of  $\text{V}^{4+}$  to  $\text{V}^{5+}$  up to the  $\text{V}_2(\text{PO}_4)_3$  composition followed by a  $\text{Li}^+$  reinsertion via a solid-solution mechanism, which persisted until the  $\text{Li}_2\text{V}_2(\text{PO}_4)_3$  composition [152].  $\text{V}^{4+}/\text{V}^{3+}$  and  $\text{Li}^+$  ordering were found to govern (de)intercalation by a two-phase mechanism, while suppression of the charge ordering in the fully extracted  $\text{V}_2(\text{PO}_4)_3$  induced random population of the Li sites on reinsertion resulting in a solid-solution regime [153,154].

According to our previous work [135] and Chen *et al.* [136], the solid solution-type deintercalation step above 3.8 V for  $\text{Na}_4\text{MnV}(\text{PO}_4)_3$  is associated with extraction of  $\text{Na}^+$  from the Na1 position. Ghosh *et al.* [155] suggested that in case of the  $\text{Na}_{3+x}\text{Mn}_x\text{V}_{2-x}(\text{PO}_4)_3$  with low  $\text{Mn}^{2+}$  content ( $x=0.25$ ) this step is related to vanadium oxidation only, and in case of high  $\text{Mn}^{2+}$  content ( $x=0.75, 1$ ) – to formation of mixed  $\text{V}^{4+}/\text{V}^{5+}$  and  $\text{Mn}^{3+}/\text{Mn}^{4+}$  redox states. The access to the  $\text{Mn}^{3+}/\text{Mn}^{4+}$  redox couple in NASICON-type compounds was also shown by Gao *et al.* [108,110]; on the basis of DFT calculations the authors proposed that although cooperative Jahn-Teller distortion of the  $\text{Mn}^{3+}$  is suppressed in the  $\text{Na}_2\text{Mn}^{3+}\text{Zr}^{4+}(\text{PO}_4)_3$ , on the local scale  $\text{MnO}_6$  octahedra are distorted, and Na is locally ordered. DFT calculations for Na-deficient NASICON phases by Wang *et al.* [112] showed that migration of transition

metal to the adjacent unoccupied Na2 site as well as transition metal / Na antisite defects are unlikely in the  $\text{NaMnV(PO}_4)_3$  and  $\text{NaMnCr(PO}_4)_3$ .

These findings may support the hypothesis that  $\text{Na}^+$  deintercalation from the  $\text{Na}_{1+x}\text{Mn}_x^{3+}\text{V}_{2-x}^{4+}(\text{PO}_4)_3$  during charge above 3.8 V may occur through depletion of the Na1 position causing local  $\text{Na}^+$  and/or charge reordering, which is in part comparable to  $\text{Li}^+$  extraction from the  $\text{LiV}_2(\text{PO}_4)_3$  [153]. Most likely that on discharge  $\text{Na}^+$  is randomly inserted into available sites, but due to kinetic limitations  $\text{Na}^+$  does not fully reoccupy the Na1 position, and a certain amount of Na vacancies affect the (de)intercalation mechanism during subsequent cycling.

To sum up, in this chapter the electrochemical features were linked with the phase transformations in  $\text{Na}_{3+x}\text{Mn}_x\text{V}_{2-x}(\text{PO}_4)_3$  ( $0 \leq x \leq 1$ ) samples by *operando* X-ray powder diffraction and *operando* X-ray absorption spectroscopy. An intermediate “ $\text{Na}_2\text{M}_2(\text{PO}_4)_3$ ” phase was found for all compounds. Increase in Mn content extends the length of the solid solution region corresponding to sodiated, intermediate and desodiated phases. The evolution of the Mn and V oxidation states during charge and discharge of  $\text{Na}_4\text{MnV(PO}_4)_3$  was studied and it was shown that at ~3.4 V the redox transition  $\text{V}^{3+}/\text{V}^{4+}$  occurs, and at ~3.65 V – the transition  $\text{Mn}^{2+}/\text{Mn}^{3+}$ . An additional voltage plateau at ~3.9 V in the  $\text{Na}_4\text{MnV(PO}_4)_3$  was associated with “unlocking” of the Na1 site in the rhombohedral phase via solid-solution mechanism. It is still a subject to investigate which redox couple ( $\text{V}^{4+}/\text{V}^{5+}$  or/and  $\text{Mn}^{3+}/\text{Mn}^{4+}$ ) is responsible for the redox activity above 3.8 V. In case of high Mn content ( $x \geq 0.4$ ), once this 3.9 V redox activity “unlocked”, reverse cycling of  $\text{Na}^+$  cations proceeds via the entire solid solution mechanism.

## **Chapter 7. Kinetic properties of the $\text{Na}_{3+x}\text{Mn}_x\text{V}_{2-x}(\text{PO}_4)_3$**

The rate performance of rechargeable batteries is limited since above some threshold charge or discharge rate, the maximum obtainable the capacity is diminished due to several factors such as slow diffusion, slow electron or ion transport, electrolyte stability, and structural transformations [156,157]. Several approaches have been undertaken to improve rate performance by optimization of particle size, electrode thickness and porosity, and electrolyte formulation [158,159]. Yet the most commonly reported experimental measurements are capacity vs rate plots, which are difficult to quantitatively relate kinetic factors to rate performance. In recent years, several semi-empirical models [160–162] were proposed for the analysis of the capacity vs rate data, which yield apparent kinetic parameters and do not allow for the reliable distinction of various rate-limitations. Here, we quantify the several factors associated with diffusional, charge transfer and nucleation-induced polarization effects of  $\text{Na}_{3+x}\text{Mn}_x\text{V}_{2-x}(\text{PO}_4)_3$  ( $x = 0, 0.1, 0.5, 1$ ) materials using well developed electrochemical methods. With this approach we can establish improved design criteria and summarize the benefits and drawbacks of Mn substitution in a host of  $\text{Na}_{3+x}\text{Mn}_x\text{V}_{2-x}(\text{PO}_4)_3$  ( $0 \leq x \leq 1$ ) compositions in comparison to the more thoroughly studied  $\text{Na}_3\text{V}_2(\text{PO}_4)_3$  material.

### **7.1 The shape of cyclic voltammograms**

As already reported in Chapter 6 and in previous publications [135,136], the increase in the Mn content results in widening of solid solution regions, which is reflected in the shape of CVs of  $\text{Na}_{3+x}\text{Mn}_x\text{V}_{2-x}(\text{PO}_4)_3$  electrodes (Fig. 7. 1).

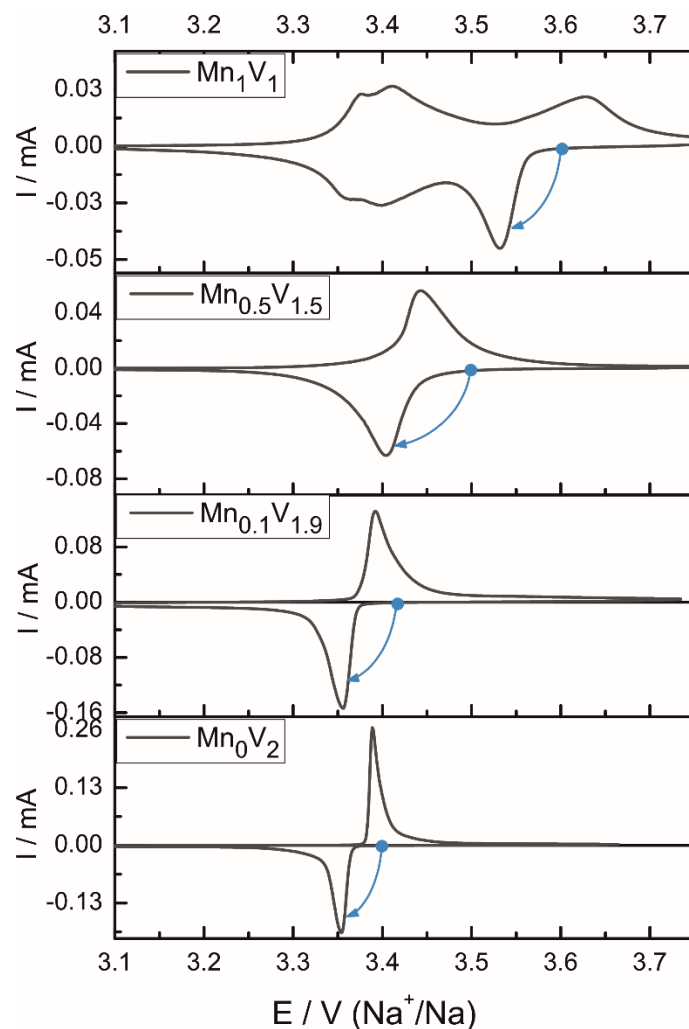


**Fig. 7. 1** CVs of  $\text{Na}_{3+x}\text{Mn}_x\text{V}_{2-x}(\text{PO}_4)_3$  ( $x=0, 0.1, 0.5, 1$ ) electrodes at  $50 \mu\text{V}\cdot\text{s}^{-1}$  scan rate in 1 M  $\text{NaPF}_6$  EC/PC (5% FEC) electrolyte. The blue dots and arrows show the direction of the potential steps in chronoamperometric measurements.

The CV of the unsubstituted NASICON material  $\text{Na}_3\text{V}_2(\text{PO}_4)_3$  ( $\text{Mn}_0\text{V}_2$ ) exhibits one pair of peaks at the formal potential of 3.370 V (vs  $\text{Na}^+/\text{Na}$ ), which correspond to the extraction/insertion of  $2\text{Na}^+$  per formula unit via a biphasic reaction, attributed to the redox activity of the  $\text{V}^{4+/3+}$  couple [83,91]. The single-phase regions, as determined from intercalation isotherms constructed from PITT data (Fig. 7. 2),

correspond to  $0.97 < \theta < 1$  ( $\theta$  – state-of-discharge) in the Na-rich phase and to  $0.025 > \theta > 0$  in the Na-poor phase.

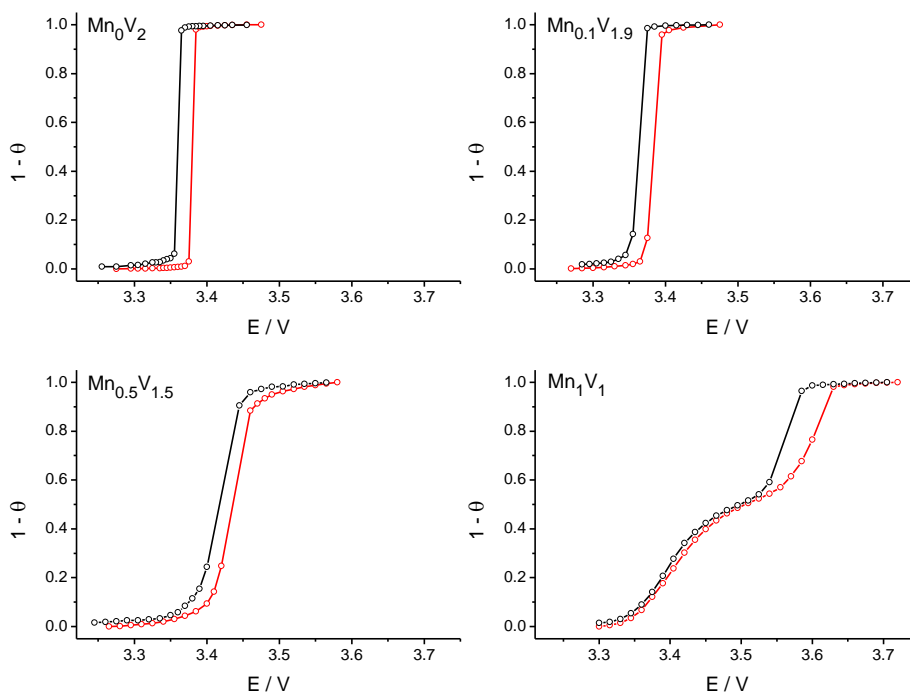


**Fig. 7. 2 Intercalation isotherms for  $\text{Mn}_0\text{V}_2$ ,  $\text{Mn}_{0.1}\text{V}_{1.9}$ ,  $\text{Mn}_{0.5}\text{V}_{1.5}$ ,  $\text{Mn}_1\text{V}_1$  materials constructed from PITT data. Sharp rises in  $\theta$  correspond to biphasic regions.**

The shape of the CV (exponential rises in current and “zero current” region in the vicinity of the formal potential) is very similar to that typically observed for  $\text{LiFePO}_4$  materials, where the kinetics of phase transformation was recently shown to be dictated by the energy penalties of the nucleation step [163–166]. The characteristic dependence of the peaks’ shape on the scan rate, with the overlap of the ascending parts of the peaks at different scan rates in the low-overvoltage regions (Fig. 7. 3) imply the predominant slow nucleation type of control for the  $\text{Mn}_0\text{V}_2$  electrodes [119,163].

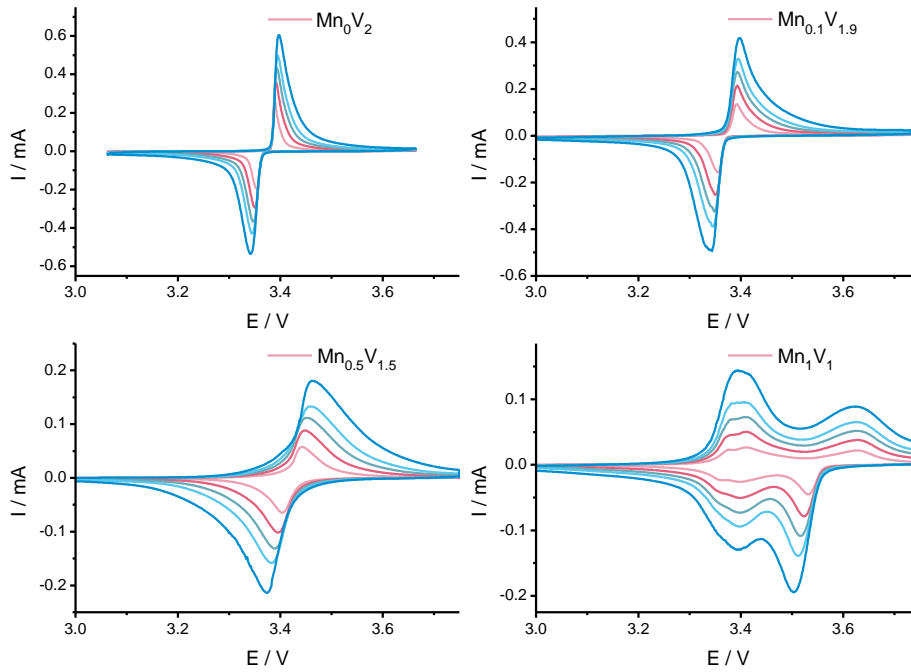


**Fig. 7. 3** CVs of  $\text{Mn}_0\text{V}_2$ ,  $\text{Mn}_{0.1}\text{V}_{1.9}$ ,  $\text{Mn}_{0.5}\text{V}_{1.5}$ ,  $\text{Mn}_1\text{V}_1$  electrodes at 0.05, 0.1, 0.15, 0.2 and 0.3 mV/s.

The length of the single-phase region in  $\text{Na}_{3.1}\text{Mn}_{0.1}\text{V}_{1.9}(\text{PO}_4)_3$  ( $\text{Mn}_{0.1}\text{V}_{1.9}$ ) cathode is increased to  $0.9 < \theta < 1$  in the Na-rich phase and to  $0.1 > \theta > 0$  in the Na-poor phase (Fig. 7. 2), which results in a substantial broadening of the CV for the  $\text{Mn}_{0.1}\text{V}_{1.9}$  electrodes (Fig. 7. 1) and in the disappearance of “zero-current” region between the anodic and cathodic peaks. Still, the observed characteristic scan rate dependence, *i.e.* the overlap of the ascending parts of the peaks at various scan rates (Fig. 7. 3) implies the predominance of the slow nucleation rate control in the potential region of low overpotentials [119]. For the  $\text{Na}_{3.5}\text{Mn}_{0.5}\text{V}_{1.5}(\text{PO}_4)_3$  ( $\text{Mn}_{0.5}\text{V}_{1.5}$ ) materials the single phase regions span at  $0.75 < \theta < 1$  and  $0.04 > \theta > 0$ , which results in further broadening of the CV in Fig. 7. 1. One can note the gradual increase of the formal potential from 3.370-3.375 V for  $\text{Mn}_0\text{V}_2$  and  $\text{Mn}_{0.1}\text{V}_{1.9}$  to 3.42 V for  $\text{Mn}_{0.5}\text{V}_{1.5}$ .

The two processes (single-phase redox process  $V^{4+}/V^{3+}$  and biphasic  $Mn^{3+}/Mn^{2+}$  redox transition [100]) become decoupled for the  $Na_4MnV(PO_4)_3$  ( $Mn_1V_1$ ) electrodes with the single-phase region corresponding to one  $Na^+$  extraction/insertion at  $E \sim 3.40$  V ( $V^{4+}/V^{3+}$ ) and a two-phase process at 3.56 V ( $Mn^{3+}/Mn^{2+}$ ) (Fig. 7. 2). The single-phase process at  $E \sim 3.40$  V can be reliably distinguished from the two-phase process at higher potential based on the CV shape dependence on the scan rate (Fig. 7. 3). In the single-phase region, the current in every point of the peak scales with the scan rate (this variation is almost linear at low scan rates), while for the process at 3.56 V only the anodic peak exhibits systematic growth, while the ascending branches of the cathodic peaks overlap at different scan rates, which is a manifestation of nucleation and growth phenomena [163,164].

We note that although structural studies of citric-based samples (Chapter 6, [167]) imply the formation of an intermediate  $Na_2M_2(PO_4)_3$  phase during charge and discharge and, correspondingly, two biphasic processes in the 2.5-3.8 V range, the *operando* X-ray diffraction, CV and chronoamperometry data obtained with oxalic-based samples do not allow to distinguish between these processes (Fig. 6. 3 right). At the same time, the differentiation of C vs. E plots shows only one pair of peaks in the two-phase regions, corresponding to a single biphasic process. The observed differences may be related to faster kinetics for the materials explored in this study. In the two-phase regions of the intercalation isotherms we thus analyze the kinetics of the effective “ $Na_3Mn_xV_{2-x}(PO_4)_3$ ” – “ $Na_{1+x}Mn_xV_{2-x}(PO_4)_3$ ” phase transition.

## 7.2 High-rate performance of the $Na_{3+x}Mn_xV_{2-x}(PO_4)_3$

The  $Na_{3+x}Mn_xV_{2-x}(PO_4)_3$  materials were further examined for their ability to operate at different C-rates (C/10 – 5C) with primarily focusing on the changes of the

hysteresis ( $\Delta E$ ) between the charging curve (at C/10) and discharge curves (at C/10 – 5C) and capacity fading at elevated current densities. The galvanostatic measurements were performed in the 2.5 – 3.8 V potential range to avoid irreversible transformations, which occur when the anodic voltage limit is further increased [135,136,155,167]. The reduced voltage range is also essential to ensure similar electrode/electrolyte reactivity, as at higher potentials the formation of cathode/electrolyte interface (CEI) layers [168–170] might result in additional kinetic polarization. The  $\Delta E$  values were determined in the two-phase regions at the state-of-charge marked with a dashed line in Fig. 7. 4.

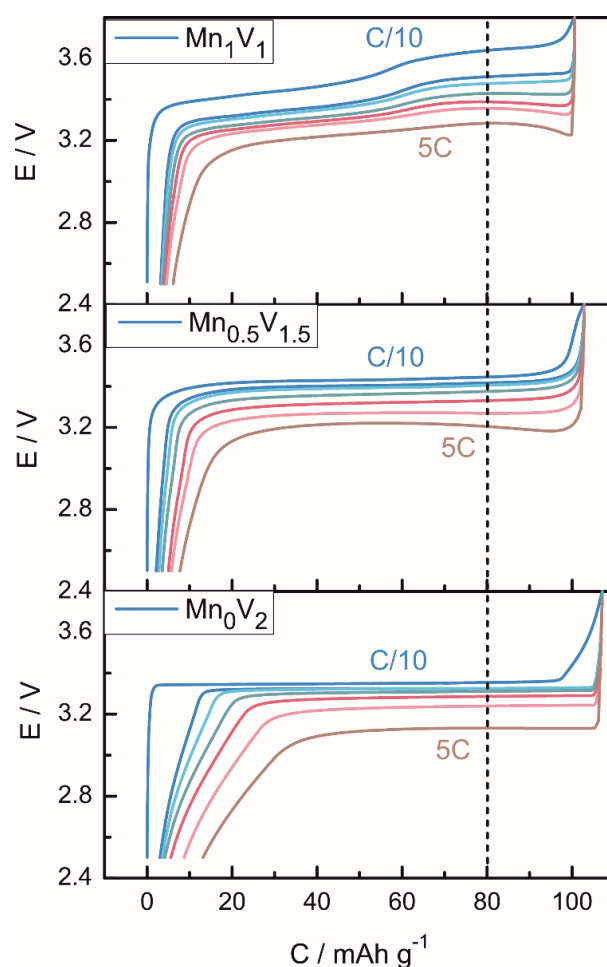


**Fig. 7. 4** Charge/discharge profiles for  $\text{Mn}_0\text{V}_2$ ,  $\text{Mn}_{0.5}\text{V}_{1.5}$  and  $\text{Mn}_1\text{V}_1$  materials at C/10, C/5, C/2, 1C, 2C and 5C rates. Dashed line shows the state-of-charge where the  $\Delta E$  values were estimated.

For the  $\text{Mn}_0\text{V}_2$  material, flat plateaus can be detected in the charge/discharge curves with a “thermodynamic” hysteresis [165] at C/10 rate of 25 mV, similar to that encountered for the  $\text{LiFePO}_4$  cathodes. At higher current densities, a pronounced increase in hysteresis values is observed, which is accompanied by the appearance of sloping parts of the discharge profiles at 0.6 – 1 states-of-discharge (Fig. 7. 4). These sloping parts are typically related to the concentration polarization, i.e. the kinetic hindrances which result from the slow ionic transport in the bulk of the cathode. With the increase in the discharge current density, the  $\Delta E$  value reaches 200 mV (Fig. 7. 5), while the capacity at 5C is only moderately diminished (from 105 at C/10 to 91 mAh  $\text{g}^{-1}$  at 5C).

For the  $\text{Mn}_{0.5}\text{V}_{1.5}$  materials, the concentration polarization issues are less pronounced, as evident from the absence of the lower-voltage distortions of the discharge curves and a small decrease of 6% of the intercalation capacity at 5C rate (from 101 at C/10 to 95 mAh  $\text{g}^{-1}$  at 5C). Yet, at the elevated current densities the hysteresis values reach 240 mV (Fig. 7. 5), which is substantially higher compared to the  $\Delta E$  for the unsubstituted  $\text{Mn}_0\text{V}_2$  material.

For the  $\text{Mn}_1\text{V}_1$  electrode, the  $\Delta E$  changes from 130 mV at C/10 to 350 mV at 5C, while the intercalation capacity decrease is only 3% at 5C rate (from 97 at C/10 to 95 mAh  $\text{g}^{-1}$  at 5C). The highest values of  $\Delta E$  are observed at the potentials corresponding to the two-phase reaction, which might imply that the losses are induced by the activation barriers of the phase-transformation process.

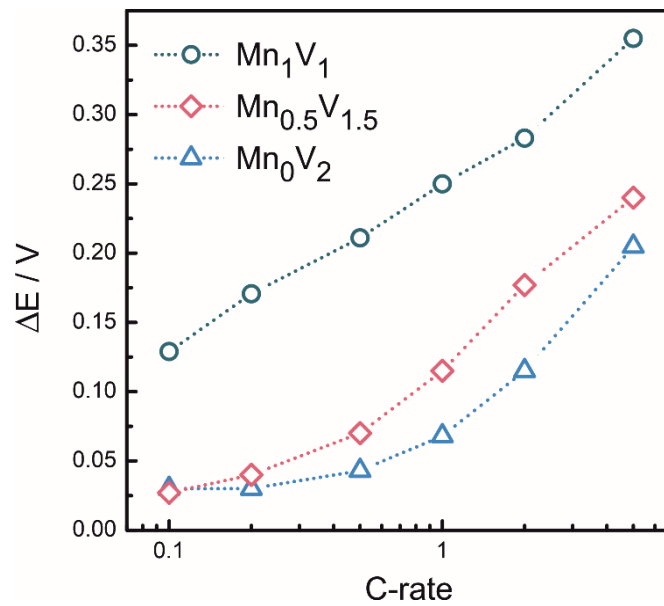


**Fig. 7. 5** Hysteresis ( $\Delta E$ ) between charging curve at  $C/10$  and discharge curves at  $C/10$ ,  $C/5$ ,  $C/2$ ,  $1C$ ,  $2C$  and  $5C$  rates.

### 7.3 Quantitative estimates of kinetic parameters

As the hysteresis values and concentration polarization effects were found to be highly dependent on the Mn content in the  $\text{Na}_{3+x}\text{Mn}_x\text{V}_{2-x}(\text{PO}_4)_3$  materials, in this section we evaluate the key kinetic factors responsible for the rate-limitations in intercalation materials – diffusion coefficients, charge transfer and surface layers' resistances and nucleation rate constants.

#### 7.3.1 Diffusional limitations

The difficulty of estimating diffusion coefficients for the materials with wide miscibility gaps originates from the general inadequacy of the  $D$  values determination in the two-phase regions, where the transport phenomena are related to the phase boundary propagation and not solely to the transport of ions in the host structure [171]. The diffusion coefficients can thus be determined in the single-phase regions, which are very narrow for the  $\text{Mn}_0\text{V}_2$  material and increase progressively toward the

Mn<sub>1</sub>V<sub>1</sub> end-member, for which ca. 1Na<sup>+</sup> can be extracted via a solid-solution route. The diffusion coefficients were calculated from PITT data in the single-phase regions of the intercalation isotherms for Mn<sub>0</sub>V<sub>2</sub>, Mn<sub>0.1</sub>V<sub>1.9</sub>, Mn<sub>0.5</sub>V<sub>1.5</sub> and Mn<sub>1</sub>V<sub>1</sub> materials taking into account the uncompensated ohmic drop, slow charge transfer kinetics and finite nature of diffusion problem in a particle of the active material (three-dimensional diffusion with a characteristic length of about 0.2 μm as derived from the particle size analysis by ImageJ, Fig. A 4, Fig. 7. 6).

For the Mn<sub>0</sub>V<sub>2</sub> material, the diffusion coefficients attain relatively high values of (20-60)·10<sup>-12</sup> cm<sup>2</sup> s<sup>-1</sup> in the Na-rich phase and lower values of (3-20)·10<sup>-12</sup> cm<sup>2</sup> s<sup>-1</sup> in the Na-poor phase. A typical sharp decrease in the *D* values is observed in the vicinity of the phase-transformation potential [171].

For the Mn<sub>0.1</sub>V<sub>1.9</sub> material with a single-phase region length increased by ca. 10%, the diffusion coefficients do not differ significantly, while for the Mn<sub>0.5</sub>V<sub>1.5</sub> material *D* values amount to (2-20)·10<sup>-12</sup> cm<sup>2</sup> s<sup>-1</sup> in the Na-rich phase and to (1-6)·10<sup>-12</sup> cm<sup>2</sup> s<sup>-1</sup> in the Na-poor phase.

For the Mn<sub>1</sub>V<sub>1</sub> material, the diffusion coefficients in the Na-rich phase are in the range (2-30)·10<sup>-12</sup> cm<sup>2</sup> s<sup>-1</sup>, while somewhat lower values of (2-5)·10<sup>-12</sup> cm<sup>2</sup> s<sup>-1</sup> are observed in the Na-poor phase.

To this point, important observation concerns the differences in ionic diffusivities in the Na-rich and Na-poor phases, with the latter providing lower (by 2-6 times) ionic mobilities.

Another point is that Na-ion diffusion coefficient values do not differ significantly for the Na<sub>3+x</sub>Mn<sub>x</sub>V<sub>2-x</sub>(PO<sub>4</sub>)<sub>3</sub> materials. The variations hardly reach half an order of magnitude with the increase in the Mn content.

Therefore it is clear that  $\text{Na}^+$  ion's reduced diffusivities in the bulk of materials cannot explain the pronounced concentration polarization effects observed in the discharge curves.

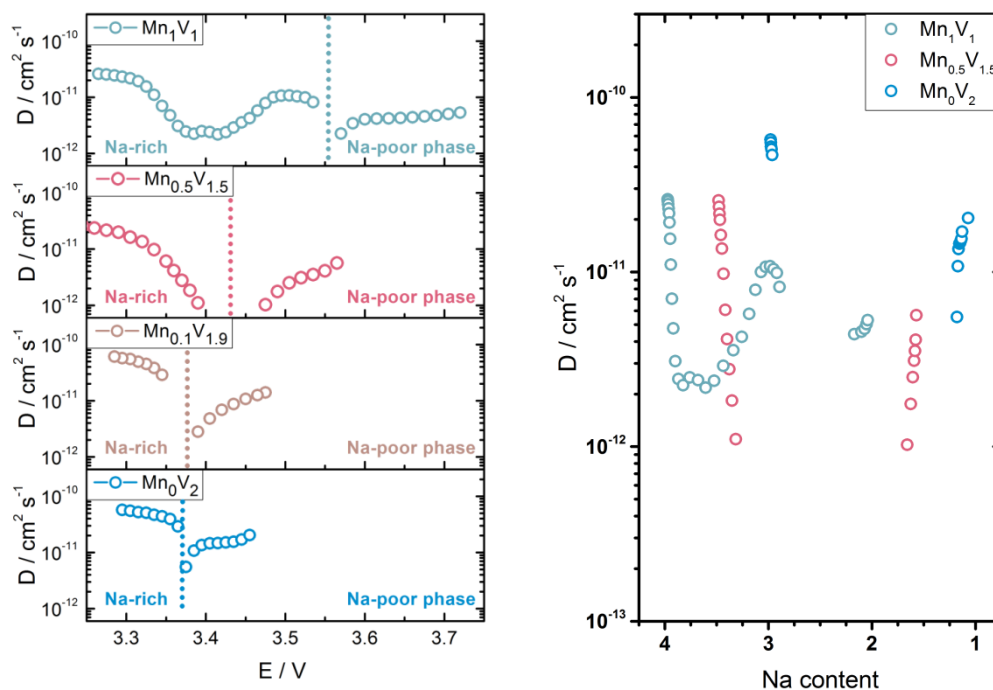


**Fig. 7. 6** Apparent diffusion coefficients for  $\text{Mn}_0\text{V}_2$ ,  $\text{Mn}_{0.1}\text{V}_{1.9}$ ,  $\text{Mn}_{0.5}\text{V}_{1.5}$  and  $\text{Mn}_1\text{V}_1$  materials as determined from PITT data in the single-phase regions as a function of formal potential (left) and of Na content (right). Dashed line indicates the phase transformation potential.

The variation in the Mn content results in significant widening of the single-phase regions for  $\text{Mn}_{0.5}\text{V}_{1.5}$  and  $\text{Mn}_1\text{V}_1$  materials. Hence for the materials with high Mn content it seems reasonable to correlate the minimization of the diffusional limitations to the predominant solid-solution route at lower voltages (Na-rich region of the isotherms). For the  $\text{Mn}_0\text{V}_2$  material, concentration polarization effects start to manifest themselves in the two-phase region of the intercalation isotherm, and therefore are related to the slow phase-boundary propagation. We note that the 5C rate

here does not result in the change of the reaction mechanism from two-phase to single-phase, as observed at higher C-rates for  $\text{LiFePO}_4$  materials [172,173], as at this rate the horizontal plateau is still clearly distinguished in the discharge curve. As at critical concentrations, corresponding to the limits of stability of Na-rich and Na-poor phases, the diffusion coefficients are generally found to decrease significantly, the maximal rates of the phase boundary propagation would be much lower than the diffusivities in the single-phase regions [174–176]. The phase boundary propagation rates are thought to decrease even further, if strain energies are taken into account [177–179]. In this regard, solid-solution pathway gives significant advantages for fast discharge of  $\text{Na}_{3+x}\text{Mn}_x\text{V}_{2-x}(\text{PO}_4)_3$  materials compared to a biphasic process in unsubstituted sample.

### 7.3.2 Charge transfer limitations

Next, we analyze the differences in the charge transfer kinetics for the  $\text{Na}_{3+x}\text{Mn}_x\text{V}_{2-x}(\text{PO}_4)_3$  materials, as kinetic polarization may result in a significant hysteresis between charge and discharge curves in intercalation materials [119]. For the transition metal-based cathodes in EC/PC electrolytes, the composition of the cathode surface impacts the thickness and the resistivity of CEI layers [180]. Impedance spectroscopy was used to quantify the interfacial resistances of  $\text{Mn}_0\text{V}_2$ ,  $\text{Mn}_{0.1}\text{V}_{1.9}$ ,  $\text{Mn}_{0.5}\text{V}_{1.5}$  and  $\text{Mn}_1\text{V}_1$  cathodes. The impedance spectra of  $\text{Na}_{3+x}\text{Mn}_x\text{V}_{2-x}(\text{PO}_4)_3$  electrodes (Fig. 7. 9, the resistances are normalized per mass of the active material) show two distinct semicircles, which can be attributed to the resistance and capacitance of surface layers,  $R_{\text{CEI}}$  and  $C_{\text{CEI}}$  (higher frequency semicircle) and to the charge transfer resistance,  $R_{\text{ct}}$ , and double layer capacitance,  $C_{\text{dl}}$  (lower frequency semicircle) [119] based on the observed potential dependence of the lower-frequency

semicircle diameter (Fig. 7. 7) [119]. The low-frequency parts of the spectra feature a sloping line, which corresponds to finite ionic diffusion and can be modelled by a spherical finite Warburg element (equivalent circuit is given in Fig. 7. 8).

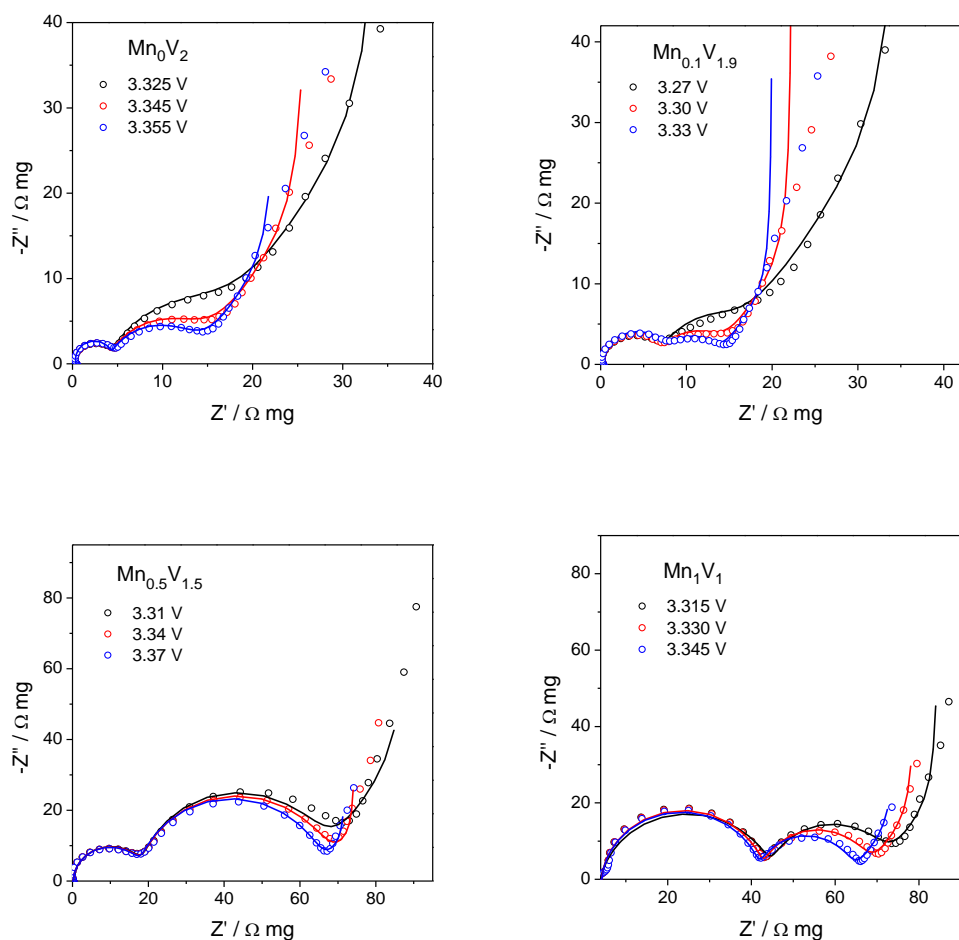


**Fig. 7. 7** EIS spectra (symbols) of  $\text{Mn}_0\text{V}_2$ ,  $\text{Mn}_{0.1}\text{V}_{1.9}$ ,  $\text{Mn}_{0.5}\text{V}_{1.5}$ ,  $\text{Mn}_1\text{V}_1$  electrodes and the fits to the equivalent circuit. Potential values are indicated in the plots.

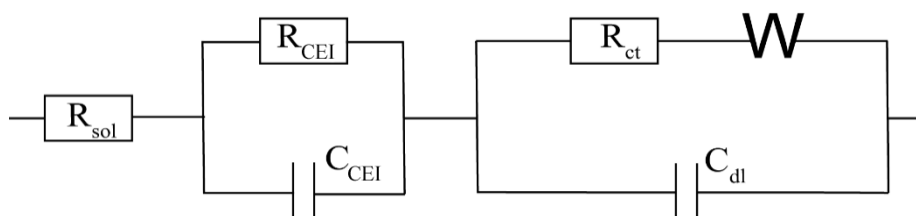


**Fig. 7. 8** Equivalent circuit used to fit the experimental impedance spectra.  $R_{\text{sol}}$  – solution resistance;  $R_{\text{CEI}}$  – resistance of surface layers;  $C_{\text{CEI}}$  – capacitance of surface layers;  $R_{\text{ct}}$  – charge

transfer resistance,  $W$  – finite Warburg element for the case of 3D diffusion ( $R_d$ ,  $C_d$  – resistance and capacitance of diffusion);  $C_{dl}$  – double layer capacitance. In the fitting procedure CPE elements were used instead of pure capacities.

Given the pronounced differences in the width of the single-phase regions for the Mn-substituted materials, the comparison of the charge transfer resistances is not trivial, as exchange current density and, hence,  $R_{ct}$  depend sharply on the state-of-charge at very low and very high intercalation levels [181], while for the  $Mn_0V_2$  and  $Mn_{0.1}V_{1.9}$  materials the single-phase regions are particularly narrow. This issue complicates the comparison of  $R_{ct}$  values at identical intercalation levels, and we draw only qualitative conclusions on the dependence of the  $R_{ct}$  semicircle diameters on the Mn content. The lowest  $R_{ct}$  values (3-5  $\Omega \cdot mg$ , Fig. 7. 9) are observed for the  $Mn_0V_2$  and  $Mn_{0.1}V_{1.9}$  materials, while for the materials with increased Mn content the  $R_{ct}$  values are 2-4 times higher (10-20  $\Omega \cdot mg$ ). The resistances of the surface layers,  $R_{CEI}$ , exhibit a systematic growth with the increase in the Mn content, which reflects the higher reactivity of surface Mn atoms compared to V atoms. The  $R_{CEI}$  values amount to 4, 9.5, 17 and 29  $\Omega \cdot mg$  for the  $Mn_0V_2$ ,  $Mn_{0.1}V_{1.9}$ ,  $Mn_{0.5}V_{1.5}$  and  $Mn_1V_1$  cathodes, respectively.

Five-fold increase in the  $R_{ct}$  (i.e. five-fold decrease in the value of the apparent electrochemical rate constant) and six-fold increase in  $R_{CEI}$  would result effectively in a maximum of 50 mV difference in the hysteresis values at 5C rate for the  $Mn_0V_2$  and  $Mn_1V_1$  samples, while the experimental difference in  $\Delta E$  amounts to 150 mV (Fig. 7. 5). This indicates that charge transfer polarization and surface layers' formation do not provide major contributions to the observed hysteretic features.

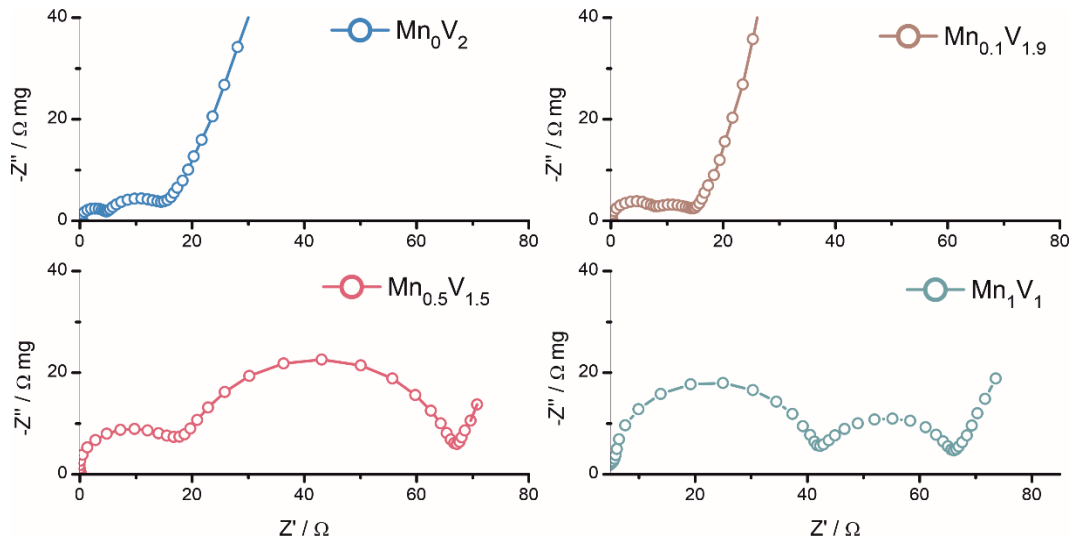


**Fig. 7. 9** Impedance spectra of  $\text{Na}_{3+x}\text{Mn}_x\text{V}_{2-x}(\text{PO}_4)_3$  ( $x=0, 0.1, 0.5, 1$ ) electrodes at  $E = 3.360$  V ( $\text{Mn}_0\text{V}_2$ ),  $E = 3.360$  V ( $\text{Mn}_{0.1}\text{V}_{1.9}$ ),  $E = 3.400$  V ( $\text{Mn}_{0.5}\text{V}_{1.5}$ ),  $E = 3.445$  V ( $\text{Mn}_1\text{V}_1$ ).

### 7.3.3 Nucleation-induced limitations

The intrinsic hysteresis between charge and discharge curves in phase-separating materials was shown to be governed by the nucleation step activation energetics [165,177] with the hysteresis values being highly dependent on the charge/discharge rate [163]. For the  $\text{Na}_{3+x}\text{Mn}_x\text{V}_{2-x}(\text{PO}_4)_3$  materials, we explored the kinetics of nucleation during the intercalation of Na ions. The nucleation kinetics can be quantified by measuring the potential dependencies of the nucleation rate constant,  $k_{\text{nucl}}$  based on large-amplitude chronoamperometric data [118,119,163,164]. In this experiment, the potential is stepped from some value in a Na-poor single-phase region (blue dot in Fig. 7. 1) to the potential, which corresponds to an equilibrium composition in the Na-rich phase (arrows in Fig. 7. 1). The registered current transient thus involves the process of phase transformation with the nucleation step activation barrier being dependent on the value of overvoltage,  $\eta$ . The overvoltage is calculated as the difference between the formal potential and the potential applied. Fig. 7. 10a shows current transients registered after the potential steps for  $\text{Mn}_0\text{V}_2$ ,  $\text{Mn}_{0.1}\text{V}_{1.9}$ ,

Mn<sub>0.5</sub>V<sub>1.5</sub> and Mn<sub>1</sub>V<sub>1</sub> electrodes at  $\eta \sim 25$  mV. The  $I$  vs  $t$  dependencies exhibit characteristic maxima, which reflect coupling of the charge transfer, diffusional and nucleation rate limitations [166,179]. The current maxima are observed to shift to longer times with the increase in the Mn content and the width of the maxima increases progressively, which indicates that nucleation-induced kinetic hindrances become much more pronounced for the materials with high Mn substitution level (Fig. 7. 10a).

As discussed in detail in refs [119,163], the nucleation rate constants can be estimated from the slopes of the linear parts of the  $\ln(I)$  vs time dependencies at low (<60 mV) overvoltages, where the slow nucleation-induced rate-limitations are likely to dominate over charge transfer and diffusional limitations. Fig. 7. 10b shows the registered current transients for the four materials in semilogarithmical coordinates with the linear parts used to estimate  $k_{\text{nuc}}$  marked with dashed lines. The linear part is chosen after the current maxima in the region with the greatest slope. Notably, linear parts appear at longer times for Mn<sub>0.5</sub>V<sub>1.5</sub> and Mn<sub>1</sub>V<sub>1</sub> electrodes and can only be detected in the short-time domain (< 500 s) for Mn-poor materials. The slope of the linear regions increases with the decrease in Mn content (Fig. 7. 10b), which indicates slower nucleation kinetics for the materials with high Mn substitution level. Fig. 7. 10c shows the potential dependence of the nucleation rate constants. For the Mn<sub>0</sub>V<sub>2</sub> and Mn<sub>1</sub>V<sub>1</sub> materials, the nucleation rate constants differ by one order of magnitude, while for Mn<sub>0.1</sub>V<sub>1.9</sub> and Mn<sub>0.5</sub>V<sub>1.5</sub>  $k_{\text{nuc}}$  attain intermediate values. For the Mn-poor compounds, the nucleation rate constants are in the range  $(0.8-6) \cdot 10^{-3} \text{ s}^{-1}$ , while for the Mn-rich materials  $k_{\text{nuc}}$  values are significantly lower  $(0.1-1.5) \cdot 10^{-3} \text{ s}^{-1}$ . The effects of reduced phase transformation rates may be attributed to the presence of Jahn-Teller

active  $\text{Mn}^{3+}$  [182,183]. The much more pronounced kinetic hindrances for the nucleation step thus explain the higher hysteresis values observed for Mn-rich materials at elevated charge/discharge rates.

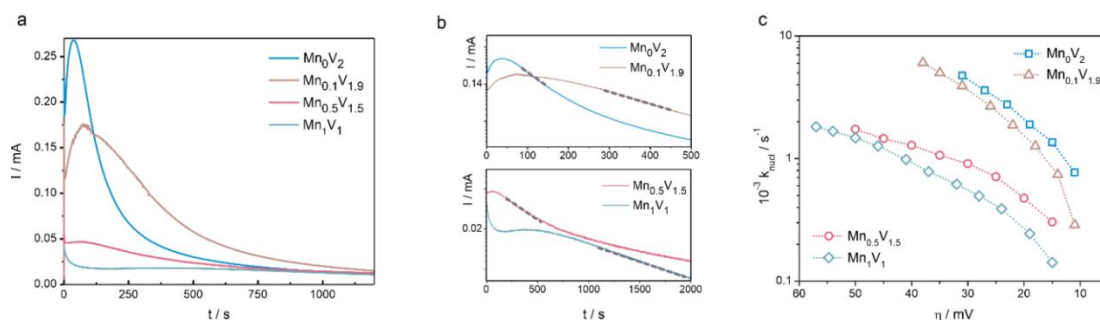


**Fig. 7.10** Current transients for the  $\text{Mn}_0\text{V}_2$ ,  $\text{Mn}_{0.1}\text{V}_{1.9}$ ,  $\text{Mn}_{0.5}\text{V}_{1.5}$  and  $\text{Mn}_1\text{V}_1$  electrodes registered after potential steps corresponding to  $\eta \sim 25$  mV in linear (a) and semilogarithmical (b) coordinates. Potential dependence of the nucleation rate constants,  $k_{\text{nucl}}$  (c).

#### 7.3.4 Practical manifestations of the measured rate-limitations

Having quantified the various sources of the rate-limitations in the  $\text{Na}_{3+x}\text{Mn}_x\text{V}_{2-x}(\text{PO}_4)_3$  materials, we further analyze the result of the interplay of the various hindering factors on the decrease of the specific energy of the materials with increasing C-rate (Fig. 7.11). At 0.1, 0.2, 0.5 C-rates the four materials behave similarly and the specific energy reduction is only a few percent. Yet, at 1C the differences in the rate capability of the materials start to appear, with the  $\text{Mn}_1\text{V}_1$  electrode demonstrating a smaller reduction in specific energy. At 5C rate, the higher rate capability of  $\text{Mn}_{0.5}\text{V}_{1.5}$  and  $\text{Mn}_1\text{V}_1$  electrodes becomes evident, as the losses in specific energy amount to 16% for  $\text{Mn}_0\text{V}_2$  and only to 8% for  $\text{Mn}_1\text{V}_1$ .

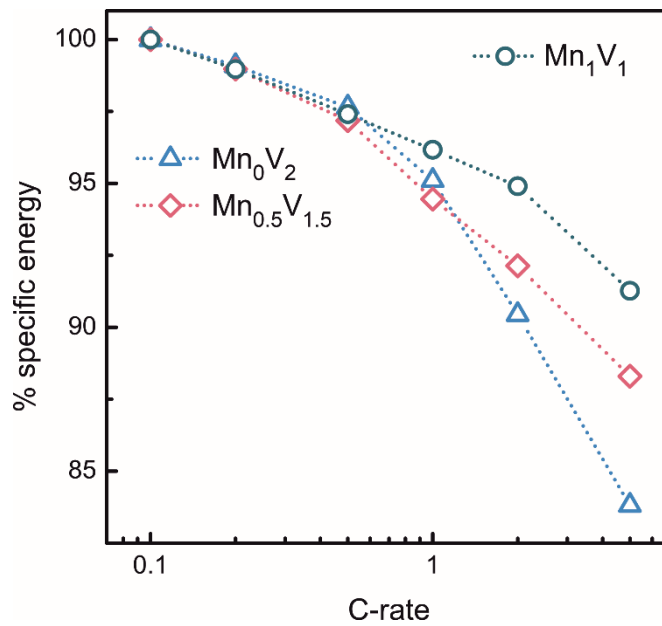


**Fig. 7. 11 C-rate dependence of the reduction in the specific energy (%).**

To sum up, this analysis allows suggesting that despite much more pronounced hysteretic effects, the materials with high Mn content outperform their Mn-poor counterparts in terms of delivered specific energy at elevated charge/discharge rates. Though the slower nucleation and higher charge transfer resistances result in much higher hysteresis values for  $\text{Na}_{3.5}\text{Mn}_{0.5}\text{V}_{1.5}(\text{PO}_4)_3$  and  $\text{Na}_4\text{MnV}(\text{PO}_4)_3$  materials, diffusional limitations related to the propagation of the phase boundary in the course of phase-transformation result in sharper decay of performance at high current densities. For the materials with wider single-phase regions, the relatively fast diffusion of ions in the crystal lattice results in much lower concentration polarization losses.

## Chapter 8. Summary and Outlook

This thesis aimed to explore new vanadium- and manganese-containing NASICON-type compounds as potential cathode materials for sodium-ion batteries to enable long-lasting high-rate and low-cost energy storage.

We have successfully prepared the  $\text{Na}_{3+x}\text{Mn}_x\text{V}_{2-x}(\text{PO}_4)_3$  ( $0 \leq x \leq 1$ ) samples by evaporation of a solution with a subsequent thermal annealing. In citric acid-based synthesis we obtained samples, which consist of irregularly formed agglomerated plates of 0.1–1.5  $\mu\text{m}$  in size, and used them to study the phase transformations and the evolution of the transition metals valence state. When oxalic acid was used, the samples consist of separate agglomerates of interconnected particles 0.1-1  $\mu\text{m}$  in size with high porosity, which allowed us to study kinetic parameters using electrochemical methods.

We then studied the phase transformation behavior of  $\text{Na}_{3+x}\text{Mn}_x\text{V}_{2-x}(\text{PO}_4)_3$  ( $0 \leq x \leq 1$ ) by *operando* X-ray diffraction. The results lead to a construction of the phase diagram V-Mn-Na, and the range of existence of solid solutions  $\text{Na}_{3+x}\text{Mn}_x\text{V}_{2-x}(\text{PO}_4)_3$  was determined. Upon extraction of 2  $\text{Na}^+$  cations at 3.8 V,  $\text{Na}^+$  reinsertion on discharge would be reversible, passing through the same (de)intercalation domains. This process utilizes  $\text{V}^{3+}/\text{V}^{4+}$  and  $\text{Mn}^{2+}/\text{Mn}^{3+}$  redox transitions, as shown by X-ray absorption spectroscopy in *operando* mode for the  $\text{Na}_4\text{MnV}(\text{PO}_4)_3$ .

Raising the voltage limit on charge of  $\text{Na}_4\text{MnV}(\text{PO}_4)_3$  above 3.8 V leads to an increase in the  $\text{Na}^+$  extraction threshold – more than 2 sodium cations per formula unit are deintercalated due to the depletion of Na1 positions, which was not previously shown during only 2 sodium cations deintercalation from only Na2 sites of  $\text{Na}_3\text{V}_2(\text{PO}_4)_3$ . This suggests that with proper choice of the substitutions in their

composition, NASICON-type cathodes can show even higher utilization of reversibly cycled charge at high voltages.

Deintercalation of more than 2 sodium cations achieved through the combination of V and Mn in the NASICON structure increases specific energy by 10% compared to  $\text{Na}_3\text{V}_2(\text{PO}_4)_3$ . The highest attained discharge specific energy of the  $\text{Na}_{3+x}\text{Mn}_x\text{V}_{2-x}(\text{PO}_4)_3$  is 415 mW·h/g in the case of  $x=0.8$  when charged up to 4.1 V. However, the compositions with high Mn content have low capacity retention in the extended voltage window. The activation of additional crystallographic sites above 3.8 V radically affects the nature of subsequent discharge-charge cycles – they proceed without signs of a first-order phase transition. Further introduction and extraction of  $\text{Na}^+$  into  $\text{Na}_4\text{MnV}(\text{PO}_4)_3$  occurs via the solid-solution mechanism in the entire voltage range above 2.5 V. Stabilization of the practical energy density above 410 mW·h/g observed for  $x>0.4$  sample is still an important challenge and further understanding of the nature of this degradation is crucial for the development of the next-generation high-energy NASICON-type cathodes. Nevertheless, the most stable cycling was shown by samples with  $x=0.2$ ; their energy capacity was 388 mW·h/g after 23 charge-discharge cycles in a potential window of 2.5-4.1 V.

Furthermore, the introduction of Mn adds to NASICON's tolerance of high rate loads. The energy losses at 5C rate are 2 times lower for samples with high Mn content. Despite the increased values of polarization in samples with  $x=0.5$  and 1 due to slow nucleation and high charge transfer resistance, the relatively fast diffusion of ions in the crystal lattice leads to significantly lower concentration polarization losses due to a broader single-phase region. These implications are expected to bring further progress in engineering high-rate NASICON-type cathodes.



## Bibliography

- [1] R.S. Carmichael, Practical Handbook of Physical Properties of Rocks and Minerals, in: Boca Raton: CRC Press, 1989.
- [2] D. Larcher, J.M. Tarascon, Towards greener and more sustainable batteries for electrical energy storage, *Nat. Chem.* 7 (2015) 19–29. doi:10.1038/nchem.2085.
- [3] M.D. Slater, D. Kim, E. Lee, C.S. Johnson, Sodium-ion batteries, *Adv. Funct. Mater.* 23 (2013) 947–958. doi:10.1002/adfm.201200691.
- [4] K. Kubota, S. Komaba, Review—Practical Issues and Future Perspective for Na-Ion Batteries, *J. Electrochem. Soc.* 162 (2015) A2538–A2550. doi:10.1149/2.0151514jes.
- [5] Faradion receives first order for sodium-ion batteries for Australian market, (n.d.). <https://www.faradion.co.uk/faradion-receives-first-order-of-sodium-ion-batteries-for-australian-market/> (accessed August 11, 2020).
- [6] Natron Energy provides backup power to Forced Physics Data Center Technology for their High-Performance Compute (HPC) Suite at the H5 Data Centers Phoenix, AZ campus, (n.d.). [https://natron.energy/wp-content/uploads/2020/04/Natron-ForcedPhysics\\_PR\\_Final.pdf](https://natron.energy/wp-content/uploads/2020/04/Natron-ForcedPhysics_PR_Final.pdf) (accessed August 11, 2020).
- [7] C. Delmas, C. Fouassier, P. Hagenmuller, Structural classification and properties of the layered oxides, *Physica.* 99B (1980) 81–85. doi:10.1016/0378-4363(80)90214-4.
- [8] N. Yabuuchi, S. Komaba, Recent research progress on iron- and manganese-based positive electrode materials for rechargeable sodium batteries, *Sci.*

- Technol. Adv. Mater. 15 (2014). doi:10.1088/1468-6996/15/4/043501.
- [9] H. Yoshida, N. Yabuuchi, K. Kubota, I. Ikeuchi, A. Garsuch, M. Schulz-Dobrick, S. Komaba, P2-type  $\text{Na}_{2/3}\text{Ni}_{1/3}\text{Mn}_{2/3-x}\text{Ti}_x\text{O}_2$  as a new positive electrode for higher energy Na-ion batteries, *Chem Commun.* 50 (2014) 3677–3680. doi:10.1039/c3cc49856e.
- [10] V. Palomares, M. Casas-Cabanas, E. Castillo-Martínez, M.H. Han, T. Rojo, Update on Na-based battery materials. A growing research path, *Energy Environ. Sci.* 6 (2013) 2312. doi:10.1039/c3ee41031e.
- [11] M. Sathiya, K. Hemalatha, K. Ramesha, J.M. Tarascon, A.S. Prakash, Synthesis, Structure, and Electrochemical Properties of the Layered Sodium Insertion Cathode Material:  $\text{NaNi}_{1/3}\text{Mn}_{1/3}\text{Co}_{1/3}\text{O}_2$ , *Chem. Mater.* 24 (2012) 1846–1853. doi:10.1021/cm300466b.
- [12] N. Yabuuchi, M. Kajiyama, J. Iwatate, H. Nishikawa, S. Hitome, R. Okuyama, R. Usui, Y. Yamada, S. Komaba, P2-type  $\text{Na}_x\text{Fe}_{1/2}\text{Mn}_{1/2}\text{O}_2$  made from earth-abundant elements for rechargeable Na batteries, *Nat Mater.* 11 (2012) 512–517. doi:10.1038/nmat3309 10.1038/NMAT3309.
- [13] D. Kim, E. Lee, M. Slater, W. Lu, S. Rood, C.S. Johnson, Layered  $\text{Na}[\text{Ni}_{1/3}\text{Fe}_{1/3}\text{Mn}_{1/3}]\text{O}_2$  cathodes for Na-ion battery application, *Electrochem. Commun.* 18 (2012) 66–69. doi:10.1016/j.elecom.2012.02.020.
- [14] D. Kim, S. Kang, M. Slater, S. Rood, J.T. Vaughey, N. Karan, M. Balasubramanian, C.S. Johnson, Enabling Sodium Batteries Using Lithium-Substituted Sodium Layered Transition Metal Oxide Cathodes, (2011) 333–336. doi:10.1002/aenm.201000061.
- [15] A. Paoletta, C. Faure, V. Timoshevskii, S. Marras, G. Bertoni, A. Guerfi, A.

- Vijh, M. Armand, K. Zaghib, A review on hexacyanoferrate-based materials for energy storage and smart windows: Challenges and perspectives, *J. Mater. Chem. A*. 5 (2017) 18919–18932. doi:10.1039/c7ta05121b.
- [16] M. Ware, Prussian blue: Artists' pigment and chemists' sponge, *J. Chem. Educ.* 85 (2008). doi:10.1021/ed085p612.
- [17] Y. You, X. Yu, Y. Yin, K.W. Nam, Y.G. Guo, Sodium iron hexacyanoferrate with high Na content as a Na-rich cathode material for Na-ion batteries, *Nano Res.* 8 (2014) 117–128. doi:10.1007/s12274-014-0588-7.
- [18] J. Qian, C. Wu, Y. Cao, Z. Ma, Y. Huang, X. Ai, H. Yang, Prussian Blue Cathode Materials for Sodium-Ion Batteries and Other Ion Batteries, *Adv. Energy Mater.* 8 (2018) 1–24. doi:10.1002/aenm.201702619.
- [19] J. Song, L. Wang, Y. Lu, J. Liu, B. Guo, P. Xiao, J. Lee, X. Yang, G. Henkelman, J.B. Goodenough, Removal of Interstitial H<sub>2</sub>O in Hexacyanometallates for a Superior Cathode of a Sodium-Ion Battery, (2015). doi:10.1021/ja512383b.
- [20] D. Yang, J. Xu, X.Z. Liao, H. Wang, Y.S. He, Z.F. Ma, Prussian blue without coordinated water as a superior cathode for sodium-ion batteries, *Chem. Commun.* 51 (2015) 8181–8184. doi:10.1039/c5cc01180a.
- [21] W.J. Li, S.L. Chou, J.Z. Wang, Y.M. Kang, J.L. Wang, Y. Liu, Q.F. Gu, H.K. Liu, S.X. Dou, Facile method to synthesize Na-enriched Na<sub>1+x</sub>FeFe(CN)<sub>6</sub> frameworks as cathode with superior electrochemical performance for sodium-ion batteries, *Chem. Mater.* 27 (2015) 1997–2003. doi:10.1021/cm504091z.
- [22] W.J. Li, C. Han, G. Cheng, S.L. Chou, H.K. Liu, S.X. Dou, Chemical Properties, Structural Properties, and Energy Storage Applications of Prussian

- Blue Analogues, *Small*. 15 (2019) 1–21. doi:10.1002/sml.201900470.
- [23] W. Ren, M. Qin, Z. Zhu, M. Yan, Q. Li, L. Zhang, D. Liu, L. Mai, Activation of Sodium Storage Sites in Prussian Blue Analogues via Surface Etching, *Nano Lett.* 17 (2017) 4713–4718. doi:10.1021/acs.nanolett.7b01366.
- [24] D.S. Kim, M.B. Zakaria, M.S. Park, A. Alowasheer, S.M. Alshehri, Y. Yamauchi, H. Kim, Dual-textured Prussian Blue nanocubes as sodium ion storage materials, *Electrochim. Acta.* 240 (2017) 300–306. doi:10.1016/j.electacta.2017.04.054.
- [25] Y. Yue, A.J. Binder, B. Guo, Z. Zhang, Z.A. Qiao, C. Tian, S. Dai, Mesoporous prussian blue analogues: Template-free synthesis and sodium-ion battery applications, *Angew. Chemie - Int. Ed.* 53 (2014) 3134–3137. doi:10.1002/anie.201310679.
- [26] Y. Huang, M. Xie, J. Zhang, Z. Wang, Y. Jiang, G. Xiao, S. Li, L. Li, F. Wu, R. Chen, A novel border-rich Prussian blue synthesized by inhibitor control as cathode for sodium ion batteries, *Nano Energy.* 39 (2017) 273–283. doi:10.1016/j.nanoen.2017.07.005.
- [27] D. Yang, J. Xu, X.Z. Liao, Y.S. He, H. Liu, Z.F. Ma, Structure optimization of Prussian blue analogue cathode materials for advanced sodium ion batteries, *Chem. Commun.* 50 (2014) 13377–13380. doi:10.1039/c4cc05830e.
- [28] Y. You, X.L. Wu, Y.X. Yin, Y.G. Guo, High-quality Prussian blue crystals as superior cathode materials for room-temperature sodium-ion batteries, *Energy Environ. Sci.* 7 (2014) 1643–1647. doi:10.1039/c3ee44004d.
- [29] J. Peng, J. Wang, H. Yi, W.J. Hu, Y. Yu, J. Yin, Y. Shen, Y. Liu, J. Luo, Y. Xu, P. Wei, Y. Li, Y. Jin, Y. Ding, L. Miao, J. Jiang, J. Han, Y. Huang, A

- Dual-Insertion Type Sodium-Ion Full Cell Based on High-Quality Ternary-Metal Prussian Blue Analogs, *Adv. Energy Mater.* 8 (2018) 1–9. doi:10.1002/aenm.201702856.
- [30] A. Bauer, J. Song, S. Vail, W. Pan, J. Barker, Y. Lu, The Scale-up and Commercialization of Nonaqueous Na-Ion Battery Technologies, *Adv. Energy Mater.* 8 (2018) 1–13. doi:10.1002/aenm.201702869.
- [31] A.K. Padhi, K.S. Nonjundaswamy, J.B. Goodenough, Phospho-olivines as Positive-Electrode Materials for Rechargeable Lithium Batteries, *J. Electrochem. Soc.* 144 (1997) 1188–1194.
- [32] D. Morgan, A. Van der Ven, G. Ceder, Li Conductivity in  $\text{Li}_x\text{MPO}_4$  (M = Mn, Fe, Co, Ni) Olivine Materials, *Electrochem. Solid-State Lett.* 7 (2004) A30. doi:10.1149/1.1633511.
- [33] Y. Wang, Y. Wang, E. Hosono, K. Wang, H. Zhou, The design of a  $\text{LiFePO}_4$ /carbon nanocomposite with a core-shell structure and its synthesis by an in situ polymerization restriction method, *Angew. Chemie - Int. Ed.* 47 (2008) 7461–7465. doi:10.1002/anie.200802539.
- [34] A.S. Andersson, J.O. Thomas, B. Kalska, L. Higgstrom, Thermal stability of  $\text{LiFePO}_4$ -based cathodes, *Electrochem. Solid-State Lett.* 3 (2000) 66–68.
- [35] B. Kang, G. Ceder, Battery materials for ultrafast charging and discharging, *Nature.* 458 (2009) 190–193. doi:10.1038/nature07853.
- [36] S.Y. Chung, J.T. Bloking, Y.M. Chiang, Electronically conductive phospho-olivines as lithium storage electrodes, *Nat Mater.* 1 (2002) 123–128. doi:10.1038/nmat732.
- [37] H.-K. Song, K.T. Lee, M.G. Kim, L.F. Nazar, J. Cho, Recent Progress in

- Nanostructured Cathode Materials for Lithium Secondary Batteries, *Adv. Funct. Mater.* 20 (2010) 3818–3834. doi:10.1002/adfm.201000231.
- [38] N. Ravet, Y. Chouinard, J.F. Magnan, S. Besner, M. Gauthier, M. Armand, Electroactivity of natural and synthetic triphylite, *J. Power Sources.* 97–98 (2001) 503–507.
- [39] B.L. Ellis, K.T. Lee, L.F. Nazar, Positive electrode materials for Li-Ion and Li-batteries, *Chem. Mater.* 22 (2010) 691–714. doi:10.1021/cm902696j.
- [40] J. Molenda, M. Mole, Composite Cathode Material for Li-Ion Batteries Based on  $\text{LiFePO}_4$  System, in: J. Cuppoletti (Ed.), *Met. Ceram. Polym. Compos. Var. Uses*, 2011. doi:10.5772/21635.
- [41] M. Avdeev, Z. Mohamed, C.D. Ling, J. Lu, M. Tamaru, A. Yamada, P. Barpanda, Magnetic structures of  $\text{NaFePO}_4$  maricite and triphylite polymorphs for sodium-ion batteries, *Inorg. Chem.* 52 (2013) 8685–8693. doi:10.1021/ic400870x.
- [42] P.P. Prosini, P. Gislou, C. Cento, M. Carewska, A. Masci, Effect of the synthesis conditions on the electrochemical properties of  $\text{LiFePO}_4$  obtained from  $\text{NH}_4\text{FePO}_4$ , *Mater. Res. Bull.* 48 (2013) 3438–3448. doi:10.1016/j.materresbull.2013.05.038.
- [43] P. Moreau, D. Guyomard, J. Gaubicher, F. Boucher, Structure and stability of sodium intercalated phases in olivine  $\text{FePO}_4$ , *Chem. Mater.* 22 (2010) 4126–4128. doi:10.1021/cm101377h.
- [44] A.R. Wizansky, P.E. Rauch, F.J.J. DiSalvo, Powerful oxidizing agents for the oxidative deintercalation of lithium from transition oxides, *J. Solid State Chem.* 81 (1989) 203–207.

- [45] M. Casas-Cabanas, V. V Roddatis, D. Saurel, P. Kubiak, J. Carretero-González, V. Palomares, P. Serras, T. Rojo, Crystal chemistry of Na insertion/deinsertion in  $\text{FePO}_4\text{-NaFePO}_4$ , *J. Mater. Chem.* 22 (2012) 17421. doi:10.1039/c2jm33639a.
- [46] S.-M. Oh, S.-T. Myung, J. Hassoun, B. Scrosati, Y.-K. Sun, Reversible  $\text{NaFePO}_4$  electrode for sodium secondary batteries, *Electrochem. Commun.* 22 (2012) 149–152. doi:10.1016/j.elecom.2012.06.014.
- [47] M. Galceran, D. Saurel, B. Acebedo, V. V Roddatis, E. Martin, T. Rojo, M. Casas-Cabanas, The mechanism of  $\text{NaFePO}_4$  (de)sodiation determined by in situ X-ray diffraction, *Phys Chem Chem Phys.* 16 (2014) 8837–8842. doi:10.1039/c4cp01089b.
- [48] Y. Zhu, Y. Xu, Y. Liu, C. Luo, C. Wang, Comparison of electrochemical performances of olivine  $\text{NaFePO}_4$  in sodium-ion batteries and olivine  $\text{LiFePO}_4$  in lithium-ion batteries, *Nanoscale.* 5 (2013) 780–787. doi:10.1039/c2nr32758a.
- [49] S.P. Ong, V.L. Chevrier, G. Hautier, A. Jain, C. Moore, S. Kim, X. Ma, G. Ceder, Voltage, stability and diffusion barrier differences between sodium-ion and lithium-ion intercalation materials, *Energy Environ. Sci.* 4 (2011) 3680–3688. doi:10.1039/c1ee01782a.
- [50] K.T. Lee, T.N. Ramesh, F. Nan, G. Botton, L.F. Nazar, Topochemical Synthesis of Sodium Metal Phosphate Olivines for Sodium-Ion Batteries, (2011) 3593–3600.
- [51] J. Moring, E. Kostiner, The Crystal Structure of  $\text{NaMnPO}_4$ , *J. Solid State Chem.* 61 (n.d.) 379–383.

- [52] J.N. Bridson, S.E. Quinlan, P.R. Tremaine, Synthesis and Crystal Structure of Maricite and Sodium Iron ( III ) Hydroxyphosphate, *4756* (1998) 763–768.
- [53] A. Bystroem, The structure of natrophilite  $\text{NaMnPO}_4$ , *Ark Kemi Miner. Geol.* 17B (1943) 1–4.
- [54] P.B. Moore, Natrophilite,  $\text{NaMn}(\text{PO}_4)$ , has ordered cations, *Am. Mineral.* 57 (1972) 1333–1344.
- [55] K.A. Wallroth, Action du sel de phosphore sur divers oxydes, *Bull. Soc. Chim.* 39 (1883) 316.
- [56] B. Matković, M. Šljukić, Synthesis and Crystallographic Data of Sodium Thorium Triphosphate,  $\text{NaTh}_2(\text{PO}_4)_3$ , and Sodium Uranium(IV) Triphosphate,  $\text{NaU}_2(\text{PO}_4)_3$ , *Croat. Chem. Acta.* 37 (1965) 115–116.
- [57] L.-O. Hagman, P. Kierkegaard, P. Karvonen, A.I. Virtanen, J. Paasivirta, The Crystal Structure of  $\text{NaM}_2^{\text{IV}}(\text{PO}_4)_3$ ;  $\text{Me}^{\text{IV}} = \text{Ge}, \text{Ti}, \text{Zr.}$ , *Acta Chem. Scand.* 22 (1968) 1822–1832. doi:10.3891/acta.chem.scand.22-1822.
- [58] M.E. Brownfield, E.E. Foord, S.J. Sutley, T. Botinelly, Kosnarite ,  $\text{KZr}_2(\text{PO}_4)_3$  , a new mineral from Mount Mica and Black Mountain, Oxford County, Maine, *Am. Mineral.* 78 (1993) 653–656.
- [59] J.B. Goodenough, H.Y. Hong, J.A. Kafalas, FAST  $\text{Na}^+$  - ION TRANSPORT IN SKELETON STRUCTURES, *Mat. Res. Bull.* 11 (1976) 203–220.
- [60] G. Collin, R. Comes, J.P. Boilot, P. Colomban, Disorder of tetrahedra in Nasicon-type structure — I.  $\text{Na}_3\text{Sc}_2(\text{PO}_4)_3$ : structures and ion-ion correlations, *J. Phys. Chem. Solids.* 47 (1986) 843–854. doi:10.1016/0022-3697(86)90055-7.
- [61] M. de la Rochère, F. D’Yvoire, G. Collin, R. Comès, J.P. Boilot, NASICON

- type materials -  $\text{Na}_3\text{M}_2(\text{PO}_4)_3$  (M=Sc, Cr, Fe):  $\text{Na}^+$ - $\text{Na}^+$  correlations and phase transitions, *Solid State Ionics*. 9–10 (1983) 825–828. doi:10.1016/0167-2738(83)90096-6.
- [62] C. Delmas, F. Cherkaoui, P. Hagenmuller, Ionic conductivity in a new NASICON related solid solution:  $\text{Na}_{3+y}\text{Cr}_{2-y}\text{Mg}_y(\text{PO}_4)_3$ . An optical characterization of the skeleton covalency, *Mater. Res. Bull.* 21 (1986) 469–477. doi:10.1016/0025-5408(86)90013-9.
- [63] F. d'Yvoire, M. Pintard-Scrépel, E. Bretey, M. de la Rochère, Phase transitions and ionic conduction in 3D skeleton phosphates  $\text{A}_3\text{M}_2(\text{PO}_4)_3$ : A = Li, Na, Ag, K; M = Cr, Fe, *Solid State Ionics*. 9–10 (1983) 851–857. doi:10.1016/0167-2738(83)90101-7.
- [64] N. Fanjat, J.L. Soubeyroux, Powder neutron diffraction study of  $\text{Fe}_2\text{Na}_3(\text{PO}_4)_3$  in the low temperature phase, *J. Magn. Mater.* 104–107 (1992) 933–934. doi:10.1016/0304-8853(92)90429-R.
- [65] C. Delmas, F. Cherkaoui, A. Nadiri, P. Hagenmuller, A nasicon-type phase as intercalation electrode:  $\text{NaTi}_2(\text{PO}_4)_3$ , *Mater. Res. Bull.* 22 (1987) 631–639. doi:10.1016/0025-5408(87)90112-7.
- [66] C. Masquelier, L. Croguennec, Polyanionic (phosphates, silicates, sulfates) frameworks as electrode materials for rechargeable Li (or Na) batteries, *Chem. Rev.* 113 (2013) 6552–6591. doi:10.1021/cr3001862.
- [67] C. Delmas, R. Olazcuaga, G. Le Flem, P. Hagenmuller, F. Cherkaoui, R. Brochu, Crystal chemistry of the  $\text{Na}_{1+x}\text{Zr}_{2-x}\text{L}_x(\text{PO}_4)_3$  (L = Cr, In, Yb) solid solutions, *Mater. Res. Bull.* 16 (1981) 285–290. doi:10.1016/0025-5408(81)90044-1.

- [68] F. Cherkaoui, J.C. Viala, C. Delmas, P. Hagemuller, Crystal chemistry and ionic conductivity of a new Nasicon-related solid solution  $\text{Na}_{1+x}\text{Zr}_{2-x/2}\text{Mg}_{x/2}(\text{PO}_4)_3$ , *Solid State Ionics*. 21 (1986) 333–337. doi:10.1016/0167-2738(86)90195-5.
- [69] Z. Jian, L. Zhao, H. Pan, Y.S. Hu, H. Li, W. Chen, L. Chen, Carbon coated  $\text{Na}_3\text{V}_2(\text{PO}_4)_3$  as novel electrode material for sodium ion batteries, *Electrochem. Commun.* 14 (2012) 86–89. doi:10.1016/j.elecom.2011.11.009.
- [70] C. Delmas, K. Olazcuaga, F. Cherkaoui, R. Brochu, G. Le Flem, A new family of phosphates with the formula  $\text{Na}_3\text{M}_2(\text{PO}_4)_3$  (M= Ti, V, Cr, Fe), *C. R. Acad. Sci. Paris Ser. C*. 287 (1978) 169–171.
- [71] I. V. Zatorovskiy, NASICON-type  $\text{Na}_3\text{V}_2(\text{PO}_4)_3$ , *Acta Crystallogr. Sect. E Struct. Reports Online*. 66 (2010) i12. doi:10.1107/S1600536810002801.
- [72] D.O. Semykina, Structural, morphological and electrochemical properties of sodium/lithium-vanadium-containing electrode materials for sodium/lithium-ion batteries, Institute of Solid State Chemistry and Mechanochemistry of the Siberian Branch of the Russian Academy of Sciences (ISSCM SB RAS), 2019. [http://www.solid.nsc.ru/upload/iblock/2ed/2019semykina\\_disser.pdf](http://www.solid.nsc.ru/upload/iblock/2ed/2019semykina_disser.pdf).
- [73] Z. Jian, C. Yuan, W. Han, X. Lu, L. Gu, X. Xi, Y.S. Hu, H. Li, W. Chen, D. Chen, Y. Ikuhara, L. Chen, Atomic structure and kinetics of NASICON  $\text{Na}_x\text{V}_2(\text{PO}_4)_3$  cathode for sodium-ion batteries, *Adv. Funct. Mater.* 24 (2014) 4265–4272. doi:10.1002/adfm.201400173.
- [74] J.-N. Chotard, G. Rousse, R. David, O. Mentré, M. Courty, C. Masquelier, Discovery of a Sodium-Ordered Form of  $\text{Na}_3\text{V}_2(\text{PO}_4)_3$  below Ambient Temperature, *Chem. Mater.* 27 (2015) 5982–5987.

- doi:10.1021/acs.chemmater.5b02092.
- [75] S.Y. Lim, H. Kim, R.A. Shakoor, Y. Jung, J.W. Choi, Electrochemical and Thermal Properties of NASICON Structured  $\text{Na}_3\text{V}_2(\text{PO}_4)_3$  as a Sodium Rechargeable Battery Cathode: A Combined Experimental and Theoretical Study, *J. Electrochem. Soc.* 159 (2012) A1393–A1397. doi:10.1149/2.015209jes.
- [76] Y. Jiang, Z. Yang, W. Li, L. Zeng, F. Pan, M. Wang, X. Wei, G. Hu, L. Gu, Y. Yu, Nanoconfined carbon-coated  $\text{Na}_3\text{V}_2(\text{PO}_4)_3$  particles in mesoporous carbon enabling ultralong cycle life for sodium-ion batteries, *Adv. Energy Mater.* 5 (2015) 1–8. doi:10.1002/aenm.201402104.
- [77] X. Rui, W. Sun, C. Wu, Y. Yu, Q. Yan, An Advanced Sodium-Ion Battery Composed of Carbon Coated  $\text{Na}_3\text{V}_2(\text{PO}_4)_3$  in a Porous Graphene Network, *Adv. Mater.* 27 (2015) 6670–6676. doi:10.1002/adma.201502864.
- [78] W. Shen, C. Wang, H. Liu, W. Yang, Towards highly stable storage of sodium ions: A porous  $\text{Na}_3\text{V}_2(\text{PO}_4)_3/\text{C}$  cathode material for sodium-ion batteries, *Chem. - A Eur. J.* 19 (2013) 14712–14718. doi:10.1002/chem.201300005.
- [79] W. Duan, Z. Zhu, H. Li, Z. Hu, K. Zhang, F. Cheng, J. Chen,  $\text{Na}_3\text{V}_2(\text{PO}_4)_3@C$  core-shell nanocomposites for rechargeable sodium-ion batteries, *J. Mater. Chem. A* 2 (2014) 8668–8675. doi:10.1039/c4ta00106k.
- [80] Y. Xu, Q. Wei, C. Xu, Q. Li, Q. An, P. Zhang, J. Sheng, L. Zhou, L. Mai, Layer-by-Layer  $\text{Na}_3\text{V}_2(\text{PO}_4)_3$  Embedded in Reduced Graphene Oxide as Superior Rate and Ultralong-Life Sodium-Ion Battery Cathode, *Adv. Energy Mater.* 6 (2016). doi:10.1002/aenm.201600389.
- [81] K. Du, H. Guo, G. Hu, Z. Peng, Y. Cao,  $\text{Na}_3\text{V}_2(\text{PO}_4)_3$  as cathode material for

- hybrid lithium ion batteries, *J. Power Sources*. 223 (2013) 284–288. doi:10.1016/j.jpowsour.2012.09.069.
- [82] W.J. Wang, H. Bin Zhao, A.B. Yuan, J.H. Fang, J.Q. Xu, Hydrothermal sol-gel method for the synthesis of a multiwalled carbon nanotube- $\text{Na}_3\text{V}_2(\text{PO}_4)_3$  composite as a novel electrode material for lithium-ion batteries, *Wuli Huaxue Xuebao/ Acta Phys. - Chim. Sin.* 30 (2014) 1113–1120. doi:10.3866/PKU.WHXB201404182.
- [83] Z. Jian, W. Han, X. Lu, H. Yang, Y.S. Hu, J. Zhou, Z. Zhou, J. Li, W. Chen, D. Chen, L. Chen, Superior electrochemical performance and storage mechanism of  $\text{Na}_3\text{V}_2(\text{PO}_4)_3$  cathode for room-temperature sodium-ion batteries, *Adv. Energy Mater.* 3 (2013) 156–160. doi:10.1002/aenm.201200558.
- [84] C. Zhu, K. Song, P.A. Van Aken, J. Maier, Y. Yu, Carbon-coated  $\text{Na}_3\text{V}_2(\text{PO}_4)_3$  embedded in porous carbon matrix: An ultrafast Na-storage cathode with the potential of outperforming Li cathodes, *Nano Lett.* 14 (2014) 2175–2180. doi:10.1021/nl500548a.
- [85] J. Hwang, K. Matsumoto, R. Hagiwara,  $\text{Na}_3\text{V}_2(\text{PO}_4)_3/\text{C}$  Positive Electrodes with High Energy and Power Densities for Sodium Secondary Batteries with Ionic Liquid Electrolytes That Operate across Wide Temperature Ranges, *Adv. Sustain. Syst.* 2 (2018) 1700171. doi:10.1002/adsu.201700171.
- [86] M. Pivko, I. Arcon, M. Bele, R. Dominko, M. Gaberscek,  $\text{A}_3\text{V}_2(\text{PO}_4)_3$  (A = Na or Li) probed by in situ X-ray absorption spectroscopy, *J. Power Sources*. 216 (2012) 145–151. doi:10.1016/j.jpowsour.2012.05.037.
- [87] Z. Jian, Y. Sun, X. Ji, A new low-voltage plateau of  $\text{Na}_3\text{V}_2(\text{PO}_4)_3$  as an anode for Na-ion batteries, *Chem. Commun.* 51 (2015) 6381–6383.

- doi:10.1039/C5CC00944H.
- [88] Z. Jian, Y.S. Hu, X. Ji, W. Chen, NASICON-Structured Materials for Energy Storage, *Adv. Mater.* 29 (2017). doi:10.1002/adma.201601925.
- [89] A. Van der Ven, M. Wagemaker, Effect of surface energies and nano-particle size distribution on open circuit voltage of Li-electrodes, *Electrochem. Commun.* 11 (2009) 881–884. doi:10.1016/j.elecom.2009.02.015.
- [90] R. Malik, A. Abdellahi, G. Ceder, A Critical Review of the Li Insertion Mechanisms in LiFePO<sub>4</sub> Electrodes, *J. Electrochem. Soc.* 160 (2013) A3179–A3197. doi:10.1149/2.029305jes.
- [91] G. Zhang, T. Xiong, M. Yan, Y. Xu, W. Ren, X. Xu, Q. Wei, L. Mai, In Operando Probing of Sodium-Incorporation in NASICON Nanomaterial: Asymmetric Reaction and Electrochemical Phase Diagram, *Chem. Mater.* 29 (2017) 8057–8064. doi:10.1021/acs.chemmater.7b00957.
- [92] W. Ren, Z. Zheng, C. Xu, C. Niu, Q. Wei, Q. An, K. Zhao, M. Yan, M. Qin, L. Mai, Self-sacrificed synthesis of three-dimensional Na<sub>3</sub>V<sub>2</sub>(PO<sub>4</sub>)<sub>3</sub> nanofiber network for high-rate sodium-ion full batteries, *Nano Energy.* 25 (2016) 145–153. doi:10.1016/j.nanoen.2016.03.018.
- [93] H. Kabbour, D. Coillot, M. Colmont, C. Masquelier, O. Mentr, Absolute Cationic Ordering in NASICON-Type Phases, *J. Am. Chem. Soc.* 2 (2011) 11900–11903.
- [94] P. Senguttuvan, G. Rouse, M.E. Arroyo y de Dompablo, H. Vezin, J.-M. Tarascon, M.R. Palacín, Low-Potential Sodium Insertion in a NASICON-Type Structure through the Ti(III)/Ti(II) Redox Couple, *J. Am. Chem. Soc.* 135 (2013) 3897–3903. doi:10.1021/ja311044t.

- [95] C. Masquelier, C. Wurm, J. Rodríguez-Carvajal, J. Gaubicher, L. Nazar, A Powder Neutron Diffraction Investigation of the Two Rhombohedral NASICON Analogues:  $\gamma$ - $\text{Na}_3\text{Fe}_2(\text{PO}_4)_3$  and  $\text{Li}_3\text{Fe}_2(\text{PO}_4)_3$ , *Chem. Mater.* 12 (2000) 525–532. doi:10.1021/cm991138n.
- [96] Y. Liu, Y. Zhou, J. Zhang, Y. Xia, T. Chen, S. Zhang, Monoclinic phase  $\text{Na}_3\text{Fe}_2(\text{PO}_4)_3$ : Synthesis, structure, and electrochemical performance as cathode material in sodium-ion batteries, *ACS Sustain. Chem. Eng.* 5 (2017) 1306–1314. doi:10.1021/acssuschemeng.6b01536.
- [97] K. Kawai, W. Zhao, S. Nishimura, A. Yamada, High-Voltage  $\text{Cr}^{4+}/\text{Cr}^{3+}$  Redox Couple in Polyanion Compounds, *ACS Appl. Energy Mater.* (2018) acsaem.7b00105. doi:10.1021/acsaem.7b00105.
- [98] D. Wang, X. Bie, Q. Fu, D. Dixon, N. Bramnik, Y.S. Hu, F. Fauth, Y. Wei, H. Ehrenberg, G. Chen, F. Du, Sodium vanadium titanium phosphate electrode for symmetric sodium-ion batteries with high power and long lifespan, *Nat. Commun.* 8 (2017) 1–7. doi:10.1038/ncomms15888.
- [99] F. Lalère, V. Seznec, M. Courty, J.N. Chotard, C. Masquelier, Coupled X-ray diffraction and electrochemical studies of the mixed Ti/V-containing NASICON:  $\text{Na}_2\text{TiV}(\text{PO}_4)_3$ , *J. Mater. Chem. A.* 6 (2018) 6654–6659. doi:10.1039/c7ta10689k.
- [100] W. Zhou, L. Xue, X. Lü, H. Gao, Y. Li, S. Xin, G. Fu, Z. Cui, Y. Zhu, J.B. Goodenough,  $\text{Na}_x\text{MV}(\text{PO}_4)_3$  (M = Mn, Fe, Ni) Structure and Properties for Sodium Extraction, *Nano Lett.* 16 (2016) 7836–7841. doi:10.1021/acs.nanolett.6b04044.
- [101] R. Liu, G. Xu, Q. Li, S. Zheng, G. Zheng, Z. Gong, Y. Li, E. Kruskop, R. Fu,

- Z. Chen, K. Amine, Y. Yang, Exploring Highly Reversible 1.5-Electron Reactions ( $V^{3+}/V^{4+}/V^{5+}$ ) in  $Na_3 VCr(PO_4)_3$  Cathode for Sodium-Ion Batteries, *ACS Appl. Mater. Interfaces.* 9 (2017) 43632–43639. doi:10.1021/acsami.7b13018.
- [102] M.J. Aragón, P. Lavela, R. Alcántara, J.L. Tirado, Effect of aluminum doping on carbon loaded  $Na_3V_2(PO_4)_3$  as cathode material for sodium-ion batteries, *Electrochim. Acta.* 180 (2015) 824–830. doi:10.1016/j.electacta.2015.09.044.
- [103] M.J. Aragón, P. Lavela, G.F. Ortiz, J.L. Tirado, Effect of Iron Substitution in the Electrochemical Performance of  $Na_3V_2(PO_4)_3$  as Cathode for Na-Ion Batteries, *J. Electrochem. Soc.* 162 (2015) A3077–A3083. doi:10.1149/2.0151502jes.
- [104] M.J. Aragón, P. Lavela, G.F. Ortiz, J.L. Tirado, Benefits of Chromium Substitution in  $Na_3V_2(PO_4)_3$  as a Potential Candidate for Sodium-Ion Batteries, *ChemElectroChem.* 2 (2015) 995–1002. doi:10.1002/celec.201500052.
- [105] R. Klee, P. Lavela, M.J. Aragón, R. Alcántara, J.L. Tirado, Enhanced high-rate performance of manganese substituted  $Na_3V_2(PO_4)_3/C$  as cathode for sodium-ion batteries, *J. Power Sources.* 313 (2016) 73–80. doi:10.1016/j.jpowsour.2016.02.066.
- [106] F. Lalère, V. Seznec, M. Courty, R. David, J.N. Chotard, C. Masquelier, Improving the energy density of  $Na_3V_2(PO_4)_3$ -based positive electrodes through V/Al substitution, *J. Mater. Chem. A.* 3 (2015) 16198–16205. doi:10.1039/C5TA03528G.
- [107] T. Zhu, P. Hu, X. Wang, Z. Liu, W. Luo, K.A. Owusu, W. Cao, C. Shi, J. Li, L.

- Zhou, L. Mai, Realizing Three-Electron Redox Reactions in NASICON-Structured  $\text{Na}_3\text{MnTi}(\text{PO}_4)_3$  for Sodium-Ion Batteries, *Adv. Energy Mater.* 9 (2019) 2–7. doi:10.1002/aenm.201803436.
- [108] H. Gao, Y. Li, K. Park, J.B. Goodenough, Sodium extraction from NASICON-structured  $\text{Na}_3\text{MnTi}(\text{PO}_4)_3$  through Mn(III)/Mn(II) and Mn(IV)/Mn(III) redox couples, *Chem. Mater.* 28 (2016) 6553–6559. doi:10.1021/acs.chemmater.6b02096.
- [109] H. Li, M. Xu, C. Gao, W. Zhang, Z. Zhang, Y. Lai, L. Jiao, Highly efficient, fast and reversible multi-electron reaction of  $\text{Na}_3\text{MnTi}(\text{PO}_4)_3$  cathode for sodium-ion batteries, *Energy Storage Mater.* 26 (2020) 325–333. doi:10.1016/j.ensm.2019.11.004.
- [110] H. Gao, I.D. Seymour, S. Xin, L. Xue, G. Henkelman, J.B. Goodenough,  $\text{Na}_3\text{MnZr}(\text{PO}_4)_3$ : A High-Voltage Cathode for Sodium Batteries, *J. Am. Chem. Soc.* 140 (2018) 18192–18199. doi:10.1021/jacs.8b11388.
- [111] J. Zhang, Y. Liu, X. Zhao, L. He, H. Liu, Y. Song, S. Sun, Q. Li, X. Xing, J. Chen, A Novel NASICON-Type  $\text{Na}_4\text{MnCr}(\text{PO}_4)_3$  Demonstrating the Energy Density Record of Phosphate Cathodes for Sodium-Ion Batteries, *Adv. Mater.* 32 (2020) 1–8. doi:10.1002/adma.201906348.
- [112] J. Wang, Y. Wang, D.H. Seo, T. Shi, S. Chen, Y. Tian, H. Kim, G. Ceder, A High-Energy NASICON-Type Cathode Material for Na-Ion Batteries, *Adv. Energy Mater.* 1903968 (2020) 1–10. doi:10.1002/aenm.201903968.
- [113] W. Zhang, H. Li, Z. Zhang, M. Xu, Y. Lai, S.L. Chou, Full Activation of  $\text{Mn}^{4+}/\text{Mn}^{3+}$  Redox in  $\text{Na}_4\text{MnCr}(\text{PO}_4)_3$  as a High-Voltage and High-Rate Cathode Material for Sodium-Ion Batteries, *Small.* 16 (2020) 1–8.

- doi:10.1002/sml.202001524.
- [114] S.S. Fedotov, N.D. Luchinin, D.A. Aksyonov, A. V. Morozov, S. V. Ryazantsev, M. Gaboardi, J.R. Plaisier, K.J. Stevenson, A.M. Abakumov, E. V. Antipov, Titanium-based potassium-ion battery positive electrode with extraordinarily high redox potential, *Nat. Commun.* 11 (2020) 1–11. doi:10.1038/s41467-020-15244-6.
- [115] F. La Mantia, C.D. Wessells, H.D. Deshazer, Y. Cui, Reliable reference electrodes for lithium-ion batteries, *Electrochem. Commun.* 31 (2013) 141–144. doi:10.1016/j.elecom.2013.03.015.
- [116] C. Montella, Discussion of the potential step method for the determination of the diffusion coefficients of guest species in host materials: Part I. Influence of charge transfer kinetics and ohmic potential drop, *J. Electroanal. Chem.* 518 (2002) 61–83. doi:10.1016/S0022-0728(01)00691-X.
- [117] E.E. Levin, S.Y. Vassiliev, V.A. Nikitina, Solvent effect on the kinetics of lithium ion intercalation into LiCoO<sub>2</sub>, *Electrochim. Acta.* 228 (2017) 114–124. doi:10.1016/j.electacta.2017.01.040.
- [118] E.E. Levin, A.A. Kokin, D.E. Presnov, A.G. Borzenko, S.Y. Vassiliev, V.A. Nikitina, K.J. Stevenson, Electrochemical Analysis of the Mechanism of Potassium-Ion Insertion into K-rich Prussian Blue Materials, *ChemElectroChem.* 7 (2020) 761–769. doi:10.1002/celec.201901919.
- [119] V.A. Nikitina, S.Y. Vassiliev, K.J. Stevenson, Metal-Ion Coupled Electron Transfer Kinetics in Intercalation-Based Transition Metal Oxides, *Adv. Energy Mater.* 10 (2020) 1–28. doi:10.1002/aenm.201903933.
- [120] J.B. Leriche, S. Hamelet, J. Shu, M. Morcrette, C. Masquelier, G. Ouvrard, M.

- Zerrouki, P. Soudan, S. Belin, E. Elkaïm, F. Baudalet, An Electrochemical Cell for Operando Study of Lithium Batteries Using Synchrotron Radiation, *J. Electrochem. Soc.* 157 (2010) A606. doi:10.1149/1.3355977.
- [121] A LRCS's innovation on the market!, (n.d.). <https://www.lrcs.u-picardie.fr/en/news-seminars/a-lrccs-innovation-on-the-market/> (accessed August 11, 2020).
- [122] Bruker AXS GmbH, Application Note XRD 608 D8 ADVANCE In Operando Characterization of Lithium Batteries using XRD, (2017) 4. [http://my.bruker.com/acton/attachment/2655/2655:f-e9c34f1d-2fcb-4a54-94e2-899be71c7956/1/u-0e45-77934/-/-/?utm\\_term=PDF\\_XRD\\_AN\\_608\\_Li\\_Batteries&&utm\\_content=landing+page&utm\\_source=Act-On+Software&utm\\_medium=landing+page&cm\\_mmc=Act-On\\_Software\\_-\\_Landing](http://my.bruker.com/acton/attachment/2655/2655:f-e9c34f1d-2fcb-4a54-94e2-899be71c7956/1/u-0e45-77934/-/-/?utm_term=PDF_XRD_AN_608_Li_Batteries&&utm_content=landing+page&utm_source=Act-On+Software&utm_medium=landing+page&cm_mmc=Act-On_Software_-_Landing) (accessed September 29, 2020).
- [123] O.A. Drozhzhin, I. V. Tereshchenko, H. Emerich, E. V. Antipov, A.M. Abakumov, D. Chernyshov, An electrochemical cell with sapphire windows for operando synchrotron X-ray powder diffraction and spectroscopy studies of high-power and high-voltage electrodes for metal-ion batteries, *J. Synchrotron Radiat.* 25 (2018) 468–472. doi:10.1107/S1600577517017489.
- [124] V. Petríček, M. Dušek, L. Palatinus, Crystallographic computing system JANA2006: General features, *Zeitschrift Fur Krist.* 229 (2014) 345–352. doi:10.1515/zkri-2014-1737.
- [125] J Rodríguez-Carvajal, Recent developments of the program FULLPROF, *Comm. Powder Diffr. (IUCr). Newsl.* 26 (2001) 12–19.
- [126] V. V. Shapovalov, A.A. Guda, N. V. Kosova, S.P. Kubrin, O.A. Podgornova,

- A.M. Aboraia, C. Lamberti, A. V. Soldatov, Laboratory operando Fe and Mn K-edges XANES and Mössbauer studies of the  $\text{LiFe}_{0.5}\text{MnPO}_{0.5}\text{PO}_4$  cathode material, *Radiat. Phys. Chem.* 175 (2018) 108065. doi:10.1016/j.radphyschem.2018.11.019.
- [127] R.D. Shannon, Revised Effective Ionic Radii and Systematic Studies of Interatomic Distances in Halides and Chalcogenides, *Acta Cryst. A* 32 (1976) 751–767.
- [128] A. Mbandza, E. Bordes, P. Courtine, Preparation and structural properties of the solid state ionic conductor  $\text{CuTi}_2(\text{PO}_4)_3$ , *Mater. Res. Bull.* 20 (1985) 251–257. doi:10.1016/0025-5408(85)90180-1.
- [129] M. Barj, G. Lucazeau, C. Delmas, Raman and infrared spectra of some chromium Nasicon-type materials: Short-range disorder characterization, *J. Solid State Chem.* 100 (1992) 141–150. doi:10.1016/0022-4596(92)90164-Q.
- [130] K.K. Rangan, J. Gopalakrishnan,  $\text{AM}^{\text{V}}\text{M}^{\text{III}}(\text{PO}_4)_3$ : New Mixed-Metal Phosphates Having NASICON and Related Structures, *Inorg. Chem.* 34 (1995) 1969–1972. doi:https://doi.org/10.1021/ic00111a055.
- [131] G. Rambabu, N. Anantharamulu, M. Vithal, M. Raghavender, G. Prasad, Preparation, characterization, and impedance studies of  $\text{LiSbM}(\text{PO}_4)_3$  (M=Al, Fe, and Cr), *J. Appl. Phys.* 100 (2006) 0–7. doi:10.1063/1.2357843.
- [132] G. Rambabu, N. Anantharamulu, K. Koteswara Rao, G. Prasad, M. Vithal, Powder X-ray diffraction, infrared and conductivity studies of  $\text{AgSbMP}_3\text{O}_{12}$  (M = Al, Ga, Fe and Cr), *Mater. Res. Bull.* 43 (2008) 1509–1518. doi:10.1016/j.materresbull.2007.06.022.
- [133] A. Rudola, D. Aurbach, P. Balaya, A new phenomenon in sodium batteries:

- Voltage step due to solvent interaction, *Electrochem. Commun.* 46 (2014) 56–59. doi:10.1016/j.elecom.2014.06.008.
- [134] R. Dugas, A. Ponrouch, G. Gachot, R. David, M.R. Palacin, J.M. Tarascon, Na Reactivity toward carbonate-based electrolytes: The effect of FEC as additive, *J. Electrochem. Soc.* 163 (2016) A2333–A2339. doi:10.1149/2.0981610jes.
- [135] M. V. Zakharkin, O.A. Drozhzhin, I. V. Tereshchenko, D. Chernyshov, A.M. Abakumov, E. V. Antipov, K.J. Stevenson, Enhancing Na<sup>+</sup> Extraction Limit through High Voltage Activation of the NASICON-Type Na<sub>4</sub>MnV(PO<sub>4</sub>)<sub>3</sub> Cathode, *ACS Appl. Energy Mater.* 1 (2018) 5842–5846. doi:10.1021/acsaem.8b01269.
- [136] F. Chen, V.M. Kovrugin, R. David, O. Mentré, F. Fauth, J.-N. Chotard, C. Masquelier, A NASICON-Type Positive Electrode for Na Batteries with High Energy Density: Na<sub>4</sub>MnV(PO<sub>4</sub>)<sub>3</sub>, *Small Methods.* 1800218 (2018) 1800218. doi:10.1002/smtd.201800218.
- [137] Y. Huang, X. Li, J. Wang, L. Miao, C. Li, J. Han, Y. Huang, Superior Na-ion storage achieved by Ti substitution in Na<sub>3</sub>V<sub>2</sub>(PO<sub>4</sub>)<sub>3</sub>, *Energy Storage Mater.* 15 (2018) 108–115. doi:10.1016/j.ensm.2018.03.021.
- [138] A. Perea, M.T. Sougrati, C.M. Ionica-Bousquet, B. Fraisse, C. Tessier, L. Aldon, J.C. Jumas, Operando <sup>57</sup>Fe Mössbauer and XRD investigation of Li<sub>x</sub>Mn<sub>y</sub>Fe<sub>1-y</sub>PO<sub>4</sub>/C composites (y = 0.50; 0.75), *RSC Adv.* 2 (2012) 9517–9524. doi:10.1039/c2ra20949g.
- [139] D.B. Ravnsbæk, K. Xiang, W. Xing, O.J. Borkiewicz, K.M. Wiaderek, P. Gionet, K.W. Chapman, P.J. Chupas, M. Tang, Y.M. Chiang, Engineering the Transformation Strain in LiMn<sub>y</sub>Fe<sub>1-y</sub>PO<sub>4</sub>/C Olivines for Ultrahigh Rate Battery

- Cathodes, *Nano Lett.* 16 (2016) 2375–2380. doi:10.1021/acs.nanolett.5b05146.
- [140] A. Yamada, Y. Kudo, K.Y. Liu, Phase Diagram of  $\text{Li}_x\text{Mn}_y\text{Fe}_{1-y}\text{PO}_4$  ( $0 \leq x, y \leq 1$ ), *J. Electrochem. Soc.* 148 (2001) A1153–A1158. doi:10.1149/1.1401083.
- [141] R. Malik, F. Zhou, G. Ceder, Phase diagram and electrochemical properties of mixed olivines from first-principles calculations, *Phys Rev B.* 79 (2009) 1–7. doi:10.1103/PhysRevB.79.214201.
- [142] J. Gaubicher, F. Boucher, P. Moreau, M. Cuisinier, P. Soudan, E. Elkaim, D. Guyomard, Abnormal operando structural behavior of sodium battery material: Influence of dynamic on phase diagram of  $\text{Na}_x\text{FePO}_4$ , *Electrochem. Commun.* 38 (2014) 104–106. doi:10.1016/j.elecom.2013.11.017.
- [143] M. Bianchini, J.M. Ateba-Mba, P. Dagault, E. Bogdan, D. Carlier, E. Suard, C. Masquelier, L. Croguennec, Multiple phases in the  $\epsilon\text{-VPO}_4\text{O-LiVPO}_4\text{O-Li}_2\text{VPO}_4\text{O}$  system: A combined solid state electrochemistry and diffraction structural study, *J. Mater. Chem. A.* 2 (2014) 10182–10192. doi:10.1039/c4ta01518e.
- [144] I. Skotheft, Redetermination of the crystal structure of  $\text{Na}_3\text{Sc}_2(\text{PO}_4)_3$ , *Solid State Ionics.* 26 (1988) 307–310. doi:10.1016/0167-2738(88)90260-3.
- [145] M.J. Aragón, P. Lavela, G.F. Ortiz, R. Alcántara, J.L. Tirado, Insight into the Electrochemical Sodium Insertion of Vanadium Superstoichiometric NASICON Phosphate, *Inorg. Chem.* 56 (2017) 11845–11853. doi:10.1021/acs.inorgchem.7b01846.
- [146] V. Dyadkin, P. Pattison, V. Dmitriev, D. Chernyshov, A new multipurpose diffractometer PILATUS@SNBL, *J. Synchrotron Radiat.* 23 (2016) 825–829. doi:10.1107/S1600577516002411.

- [147] M. Morcrette, J.B. Leriche, S. Patoux, C. Wurm, C. Masquelier, In situ X-ray diffraction during lithium extraction from rhombohedral and monoclinic  $\text{Li}_3\text{V}_2(\text{PO}_4)_3$ , *Electrochem. Solid-State Lett.* 6 (2003) 80–84. doi:10.1149/1.1563871.
- [148] K. Momma, F. Izumi, VESTA 3 for three-dimensional visualization of crystal , volumetric and morphology data, *J. Appl. Crystallogr.* 44 (2011) 1272–1276. doi:10.1107/S0021889811038970.
- [149] A. Yamada, Y. Takei, H. Koizumi, N. Sonoyama, R. Kanno, K. Itoh, M. Yonemura, T. Kamiyama, Electrochemical, Magnetic, and Structural Investigation of the  $\text{Li}_x\text{Mn}_y\text{Fe}_{1-y}\text{PO}_4/\text{C}/\text{C}$  Olivine Phases, *Chem. Mater.* 18 (2006) 804–813. doi:10.1021/cm051861f.
- [150] M. Schindler, F.C. Hawthorne, W.H. Baur, Crystal chemical aspects of vanadium: Polyhedral geometries, characteristic bond valences, and polymerization of  $(\text{VO}_{(n)})$  polyhedra, *Chem. Mater.* 12 (2000) 1248–1259. doi:10.1021/cm990490y.
- [151] M.J. Aragón, P. Lavela, P. Recio, R. Alcántara, J.L. Tirado, On the influence of particle morphology to provide high performing chemically desodiated  $\text{C}@\text{NaV}_2(\text{PO}_4)_3$  as cathode for rechargeable magnesium batteries, *J. Electroanal. Chem.* 827 (2018) 128–136. doi:10.1016/j.jelechem.2018.09.013.
- [152] S.-C. Yin, H. Grondy, P. Strobel, H. Huang, L.F. Nazar, Charge Ordering in Lithium Vanadium Phosphates: Electrode Materials for Lithium-Ion Batteries, *J. Am. Chem. Soc.* 125 (2002) 31. doi:10.1021/JA028973H.
- [153] S.C. Yin, H. Grondy, P. Strobel, M. Anne, L.F. Nazar, Electrochemical property: Structure relationships in monoclinic  $\text{Li}_{3-y}\text{V}_2(\text{PO}_4)_3$ , *J. Am. Chem.*

- Soc. 125 (2003) 10402–10411. doi:10.1021/ja034565h.
- [154] J. Yoon, S. Muhammad, D. Jang, N. Sivakumar, J. Kim, W.H. Jang, Y.S. Lee, Y.U. Park, K. Kang, W.S. Yoon, Study on structure and electrochemical properties of carbon-coated monoclinic  $\text{Li}_3\text{V}_2(\text{PO}_4)_3$  using synchrotron based in situ X-ray diffraction and absorption, *J. Alloys Compd.* 569 (2013) 76–81. doi:10.1016/j.jallcom.2013.03.188.
- [155] S. Ghosh, N. Barman, M. Mazumder, S.K. Pati, G. Rouse, P. Senguttuvan, High Capacity and High-Rate NASICON- $\text{Na}_{3.75}\text{V}_{1.25}\text{Mn}_{0.75}(\text{PO}_4)_3$  Cathode for Na-Ion Batteries via Modulating Electronic and Crystal Structures, *Adv. Energy Mater.* 1902918 (2019) 1–11. doi:10.1002/aenm.201902918.
- [156] A. Eftekhari, Lithium-Ion Batteries with High Rate Capabilities, *ACS Sustain. Chem. Eng.* 5 (2017) 2799–2816. doi:10.1021/acssuschemeng.7b00046.
- [157] A. Tomaszewska, Z. Chu, X. Feng, S. O’Kane, X. Liu, J. Chen, C. Ji, E. Endler, R. Li, L. Liu, Y. Li, S. Zheng, S. Vetterlein, M. Gao, J. Du, M. Parkes, M. Ouyang, M. Marinescu, G. Offer, B. Wu, Lithium-ion battery fast charging: A review, *ETransportation.* 1 (2019) 100011. doi:10.1016/j.etrans.2019.100011.
- [158] G.L. Zhu, C.Z. Zhao, J.Q. Huang, C. He, J. Zhang, S. Chen, L. Xu, H. Yuan, Q. Zhang, Fast Charging Lithium Batteries: Recent Progress and Future Prospects, *Small.* 15 (2019) 1–14. doi:10.1002/smll.201805389.
- [159] Y. Liu, Y. Zhu, Y. Cui, Challenges and opportunities towards fast-charging battery materials, *Nat. Energy.* 4 (2019) 540–550. doi:10.1038/s41560-019-0405-3.
- [160] R. Tian, S.H. Park, P.J. King, G. Cunningham, J. Coelho, V. Nicolosi, J.N. Coleman, Quantifying the factors limiting rate performance in battery

- electrodes, *Nat. Commun.* 10 (2019) 1–11. doi:10.1038/s41467-019-09792-9.
- [161] C. Heubner, J. Seeba, T. Liebmann, A. Nickol, S. Börner, M. Fritsch, K. Nikolowski, M. Wolter, M. Schneider, A. Michaelis, Semi-empirical master curve concept describing the rate capability of lithium insertion electrodes, *J. Power Sources.* 380 (2018) 83–91. doi:10.1016/j.jpowsour.2018.01.077.
- [162] R. Cornut, D. Lepage, S.B. Schougaard, Interpreting lithium batteries discharge curves for easy identification of the origin of performance limitations, *Electrochim. Acta.* 162 (2015) 271–274. doi:10.1016/j.electacta.2014.11.035.
- [163] S.Y. Vassiliev, E.E. Levin, D.E. Presnov, V.A. Nikitina, Electrochemical Patterns of Phase Transforming Intercalation Materials: Diagnostic Criteria for the Case of Slow Nucleation Rate Control, *J. Electrochem. Soc.* 166 (2019) A829–A837. doi:10.1149/2.1241904jes.
- [164] A.R. Iarchuk, V.A. Nikitina, E.A. Karpushkin, V.G. Sergeyev, E. V. Antipov, K.J. Stevenson, A.M. Abakumov, Influence of Carbon Coating on Intercalation Kinetics and Transport Properties of LiFePO<sub>4</sub>, *ChemElectroChem.* 6 (2019) 5090–5100. doi:10.1002/celec.201901219.
- [165] W. Dreyer, J. Jamnik, C. Gohlke, R. Huth, J. Moškon, M. Gaberšček, The thermodynamic origin of hysteresis in insertion batteries, *Nat. Mater.* 9 (2010) 448–453. doi:10.1038/nmat2730.
- [166] P. Bai, G. Tian, Statistical kinetics of phase-transforming nanoparticles in LiFePO<sub>4</sub> porous electrodes, *Electrochim. Acta.* 89 (2013) 644–651. doi:10.1016/j.electacta.2012.11.070.
- [167] M. V. Zakharkin, O.A. Drozhzhin, S. V. Ryazantsev, D. Chernyshov, M.A. Kirsanova, I. V. Mikheev, E.M. Pazhetnov, E. V. Antipov, K.J. Stevenson,

- Electrochemical properties and evolution of the phase transformation behavior in the NASICON-type  $\text{Na}_{3+x}\text{Mn}_x\text{V}_{2-x}(\text{PO}_4)_3$  ( $0 \leq x \leq 1$ ) cathodes for Na-ion batteries, *J. Power Sources.* 470 (2020) 1–8. doi:10.1016/j.jpowsour.2020.228231.
- [168] Y. Huang, L. Zhao, L. Li, M. Xie, F. Wu, R. Chen, Electrolytes and Electrolyte/Electrode Interfaces in Sodium-Ion Batteries: From Scientific Research to Practical Application, *Adv. Mater.* 31 (2019) 1–41. doi:10.1002/adma.201808393.
- [169] K. Li, J. Zhang, D. Lin, D.W. Wang, B. Li, W. Lv, S. Sun, Y.B. He, F. Kang, Q.H. Yang, L. Zhou, T.Y. Zhang, Evolution of the electrochemical interface in sodium ion batteries with ether electrolytes, *Nat. Commun.* 10 (2019) 1–10. doi:10.1038/s41467-019-08506-5.
- [170] Q. Li, Y. Wang, X. Wang, X. Sun, J.N. Zhang, X. Yu, H. Li, Investigations on the Fundamental Process of Cathode Electrolyte Interphase Formation and Evolution of High-Voltage Cathodes, *ACS Appl. Mater. Interfaces.* 12 (2020) 2319–2326. doi:10.1021/acsami.9b16727.
- [171] M.D. Levi, D. Aurbach, Frumkin intercalation isotherm - a tool for the description of lithium insertion into host materials: a review, *Electrochim. Acta.* 45 (1999) 167–185. doi:10.1016/S0013-4686(99)00202-9.
- [172] R. Malik, F. Zhou, G. Ceder, Kinetics of non-equilibrium lithium incorporation in  $\text{LiFePO}_4$ , *Nat. Mater.* 10 (2011) 587–590. doi:10.1038/nmat3065.
- [173] P. Bai, D.A. Cogswell, M.Z. Bazant, Suppression of Phase Separation in  $\text{LiFePO}_4$  Nanoparticles During Battery Discharge, *Nano Lett.* 11 (2011) 4890–4896. doi:10.1021/nl202764f.

- [174] C. Wang, U.S. Kasavajjula, P.E. Arce, A discharge model for phase transformation electrodes: Formulation, experimental validation, and analysis, *J. Phys. Chem. C*. 111 (2007) 16656–16663. doi:10.1021/jp074490u.
- [175] U.S. Kasavajjula, C. Wang, P.E. Arce, Discharge Model for LiFePO<sub>4</sub> Accounting for the Solid Solution Range, *J. Electrochem. Soc.* 155 (2008) A866. doi:10.1149/1.2980420.
- [176] A. Khandelwal, K.S. Hariharan, V. Senthil Kumar, P. Gambhire, S.M. Kolake, D. Oh, S. Doo, Generalized moving boundary model for charge-discharge of LiFePO<sub>4</sub>/C cells, *J. Power Sources*. 248 (2014) 101–114. doi:10.1016/j.jpowsour.2013.09.066.
- [177] D.A. Cogswell, M.Z. Bazant, Coherency strain and the kinetics of phase separation in LiFePO<sub>4</sub> nanoparticles, *ACS Nano*. 6 (2012) 2215–2225. doi:10.1021/nn204177u.
- [178] L. Hong, L. Li, Y.K. Chen-Wiegart, J. Wang, K. Xiang, L. Gan, W. Li, F. Meng, F. Wang, J. Wang, Y.M. Chiang, S. Jin, M. Tang, Two-dimensional lithium diffusion behavior and probable hybrid phase transformation kinetics in olivine lithium iron phosphate, *Nat. Commun.* 8 (2017) 1–13. doi:10.1038/s41467-017-01315-8.
- [179] M.Z. Bazant, Theory of Chemical Kinetics and Charge Transfer based on Nonequilibrium Thermodynamics, *Acc. Chem. Res.* 46 (2013) 1144–1160. doi:10.1021/ar300145c.
- [180] M. Gauthier, T.J. Carney, A. Grimaud, L. Giordano, N. Pour, H.H. Chang, D.P. Fenning, S.F. Lux, O. Paschos, C. Bauer, F. Maglia, S. Lupart, P. Lamp, Y. Shao-Horn, Electrode-Electrolyte Interface in Li-Ion Batteries: Current

- Understanding and New Insights, *J. Phys. Chem. Lett.* 6 (2015) 4653–4672.  
doi:10.1021/acs.jpcllett.5b01727.
- [181] V.A. Nikitina, Charge transfer processes in the course of metal-ion electrochemical intercalation, *Curr. Opin. Electrochem.* 19 (2020) 71–77.  
doi:10.1016/j.coelec.2019.10.006.
- [182] H. Gwon, D.H. Seo, S.W. Kim, J. Kim, K. Kang, Combined first-principle calculations and experimental study on multi-component olivine cathode for lithium rechargeable batteries, *Adv. Funct. Mater.* 19 (2009) 3285–3292.  
doi:10.1002/adfm.200900414.
- [183] N. Meethong, H.Y.S. Huang, S.A. Speakman, W.C. Carter, Y.M. Chiang, Strain accommodation during phase transformations in olivine-based cathodes as a materials selection criterion for high-power rechargeable batteries, *Adv. Funct. Mater.* 17 (2007) 1115–1123. doi:10.1002/adfm.200600938.
- [184] C.A. Schneider, W.S. Rasband, K.W. Eliceiri, NIH Image to ImageJ: 25 years of image analysis, *Nat. Methods.* 9 (2012) 671–675. doi:10.1038/nmeth.2089.

## Appendices A

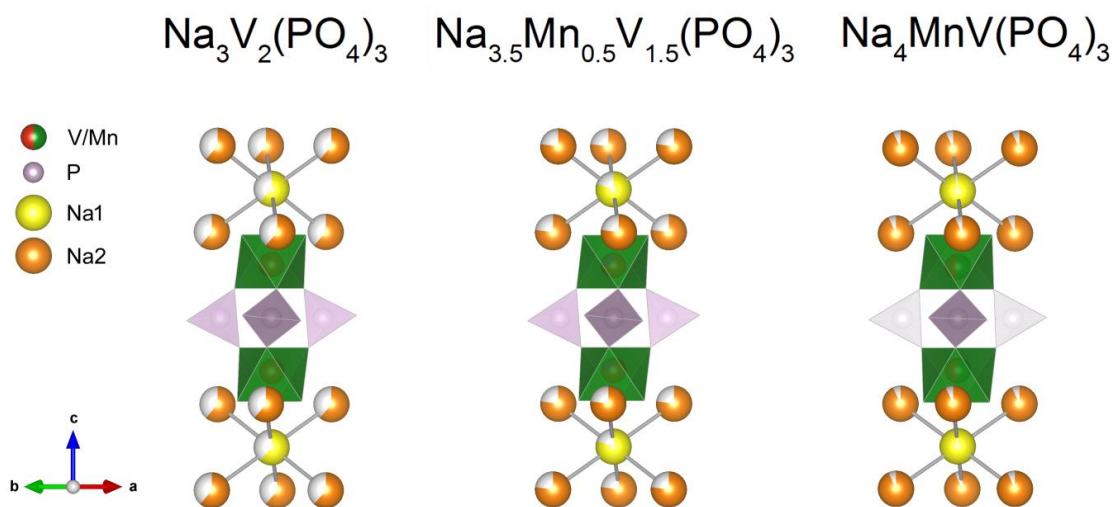


**Fig. A 1** Schematic representation of the “lantern” units  $\text{Mn}_x\text{V}_{2-x}(\text{PO}_4)_3$  in the as-synthesized  $\text{Na}_{3+x}\text{Mn}_x\text{V}_{2-x}(\text{PO}_4)_3$  ( $x=0, 0.5, 1$ ), with Na ions located in the interstitial positions [148].

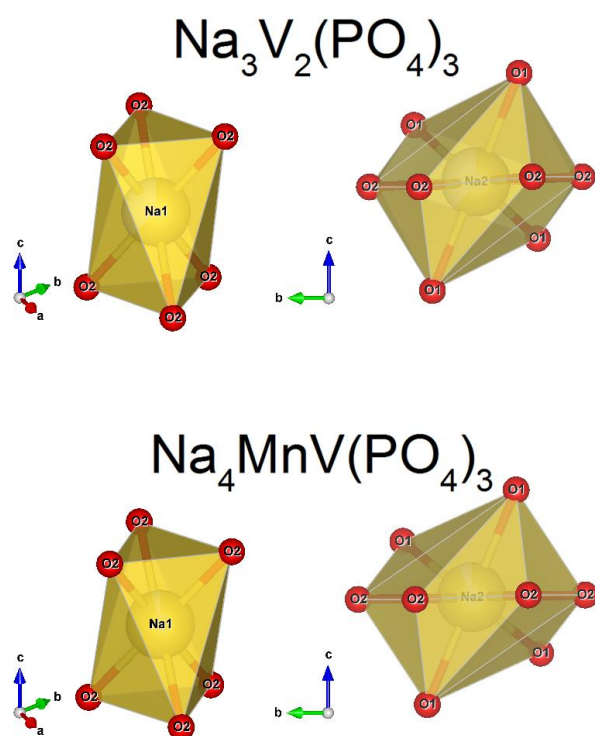


**Fig. A 2** Na1 and Na2 polyhedra structures in the as-synthesized  $\text{Na}_{3+x}\text{Mn}_x\text{V}_{2-x}(\text{PO}_4)_3$  ( $x=0$  and  $1$ ) [148]

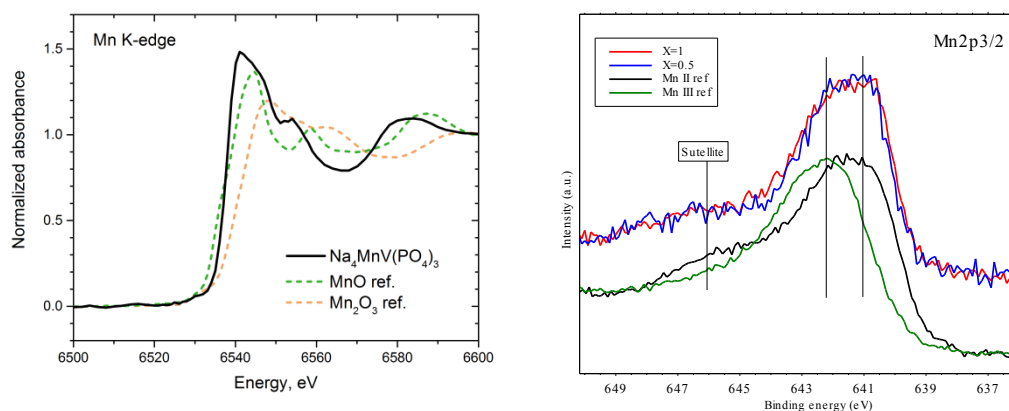


**Fig. A 3** (left) X-ray absorption spectra of the  $\text{Na}_4\text{MnV}(\text{PO}_4)_3$  powder at the K-edge of Mn (left) and  $\text{Mn}2p_{3/2}$  X-ray photoelectron spectra of the  $\text{Na}_{3.5}\text{Mn}_{0.5}\text{V}_{1.5}(\text{PO}_4)_3$  and  $\text{Na}_4\text{MnV}(\text{PO}_4)_3$  powders with the  $\text{Mn}^{2+}$  and  $\text{Mn}^{3+}$  standards.

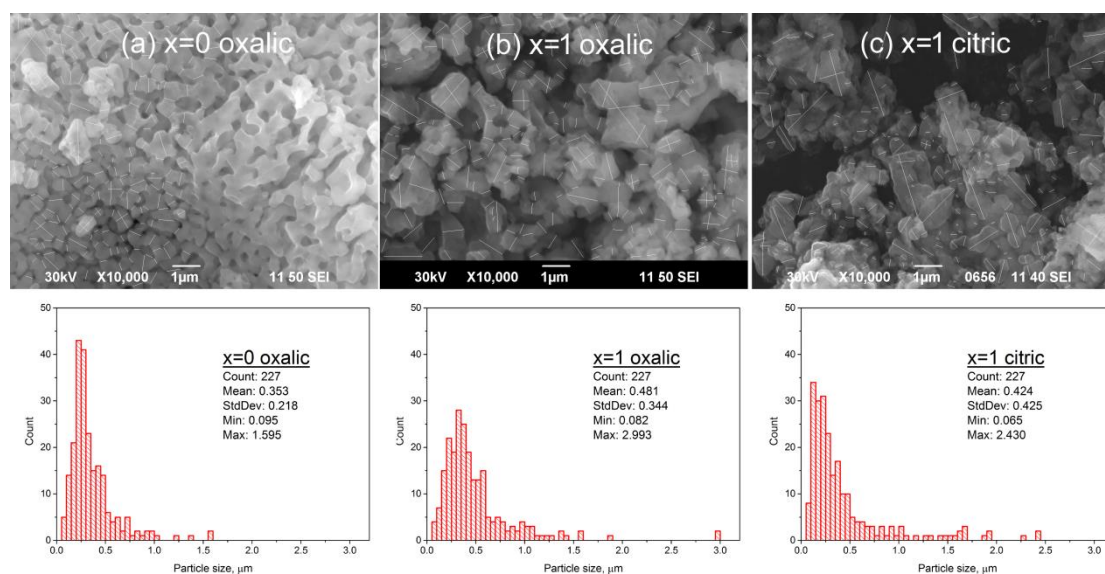


**Fig. A 4** SEM images and the histograms of the  $\text{Na}_{3+x}\text{Mn}_x\text{V}_{2-x}(\text{PO}_4)_3$  particle size distributions derived with the ImageJ software [184] (a)  $x=0$ , synthesized with oxalic acid, (b)  $x=1$ , synthesized with oxalic acid, (c)  $x=1$ , synthesized with citric acid.

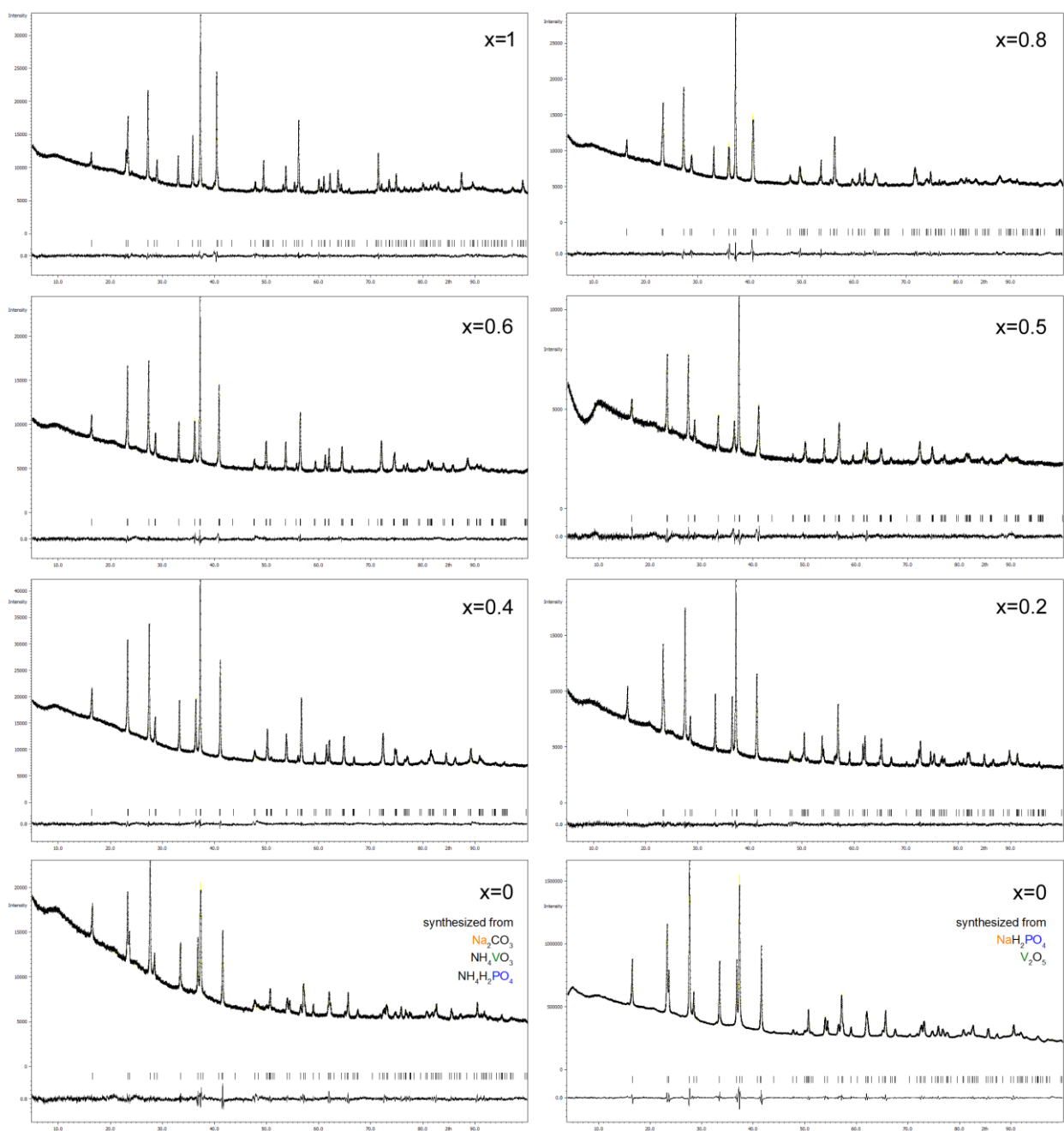


**Fig. A 5** Le Bail fit of XRPD data of the as-synthesized  $\text{Na}_{3+x}\text{Mn}_x\text{V}_{2-x}(\text{PO}_4)_3$  ( $0 \leq x \leq 1$ ) in the  $R\bar{3}c$  space group. The peculiarities in the small angle area below 10 degrees are related to the features of the particular Image Plate detector. Measured with a Huber G670 Guiner Camera ( $\text{Co K}\alpha_1$  radiation).

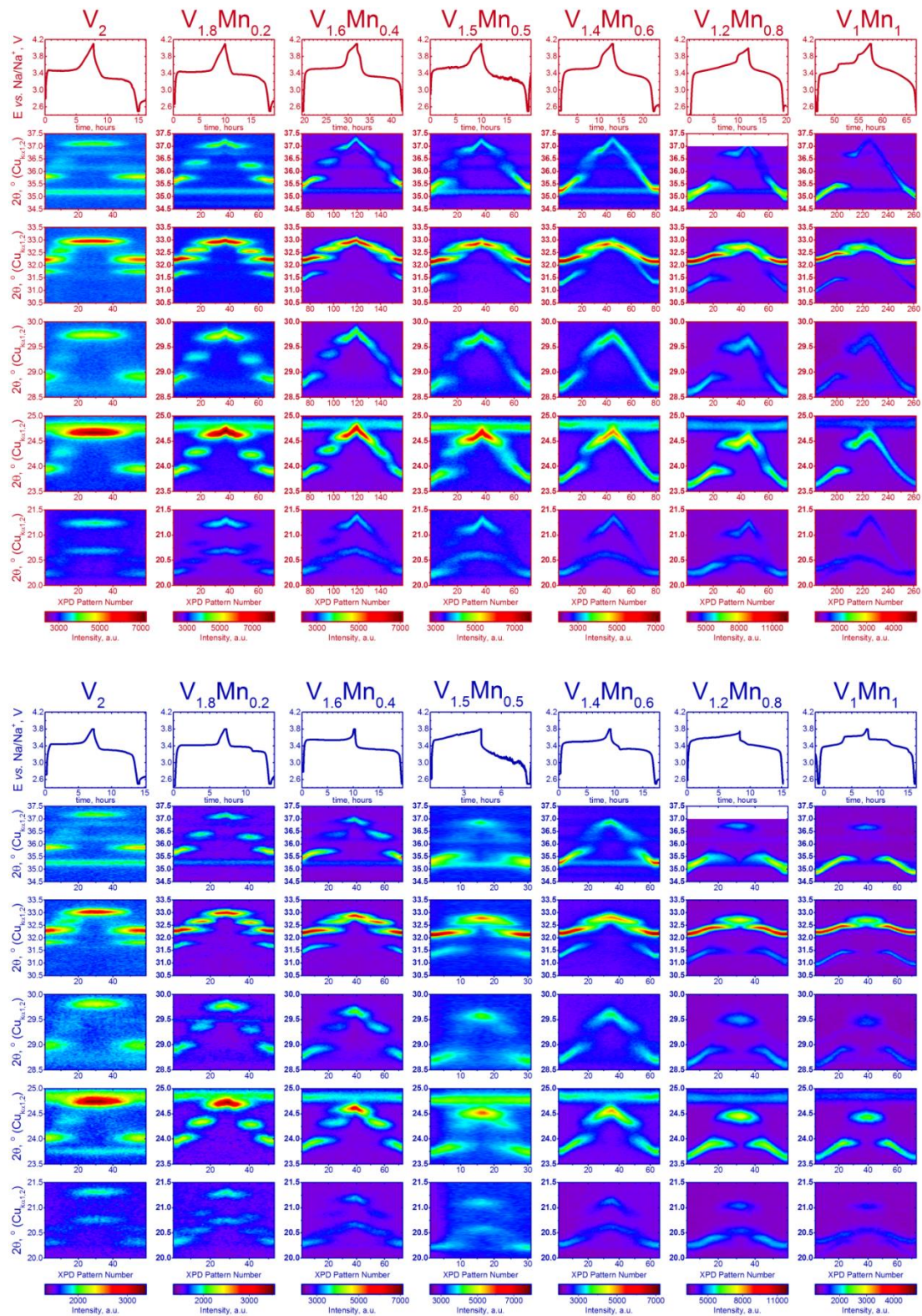


**Fig. A 6 Transformations of the selected regions ( $20.0-21.5^\circ$ ,  $23.5-25.0^\circ$ ,  $28.5-30.0^\circ$ ,  $31.5-33.5^\circ$ ,  $34.5-37.5^\circ$ ,  $\text{Cu}_{K\alpha 1/K\alpha 2}$ ) of XRPD patterns during *operando* charge-discharge in the 2.5-3.8V and**

2.5-4.1V voltage windows for  $\text{Na}_3\text{V}_2(\text{PO}_4)_3$ ,  $\text{Na}_{3.2}\text{Mn}_{0.2}\text{V}_{1.8}(\text{PO}_4)_3$ ,  $\text{Na}_{3.4}\text{Mn}_{0.4}\text{V}_{1.6}(\text{PO}_4)_3$ ,  
 $\text{Na}_{3.5}\text{Mn}_{0.5}\text{V}_{1.5}(\text{PO}_4)_3$ ,  $\text{Na}_{3.6}\text{Mn}_{0.6}\text{V}_{1.4}(\text{PO}_4)_3$ ,  $\text{Na}_{3.8}\text{Mn}_{0.8}\text{V}_{1.2}(\text{PO}_4)_3$ ,  $\text{Na}_4\text{MnV}(\text{PO}_4)_3$ .

Table A 1 Unit Cell Volume ( $\text{\AA}^3$ ) of  $\text{Na}_{3+x}\text{Mn}_x\text{V}_{2-x}(\text{PO}_4)_3$  ( $0 \leq x \leq 1$ ) at different states of charge

Substitution level x	$\text{Na}_{3+x}\text{M}_2(\text{PO}_4)_3$	$\Delta V$	$\text{Na}_3\text{M}_2(\text{PO}_4)_3$	$\Delta V$	$\text{Na}_2\text{M}_2(\text{PO}_4)_3$	$\Delta V$	$\text{Na}_{1+x}\text{M}_2(\text{PO}_4)_3$ (3.8V)	$\Delta V$	4.1V
0	1442.6	-2.2	1440.4	-52.1	1388.3	-65.9	1322.4	0	1322.4
0.2	1452.7	-11.1	1441.6	-56.7	1384.9	-56.6	1328.3	-0.8	1327.5
0.4	1466.6	-20.7	1445.9	-63.7	1382.2	-45	1337.2	-9.1	1328.1
0.6	1481.3	--	--	--	--	-139.2	1342.1	-7.4	1334.7
0.8	1493.5	-39.4	1454.1	--	--	-97.2	1356.9	-3.6	1353.3 <sup>(4.0V)</sup>
1	1497.6	-41.9	1455.7	--	--	-86.1	1369.6	-23.2	1346.4

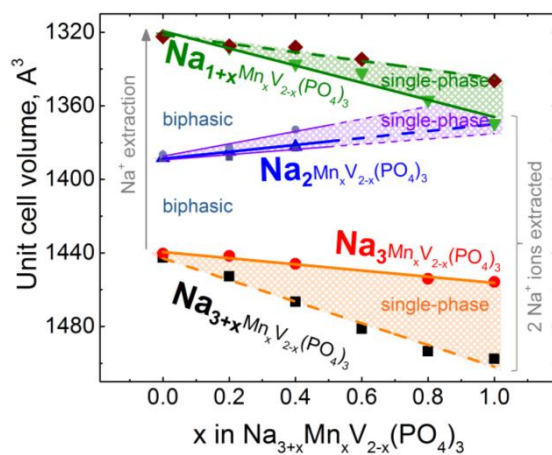


Fig. A 7 Schematic illustration of the  $\text{Na}^+$  deintercalation regimes from  $\text{Na}_{3+x}\text{Mn}_x\text{V}_{2-x}(\text{PO}_4)_3$  ( $0 \leq x \leq 1$ ) during  $\text{Na}^+$  extraction

**Table A 2 Crystallographic data for Na<sub>4-x</sub>MnV(PO<sub>4</sub>)<sub>3</sub> at different state of charge.**

State of charge	Pristine	Charged to 3.5V	Charged to 3.8V	Charged to 4.0V	Discharged to 2.5V
Formula	Na <sub>3.66(3)</sub> MnV(PO <sub>4</sub> ) <sub>3</sub>	Na <sub>2.96(8)</sub> MnV(PO <sub>4</sub> ) <sub>3</sub>	Na <sub>1.90(4)</sub> MnV(PO <sub>4</sub> ) <sub>3</sub>	Na <sub>1.77(2)</sub> MnV(PO <sub>4</sub> ) <sub>3</sub>	Na <sub>3.71(2)</sub> MnV(PO <sub>4</sub> ) <sub>3</sub>
Space group	<i>R</i> $\bar{3}c$	<i>C</i> 2/ <i>c</i>	<i>R</i> $\bar{3}c$	<i>R</i> $\bar{3}c$	<i>R</i> $\bar{3}c$
<i>a</i> , Å	8.9434(4)	15.3185(6)	8.5140(9)	8.4499(7)	8.9394(4)
<i>b</i> , Å		8.8425(3)			
<i>c</i> , Å	21.4545(9)	8.7651(3)	21.689(2)	21.806(2)	21.493(1)
$\beta$ , deg.		125.557(2)			
<i>V</i> , Å <sup>3</sup>	1486.1(1)	965.88(7)	1361.5(3)	1348.4(2)	1487.4(1)
<i>Z</i>	6	4	6	6	6
$\rho$ , g/cm <sup>3</sup>	3.184	3.1542	3.179	3.188	3.190
Radiation	Synchrotron X-ray				
	$\lambda = 0.689871$ Å	$\lambda = 0.68987$ Å	$\lambda = 0.68987$ Å	$\lambda = 0.68987$ Å	$\lambda = 0.68987$ Å
2 $\theta$ range, deg.	5.4 – 39.6	5.4 – 39.7	5.4 – 31.6	5.4 – 31.6	5.4 – 39.6
Number of reflections	153	444	68	69	112
Parameters refined	10	23	9	10	10
R <sub>F</sub> , R <sub>P</sub> , R <sub>WP</sub>	0.064, 0.006, 0.009	0.055, 0.005, 0.007	0.050, 0.006, 0.007	0.045, 0.006, 0.007	0.067, 0.006, 0.008

**Table A 3 Selected interatomic distances (Å) for Na<sub>4-x</sub>MnV(PO<sub>4</sub>)<sub>3</sub> at different states of charge**

State of charge	Pristine	Charged to 3.5V	Charged to 3.8V	Charged to 4.0V	Discharged to 2.5V
M1-O1	2.014(3) ×3	2.05(1)	1.89(1) ×3	1.86(2) ×3	2.02(1) ×3
M1-O2	2.096(7) ×3	1.99(1)	1.88(1) ×3	1.85(1) ×3	2.112(7) ×3
M1-O3	-	2.21(1)	-	-	-
M1-O4	-	1.82(3)	-	-	-
M1-O5	-	2.16(2)	-	-	-
M1-O6	-	1.99(2)	-	-	-
$\bar{d}(\text{M1-O})$	2.06	2.04	1.89	1.86	2.06

Octahedral distortion

$$\Delta d = \frac{10^3}{N} \sum_{i=1}^N \frac{d_i - \bar{d}}{\bar{d}}$$

0.398

3.85

0.003

0.014

0.541

Shape of the transitional metal octahedron[148]

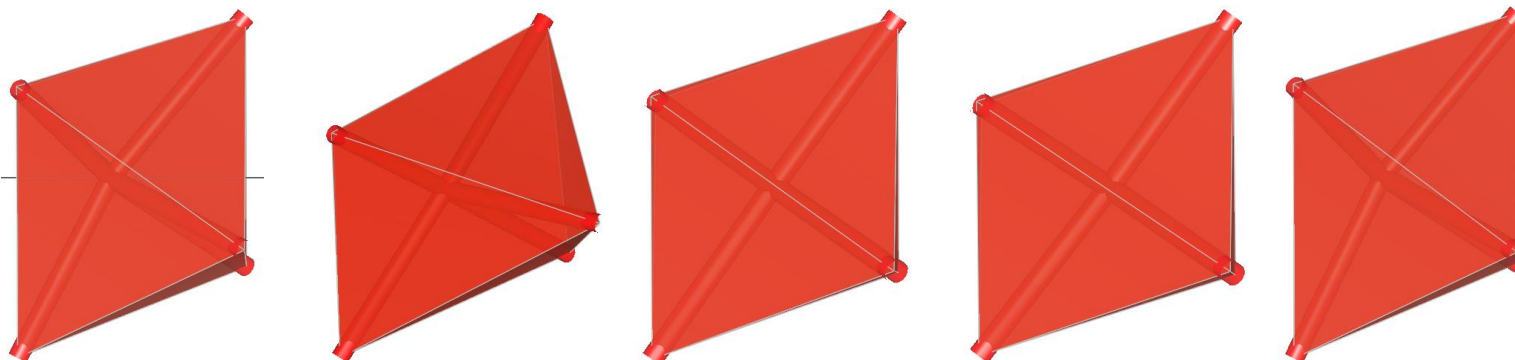


**Table A 3 (continued) Selected interatomic distances (Å) for Na<sub>4-x</sub>MnV(PO<sub>4</sub>)<sub>3</sub> at different states of charge**

State of charge	Pristine	Charged to 3.5V	Charged to 3.8V	Charged to 4.0V	Discharged to 2.5V
Na1-O2	2.452(5) ×6		2.545(9) ×6	2.55(1) ×6	2.468(6) ×6
Na1-O1		2.43(2) ×2			
Na1-O3		2.423(9) ×2			
Na1-O6		2.52(1) ×2			
$\bar{d}(\text{Na1-O})$	2.45	2.46	2.55	2.55	2.47
Na2-O1	2.572(7) ×2		2.63(1) ×2	2.70(2) ×2	2.548(9) ×2
Na2-O2	2.452(8) ×2		2.21(2) ×2	1.95(2) ×2	2.46(1) ×2
Na2-O2	2.546(8) ×2		2.36(1) ×2	2.46(2) ×2	2.59(1) ×2
Na2-O1		2.37(1) ×2			
Na2-O3		2.46(2) ×2			
Na2-O6		2.24(3) ×2			
Na3-O1		2.33(2)			
Na3-O1		2.49(2)			
Na3-O3		2.33(3)			
Na3-O5		2.32(2)			
Na3-O6		2.74(3)			
$\bar{d}(\text{Na2,3-O})$	2.52	2.41	2.40	2.37	2.53
P – O	1.535	1.535	1.535	1.535	1.535

**Table A 4 Fractional atomic coordinates, occupancy factors and atomic displacement parameters for pristine Na<sub>4-x</sub>MnV(PO<sub>4</sub>)<sub>3</sub>.**

Atom	Position	Occupancy	<i>x/a</i>	<i>y/b</i>	<i>z/c</i>	U <sub>iso</sub> , Å <sup>2</sup>
Na1	6 <i>b</i>	0.949(9)	0	0	0	0.0048(6)
Na2	18 <i>e</i>	0.904(4)	0.6423(5)	0	3/4	0.0048(6)
M1	12 <i>c</i>	0.5V/0.5Mn	0	0	0.64879(8)	0.0048(6)
P1	18 <i>e</i>	1	0.2995(6)	0	3/4	0.0048(6)
O1	36 <i>f</i>	1	0.1952(9)	-0.0094(9)	0.6919(3)	0.0048(6)
O2	36 <i>f</i>	1	0.4777(6)	0.1640(7)	0.7471(2)	0.0048(6)

**Table A 5 Fractional atomic coordinates, occupancy factors and atomic displacement parameters for Na<sub>4-x</sub>MnV(PO<sub>4</sub>)<sub>3</sub> charged to 3.5V.**

Atom	Position	Occupancy	<i>x/a</i>	<i>y/b</i>	<i>z/c</i>	U <sub>iso</sub> , Å <sup>2</sup>
Na1	4 <i>d</i>	0.98(1)	1/4	1/4	1/2	0.0039(6)
Na2	4 <i>e</i>	0.54(3)	0	0.392(3)	1/4	0.0039(6)
Na3	8 <i>f</i>	0.72(2)	0.325(1)	0.436(2)	0.293(2)	0.0039(6)
M1	8 <i>f</i>	0.5V/0.5Mn	0.1024(4)	0.2562(7)	0.0517(3)	0.0039(6)
P1	8 <i>f</i>	1	0.3550(5)	0.1157(6)	0.2594(9)	0.0039(6)
O1	8 <i>f</i>	1	0.2566(7)	0.187(2)	0.237(1)	0.0039(6)
O2	8 <i>f</i>	1	0.4566(7)	0.159(2)	0.452(1)	0.0039(6)
O3	8 <i>f</i>	1	0.343(2)	0.9429(6)	0.245(2)	0.0039(6)
O4	8 <i>f</i>	1	0.364(2)	0.174(1)	0.100(2)	0.0039(6)
P2	4 <i>e</i>	1	0	0.062(1)	1/4	0.0039(6)
O5	8 <i>f</i>	1	0.9234(9)	0.958(2)	0.083(2)	0.0039(6)
O6	8 <i>f</i>	1	0.9344(9)	0.175(2)	0.278(2)	0.0039(6)

**Table A 6 Fractional atomic coordinates, occupancy factors and atomic displacement parameters for Na<sub>4-x</sub>MnV(PO<sub>4</sub>)<sub>3</sub> charged to 3.8V.**

Atom	Position	Occupancy	<i>x/a</i>	<i>y/b</i>	<i>z/c</i>	U <sub>iso</sub> , Å <sup>2</sup>
Na1	6 <i>b</i>	1	0	0	0	0.024(2)
Na2	18 <i>e</i>	0.300(5)	0.604(2)	0	3/4	0.024(2)
M1	12 <i>c</i>	0.5V/0.5Mn	0	0	0.6446(1)	0.024(2)
P1	18 <i>e</i>	1	0.2889(5)	0	3/4	0.024(2)
O1	36 <i>f</i>	1	0.167(2)	-0.028(2)	0.6940(4)	0.024(2)
O2	36 <i>f</i>	1	0.476(1)	0.168(2)	0.7395(3)	0.024(2)

**Table A 7 Fractional atomic coordinates, occupancy factors and atomic displacement parameters for Na<sub>4-x</sub>MnV(PO<sub>4</sub>)<sub>3</sub> charged to 4.0V.**

Atom	Position	Occupancy	<i>x/a</i>	<i>y/b</i>	<i>z/c</i>	U <sub>iso</sub> , Å <sup>2</sup>
Na1	6 <i>b</i>	0.87(1)	0	0	0	0.016(2)
Na2	18 <i>e</i>	0.298(9)	0.573(3)	0	3/4	0.016(2)
M1	12 <i>c</i>	0.5V/0.5Mn	0	0	0.6444(2)	0.016(2)
P1	18 <i>e</i>	1	0.2905(6)	0	3/4	0.016(2)
O1	36 <i>f</i>	1	0.162(2)	-0.021(2)	0.6967(6)	0.016(2)
O2	36 <i>f</i>	1	0.479(1)	0.168(2)	0.7386(5)	0.016(2)

**Table A 8 Fractional atomic coordinates, occupancy factors and atomic displacement parameters for Na<sub>4-x</sub>MnV(PO<sub>4</sub>)<sub>3</sub> discharged to 2.5V.**

Atom	Position	Occupancy	<i>x/a</i>	<i>y/b</i>	<i>z/c</i>	U <sub>iso</sub> , Å <sup>2</sup>
Na1	6 <i>b</i>	0.986(8)	0	0	0	0.0190(7)
Na2	18 <i>e</i>	0.909(3)	0.6491(5)	0	3/4	0.0190(7)
M1	12 <i>c</i>	0.5V/0.5Mn	0	0	0.64936(9)	0.0190(7)
P1	18 <i>e</i>	1	0.2966(3)	0	3/4	0.0190(7)
O1	36 <i>f</i>	1	0.196(1)	-0.013(1)	0.6904(3)	0.0190(7)
O2	36 <i>f</i>	1	0.4767(7)	0.1615(9)	0.7468(3)	0.0190(7)

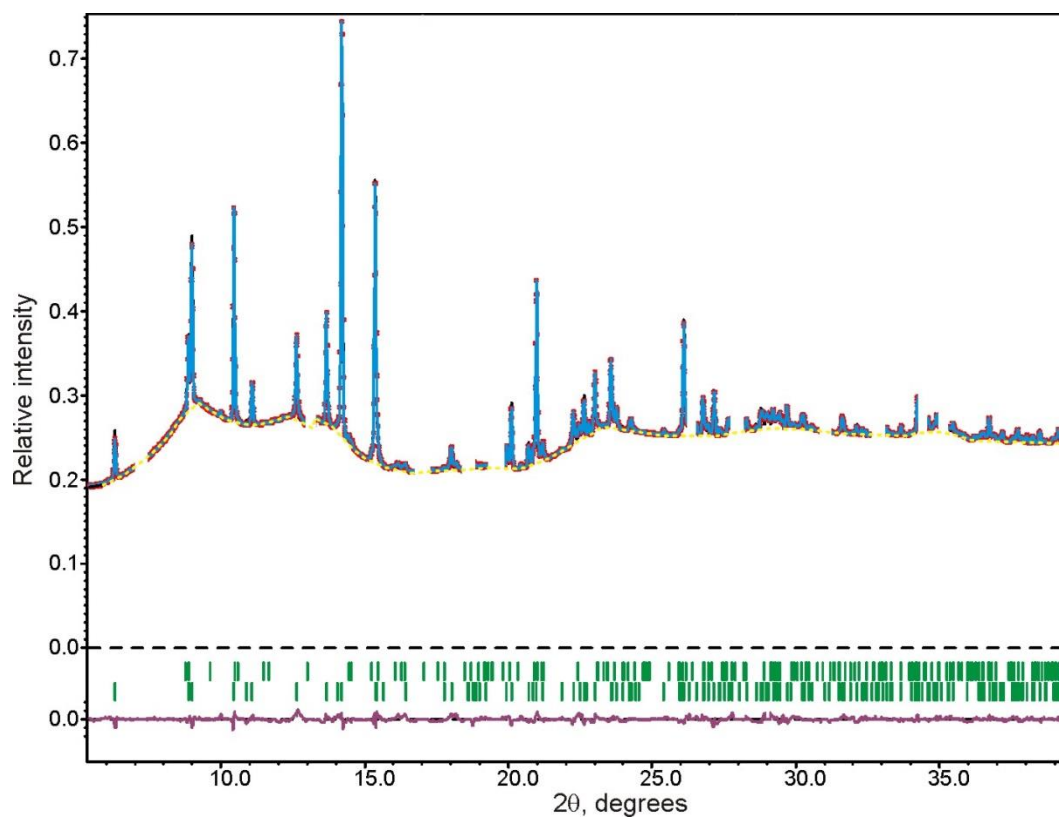


**Fig. A 8** Experimental, calculated and difference synchrotron X-ray diffraction patterns of pristine  $\text{Na}_{4-x}\text{MnV}(\text{PO}_4)_3$  after the Rietveld refinement. The contributions from the cell, anode and current collectors are omitted. Top row of bars indicate the reflections of the  $\text{NaMnPO}_4$  admixture (2.7 wt.%).

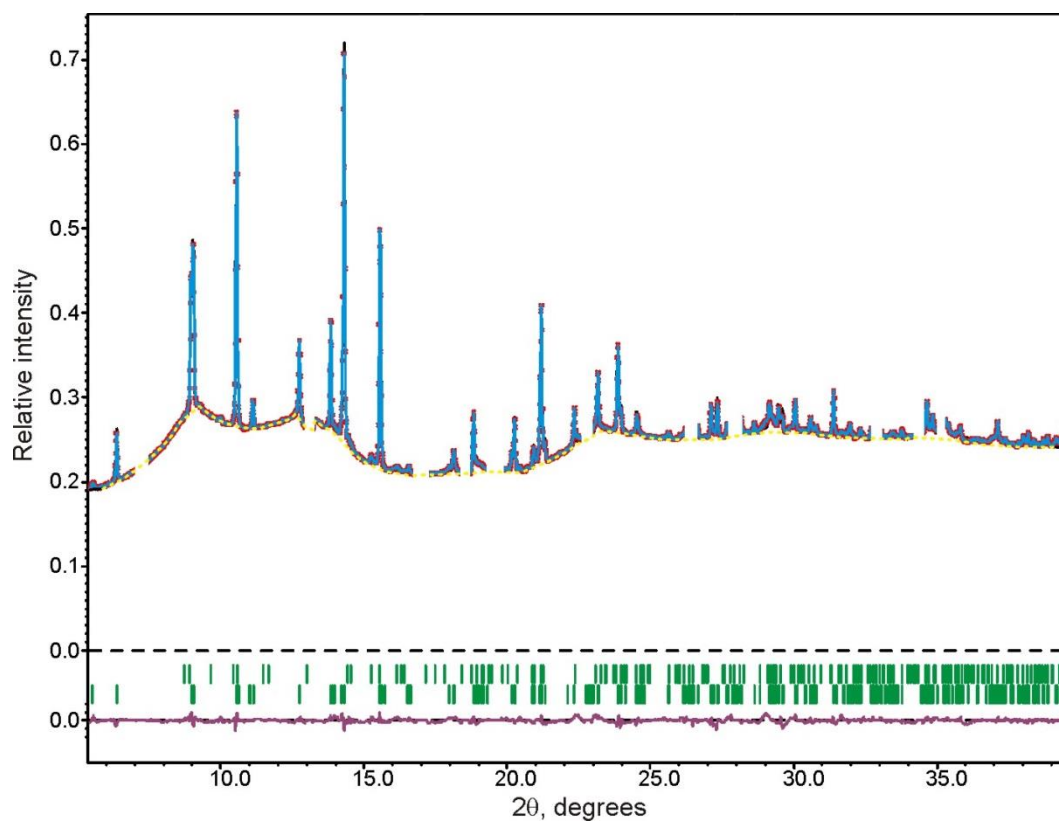


**Fig. A 9** Experimental, calculated and difference synchrotron X-ray diffraction patterns of Na<sub>4-x</sub>MnV(PO<sub>4</sub>)<sub>3</sub> charged to 3.5V after the Rietveld refinement. The contributions from the cell, anode and current collectors are omitted. Top row of bars indicate the reflections of the NaMnPO<sub>4</sub> admixture.

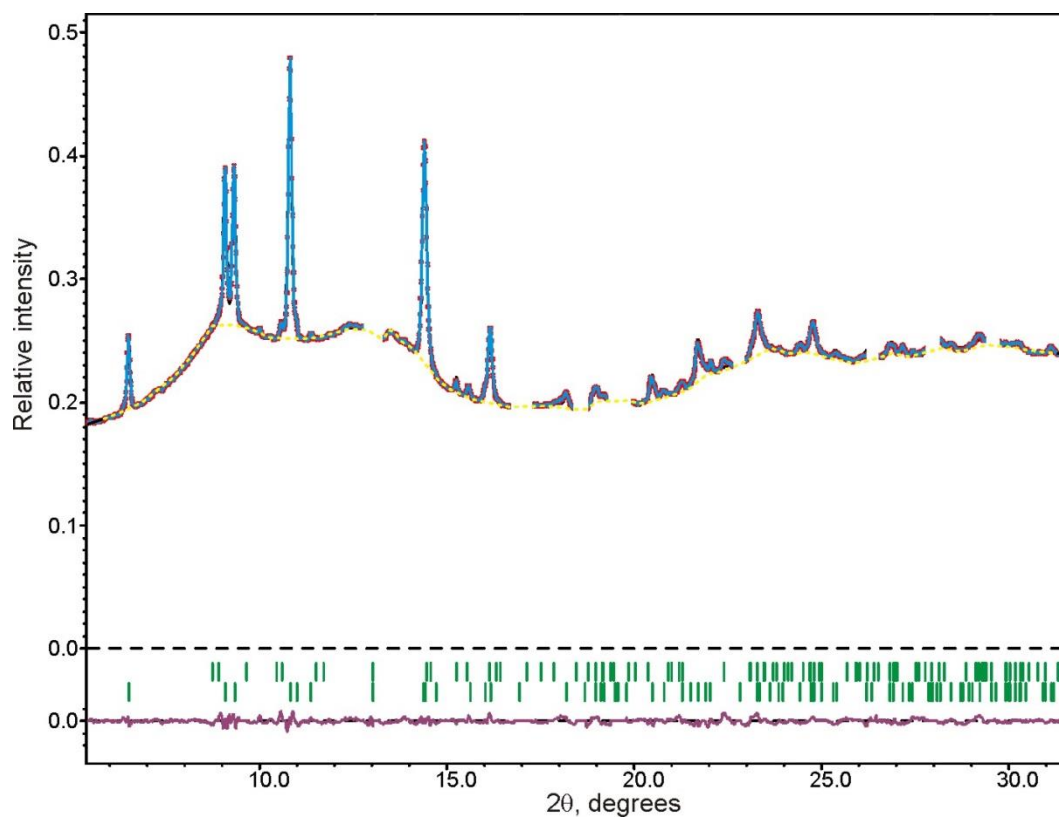


**Fig. A 10** Experimental, calculated and difference synchrotron X-ray diffraction patterns of  $\text{Na}_{4-x}\text{MnV}(\text{PO}_4)_3$  charged to 3.8V after the Rietveld refinement. The contributions from the cell, anode and current collectors are omitted. Top row of bars indicate the reflections of the  $\text{NaMnPO}_4$  admixture.

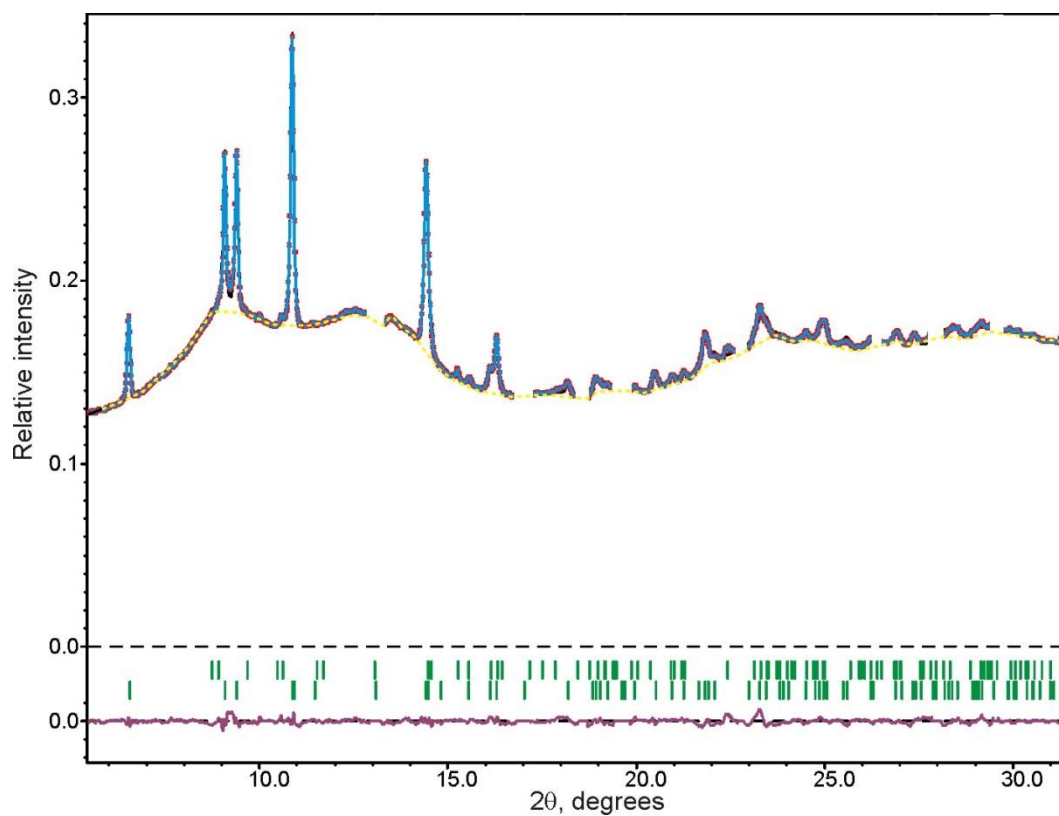


**Fig. A 11** Experimental, calculated and difference synchrotron X-ray diffraction patterns of  $\text{Na}_{4-x}\text{MnV}(\text{PO}_4)_3$  charged to 4.0V after the Rietveld refinement. The contributions from the cell, anode and current collectors are omitted. Top row of bars indicate the reflections of the  $\text{NaMnPO}_4$  admixture.

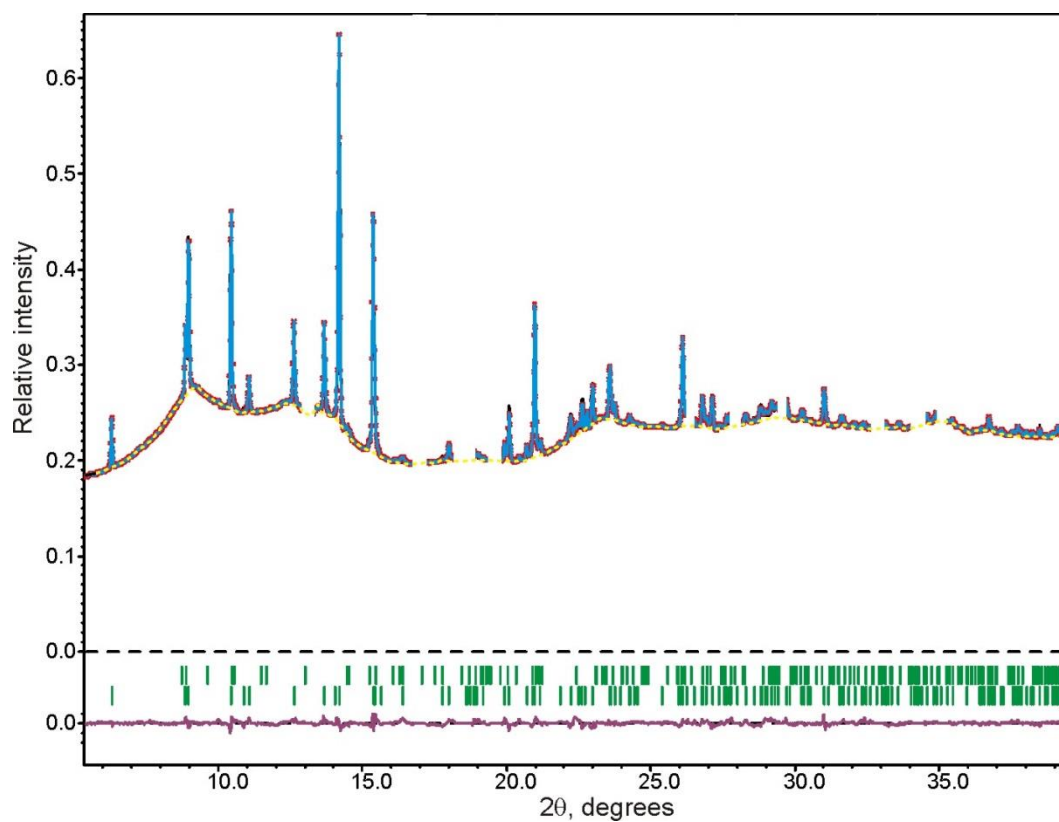


**Fig. A 12** Experimental, calculated and difference synchrotron X-ray diffraction patterns of  $\text{Na}_{4-x}\text{MnV}(\text{PO}_4)_3$  discharged to 2.5V after the Rietveld refinement. The contributions from the cell, anode and current collectors are omitted. Top row of bars indicate the reflections of the  $\text{NaMnPO}_4$  admixture.